COUPLING EFFECTS IN DIELECTRIC MICROCAVITIES

By

ELIJAH BRANDON DALE

Bachelor of Science
Oklahoma State University
Stillwater, Oklahoma
2005

Submitted to the Faculty of the
Graduate College of the
Oklahoma State University
In partial fulfillment of
The requirements for
The Degree of
DOCTOR OF PHILOSOPHY
May, 2010

COUPLING EFFECTS IN DIELECTRIC

MICROCAVITIES

Dissertation Approved:

Dr. Albert T. Rosenberger

Dissertation Advisor

Dr. Donna K. Bandy

Dr. Girish S. Agarwal

Dr. Bruce J. Ackerson

Dr. Eduardo G. Yukihara

Dr. Daniel R. Grischkowsky

Dr. A. Gordon Emslie

Dean of Graduate College

Acknowledgments

I would like to thank my family, friends and colleagues whose support has enabled me to fulfill a lifelong dream. In particular I would like to thank my advisor Dr. A. T. Rosenberger whose work is the foundation for this document in its entirety, even when not cited directly.

Foreword

The purpose of this document is both to inform the reader of the results of the work at hand as well as to provide a global perspective on the theoretical and experimental treatment of the system. Therefore, the mathematical formalism is limited to physically insightful derivations whenever possible and the reader is referred to more detailed demonstrations of formal analysis when necessary.

Some portions of this work originally appeared in an earlier oral qualifier document. As the oral qualifier was intended to be an early draft of this document these portions have been revised as necessary.

Table of Contents

List of Select Equations

Table of Figures

List of Common Symbols

Symbol	*Description*
α	Absorption Coefficient
α_s	Argument of Fiber Fields
$\widehat{\boldsymbol{a}}$	Debye Polarization Vector
a	Fiber Core Radius
b	Fiber Cladding Radius, Thermal Frequency Shift
β	Propagation Constant
c	Speed of Light, Heat Capacity
δ	Cavity Phase Detuning
C_{ij}	Waveguide Interaction Energy
χ	Scattering Amplitude Coefficient
ϵ	Emissivity
ϵ_i	Dielectric Constant
$E, \boldsymbol{E}$	Electric Field (Scalar, Vector)
F_c, F_i	Coupling enhancement, Intrinsic enhancement
F	Cavity Coefficient of Finesse
$\mathcal{F}$	Cavity Finesse
γ	Damping constant
Γ	Thermal Decay Rate
Υ	Ratio of Absorption Loss to Total Loss
$H, \boldsymbol{H}$	Magnetic field (scalar, vector)
$k, \boldsymbol{k}$	Wavenumber, Wavevector
K	Field Decay Rate
$\hbar_{ij}$	Cross Section Overlap Integral
κ_{ij}	Full Overlap Integral
k_{air}	Thermal Surface/Gas Conductivity
L	Circumference
l	Mode Indice
$\boldsymbol{L}$	Debye Vector
m	Dip Depth, Mode Indice
M	Mass
$\boldsymbol{M}$	Debye Vector
$\boldsymbol{N}$	Debye Vector
n_i, n_{eff}	Index of Refraction, Effective Index of Refraction
η	Polarization Basis Alignment Angle
ν, ν_0	Frequency, Central Frequency
$\Delta\nu, \Delta\nu_c, \Delta\nu_i$	Spectral Width (Total, Coupling, Intrinsic)
$\delta\nu$	Free Spectral Range
ω, ω_o	Angular Frequency, Angular Central Frequency

P_i	Power, Depolarization Factor
ϕ	Polarization Phase Angle
ψ	Scalar Debye Potential
Q_l, Q_c, Q_i	Quality Factor (Loaded, Coupling, Intrinsic)
R	Reflection Probability
r_i	Reflection Amplitude Coefficient
R_s	Microsphere Radius
σ	Stefan-Boltzmann Constant
T	Transmission Probability
t	Amplitude Transmission Coefficient
T_{rm}	Deviation from Room Temperature
$\tau_{thermal}, \tau_{\mathrm{rt}}, \tau_c$	Lifetime (Thermal, Round-Trip, Cavity)
μ_o	Vacuum Permeability
θ	Half Linewidths
v	Phase Velocity
x	Ratio of Coupling to Intrinsic Loss
ξ	Power Enhancement Factor

A number of symbols are used in a context based manner most notably m, b, ϵ, E and n. The reader should take care as to avoid confusion when the variables are encountered and consult the surrounding material for an unambiguous usage.

Chapter 1 Introduction

For many years highly confined traveling wave optical resonances of dielectric cavities, known as whispering gallery modes (WGMs), have been of great interest to scientists in a plethora of disciplines [1-11]. The historical roots of the analogous acoustic effect, also called WGMs, can be used to give one a conceptual insight into the structure and confinement of the optical field within the cavity. In 1938 A. E. Bate wrote [12] in the Proceedings of the Physical Society of a disagreement between Lord Rayleigh and C. V. Raman concerning the nature of acoustic wave propagation in St. Paul's Cathedral in London; in his paper he states:

> ***"Sabine… referred to a whispering gallery as one so shaped that faint sounds can be heard at extraordinary distances, as a result either of focusing or of the creeping (as Rayleigh… termed it) of sound waves round a curved wall. The phenomenon in those buildings in which focusing occurs requires no explanation, and is usually apparent at one region only, the focus; but the galleries of the second category, that in St Paul's being the classic example, still await complete explanation."***

He concludes, after experimental investigation of the cathedral:

> ***"The sound which is heard is that which travels round the wall by successive reflections along short chords. This sound suffers very little absorption at the hard smooth wall during reflection, so that the main energy-loss would appear to be due to the divergence of the sound. This, however, is minimized by the reinforcement of incident and reflected waves which combine to produce waves with fronts traveling at right angles to the wall."***

This is also the very structure that an optical field will assume if "whispered" into a dielectric cavity. How then does one whisper into an optical cavity? One can whisper into a cavity

through an effect not described by the classical mechanics which governed the disagreement between Lord Rayleigh and C. V. Raman. The optical field, or photons as we would say today, must be tunneled into and out of the cavity in order to effectively trap light within. To that end, optical whispers can always be found, due to continuity boundary conditions when an electromagnetic field is subject to total internal reflection, and are fittingly termed evanescent: "to vanish". These exponentially decaying evanescent fields extend into the adjacent medium and allow one to "whisper", conceptually speaking, into an optical cavity with but a slight perturbation on the structure of a resonance. The optical WGM excited within the dielectric cavity itself remains a "whisper" in the sense that it travels just under the surface, tightly confined by total internal reflection and producing its own external evanescent field. Perturbation is an important point to stress, because to achieve the many fundamental physical effects that modern research scientists are interested in, one can not disrupt the low-loss, high-confinement nature of the resulting resonance with a strong coupling mechanism. It is this very feature set that produces the rich physical environment of high cavity quality factors and small effective mode volumes that can be used to explore a myriad of fundamental and applied processes including cavity quantum electrodynamics [1], nonlinear optics [2-3], microlasers [4-5], laser stabilization [6], mechanical mode cooling [7], evanescent-wave sensors [8-9], optical switches [10], optical capacitors [11] and photonic clocks [7].

Experimentally, there are two preferred methods in use to "whisper" into a dielectric cavity. The older of the two, termed prism coupling, places the cavity in contact with a prism where a tunable laser is focused to a small spot size at the prism-resonator interface at an angle greater than the critical angle [6]. The total internal reflection of the laser field produces an evanescent field extending from the prism surface into the volume of the cavity which allows for energy transfer into the cavity. The reverse is also true, in that the cavity produces an evanescent field

within that prism or a second diametrically opposed prism which allows energy to flow out of the system. While effective, this type of coupling is rarely used in current research as it is notoriously difficult experimentally. The far more common practice of fiber coupling, in which a step index optical fiber is radically tapered, say from an initial diameter of 125 μm to 2 μm, is conceptually similar [13]. When the field is propagating in the untapered region of the fiber it is confined within the core due to total internal reflection between the core and the cladding. As the field propagates into the tapered region it transforms from core-cladding guidance to cladding-air guidance, producing an external evanescent field which extends into an adjacent cavity. Likewise, the evanescent field of the cavity extends simultaneously, while in steady state, back into the fiber providing a ready means of energy transport out of the system. In either coupling method, by using a second coupler one can monitor the signal transmitted through the system, a resonance peak; using a single coupler one typically monitors the sum of the transmitted and incident signals, a resonance dip. Fiber coupling is considered exclusively for the remainder of this dissertation, whereas prism coupling has been presented only for conceptual completeness.

It is the intention of this dissertation to present the treatment of these micro-resonator systems in a coherent global perspective for the reader. Because of this, the novel additions to the breadth of previous scientific work have been intentionally wrapped, seamlessly, into the text. However, chapter 6, which summarizes this work sets forth to make those distinctions of novelty and attribution that the preceding chapters have obscured. The reader is then referred to this summary chapter for both attribution and specific novel additions to the scientific literature. The remaining chapters are structured as follows. Chapter 2 sets out both to derive a formal mathematical framework to understand the system and further to validate the conclusions through independent analysis. In chapter 3 we extend the previous formal

framework to include multiple resonant waveguide coupling and apply this model to an experimental system for verification. We once again extend the basic framework in chapter 4 to include optical surface plasmonic coupling effects and experimental applications of these extensions. Finally, chapter 5 revisits the basic model, generalizing it, to include internal and external polarization coupling effects encountered in the experimental system.

Chapter 2 General Methodology: The Foundations of Microcavity Modeling

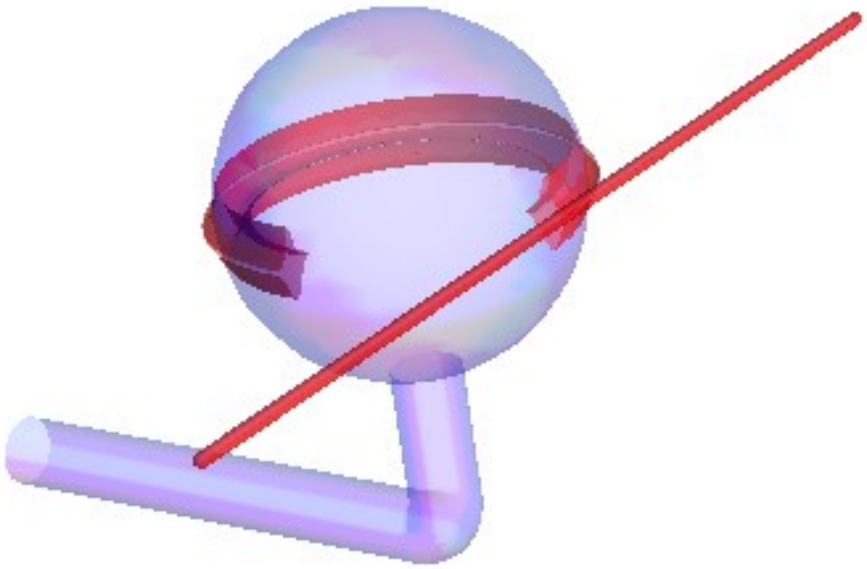

Figure 1. Microcavity which is being pumped by a tapered fiber, where red indicates laser light. This system is the starting point for modeling.

In almost all experimental systems, little information can be obtained through direct observation of a system's response. Rather, these observations must be put into the context of an appropriate theory which allows for the extraction of pertinent information regarding the system. This basic theory, when applied to an experimental system, can be considered a

mathematical model of the physical system. It is through the relative comparison of known changes to the experimental system parameters and the corresponding changes to the model parameters that one may verify the validity of the model. This process is a crucial first step in establishing not only the fundamental physics that governs a system response, but also the applied physics that can be employed when one attempts to use the system for some practical purpose. The intent of the following chapter is to demonstrate the derivation of a straightforward experimentally useful microcavity model of the system, shown in Fig. 1, which has been fully verified. This is a critical first step in establishing the validity of the foundation that the remaining work will be built on. The preliminary model will be validated through additional modeling based on fundamental physics concepts which then can be experimentally determined. Finally, the individual pieces will be combined with the preliminary model and shown to be accurately predictive of the overall experimental system response to various changes.

Experimental System:

Given that the experimental system, sketched in Fig. 2, will be employed at every conceivable juncture to verify and extend the model, it is pertinent to describe it first. The experimental setup employs a free space tunable diode laser that is injected into an integrated fiber optic component network which includes the fiber-microsphere system. The laser is frequency scanned across a WGM resonance while the system's output power and polarization are monitored in both directions, and the system's transient (~ 1 ns) responses are monitored in the forward direction without polarization analysis. The detector signals are captured with the oscilloscopes which are further connected to a laptop computer (not shown) for additional data analysis.

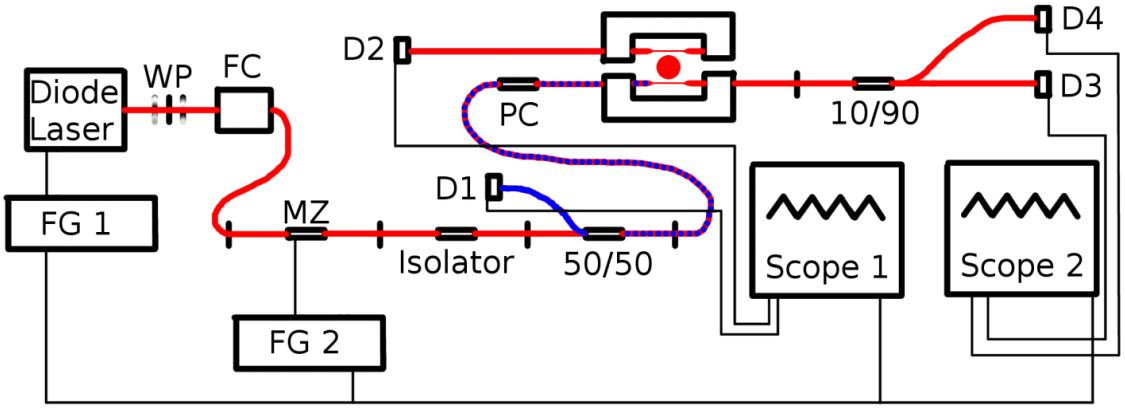

Figure 2. The experimental setup. Black lines represent electrical connects, red lines represent forward propagating laser light, and blue lines represent backward propagating laser light.

- *Black Vertical Lines: butt connections between fiber optic components*
- *Diode Laser: New Focus Velocity tunable diode laser (1508 nm to 1580 nm)*
- *WP: wave plates, one half wave and two quarter wave*
- *FC: free space fiber coupler on a high resolution 3D stage*
- *MZ: fiber coupled high speed (1 MHz) Mach- Zehnder modulator*
- *Isolator: fiber coupled optical isolator*
- *50/50: reverse installed 50% fiber coupled splitter*
- *PC: compression based polarization controller (effectively 3 fractional waveplates)*
- *10/90: forward installed 10%/90% fiber coupled splitter*
- *FG1: 100 MHz arbitrary function generator to drive the laser frequency scan (operated typically at 10 Hz)*
- *FG2: 100 MHz arbitrary function generator to drive Mach-Zehnder modulator, triggered by FG1*
- *Scope 1: oscilloscope, triggered by FG1*
- *Scope 2: oscilloscope, triggered by FG1*
- *D1: Newport NIR photodetector, monitors backscattered power*
- *D2: Newport NIR photodetector, monitors drop fiber transmitted cavity power and polarization*
- *D3: Newport NIR photodetector array, monitors system through power and polarization (see Fig. 10)*
- *D4: Thor Labs high speed photo detector, monitors transient system responses of nanosecond order*

Ring Cavity:

While the particular physical structure of the electromagnetic fields in both the microcavity and tapered fiber will be shown to be important (see coupled mode theory below), the fundamental physical system response can be most readily analyzed using a resonant cavity model. Given the spherical geometry of the experimental cavity and the planar optical path within, the natural choice of an analogous cavity is a ring cavity [14-15]. This choice is justified

by the fact that it is possible to choose parameters of the experimental fiber-microsphere system to ensure that a single fiber mode is interacting with one WGM of the sphere at a time [14, 16]. This ring cavity is treated as four mirrors, with all but one mirror having perfect reflectance; see Fig. 3. In the treatment of any cavity structure one must be careful with the treatment of phase, and in this analogy we explicitly treat reflections as accumulating no phase and transmissions as accumulating a $\pi/2$ phase shift. Therefore a field transmitted into the cavity and then back out of the cavity, on resonance, accumulates a total phase shift of π with respect to the incident field.

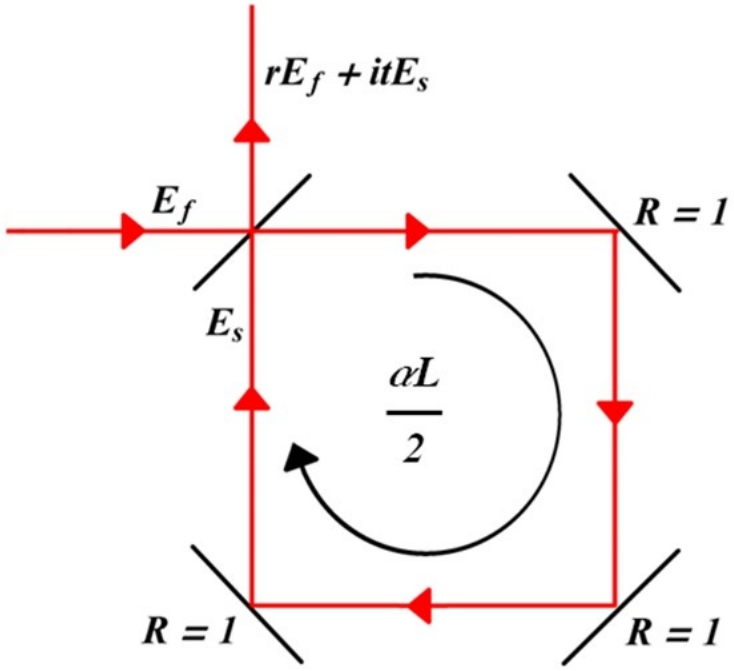

Figure 3. Analogous ring cavity to describe resonance behavior of the WGM.

To find the sphere field E_s we consider transmission into the cavity from the fiber field E_f , after one round trip at the location just before the field re-encounters the partially transmitting mirror, and then sum over cavity round trips:

$$E_s = itE_f e^{-\frac{\alpha L}{2}} e^{i\delta} + r\left(e^{-\frac{\alpha L}{2}} e^{i\delta}\right)^2 itE_f + r\left(e^{-\frac{\alpha L}{2}} e^{i\delta}\right)^2 \left(re^{-\frac{\alpha L}{2}} e^{i\delta}\right) itE_f \qquad (1)$$

$$+ r\left(e^{-\frac{\alpha L}{2}} e^{i\delta}\right)^2 \left(re^{-\frac{\alpha L}{2}} e^{i\delta}\right)\left(re^{-\frac{\alpha L}{2}} e^{i\delta}\right) itE_f + \cdots$$

$$= itE_f e^{-\frac{\alpha L}{2}} e^{i\delta} \left(1 + \left(re^{-\frac{\alpha L}{2}} e^{i\delta}\right) + \left(re^{-\frac{\alpha L}{2}} e^{i\delta}\right)^2 + \ldots\right).$$

Here it is the amplitude transmission coefficient into the cavity and is taken to be imaginary, r is the (real) amplitude reflection coefficient of the cavity, δ is the phase detuning from cavity resonance (defined in detail later) and αL is the round trip cavity power loss ($\alpha L/2$ the field loss); here α is an effective intrinsic loss (scattering + absorption) coefficient, and $L = 2\pi R_s$ is the circumference of the sphere of radius R_s. This sum can be written in closed form as

$$E_s = itE_f e^{-\frac{\alpha L}{2}} e^{i\delta} \sum_{n=0}^{\infty} (re^{-\frac{\alpha L}{2}} e^{i\delta})^n = \frac{itE_f e^{-\frac{\alpha L}{2}} e^{i\delta}}{1 - re^{-\frac{\alpha L}{2}} e^{i\delta}}. \qquad (2)$$

To coincide with experimental data we sum the untransmitted fiber field and the out-of-phase cavity output:

$$E_t = rE_f + itE_s = rE_f - \frac{t^2 e^{-\frac{\alpha L}{2}} e^{i\delta}}{1 - re^{-\frac{\alpha L}{2}} e^{i\delta}} E_f = E_f \left(\frac{r - e^{-\frac{\alpha L}{2}} e^{i\delta}}{1 - re^{-\frac{\alpha L}{2}} e^{i\delta}}\right). \qquad (3)$$

The measured throughput power P_t is then computed from the incident fiber power, P_f, as:

$$P_t \equiv P_f \left|\frac{E_t}{E_f}\right|^2 = P_f \left(\frac{r - e^{-\frac{\alpha L}{2}} e^{i\delta}}{1 - re^{-\frac{\alpha L}{2}} e^{i\delta}}\right)\left(\frac{r - e^{-\frac{\alpha L}{2}} e^{-i\delta}}{1 - re^{-\frac{\alpha L}{2}} e^{-i\delta}}\right). \qquad (4)$$

$$P_t = P_f \frac{1 + e^{\alpha L} r^2 - 2e^{\frac{\alpha L}{2}} r \cos(\delta)}{e^{\alpha L} + r^2 - 2e^{\frac{\alpha L}{2}} r \cos(\delta)}. \quad (5)$$

The relationship of observed throughput power to phase (or frequency) detuning takes the structure of a Lorentzian dip, shown in Fig. 4, as would be expected for a damped harmonic oscillator [17] (pg. 500).

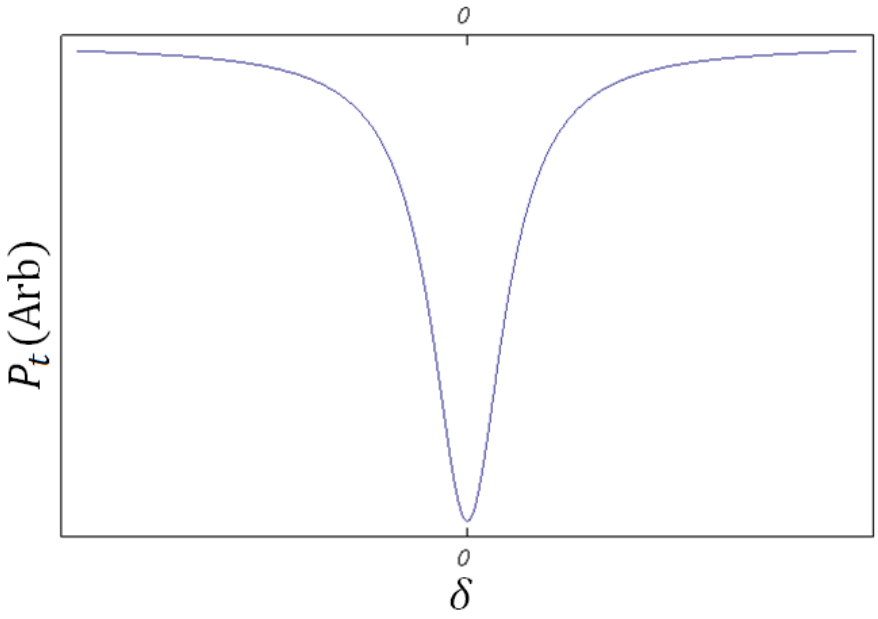

Figure 4. Lorentzian line shape structure of the analogous ring cavity resonance for arbitrary parameters.

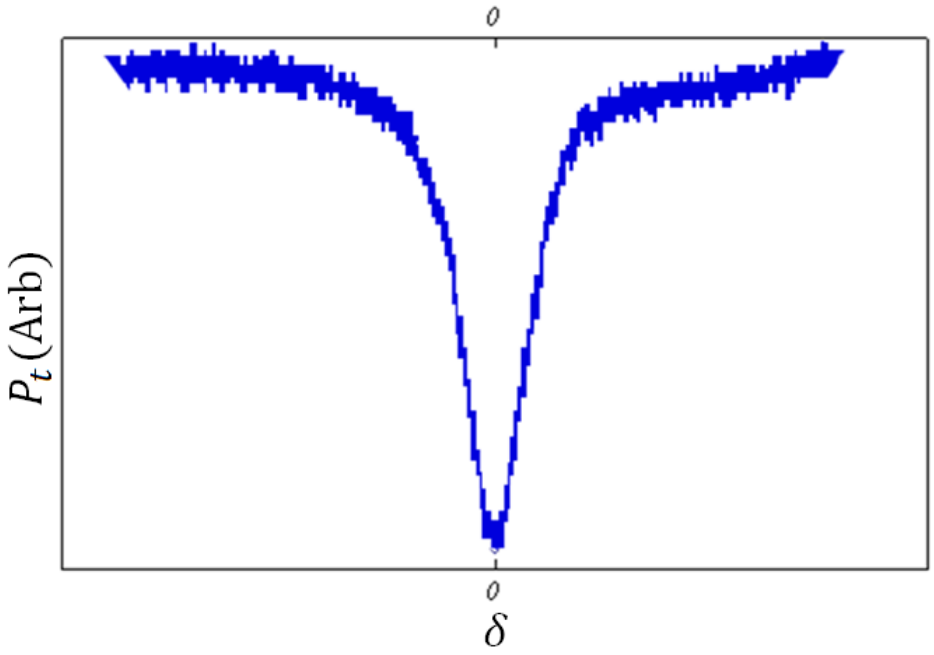

Figure 5. Lorentzian structure of an experimentally observed resonance. The slight asymmetry visible on the right is caused by a weak overlapping second resonance.

This coincides very nicely with the observed experimental resonance structure shown in Fig. 5. With the model now in place the system can begin to be characterized in terms of experimental observables. Once beyond the general structure of the resonance, which is observed to be Lorentzian, there are two prominent observables: the decrease in throughput power on resonance (dip depth m), and the spectral width of the resonance $\Delta\nu$.

Before beginning the actual analysis let us verify our ansatz on the phase relation between cavity transmission and reflection coefficients. We can construct a power conservation equation from Eq. (3) by dropping the assumed phase relations and taking the cavity to be on resonance with no loss. In this construction then input and output powers must be identical and we can use this to determine the structure of the aforementioned coefficients. Assuming that the reflection, r, and transmission, t, coefficients for incidence from either side of the partially

transmitting mirror are symmetric the power conservation equation is constructed from the fields as,

$$E_f = E_t = rE_f + \frac{t^2}{1-r}E_f, \tag{6}$$

$$1 = r + \frac{t^2}{1-r} = \frac{r(1-r)}{1-r} + \frac{t^2}{1-r} = \frac{r + (t^2 - r^2)}{1-r}.$$

Now if we take the square modulus we find the required power conservation equation,

$$1 = \frac{r^*r + r(t^2 - r^2)^* + r^*(t^2 - r^2) + (t^2 - r^2)^*(t^2 - r^2)}{r^*r - r - r^* + 1}, \tag{7}$$

which can be satisfied if $(t^2 - r^2) = -1$ subject to the constraints imposed by conservation of energy, namely $r^*r + t^*t = 1$. To check that our treatment enforces power conservation let the transmission coefficient be pure imaginary and the reflection coefficient be real

$$t \equiv i\,\xi, \tag{8}$$

$$r = \sqrt{1 - t^*t} = \sqrt{1 - \xi^2},$$

$$1 = r^2 - t^2 = (\sqrt{1 - \xi^2})^2 - (i\,\xi)^2 = 1 - \xi^2 + \xi^2 = 1.$$

Thus we can conclude that, given our prior assumptions, there is a required i phase shift between reflection and transmission amplitude coefficients and that the power is conserved in our system.

To find the dip depth we begin with a dimensionless version of Eq. (5) taken to be on resonance ($\delta = 0$):

$$m \equiv 1 - \frac{P_t(0)}{P_f}. \tag{9}$$

With simplification this can be expressed as

$$m = 1 - \frac{(e^{\alpha L/2} r - 1)^2}{(e^{\alpha L/2} - r)^2}. \tag{10}$$

Now let us assume the loss term is small, $\alpha L << 1$. While the validity of this is yet to be determined it allows for a series expansion around zero for the exponential. When substituted into Eq. (10) we have

$$m \simeq 1 - \frac{((1 + \frac{\alpha L}{2}) r - 1)^2}{((1 + \frac{\alpha L}{2}) - r)^2}. \tag{11}$$

Rather than expressing m in terms of an amplitude reflection coefficient it would be experimentally advantageous to express m in terms of the real power transmission coefficient, $T \equiv t^* t$. For this, conservation of energy is employed in the traditional manner,

$$r^* r + t^* t = R + T = 1 \tag{12}$$

$$\text{or rather, since } r \text{ is real,}$$

$$r = \sqrt{1 - T}.$$

With this substitution m becomes

$$m \simeq \frac{\frac{T}{\alpha L}(4 + \alpha L)}{(\frac{2}{\alpha L} - \frac{2}{\alpha L}\sqrt{1 - T} + 1)^2}. \tag{13}$$

Let us assume the transmission to be small, $T << 1$, and take a series expansion to first order in T so that $\sqrt{1-T} \simeq 1 - \mathrm{T}/2$. The dip depth then becomes

$$m \simeq \frac{\frac{T}{\alpha L}(4+\alpha L)}{(\frac{T}{\alpha L}+1)^2}. \tag{14}$$

Now since it has been assumed that the loss term is small, $4 + \alpha L \simeq 4$, the dip depth can be expressed in terms of the dimensionless variable x as

$$m \simeq \frac{4x}{(1+x)^2}, \tag{15}$$

where the dimensionless variable x is defined as

$$x \equiv \frac{T}{\alpha L}. \tag{16}$$

This then has the physical significance that the on-resonance power observed in the through fiber is singularly a function of the ratio of coupling to intrinsic losses. Further physical insight can be garnered by further evaluating the power enhancement in the sphere as a function of this ratio. We define the dimensionless power enhancement ξ as the ratio of input power to power within the sphere on resonance, which is expressed as the square modulus of Eq. (2) with $\delta = 0$,

$$\xi = \frac{T\, e^{-\alpha L}}{\left(1 - e^{-\frac{\alpha L}{2}} r\right)^2} \simeq \frac{4T}{(T+\alpha L)^2} = \frac{m}{\alpha L}. \tag{17}$$

We then seek to maximize this function by minimizing the first derivatives in terms of the ratio x. We rigorously maximize the enhancement by varying the coupling loss with fixed intrinsic loss as

$$\frac{\partial \xi}{\partial T} = \frac{e^{\alpha L/2} + e^{3\alpha L/2} + \dfrac{e^{\alpha L}(-2+T)}{\sqrt{1-T}}}{1 + e^{\alpha L} - 2e^{\alpha L/2}\sqrt{1-T} - T} = 0. \tag{18}$$

This is solved as

$$\alpha L = \ln\left(\frac{1}{1-T}\right) \simeq T. \tag{19}$$

We can arrive at this very same conclusion in a more intuitive manner by fixing the intrinsic loss in Eq. (17) and maximizing the dip depth m as

$$\xi_{max} \simeq \frac{m_{max}}{\alpha L} = \frac{1}{\alpha L}, \tag{20}$$

where we can recognize that maximum obtainable dip depth is unity and this occurs when $\alpha L = T$. Physically we conclude that the maximum obtainable power enhancement of the sphere field for any given intrinsic loss will be when parameter x is unity or rather when the transmission coefficient and intrinsic cavity loss are equal.

With the knowledge afforded from the parameter x, we can now make an analogy to the classical harmonic oscillator. Just as this type of oscillator [18] (Pg. 110) has three distinct regimes of system response based on the strength of damping in the system (underdamped, critically damped and overdamped) the optical oscillator will likewise have three distinct damping regimes. However, we must make the distinction that in our optical system damping is not the most pertinent parameter, but rather the pertinent observable is coupling strength.

With this the response regimes are undercoupled: $T < \alpha L$, critically coupled: $T = \alpha L$ and overcoupled: $T > \alpha L$. Furthermore, these regimes clearly correspond to $x < 1$, $x = 1$ and $x > 1$ respectively. Notice that the dip depth m (Eq. (15)) is quadratic in the parameter x. This then leads to two solutions for x given any particular dip depth which is less than 100%. These two solutions are analogous to both under- and overcoupled regimes of a damped harmonic oscillator.

For further analysis it becomes convenient to derive an analytic Lorentzian form for the power spectrum of an observed WGM. To begin assume that the intracavity power can be expressed in terms of a familiar optical Lorentzian with resonance centered at zero as [17] (pg 500),

$$P_s(\delta) = P_s(0)\frac{(\frac{\gamma}{2})^2}{(\delta)^2 + (\frac{\gamma}{2})^2}, \tag{21}$$

where γ is a damping constant which is to be determined. We then relate this to the known analytic expression for the microcavity power (proportional to Eq. (2)'s modulus squared) and solve for the damping constant. Given that we are only interested in a particular resonance and the cavity will have a resonance every free spectral range ($\cos(\delta) = 1 \Rightarrow \delta = 2\pi n$ for $n = 1,2,3 \ldots$), it is necessary to expand the analytic detuning parameter $\cos(\delta)$ to second order in δ around 0 to avoid a transcendental solution for damping. Applying this alongside our previous assumptions on small transmission and low intrinsic loss, Eq. (2) becomes,

$$\frac{E_s}{E_f} \simeq \frac{ite^{-\frac{\alpha L}{2}}e^{i\delta}}{1 - r\left(1 - \frac{\alpha L}{2}\right)(1 + i\delta)} \simeq \frac{ite^{-\frac{\alpha L}{2}}e^{i\delta}}{1 - r - i\delta + \frac{\alpha L}{2}}. \tag{22}$$

Taking the square modulus we regain an equation in terms of power as

$$\frac{P_s}{P_f} \simeq \frac{T}{\left(\frac{T+\alpha L}{2}\right)^2 + \delta^2} = \frac{4T}{T+\alpha L} \frac{\left(\frac{T+\alpha L}{2}\right)^2}{\left(\frac{T+\alpha L}{2}\right)^2 + \delta^2}. \tag{23}$$

We can now compare forms with that of the analytic Lorentzian given in Eq. (21) to identify the damping parameter γ as

$$\gamma \simeq T + \alpha L. \tag{24}$$

Notice now that Eq. (17) for peak power enhancement can be expressed in a more concise form as

$$\xi = \frac{4\,T}{\gamma^2}. \tag{25}$$

Finally, the total expression for the sphere power can be written concisely as

$$P_s(\delta) = P_f \frac{4\,T}{\gamma^2} \left(\frac{\left(\frac{\gamma}{2}\right)^2}{(\delta)^2 + \left(\frac{\gamma}{2}\right)^2} \right), \tag{26}$$

and the detuning dependent power enhancement as

$$\xi(\delta) = \frac{4\,T}{\gamma^2} \left(\frac{\left(\frac{\gamma}{2}\right)^2}{(\delta)^2 + \left(\frac{\gamma}{2}\right)^2} \right). \tag{27}$$

With the microcavity power spectrum now expressed in a traditional Lorentzian form the spectral width can be readily evaluated. By inspection the half width of the resonance will be achieved when the denominator of Eq. (27) doubles, $\delta_{\pm} = \pm\,\gamma/2$. This will then produce a full

width at half max power width (FWHM) of γ. Notice that δ is dimensionless in the above expression and as such requires physical interpretation.

Let us assume a plane wave propagating with angular frequency ω and wave vector k along a circular path of length $L = 2\pi R_s$ where the cavity radius is again R_s. Further, let us assume an adjacent natural resonance of the system with characteristics ω_o and k_o is available in the cavity. The relative phase detuning of the plane wave from the cavity resonance can then be expressed as the difference between the phases after one round trip *L* , or rather,

$$\delta = kL - k_o L = (k - k_o)L. \tag{28}$$

The wave vector k can now be expressed as the ratio of angular frequency (ω) to propagation velocity *v*. This allows the detuning to be expressed in terms of the cavity mode's effective index of refraction $n_{eff} \equiv c/v$ and frequency ν as,

$$\delta = \left(\frac{\omega}{v} - \frac{\omega_o}{v}\right) L = \left(\frac{2\pi n_{eff}\nu}{c} - \frac{2\pi n_{eff}\nu_o}{c}\right) L = \frac{2\pi n_{eff} L}{c}(\nu - \nu_0). \tag{29}$$

Where an effective index has been used rather than the material index because the cavity modes will be shown, see page 29, to have a slightly lower phase velocity (by 1-2% in our system) than the material index would suggest. Notice that the pre-factor term is the ratio of the cavity's optical path length to propagation velocity and therefore has the physical significance of the time associated with a single round trip ($\tau_{\mathrm{rt}} \equiv n_{eff} L/c$). The round trip time is also the inverse of the free spectral range of the cavity $\delta\nu$ which is defined as the frequency spacing between adjacent identical resonant modes, or rather a full rotation in the cosine term of Eq. (5). The detuning can then be written succinctly in measurable quantities as

$$\delta = 2\pi\tau_{rt}(\nu - \nu_0) = \frac{2\pi(\nu - \nu_0)}{\delta\nu}. \tag{30}$$

Let us now derive a physical interpretation of the measurable spectral width of the resonance defined, in terms of phase, by γ. Looking at the positive and negative detuning from the central frequency ν_0 we have

$$\gamma = \delta_+ - \delta_- = 2\pi\tau_{rt}(\nu_+ - \nu_0 - \nu_- + \nu_0) \equiv 2\pi\tau_{rt}(\Delta\nu) = 2\pi\frac{\Delta\nu}{\delta\nu}. \tag{31}$$

However, from the previous analysis we also know the phase spectral width (or phase linewidth) in terms of the cavity round trip loss. Equating these expressions we have

$$\gamma = T + \alpha L \equiv 2\pi\tau_{rt}(\Delta\nu) = 2\pi\frac{\Delta\nu}{\delta\nu}. \tag{32}$$

Solving for the measurable linewidth $\Delta\nu$ we have

$$\Delta\nu = \frac{c}{2\pi n_{eff}}\left(\frac{T}{L} + \alpha\right). \tag{33}$$

Let us now separate the contributions to the total linewidth into components caused by coupling (*c*) and intrinsic loss (*i*) written in terms of partial linewidths as

$$\Delta\nu_i \equiv \frac{c\alpha}{2\pi n_{eff}}, \tag{34}$$

$$\Delta\nu_c \equiv \frac{cT}{2\pi n_{eff}L}.$$

The linewidth written in component form then becomes

$$\Delta\nu = \Delta\nu_i + \Delta\nu_c. \tag{35}$$

We can now begin the discussion on the cavity quality factor Q which can be thought of as the ratio of the energy of an undamped oscillation divided by the work done per cycle [19] (pages 317-372). Formally, the Q can be expressed as $2\,\pi$ times the ratio of time-averaged energy stored in the cavity to the cavity's energy loss per optical cycle. Mirroring the derivation outlined in Jackson [19] (pages 317-372), if U is defined as the average energy in a cavity then the time rate of change of the energy is the power dissipated per cycle and the quality factor can be expressed as

$$Q = \omega_o \frac{U}{-\frac{\partial U}{\partial t}}. \tag{36}$$

This provides us with a first order differential equation which is solved simply as

$$\frac{\partial U}{\partial t} = -\frac{\omega_o}{Q} U, \tag{37}$$

$$U(t) = U(0) e^{-\frac{\omega_o}{Q} t}.$$

We can immediately recognize that the energy will therefore have a characteristic cavity energy lifetime given by $\tau_c \equiv Q/\omega_o$. For further analysis we must now relate the measured spectral width to the cavity Q. Let us define a cavity field with ohmic losses given by Eq. (37) and single angular frequency ω_o as

$$E(t) = e^{-\frac{\tau_c}{2} t} e^{-i\,\omega_o t}. \tag{38}$$

Now taking the Fourier transform of the cavity field to shift to a frequency domain we find

$$E(\omega) = \frac{1}{\sqrt{2\pi}}\int_0^\infty E(t)e^{i\omega t}\,dt = \frac{1}{\sqrt{2\pi}}\frac{i}{(\omega-\omega_o)+i\frac{\tau_c}{2}}. \tag{39}$$

By taking the square modulus of Eq. (39) we find an expression that is proportional to the power spectrum:

$$E(\omega)^* E(\omega) = \frac{1}{2\pi}\frac{1}{(\omega-\omega_o)^2+\left(\frac{\tau_c}{2}\right)^2} = \frac{1}{2\pi}\frac{1}{(\omega-\omega_o)^2+\left(\frac{\omega_o}{2Q}\right)^2}. \tag{40}$$

We can now see that the field initially at a single frequency ω_o has been broadened by an amount $\Delta\omega = \omega_o/Q$. Solving for Q we have the bridge to interpret the spectral width derived from the ring cavity model as

$$Q = \frac{\omega_0}{\Delta\omega} = \frac{\nu_0}{\Delta\nu}. \tag{41}$$

This parameter then gives one a dimensionless parameter that can be used to compare resonant responses of cavities with similar or vastly different configurations, for example a mass on a spring as compared to a capacitor or even a photonic crystal cavity. In our case using the results of Eq. (35) we have

$$Q = \frac{\nu_0}{\Delta\nu_c + \Delta\nu_i}. \tag{42}$$

Observing the structure of Eq. (42) allows one to rewrite the total Q into the contributions due to the coupling and intrinsic losses separately as

$$Q = \frac{Q_i Q_c}{Q_i + Q_c}. \tag{43}$$

Or more traditionally we may also write the inverse of Q as a sum of parallel impedances,

$$\frac{1}{Q} = \frac{1}{Q_c} + \frac{1}{Q_i}. \tag{44}$$

Where the contributions have been expressed in the same manner as Eq. (42) by sequentially setting each loss term to zero,

$$Q_i \equiv \frac{\nu_0}{\Delta\nu_i}, \tag{45}$$

$$Q_c \equiv \frac{\nu_0}{\Delta\nu_c}.$$

From the results of Eq. (37) we can express the Q as

$$Q = 2\pi\nu_0\tau_c. \tag{46}$$

With this we can now see the physical meaning of the lifetime by equating Eq. (42) and Eq. (46):

$$\tau_c = \frac{1}{2\pi(\Delta\nu_c + \Delta\nu_i)} \equiv \frac{1}{2K}. \tag{47}$$

As one would expect the cavity lifetime is inversely proportional to the total cavity loss and this allows us to define a field decay rate K, or rather a power decay rate of $2K$.

If dephasing is present the Q derived from spectral width in Eq. (41) will not be the same as that explicitly derived from cavity lifetime as the lifetime is only dependent on loss, not dephasing. The proper definition of Q is that derived in Eq. (46) while Eq. (41) is an approximation, valid when dephasing is not present, so this must be verified before use. The aforementioned dephasing is the result of fluctuations in phase while the mode propagates within the cavity. For example, the round-trip phase (δ) or time (τ_{rt}) may not have the same value for every

round trip of a photon, clearly leading to a broadening of the resonance without adding more loss. This could come about due to thermal fluctuations, multiple scattering, or tunneling into and immediately back out of the coupling fiber.

The final bit of physical analysis that remains to be done is in regard to the cavity's free spectral range and finesse. The free spectral range is simply the frequency spacing between adjacent identical resonant modes while the cavity finesse is the number of resonance widths (FWHM) within one free spectral range. These properties are intimately related and also related to physical properties derived in the preceding analysis. The relationship between the cavity finesse $\mathcal{F}$, free spectral range $\delta\nu$, and coefficient of finesse F is given by

$$\mathcal{F} = \frac{\pi}{2\ sin^{-1}(\frac{1}{\sqrt{F}})} = \frac{\delta\nu}{\Delta\nu}. \tag{48}$$

Assuming no intrinsic loss, the coefficient of finesse for a ring cavity with one partial reflector (as in Fig. 3) can be expressed in terms of the reflection coefficient r or coupling loss T (for $T \ll 1$) as

$$F \equiv \frac{4r}{(1-r)^2} \simeq \frac{16}{T^2}. \tag{49}$$

Now, the finesse is found to be

$$\mathcal{F} \simeq \frac{2\pi}{T}. \tag{50}$$

Generalizing this to include intrinsic loss gives

$$\mathcal{F} \simeq \frac{2\pi}{T + \alpha L} = \frac{2\pi}{\gamma} = \frac{\delta\nu}{\Delta\delta}. \tag{51}$$

While the amount of analysis that can be performed on the simple ring cavity structure is rather staggering, the methods developed in the above analysis will be shown to be crucial tools required to adequately understand the physical system. If one applies these tools to a physical system, momentarily ignoring that the model has yet to be verified, we find that a typical microsphere of radius $R_s \sim 400\ \mu\text{m}$ used at a wavelength of $\lambda \sim 1.5\ \mu\text{m}$ has the following physical characteristics:

$$\begin{aligned} T &\simeq 1 \times 10^{-4} \\ \alpha L &\simeq 1 \times 10^{-4} \\ \Delta\nu &\simeq 2\ \text{MHz} \\ Q &\simeq 1 \times 10^{8} \\ \tau_c &\simeq 100\ \text{ns} \\ \mathcal{F} &\simeq 3 \times 10^{4} \\ \delta\nu &= 75\ \text{GHz} \end{aligned} \tag{52}$$

Based on the above properties one can begin to surmise why these microcavities are of such interest to scientists. Their ease of construction and low cost coupled with the very narrow linewidths and large free spectral ranges lead to a myriad of applications from very high bandwidth device applications in optical networking to ultra-sensitive traveling wave evanescent sensors. All of these properties can be had for a cost of around 5¢ and an investment of 5 minutes of time.

Modeling to find Transmission:

Let us begin the process of model verification with a rigorous coupled mode treatment of the transmission probability (T; probability of photon tunneling between the waveguide and

the resonator) used in the experimental system. The coupled-mode treatment in this case is under the weak coupling regime ansatz which physically means that the assumed interaction between the guides is only a modest perturbation and as such the orthonormal modal expansion in each guide is still a "good" basis set to describe the electromagnetic fields [20]. This is along the line of the arguments presented in the derivations for the ring cavity, i.e. $T << 1$. This then allows us to find the unperturbed modes of each guide and use them to characterize the transmission probability. This is done through what is typically termed an overlap integral [13, 20] and in effect is the dot product of the vector fields, including phase, which is then integrated over the interaction volume of the guide into which power is flowing. Our path towards verification therefore begins with modal expansions of the fields in both the tapered fiber and the microsphere and ends in the actual computation of the overlap integrals of interest.

Fiber Modes:

The propagation of electromagnetic fields within a typical step-index azimuthally uniform fiber (see Figs. 6 and 7) can be described in both the ray picture of light, in which one treats ray reflections due to total internal reflection, or with full field solutions to Maxwell's equations [21] (Pgs. 3 and 205). While the ray picture of light propagation in the waveguide provides for a more readily accessible conceptual overview of the system, its simpler methodology limits the rigorous analysis of fundamental effects within the guide. As our system is expected to include these fundamental effects we limit our treatment to the much more rigorous field analysis.

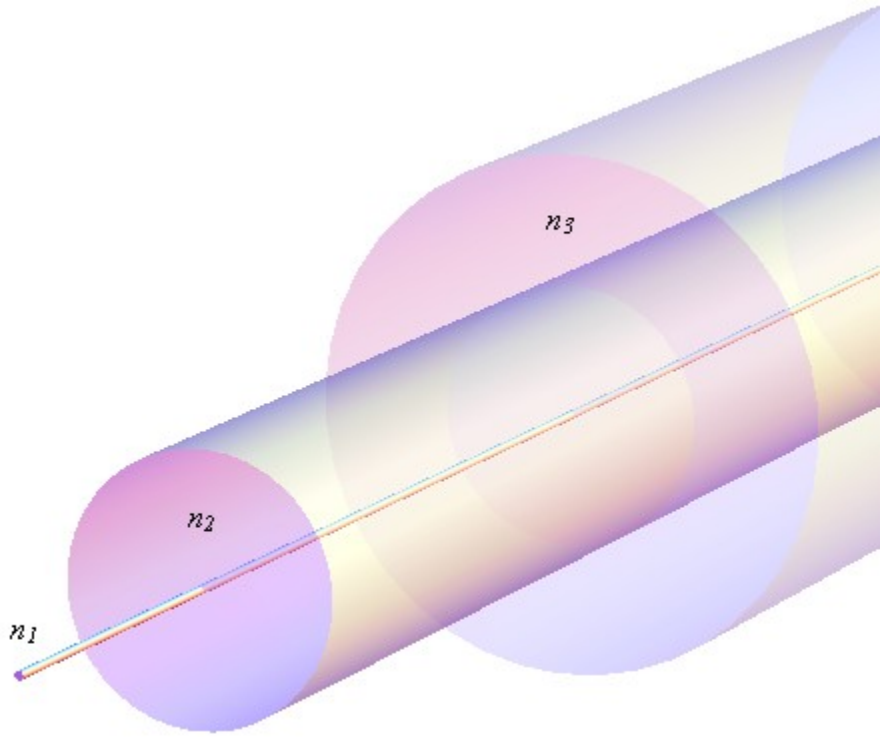

Figure 6. A typical step index fiber waveguide. The radii of regions 1 (core radius a) and 2 (cladding radius b) are shown to scale. Here, $n_1 > n_2 > n_3$.

Let us begin with a basic wave equation in an isotropic homogenous medium with assumed harmonic time dependence of the field. This leads to what is known as the vector Helmholtz equation and it takes the form [19] (Pg. 380)

$$(\nabla^2 + k^2)\boldsymbol{E} = 0, \tag{53}$$

where ∇^2 is the Laplacian operator, k is a potentially complex wavenumber for the dielectric medium and $\boldsymbol{E}$ is a vector electric field. We can note that while k can be complex in general, the real component represents power flow and will be termed the propagation constant or

wavenumber while the imaginary component will represent attenuation of the propagating wave and is typically denoted in optics by the negative of half the absorption coefficient α [19] (Pg. 310). Notice that attenuation will then appear as a decreasing exponential, such that we will expressly treat k as real and include exponential attenuation when it is physically necessary, as in the ring cavity. For the moment let us assume a constant phase plane solution such that there is no transverse field gradient, i.e. the field is linearly polarized in the transverse plane, propagating along z with an exclusively real wavenumber k. The Helmholtz equation then becomes

$$(\frac{\partial^2}{\partial^2 z} + k^2)\boldsymbol{E} = 0. \tag{54}$$

This then is solved as,

$$\boldsymbol{E} = \boldsymbol{E_o} e^{-ikz}, \tag{55}$$

which is the proverbial plane wave solution. Throughout the remainder of this chapter, the convention $e^{-i(kz-\omega t)}$ will be used for plane waves propagating along z. Now consider the consequences of disregarding the previous assumption on transverse field variation. This amounts to lifting the assumption of a uniform transverse dielectric profile, but still allows for real propagation along z with the transverse behavior determined by the perturbation of, or rather deviation from, a free space linearly polarized plane wave. Let us then take a form that has planar wavefronts orthogonal to its propagation along z as:

$$\boldsymbol{E} = \boldsymbol{E}(x, y) e^{-i\beta z}, \tag{56}$$

where β is the propagation constant in the medium. If we then insert this into the preceding Helmholtz equation we find the transverse response is governed by

$$\left(\nabla_t{}^2 + (k^2 - \beta^2)\right)\boldsymbol{E}(x,y) = 0, \tag{57}$$

where $\nabla_t{}^2$ is the transverse Laplacian. Notice the implications of allowing $\beta \to k$: we regain a linearly polarized plane wave solution as the transverse field gradient must also collapse in this limit. Thus $\beta \neq k$ represents the divergence of the field solution from that of a pure linearly polarized plane wave, or the strength of the polarization modifications of said plane wave due to the presence of a transverse dielectric profile.

For a single homogeneous dielectric boundary problem such as Fig. 6 in the limit $b \to \infty$**,** termed a step index waveguide, it can be shown [21] (Pg. 226) that β must be strictly bounded by the wavenumbers of plane waves propagating along z in each of the two media i and j independently as

$$k_i > \beta > k_j, \tag{58}$$

where the wavenumbers are defined such that $k_i > k_j$. Physically, this relationship is easier to discuss if one defines an effective index of refraction, which represents some weighted average of the two indices, experienced by the guided field:

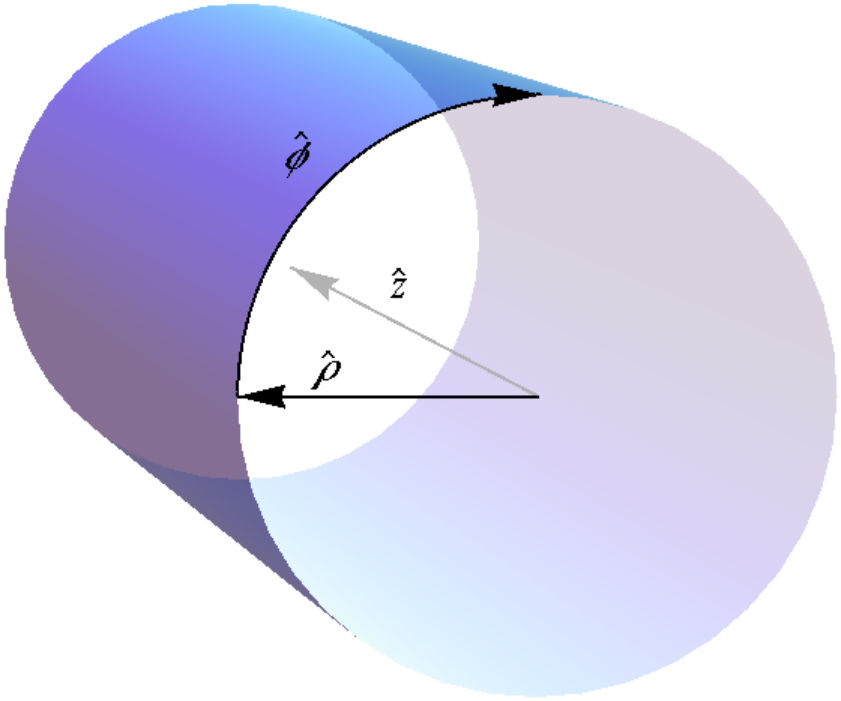

Figure 7. The cylindrical coordinate system used for modeling for a step-index fiber.

$$\beta = n_{\text{eff}}\frac{\omega}{c}. \tag{59}$$

Now in terms of indices of refraction we have

$$n_i > n_{\text{eff}} > n_j. \tag{60}$$

The physical meaning of the effective index should be clear in that as the effective index approaches either of the two limits we can approximate the solution as a linearly polarized plane wave. The higher of the two limits in which $n_{\text{eff}} \simeq n_i$ represents the strong confinement limit in which the field is almost entirely bound in medium i and as such only has minor polarization nonuniformity over a small outer portion of the mode cross section. In the second

limit in which $n_{\text{eff}} \simeq n_j$ the confinement is weak and the field propagates almost entirely in medium j with a small polarization nonuniformity only in a small region at the core. Similar conclusions can also be drawn about the effective phase velocity of the field within the guide as the phase velocity will therefore increase as the field effective index approaches that of n_j and loses confinement.

It has been shown [21] (Pg. 592) that given a longitudinally invariant waveguide the transverse field components can be found analytically given a known longitudinal solution to Maxwell's equations. We begin by assuming an orthonormal expansion of the field which in electromagnetic circles is termed a modal expansion of the field. In this treatment each solution is vector orthogonal with discrete indices in amplitude coefficients and effective wavenumbers. Given a particular geometry only modes of certain discrete indices propagate; this is termed cutoff and is the reason some optical fibers are termed single-mode. In these fibers the ratios of core and cladding radii and indices is such that only the mode which has an effective index closest to that of the core can propagate without loss. This mode is termed the fundamental mode and has an intensity profile and vector field structure given by Fig. 8 and Fig. 9 respectively. It is typically denoted by its hybrid electric-magnetic field structure as HE_{11}. These modes are termed hybrid as the confinement is sufficiently strong as to mix the fields such that neither the electric nor magnetic fields are entirely confined to a transverse polarization plane. Because a tapered fiber is used for coupling to the resonator, Figs. 8 and 9 reflect this, with the guiding interface being that between cladding and air.

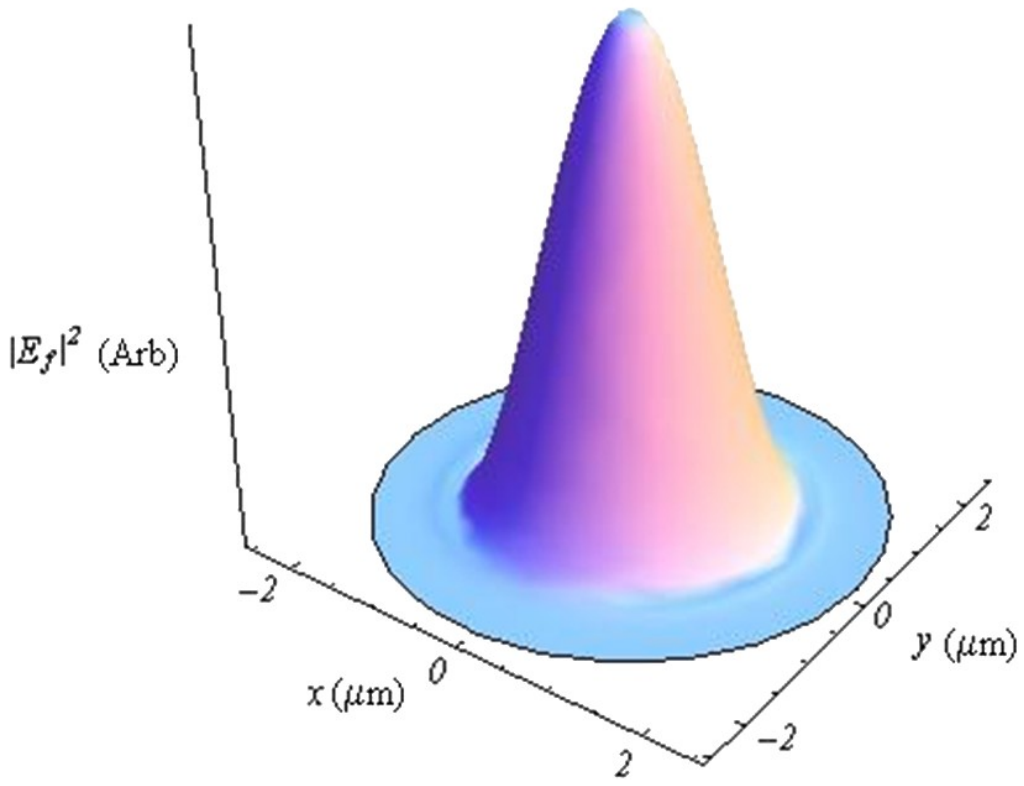

Figure 8. Cross-section power plot of the fundamental tapered-fiber mode where propagation is in the z direction. Notice the development of the evanescent field at the fiber-air interface (1.7 μm radius).

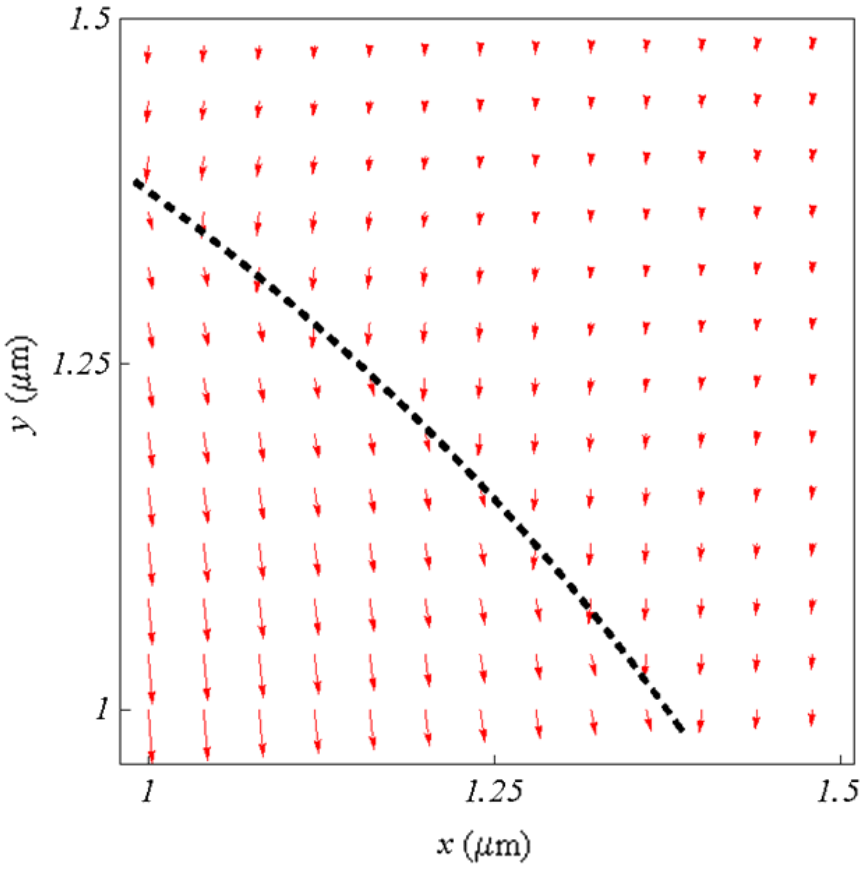

Figure 9. Polarization characteristics of the fundamental fiber mode along the dielectric interface with air.

As the experimental system is intentionally single-mode and the explicit treatment of higher mode families has been studied elsewhere [14] the remaining discussion will focus exclusively on the fundamental mode.

We revisit the Helmholtz equation for the z components of the fields in cylindrical coordinates:

$$\left(\nabla_t{}^2 + (k^2 - \beta^2)\right)\begin{pmatrix} E_z \\ H_z \end{pmatrix} = 0. \tag{61}$$

Here we have taken the explicit propagation dependence of the fields as

$$\boldsymbol{E}(\rho,\phi,z) = \boldsymbol{E_o}(\rho,\phi)e^{i(\omega t-\beta z)}$$
$$\boldsymbol{H}(\rho,\phi,z) = \boldsymbol{H_o}(\rho,\phi)e^{i(\omega t-\beta z)} \quad (62)$$

with the propagation constant along z again defined to be β. If the Laplacian operator is then expanded in polar coordinates, as a general form in the scalar parameter $A = \{E_z, H_z\}$, we find

$$\frac{\partial^2 A}{\partial \rho^2} + \frac{1}{\rho}\frac{\partial A}{\partial \rho} + \frac{1}{\rho^2}\frac{\partial^2 A}{\partial \phi^2} + (k^2 - \beta^2)A = 0. \quad (63)$$

Let us now take the traditional step of assuming a separable solution of the form

$$A(\rho,\phi,z,t) = P(\rho)\Phi(\phi)Z(z)T(t). \quad (64)$$

In this regard we have already taken the form of the time and longitudinal dependence to be

$$Z(z)T(t) = e^{-i\beta z}e^{i\omega t}. \quad (65)$$

Now observing that the waveguide is rotationally invariant in ϕ allows us to further assume harmonic rotation dependence as:

$$\Phi(\phi) = e^{im\phi}, \quad (66)$$

subject to the constraint that m must be an integer such that $\Phi(\phi) = \Phi(\phi + 2\pi m)$. Now inserting this back into Eq. (63) gives,

$$\frac{\partial^2 P}{\partial \rho^2} + \frac{1}{\rho}\frac{\partial P}{\partial \rho} + (k^2 - \beta^2 - \frac{m^2}{\rho^2})P = 0. \quad (67)$$

This can be readily recognized as Bessel's equation with the typical known solutions for each dielectric region given by

$$P(\rho < a) = A_1\, J_m(a_1\rho) + A_2\, Y_m(a_1\rho), \tag{68}$$

$$P(a < \rho < b) = A_3\, I_m(a_2\rho) + A_4\, K_m(a_2\rho),$$

$$P(\rho > b) = A_5\, I_m(a_3\rho) + A_6\, K_m(a_3\rho).$$

Where J_m, Y_m, I_m and K_m are Bessel functions of the first and second kind and modified Bessel functions of the first and second kind of order m, respectively, with amplitude coefficients given by A_k. The cofactor in each argument is given by the root square deviation of the propagation constant from that of a linearly polarized plane wave:

$$a_i = \sqrt{{k_i}^2 - \beta^2}. \tag{69}$$

Notice that the generalized complex Bessel functions are used in regions 2 and 3 because in these regions a_i will be explicitly imaginary while core guidance is maintained, $k_1 > \beta > k_2 > k_3$. These expressions simplify somewhat when physicality is imposed on the solution set as Y_m and I_m have singularities at zero and infinity respectively. For these components we must set the amplitude coefficients to zero and the full solution set then becomes

$$A(\rho < a) = A_1 J_m(a_1\rho)e^{i(\omega t-\beta z-m\phi)}, \tag{70}$$

$$A(a < \rho < b) = A_2\, I_m(a_2\rho)e^{i(\omega t-\beta z-m\phi)} + A_3\, K_m(a_2\rho)e^{i(\omega t-\beta z-m\phi)},$$

$$A(\rho > b) = A_4 K_m(a_3\rho)e^{i(\omega t-\beta z-m\phi)},$$

where the amplitude coefficients have been renumbered for simplicity. From this general scalar solution in the z field components all the remaining scalar field components are found [21] (Pg. 593) in each medium i from

$$\boldsymbol{E_i}\cdot\hat{\boldsymbol{\rho}} = \frac{-i}{{a_i}^2}\left(\beta\frac{\partial(\boldsymbol{E_i}\cdot\hat{\boldsymbol{z}})}{\partial\rho} + \frac{\omega\mu_0}{\rho}\frac{\partial(\boldsymbol{H_i}\cdot\hat{\boldsymbol{z}})}{\partial\phi}\right), \tag{71}$$

$$\boldsymbol{E_i}\cdot\hat{\boldsymbol{\phi}} = \frac{-i}{{a_i}^2}\left(\frac{\beta}{\rho}\frac{\partial(\boldsymbol{E_i}\cdot\hat{\boldsymbol{z}})}{\partial\phi} - \omega\mu_0\frac{\partial(\boldsymbol{H_i}\cdot\hat{\boldsymbol{z}})}{\partial\rho}\right),$$

$$\boldsymbol{H_i}\cdot\hat{\boldsymbol{\rho}} = \frac{-i}{{a_i}^2}\left(\beta\frac{\partial(\boldsymbol{H_i}\cdot\hat{\boldsymbol{z}})}{\partial\rho} - \frac{\omega\epsilon_i}{\rho}\frac{\partial(\boldsymbol{E_i}\cdot\hat{\boldsymbol{z}})}{\partial\phi}\right),$$

$$\boldsymbol{H_i}\cdot\hat{\boldsymbol{\phi}} = \frac{-i}{{a_i}^2}\left(\frac{\beta}{\rho}\frac{\partial(\boldsymbol{H_i}\cdot\hat{\boldsymbol{z}})}{\partial\phi} + \omega\epsilon_i\frac{\partial(\boldsymbol{E_i}\cdot\hat{\boldsymbol{z}})}{\partial\rho}\right).$$

Where the longitudinal components in dielectric i have been expressed as

$$\{E_z\,, H_z\} \equiv \{(\boldsymbol{E_i}\cdot\hat{\boldsymbol{z}}), (\boldsymbol{H_i}\cdot\hat{\boldsymbol{z}})\}, \tag{72}$$

and the convention is taken that these components are purely imaginary while the transverse components are taken to be purely real. Enforcement of continuity boundary conditions at each interface for the longitudinal (z) and azimuthal (ϕ) field components of E_i and H_i allow us to find an expression for the unknown amplitude coefficients A_k as well as to formulate an

eigenvalue equation for β. Traditionally, the amplitude coefficients are treated analytically [14] by first assuming $b \to \infty$ and ignoring the second interface. This will be shown to be valid under the experimental conditions we are interested in, but the more generalized two-interface methodology allows for the treatment of more complex dielectric structures and power transfer between core and cladding field guidance. This generality comes at a price however, as the increased complexity of including the second interface typically requires a numerical treatment in order to find approximate solutions to the boundary value problem.

With the boundary conditions established one can then formulate an eigenvalue equation from the matrix form of the boundary conditions equations [14]. The eigenvalues found here represent the discrete effective wavenumbers of the allowed bound modes, each of which will have a unique set of amplitude coefficients. The resulting eigenvalue equation in either the single or double boundary problem, however, is transcendental in β and must be treated numerically. We must then consider the ramifications of inserting a potential numerical solution of the β eigenvalue equation which is not strictly real into the field solution we have found. The imaginary component, which strictly means that the solution is not an "eigenvalue" of the analytic eigenvalue equation, will lead to an effective field loss term as $e^{-\mathrm{Im}\{\beta\}z}$ which can be considered a radiation loss, as the mode becomes unbounded. Numerically, then, we must always minimize the imaginary component of a particular solution to approximate a "good" eigenvalue for the system. With a particular solution numerically isolated the boundary conditions are evaluated for determination of the amplitude coefficients.

For a general two-boundary system we expect two regions of solutions: those that are guided by the $n_1 \to n_2$ interface, aka core-guided modes, and those guided by the $n_2 \to n_3$ interface, aka cladding-guided. Physically, when the effective index is found to lie between the indices of

any two regions we can conclude that it is this limiting dielectric interface that is responsible for guiding the mode. This turns out to be important only in the treatment of power transfer between the core and cladding guided modes in the taper transition region of the fiber. In the untapered region the power is core confined while in the fully tapered region the power is cladding confined. However, in the taper transition region the power is simultaneously guided by both the core and cladding. Thus a full field treatment is thereby only strictly necessary if one is to model the power transfer within the waveguide itself to limit non-orthogonal couplings to modes of varying symmetries. Making these internal power transfers negligible is typically referred to as fiber adiabaticity in the sense that a single mode fiber will then maintain a single mode nature even in the fully tapered region. These power couplings are then controlled by maintaining high symmetry between the core and cladding guided modes to facilitate near orthonormality in the field expansions of the guide. In this sense the tapering of the guide can be thought of as a perturbation to the orthonormal field expansion of the guide and as long as this expansion remains a "good" basis set the internal power transfer within the guide will not be lossy due to couplings to higher order fiber modes.

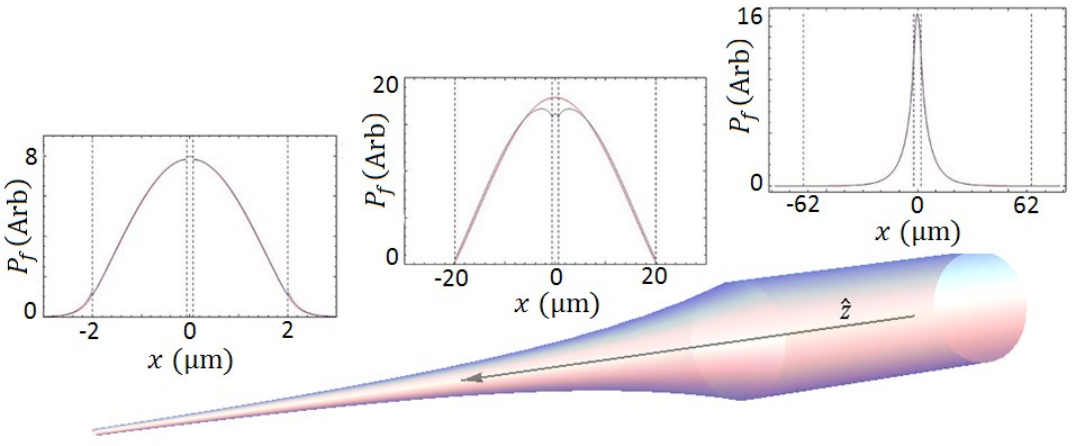

Figure 10. Fundamental mode profiles for a tapered fiber as a function of position along the taper transition region. The blue trace is the solution to the two-boundary problem while the red trace is that of a single-boundary approximation.

One can note that in the above figure (Fig. 10) the single boundary approximation is reasonable in both the strictly core- and cladding-guided regions. In the core-guided region both solutions are in perfect agreement, while in the cladding-guided region the solutions are very similar with the core of the two-boundary solution maintaining some weak guidance. This shows that the experimental system, in which the interaction is occurring in the cladding-guided region, can be modeled as a single-boundary problem for power transfer calculations given that adiabatic fibers are used. It is of some merit, however, to observe the evolution of power guidance as the field encounters the tapered region. Notice that phenomenologically we can observe the peak power moving away from the core into the cladding, filling and broadening the mode until only a small fraction of the total power is contained in the core.

Sphere Modes:

The solutions to the field expansions in a spherical cavity with the modified spherical coordinate representation depicted in Fig. 11 can be found in a manner which is intuitively similar to that for the fiber. One begins with the same Helmholtz equation and arguments associated with it. The form of the time dependence and propagation direction and effective wavenumber are taken identically with the exception that the propagation is taken to be along a cut equatorial plane of the sphere in the $\hat{\phi}$ direction. Unlike the fiber, in which the dimensionality of the guiding fiber is of the order of the wavelength, causing the modal fields to experience the dielectric interface in all transverse directions simultaneously, the much larger dimensions of the spherical cavity with respect to the wavelength will lead to fields confined to a very small fraction of the total cavity volume. Because the guidance is only along a single one-sided boundary in this type of cavity we can treat the field polarizations in the natural

coordinates [13] shown in Fig. 11. The modes of this type of cavity are then decomposed into pure transverse electric (TE) and magnetic (TM) polarizations. What this means in practical terms is that we can assume the direction of the electric or magnetic field because the fields are not dependent or mixed as they were in the fiber.

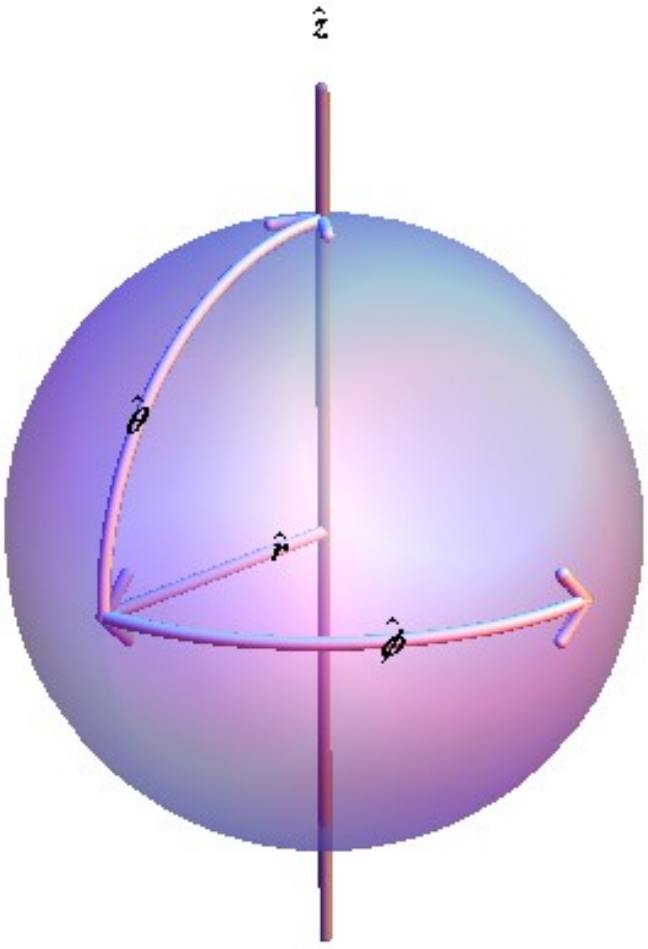

Figure 11. Coordinate representation of the microsphere. Field propagation is assumed to be along ϕ.

As was first illustrated by Mie and Debye, just after the turn of the century and later fully fleshed out by Hansen [22], when one considers a generalized scalar solution ψ to the Helmholtz equation,

$$(\nabla^2 + k^2)\,\psi = 0, \tag{73}$$

then this solution can further be used as a generating function as elucidated by Stratton for a generalized complex wavenumber k [23] (Pg. 415), or rather potential, to generate two independent vector solutions to the Helmholtz equation. These vector functions are expressed as

$$\boldsymbol{L} = \frac{1}{k}\nabla\psi, \tag{74}$$

$$\boldsymbol{M} = \nabla \times (\hat{\boldsymbol{a}}\,\psi),$$

$$\boldsymbol{N} = \frac{1}{k}\nabla \times \boldsymbol{M},$$

which ($\hat{\boldsymbol{a}}$ is an arbitrary unit vector) all satisfy Eq. (73). For the current case of interest these reduce, due to the harmonic time dependence, to two orthogonal coupled vector ($\boldsymbol{M}, \boldsymbol{N}$) solutions (for a given polarization, referenced to $\hat{\boldsymbol{a}}$) which are then determined by a scalar potential ψ, or generating function, termed a Debye potential. Given the orthogonal nature of these solutions they are therefore appropriate representations of the vector fields $\boldsymbol{E}$ and $\boldsymbol{H}$. The brunt of the work then lies in the derivation of the form of the Debye potential for a particular system of interest. In the case of standard spherical coordinates the Helmholtz equation acting on a particular potential $\psi(r,\theta,\phi) = R(r)\Theta(\theta)\Phi(\phi)$ is separable:

$$\frac{d^2}{dr^2}R(r)+\frac{2}{r}\frac{d}{dr}R(r)+\left(k^2-\frac{p^2}{r^2}\right)R(r)=0, \tag{75}$$

$$\frac{1}{sin(\theta)}\frac{d}{d\theta}(sin(\theta)\frac{d}{d\theta}\Theta(\theta))+(p^2-\frac{s^2}{sin^2(\theta)})\Theta(\theta)=0,$$

$$\frac{d^2}{d\phi^2}\Phi(\phi)+s^2\Phi(\phi)=0,$$

where s and p are separation constants to be determined. We can immediately note that any solution that has ϕ dependence is subject to periodic boundary conditions as $\Phi(\phi)=\Phi(\phi+2\pi)$. This is solved as a simple complex exponential in the integer index m which determines the first separation constant as $s=m$. The second constant can be found by noting that the differential equation governing the θ component is solved by an associated Legendre function. To maintain physicality, specifically finiteness at the poles, in our solution we must truncate one of the associated Legendre series solutions by choosing $p^2=l(l+1)$, where l is a positive integer. Now with the differential equations fully defined let us clean things up a bit before actually solving them.

Given that we treat field propagation within the microsphere to occur at the equatorial plane, $\theta=\pi/2$, it is a matter of convenience to symmetrize the fields by a rotation in the coordinate system definitions such that $\theta=0$ is along this plane. This amounts to simply replacing terms as $sin(\theta)\rightarrow sin(\pi/2-\theta)=cos(\theta)$. With the equation symmetrized we may further note that the dimensions of the system of interest are such that a small angle approximation in θ to second order is quite reasonable for the region of field confinement *($\theta_{max}\approx\pm\pi/64$).* Now observe that the solution of the differential equation that describes the

radial dependence is a spherical Bessel function. While these analytical solutions are readily available some further approximations can be quite insightful. While the interior dielectric solution gives no additional insight under approximation the evanescent portion is very insightful, because it will have a fast exponential decay with dimensionality on the order of a wavelength. Under these conditions it is appropriate to rescale the radial dependence in a relative coordinate defined from the surface of the sphere with radius R_s as $r = R_s(1 + x/R_s)$ and examine the radial equation in the exterior near field ($x/R_s \ll 1$) [13]:

$$\frac{d^2}{dx^2}R(x) + \left(k_0^2 - \frac{l(l+1)}{{R_s}^2} + \frac{2x(l(l+1)+2)}{{R_s}^3}\right)R(x) = 0, \tag{76}$$

which is related to the Airy equation and the wavenumber k_0 has been defined through $k_i \equiv n_i(\omega/c)$ for the external index n_0. This can be even further simplified by neglecting the third multiplier of $R(x)$, giving

$$\frac{d^2}{dx^2}R(x) + \left(k_0^2 - \frac{l(l+1)}{{R_s}^2}\right)R(x) = 0. \tag{77}$$

This, as per our early discussion, suggests a localized plane wave with an effective wavenumber given by $\beta^2 = l\,(l+1)/{R_s}^2$. In full reduced form our differential equations become

$$\begin{cases} \dfrac{d^2}{dr^2}R(r) + \dfrac{2}{r}\dfrac{d}{dr}R(r) + \left(k_s^2 - \dfrac{l(l+1)}{r^2}\right)R(r) = 0, & for\ r < R_s \\ \dfrac{d^2}{dx^2}R(x) + \left(k_0^2 - \dfrac{l(l+1)}{{R_s}^2}\right)R(x) = 0, & for\ r = (R_s + x) > R_s \end{cases} \quad (78)$$

$$\frac{d^2}{d\theta^2}\Theta(\theta) - \theta\frac{d}{d\theta}\Theta(\theta) + (l(l+1) - m^2(1+\theta^2))\Theta(\theta) = 0,$$

$$\frac{d^2}{d\phi^2}\Phi(\phi) + m^2\Phi(\phi) = 0,$$

where the wavenumber k_s is defined by the sphere's index of refraction n_s. The radial solutions are then found to be,

$$R(r) = \begin{cases} B_1\, j_l(k_s r), & for\ r < R_s \\ B_2 e^{-\alpha_s(r-R_s)}, & for\ r > R_s \end{cases} \quad (79)$$

where $j_l(k_s r)$ is the spherical Bessel function of the first type (the general solution also contains a spherical Bessel function of the second type which has been set to zero for physicality) B_i is an undetermined amplitude coefficient, and $\alpha_s = \sqrt{\beta^2 - k_0^2}$ with $\beta \equiv \sqrt{l\,(l+1)/{R_s}^2}$.

If we assume the integers m and l are large and roughly equal the polar solution is found to be

$$\Theta(\theta) = B_3\, e^{g\theta^2}\left(H_N(h\theta) {}_1F_1\left(-N, \frac{1}{2}, h^2\right)\right) \simeq B_3\, e^{-\frac{m}{2}\theta^2} H_{(l-m)}\left(\sqrt{m}\theta\right), \quad (80)$$

where $H_N(h\theta)$ is the Hermite polynomial function, ${}_1F_1\left(-N, \frac{1}{2}, h^2\right)$ is the Kummer confluent hypergeometric function, and the remaining variables are given and approximated as

$$g = \left(\frac{1}{4} - \sqrt{\frac{1}{16} + \frac{m^2}{4}}\right) \simeq -\frac{m}{2}, \tag{81}$$

$$h = \frac{\sqrt[4]{1+4m^2}}{\sqrt{2}} \simeq \sqrt{m},$$

$$N = \frac{1 + 2l(1+l) - 2m^2 - \sqrt{1+4m^2}}{2\sqrt{1+4m^2}} \simeq l - m.$$

The last solution, to the azimuthal equation, is found simply to be

$$\Phi(\phi) = B_4 e^{im\phi}. \tag{82}$$

Now, with the scalar solution in hand we are seemingly ready to use the vector relations of Eq. (74) to find the field components, where once again we have taken the transverse components to be purely real and the longitudinal components to be pure imaginary. There is a subtlety here however that has been overlooked. We have said very little about the assumed arbitrary unit vector $\widehat{\boldsymbol{a}}$. This vector will determine the field polarization as TE or TM. While the development of the scalar Debye potential is quite valid, the vector fields which are found will have little physical usefulness if one cannot represent either $\boldsymbol{E}$ or $\boldsymbol{H}$ as directed having a zero radial component (meaning the field is transverse). For this reason the methodology employed for representing the fields of the fiber has a much different development than that of the microsphere as the fiber fields will never be found to have a zero component. With this subtlety illuminated we can then freely assume the aforementioned polarization basis by setting $\widehat{\boldsymbol{a}}$ along $\hat{\boldsymbol{r}}$, or explicitly $\widehat{\boldsymbol{a}} = \langle 1,0,0 \rangle$, and letting $\boldsymbol{M} = (\boldsymbol{E}, \boldsymbol{H})$ for the polarizations (TE, TM) respectively. With either $(\boldsymbol{E}, \boldsymbol{H})$ now defined through $\boldsymbol{M}$ the other can be determined through $\boldsymbol{N}$; notice that the third of Eqs. (74) for a generalized complex wavenumber reduces to

Maxwell's curl equations [23] (Pg. 414) for a harmonic wave with finite conductance. Thus our formulation to this point is entirely congruent with a typical Maxwellian treatment.

The remaining treatment is an eigensystem treatment just as for the fiber fields. Just as before we are tasked with solving the discrete eigenvalue equation and eigenvector equations for the microsphere which in practical terms means finding the effective wavenumbers of the modes, β, and the amplitude coefficients, B_i, which meet the transverse field continuity boundary conditions. The resulting solutions in β will therefore depend on the separation constants (l, m, q) which will both define the spatial profile of the mode and determine the modes resonance frequency centered at ω_o. Thus, each solution with differing indices will have a different resonance frequency and spatial profile.

Given that an analytical or numerical treatment is nearly identical to that for the fiber the methodology will not be revisited, but the results are interesting and worth discussion. In particular, the resulting fields of the solved eigensystem elucidate the physical interpretation of the indices found as separation constants in the proceeding discussion. If we label the modal solutions as is typical for this type of treatment [13] $\psi = \psi_{lmq}$, q then enumerates the order of the solution to the characteristic equation beginning at one, l is the number of integer wavelengths in one round trip and m is not explicitly determined. Physically then, q will determine the number of radial intensity (r) maxima, $l - m + 1$ the number of polar intensity maxima (θ) and $2l$ the number of azimuthal field extrema (ϕ).

Furthermore, we can also deduce from the near field radial solution that much like the fiber each solution will have an effective wavenumber $\beta_l \equiv \sqrt{l\,(l+1)/{R_s}^2}$, where we have added an explicit subscript l. Notice the path described by β_l does not contain all of the modal indices (it

lacks m dependence) and therefore cannot describe the propagation of the mode as a whole; rather this can thought of as the path a particular photon would take within the cavity. The fields, which are described by the cumulative effect of many photons, must strictly depend on all indices and will only then describe the propagation of the mode as a whole. If then we look at the mode of lowest polar order $l = m$ such that $\beta_m \equiv \beta_{l=m} \simeq m/R_s$, which is taking the projection of β_l onto the equatorial plane, we see that the total propagation constant is fully dependent on all pertinent indices as we require and describes the modal propagation as seen in Fig. 12 below. For this reason β_m is what is typically termed the propagation constant for the sphere mode, because it gives a full description of the mode's propagation, and defines the mode's effective index through $\beta_m = n_{eff}(\omega/c)$.

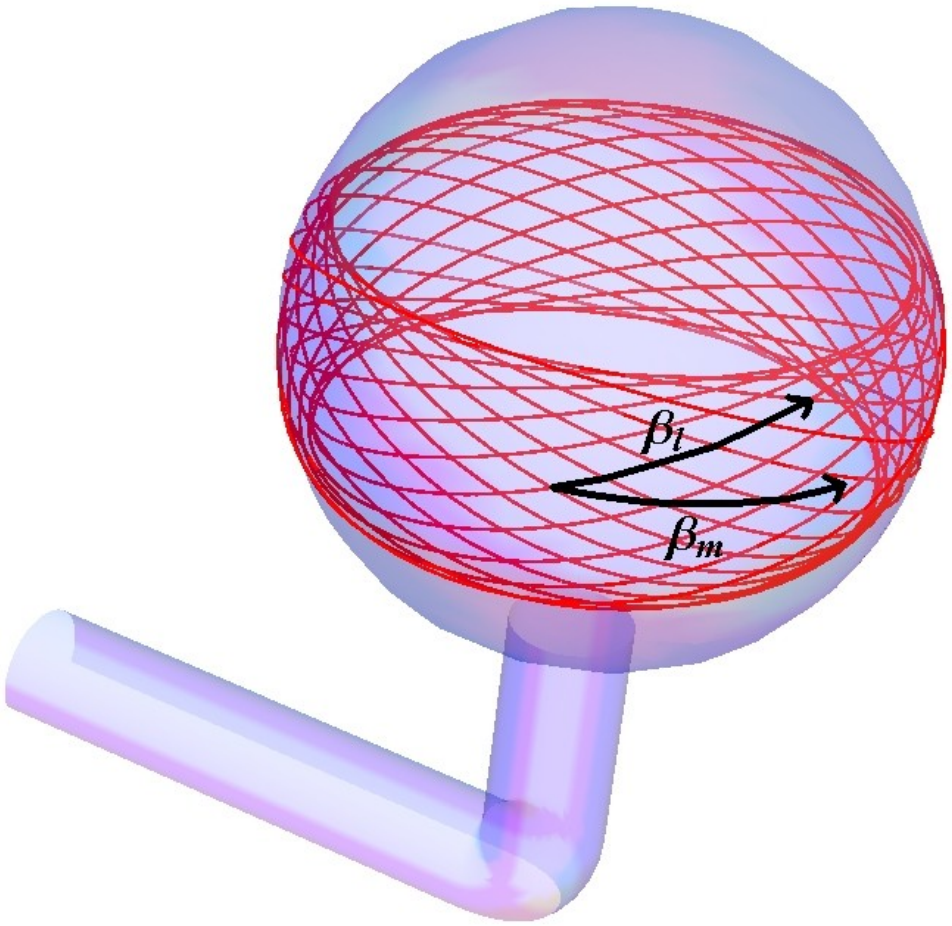

Figure 12. A high angle (exaggerated) polar mode which comprises the superposition of precessional modes (see chapter 5) can be used to attribute physicality to the two propagation constants of the microsphere mode. From this analysis β_l is the photon propagation path while β_m is the cumulative mode propagation path.

Just as for the fiber fields we can define what is termed a fundamental mode, which is a mode of either polarization with one intensity maximum and is defined by ψ_{ll1}; see Fig. 13. The modes of the microsphere per our construction are either TE or TM polarized for all mode orders as seen in Fig. 14. The TE and TM polarized fundamental modes are treated exclusively in this study as the general properties of interest here have been found to be only weakly dependent on mode order [16].

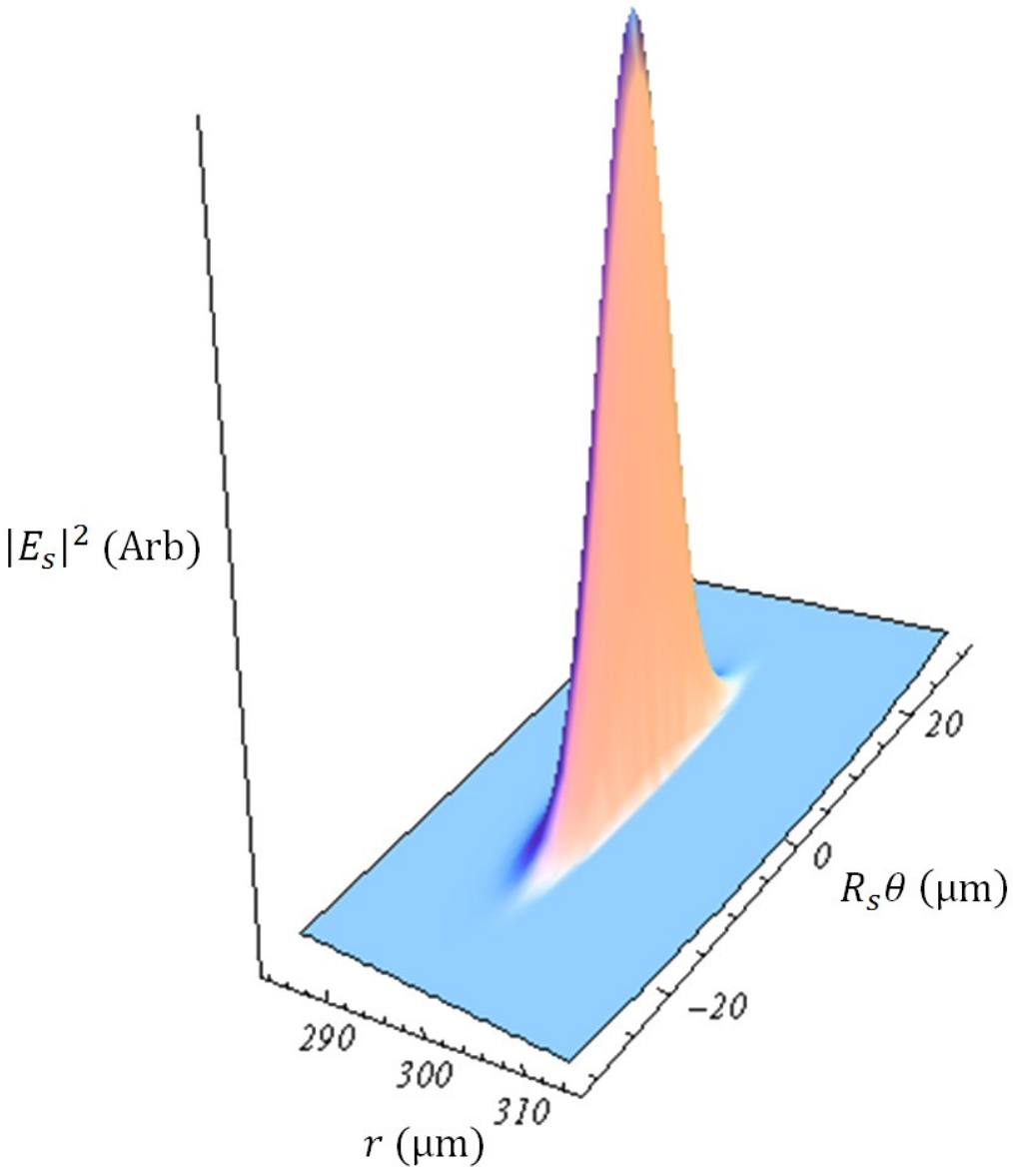

Figure 13. A fundamental TE sphere mode plotted in cross section at the equator. The sphere-air interface occurs at 300 μm.

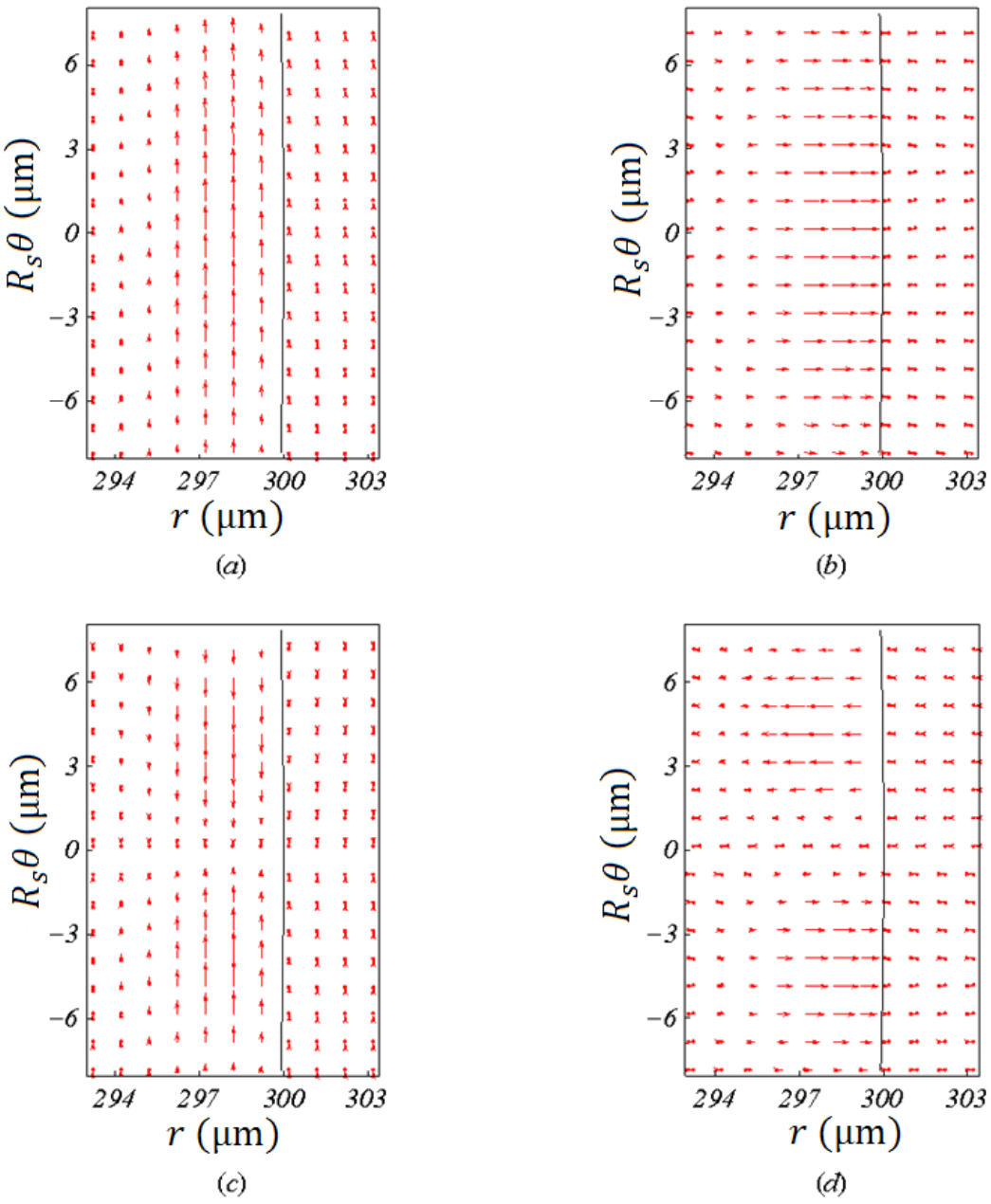

Figure 14. Vector electric field plot of (a) TE fundamental mode, (b) TM Fundamental mode, (c) TE 3rd order polar mode, (d) TM 3rd order polar mode. Notice that the field vectors are either tangent to or normal to the surface, thereby defining the polarization basis.

Coupled Mode Theory:

Coupled mode theory was originally used as a tool to understand the amount of cross talk, or power transfer, to expect between adjacent fiber optic cables [14, 20]. In the original inception these power transfer models were based on scalar treatments for waveguides in an energy orthogonal basis. However, as optical waveguides gained interest among scientists, around the time of the first commercially available optical fiber, many worked to extend the basic methodology first to a full vector treatment and then to waveguides with non-orthogonal energy bases. The following formulation is termed "non-orthogonal vector coupled-mode theory" and is reasonably well suited to our needs, as will be shown. Foremost in all formulations one begins with a power conservation argument. One would like to argue that the power loss in one guide is the negative of that of the second guide. For this reason the treatment typically begins with a derivation of a reciprocity relation between the guides which in turn leads to factors which can then be characterized as power transfer coefficients. This treatment of reciprocity in electromagnetics is closely related to the treatment of Hermitian operators in quantum systems in that label exchange should not affect the physicality of the outcome. We can again begin with two of Maxwell's equations in a lossless source free region;

$$\begin{aligned} \boldsymbol{\nabla} \times \boldsymbol{E_i} &= -i\omega\mu_o \boldsymbol{H_i}, \\ \boldsymbol{\nabla} \times \boldsymbol{H}_i &= i\omega\epsilon_i \boldsymbol{E}_i. \end{aligned} \tag{83}$$

where $\epsilon_i = \epsilon_i^*$ and μ_o are the medium dependent permittivity and vacuum permeability respectively. Using a procedure analogous to the derivation of Lorentz reciprocity which relies fundamentally on the general expansions of the vector operators we have

$$\boldsymbol{\nabla} \cdot \left(\boldsymbol{E}_i \times \boldsymbol{H}_j^*\right) = i\omega\epsilon_j \, \boldsymbol{E}_i \cdot \boldsymbol{E}_j^* - i\omega\mu_o \, \boldsymbol{H}_i \cdot \boldsymbol{H}_j^*. \tag{84}$$

The indices i and j allow for the consideration of the fields of two systems. Notice the symmetry under exchange of the indices

$$\boldsymbol{\nabla} \cdot \left(\boldsymbol{E}_j^* \times \boldsymbol{H}_i\right) = -i\omega\epsilon_i \, \boldsymbol{E}_i \cdot \boldsymbol{E}_j^* + i\omega\mu_o \, \boldsymbol{H}_i \cdot \boldsymbol{H}_j^*. \tag{85}$$

If Eq. (84) and Eq. (85) are summed we arrive at a useful reciprocity relation:

$$\boldsymbol{\nabla} \cdot \left(\boldsymbol{E}_i \times \boldsymbol{H}_j^* + \boldsymbol{E}_j^* \times \boldsymbol{H}_i\right) = -i\omega(\epsilon_i - \epsilon_j) \, \boldsymbol{E}_i \cdot \boldsymbol{E}_j^*. \tag{86}$$

As we are only interested in power transfer, which has been defined to propagate along $\hat{\boldsymbol{z}}$, let us convert this into an integral expression over an infinitesimal Δz as

$$\frac{\partial}{\partial z} \iint_{-\infty}^{\infty} \left(\boldsymbol{E}_i \times \boldsymbol{H}_j^* + \boldsymbol{E}_j^* \times \boldsymbol{H}_i\right) \cdot \hat{\boldsymbol{z}} \, dA = -i\omega \iint_{-\infty}^{\infty} (\epsilon_i - \epsilon_j) \boldsymbol{E}_i \cdot \boldsymbol{E}_j^* \, dA, \tag{87}$$

where the dielectric constants are left within the integrand as a generality to account for a transverse profile and A is the cross sectional area. One may note here that while we are interested in the coupling effects along the direction of propagation we have dropped the analogous transverse components on the left-hand side of Eq. (86). Rigorously these components have not been dropped at all but rather, as we have both defined propagation to be along $\hat{\boldsymbol{z}}$ and further neglected radiation losses in these field solutions to the Helmholtz equation along $\hat{\boldsymbol{z}}$, the transverse components on the left hand side can be shown to ultimately have no contribution [24].

A casual observation at this point, as the structure of Eq. (86) is that of a Poynting vector, would seem to imply that the derivations done would seem to represent power flow. This is caused by the direct derivation of the reciprocity theorem without the context of the actual fields to be

used. The preceding derivation is rigorous and correct but without context we are left with a result which cannot be interpreted. Strictly speaking, we must find the coupled mode equations which show analytically how the fields respond to coupling.

Let us construct a system of two-single mode unperturbed waveguides labeled 1 and 2, embedded in a uniform background dielectric. The two guides have identical transverse permittivity profiles $\epsilon_1(\mathrm{x},\mathrm{y}) \equiv \epsilon_1$ in guide 1 and $= \epsilon_o$ elsewhere, and $\epsilon_2(\mathrm{x},\mathrm{y}) \equiv \epsilon_2$ in guide two and $= \epsilon_o$ elsewhere. We begin the analysis by perturbing the forward propagating field of a particular guide by interacting it with the field of the total system through the reciprocity relation. We must construct the permittivity profile of the total system; however, it cannot be a simple summation of the individual guide profiles because they simultaneously exist in the same background dielectric. We will treat the system's permittivity profile then as a series of steps, i.e., $\epsilon(\mathrm{x},\mathrm{y}) = \epsilon_1$ in guide 1, = ϵ_2 in guide 2, and = ϵ_o elsewhere. The fields of the total system are constructed from a linear superposition of the fields of the unperturbed guides as

$$\begin{aligned} \boldsymbol{E}^t &= a(z)\boldsymbol{E}_1^t + b(z)\boldsymbol{E}_2^t, \\ \boldsymbol{E}^z &= a(z)\frac{\epsilon_1}{\epsilon}\boldsymbol{E}_1^z + b(z)\frac{\epsilon_2}{\epsilon}\boldsymbol{E}_2^z, \\ \boldsymbol{H} &= a(z)\boldsymbol{H}_1 + b(z)\boldsymbol{H}_2, \end{aligned} \tag{88}$$

where $a(z)$ and $b(z)$ are unknown amplitude coefficients and the superscripts (t, z) represent the transverse and longitudinal field components. Notice that the longitudinal components of the electric field are modified by the dielectric function of that particular guide's ratio to that of the total system. The total longitudinal components are bound to the total transverse components just as we have seen in the derivation of the fiber fields (Eq. (71)) due to Maxwell's equations and this leads to dielectric coupling. The system field is placed back into the

reciprocity relation as the i^{th} field while the j^{th} field is taken individually as that of either guide one or two. The result is found to be

$$\frac{da(z)}{dz}+\frac{C_{12}+C_{21}}{2}\frac{db(z)}{dz}=i(\kappa_{11}-\beta_1)a(z)+i\left(\kappa_{21}-\beta_1\frac{C_{12}+C_{21}}{2}\right)b(z), \quad (89)$$

$$\frac{C_{12}+C_{21}}{2}\frac{da(z)}{dz}+\frac{db(z)}{dz}=i(\kappa_{12}-\beta_2\frac{C_{12}+C_{21}}{2})a(z)+i(\kappa_{22}-\beta_2)b(z)$$

for guides one and two respectively. Here we have defined the constants to be

$$\kappa_{ij}=-\frac{\omega}{4}\iint_{-\infty}^{\infty}(\epsilon-\epsilon_i)(\boldsymbol{E}_i^t\cdot\boldsymbol{E}_j^{t^*}+\frac{\epsilon_j}{\epsilon}E_i^zE_j^{z^*})\,dA, \quad (90)$$

$$C_{ij}=\frac{1}{2}\iint_{-\infty}^{\infty}\boldsymbol{E}_j^{t^*}\times\boldsymbol{H}_i^t\,dA.$$

Notice that κ_{ij} is almost identical to the right-hand side of the reciprocity theorem with the additional inclusion of systemic dielectric effects. The reader should also note that because we have taken the convention that the transverse and longitudinal field components are purely real and imaginary, respectively, that both the κ_{ij} and C_{ij} integrals will evaluate to be purely real. The general solution to the coupled differential equations above does not readily lend itself to providing physical insight. For physical perspective, not rigor, let us assume identical couplers with the unity power contained initially only in waveguide 2. This effectively reduces our treatment to that of the earliest formulation of coupled mode theory in microwave cavities of the Manhattan-Project era [25] such that,

$$a(z) = \frac{1}{2}\left(e^{iz(\not{k}-\beta)} - e^{-iz(\beta+\not{k})}\right), \tag{91}$$

$$b(z) = \frac{1}{2}\left(e^{-iz(\beta+\not{k})} + e^{iz(\not{k}-\beta)}\right),$$

The power in a particular guide as a function of distance is then,

$$P_a(z) = a(z)^* a(z) = \sin^2(\not{k}z) \tag{92}$$

$$P_b(z) = b(z)^* b(z) = \cos^2(\not{k}z)$$

While this is a crude treatment it does give the physical interpretation of the reciprocity relation we are interested in. This can be observed most readily by making a small angle approximation, or rather small interaction length approximation, of the argument of the trigonometric functions as;

$$P_a(z) \propto \not{k}^2, \tag{93}$$

$$P_b(z) \propto 1 - \not{k}^2.$$

We can conclude that $\not{k}$ represents the z dependent amplitude coupling between the guides, much like as that seen in nonlinear optics [26] (Pg. 92), and $\not{k}^2$ represents power transmission between guides. This is readily observed graphically when the powers in the simplified guides are plotted vs. propagation as seen in Fig. 15; power is clearly conserved at all z.

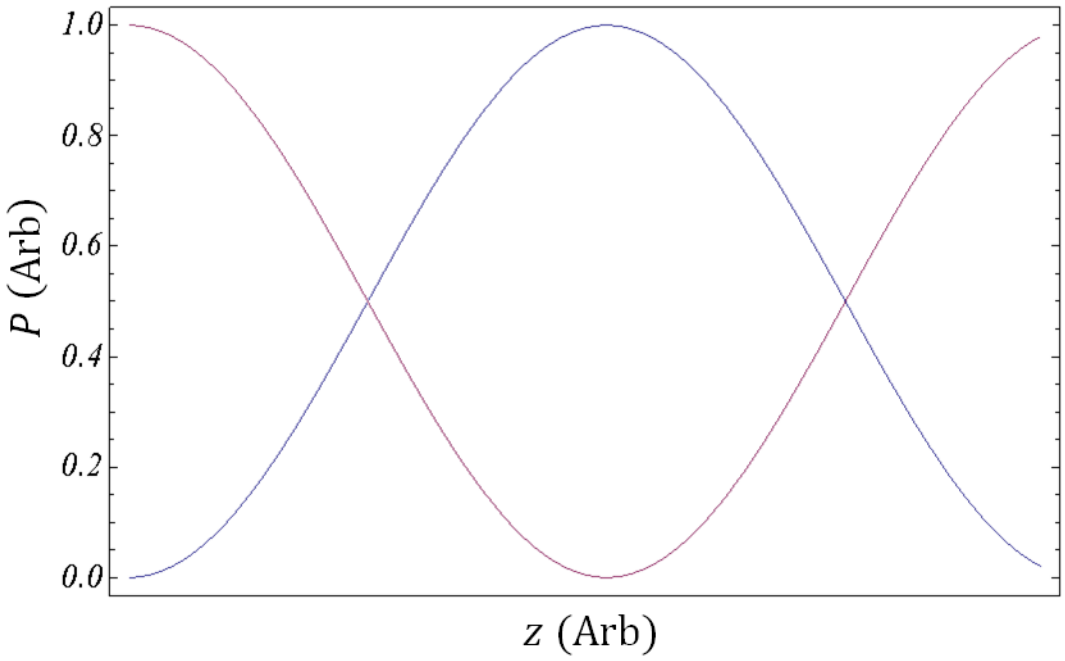

Figure 15. Power transfer as a function of propagation for the simplified waveguides for guide a(blue) and b(red) . Notice that the power is conserved for all z.

This is all that is needed to continue along the verification of the ring cavity model, but let us take one final step and look rigorously at power conservation in the system. The power of the total system can be found directly through the Poynting vector of the total fields, Eq. (88) as,

$$P(z) = |a(z)|^2 + |b(z)|^2 + \frac{1}{2}(C_{12}(z) + C_{21}(z))\Re(a(z)b(z)^*) \qquad (94)$$

where only the real component of the cross term is taken to represent power flow on physical grounds. The power can be made invariant if the conditions of Eq. (89) are solved simultaneously as,

$$\kappa_{12}(z) - C_{21}\frac{(\beta_2 - \beta_1)}{2} = \kappa_{21}(z) - C_{12}\frac{(\beta_1 - \beta_2)}{2}. \qquad (95)$$

Which we can immediately note implies the amplitude coupling coefficients will be unequal if the waveguides are not phase-matched, i.e., $\beta_2 \neq \beta_1$. This is not the problem it would appear to be from the surface. Looking back at the form of both $\mathcal{k}$ and C in Eq. (90), we can note that while C is an unbounded integral the system dielectric profile of the $\mathcal{k}$ integral will cause the integrals outside the waveguide being coupled into to go to zero. Physically then we can think of the interaction energy as having two parts; one a local energy transfer and the other a systemic depression in the modal energy due to the presence of another dielectric structure, something akin to an induced polarization in the adjacent dielectric structure. If the field extent, and thus phase velocity, is vastly different between the guides we would expect the relative strength of field perturbation to be dissimilar, thus limiting the energy available to transfer.

With the groundwork firmly established we can move on to actual computation. The fundamental assumption that the theory relies on, a fact which is not immediately apparent, is that the guides must be parallel; or rather the waveguides must be linear since we are to enforce power conservation in some cardinal direction. In applying this method to fiber-sphere coupling we must treat the sphere as a linear waveguide, which is not as poor an approximation as it sounds, and enforce power conservation along the propagation direction of the fiber. The validity of this assumption lies in the very short interaction region between the guides, something on the order of a few μm. Within this region the curvature of the sphere (typical radius $\sim$ 400 μm) is small compared to a wavelength and thus our assumption amounts to something of a small angle approximation in the dot product of the wavevectors of the two guides:

$$\boldsymbol{k}_s \cdot \boldsymbol{k}_f = |\boldsymbol{k}_s||\boldsymbol{k}_f|\cos(\phi(z)) \cong |\boldsymbol{k}_s||\boldsymbol{k}_f|. \tag{96}$$

Furthermore, for the results of the overlap integration to be of merit one must also properly normalize the fields in each guide. As power transfer is of fundamental interest the waveguide power is normalized to unity over the cross sectional area. Thus when the power transmission probabilities, $T_{ij} \equiv \hbar_{ij}^{*}\hbar_{ij}$, are found they will directly represent the power flow between the guides.

With the fields found for each of the guides the most challenging aspect of actually computing these transmission probabilities is in the coordinate transforms that are required to convert one coordinate system to the next and account for polarization and physical geometry in the new coordinate system. The field in the guide not being integrated over must first be converted, via a unitary transform, into a Cartesian basis so a linear offset can be added, placing the two guides together at the bounding surface. The field must then be converted into the basis of the guide being integrated over, all the while allowing for arbitrary polarization and potential misalignment in the unitary transform. This process, if not completed rigorously, can readily lead to erroneous results. Let us begin by deriving the transforms that place the microsphere fields in the fiber's coordinate system. The fiber coordinate system must first be decomposed into a Cartesian basis so the microsphere's Cartesian coordinates can be expressed in the fiber's Cartesian basis:

$$x_f \equiv x_f(r,\theta) = rcos(\theta), \tag{97}$$

$$y_f \equiv y_f(r,\theta) = rsin(\theta),$$

$$z_f \equiv z,$$

where the explicit coordinate dependences have been dropped and the radial and azimuthal coordinates of the fiber have been redefined, $r \equiv \rho$ and $\theta \equiv \phi$, to provide notational similarity

between the spherical and cylindrical coordinate systems. This serves to simplify the respective transforms as the radial and azimuthal coordinates then have the same meaning in both systems. Angular and linear offsets can be added to each component to account for arbitrary alignment between the guides, such as

$$x_{sf} \equiv x_f + (R_s + S_o)cos\,(\theta_{off}), \tag{98}$$

$$y_{sf} \equiv y_f + (R_s + S_o)sin\,(\theta_{off}),$$

$$z_{sf} \equiv z_f,$$

where R_s is the microsphere radius, S_o is the gap distance between guides and θ_{off} is the angular position of the fiber center with respect to the microsphere's equatorial ($x_{sf} - z_{sf}$) plane. New spherical coordinates can be found from the transformed Cartesian components of the fiber as

$$r_{sf} = \sqrt{{x_{sf}}^2 + {y_{sf}}^2 + {z_{sf}}^2}, \tag{99}$$

$$\theta_{sf} = sin^{-1}\left(\frac{y_{sf}}{r_{sf}}\right),$$

$$\phi_{\mathrm{sf}} = tan^{-1}\left(\frac{z_{sf}}{x_{sf}}\right).$$

These transforms appear structurally unfamiliar because we made the z component of the spherical system congruent with that of the cylindrical system and defined θ as the angle up from the new equatorial plane. We construct a unitary transform in terms of base cylindrical

coordinates that transforms the native spherical coordinates into transformed cylindrical coordinates as

$$\boldsymbol{U}_{sf} \equiv \begin{pmatrix} cos(\theta) & sin(\theta) & 0 \\ -sin(\theta) & cos(\theta) & 0 \\ 0 & 0 & 1 \end{pmatrix} \cdot \tag{100}$$

$$\begin{pmatrix} cos(\theta_{sf})cos(\phi_{sf}) & -sin(\theta_{sf})cos(\phi_{sf}) & -sin(\phi_{sf}) \\ sin(\theta_{sf}) & cos(\theta_{sf}) & 0 \\ cos(\theta_{sf})sin(\phi_{sf}) & -sin(\theta_{sf})sin(\phi_{sf}) & cos(\phi_{sf}) \end{pmatrix}.$$

Finally, the microsphere fields can be defined in the modified fiber basis as,

$$\boldsymbol{E}_{sf}(r,\theta,z) = \boldsymbol{U}_{sf}(r,\theta,z) \cdot \boldsymbol{E_s}\left(r_{sf}(r,\theta,z), \theta_{sf}(r,\theta,z), \phi_{sf}(r,\theta,z)\right), \tag{101}$$

$$\boldsymbol{H}_{sf}(r,\theta,z) = \boldsymbol{U}_{sf}(r,\theta,z) \cdot \boldsymbol{H_s}\left(r_{sf}(r,\theta,z), \theta_{sf}(r,\theta,z), \phi_{sf}(r,\theta,z)\right),$$

where $\boldsymbol{E_s}$ and $\boldsymbol{H_s}$ are the base fields of the microsphere and the explicit dependence of fiber coordinates has been included for completeness.

The fiber fields must be treated in an analogous manner before the transmission probabilities can be found. We begin with a decomposition into Cartesian coordinates,

$$x_s \equiv x_s(r,\theta,\phi) = rcos(\theta)cos\,(\phi), \tag{102}$$

$$y_s \equiv y_s(r,\theta) = rsin(\theta),$$

$$z_s \equiv z_s(r,\theta,\phi) = rcos(\theta)sin(\phi).$$

The offset Cartesian components are then found to be

$$x_{fs} \equiv x_s - (R_s + S_o)cos\,(\theta_{off}), \tag{103}$$

$$y_{fs} \equiv y_s - (R_s + S_o)sin\,(\theta_{off}),$$

$$z_{fs} \equiv z_s$$

Just as before we can now derive transformed cylindrical coordinates as

$$r_{fs} = \sqrt{{x_{fs}}^2 + {y_{fs}}^2}, \tag{104}$$

$$\theta_{fs} = tan^{-1}\left(\frac{y_{fs}}{x_{fs}}\right),$$

$$z_{fs} = z_s.$$

The unitary transformation matrix for native cylindrical to modified spherical coordinates is derived to be

$$\boldsymbol{U}_{fs} \equiv \begin{pmatrix} cos(\theta)\cos\,(\phi) & sin(\theta) & cos(\theta)\sin(\phi) \\ -sin(\theta)\cos\,(\phi) & cos(\theta) & -\sin\,(\theta)\sin(\phi) \\ -\sin(\phi) & 0 & \cos\,(\phi) \end{pmatrix} \cdot \tag{105}$$

$$\begin{pmatrix} cos(\theta_{fs}) & -sin(\theta_{fs}) & 0 \\ sin(\theta_{fs}) & cos(\theta_{fs}) & 0 \\ 0 & 0 & 1 \end{pmatrix}.$$

The fiber fields can now be expressed in the modified spherical coordinates as

$$\boldsymbol{E}_{fs}(r,\theta,\phi) = \boldsymbol{U}_{fs}(r,\theta,\phi)\cdot\boldsymbol{E}_f\left(r_{fs}(r,\theta,\phi),\theta_{fs}(r,\theta,\phi),z_{fs}(r,\theta,\phi)\right), \tag{106}$$

$$\boldsymbol{H}_{fs}(r,\theta,\phi) = \boldsymbol{U}_{fs}(r,\theta,\phi)\cdot\boldsymbol{H}_f\left(r_{fs}(r,\theta,\phi),\theta_{fs}(r,\theta,\phi),z_{fs}(r,\theta,\phi)\right),$$

where $\boldsymbol{E}_f$ and $\boldsymbol{H}_f$ are the native fiber fields and the explicit dependence of the transformations are included for completeness. Let us now explicitly define the fiber and microsphere fields for the two polarizations used in the computations. The sphere fields are found in terms of the Debye potential and Maxwell's equations to be

$$TE = \begin{cases} \boldsymbol{E}_s(r,\theta,\phi) = \boldsymbol{\nabla}\times(\hat{\boldsymbol{r}}\,\psi) \\ \boldsymbol{H}_s(r,\theta,\phi) = \dfrac{i}{\omega\mu}\boldsymbol{\nabla}\times\boldsymbol{E_s} \end{cases}, \tag{107}$$

$$TM = \begin{cases} \boldsymbol{E}_s(r,\theta,\phi) = \dfrac{-i}{\omega\epsilon_s}\boldsymbol{\nabla}x\boldsymbol{H}_s \\ \boldsymbol{H}_s(r,\theta,\phi) = \boldsymbol{\nabla}\times(\hat{\boldsymbol{r}}\,\psi) \end{cases}.$$

For the fiber we will define the polarization based on the sphere polarization basis rather than the absolute lab basis. When the mean polarization, in the sense that the fiber's polarization is not uniform, of the electric field of the fiber is along $\widehat{\boldsymbol{\theta}}$ we will term this TE polarized and when the magnetic field is along $\widehat{\boldsymbol{\theta}}$ it will be termed TM polarized. Let us not rewrite the field expressions derived earlier, but rather express the solution as

$$\boldsymbol{E}_f(r,\theta,z) = \langle \boldsymbol{E}_f^r(r,\theta,z), \boldsymbol{E}_f^\theta(r,\theta,z), \boldsymbol{E}_f^z(r,\theta,z)\rangle, \tag{108}$$

$$\boldsymbol{H}_f(r,\theta,z) = \langle \boldsymbol{H}_f^r(r,\theta,z), \boldsymbol{H}_f^\theta(r,\theta,z), \boldsymbol{H}_f^z(r,\theta,z)\rangle.$$

This allows us to readily assign an arbitrary mean polarization direction to the fields by the addition of a rotation to the coordinate θ as $\theta \to \theta + p$. The particular polarization directions we are interested in can be expressed as

$$\mathrm{TE} = \begin{cases} \boldsymbol{E}_f(r,\theta,z), \\ \boldsymbol{H}_f(r,\theta,z), \end{cases} \tag{109}$$

$$\mathrm{TM} = \begin{cases} \boldsymbol{E}_f\left(r,\theta+\frac{\pi}{2},z\right), \\ \boldsymbol{H}_f\left(r,\theta+\frac{\pi}{2},z\right). \end{cases}$$

As we are interested not in the differential transfer of power as expressed in Eq. (90) above, but rather the total power transfer, the overlap integrals must be further integrated along z. This has no effect on the analysis presented previously; it only changes the form of the overlap integral to

$$\kappa_{ij} \equiv \int_{-\infty}^{\infty} \not{\kappa}_{ij} dz = -\frac{\omega}{4} \iiint_{-\infty}^{\infty} (\epsilon - \epsilon_i)(\boldsymbol{E}_i^t \cdot \boldsymbol{E}_j^{t^*} + \frac{\epsilon_j}{\epsilon} E_i^z E_j^{z^*})\, dA dz. \tag{110}$$

With the fields properly normalized and the polarizations defined the overlap integrals can be evaluated to find the transmission coefficients. The overlap integrals are,

$$\kappa_{fs} = -\frac{\omega\epsilon_0}{4}({n_s}^2 - {n_o}^2) \iiint_{V_s} \left(\boldsymbol{E}_s \cdot {\boldsymbol{E}_{fs}}^*\right) r\cos(\theta)\, dr d\theta dz, \tag{111}$$

$$\kappa_{sf} = -\frac{\omega\epsilon_0}{4}\left({n_f}^2 - {n_o}^2\right) \iiint_{V_f} \left(\boldsymbol{E}_f \cdot {\boldsymbol{E}_{sf}}^*\right) r\, dr d\theta dz,$$

where the convention is taken that the coupling direction is $i \rightarrow j$ which is counter to the typical treatment in the literature [16]. Notice that the systemic dielectric constant has limited the overlap regions to only the volume of interest. Although both the fiber and sphere are made of fused silica, their refractive indices are written as n_f and n_s, respectively. Before evaluating the overlap let us check the validity of the transforms graphically. In each of the vector field plots below every aspect: boundaries, vector fields and strengths have been plotted rigorously using the coordinate transforms cited above. We can observe that the characteristics of the fields and their respective physical location are summarily identical in both the fiber, Fig. 16, and microsphere, Fig. 17, native coordinate systems. With the transformational symmetry confirmed we can begin computing the transmission probabilities.

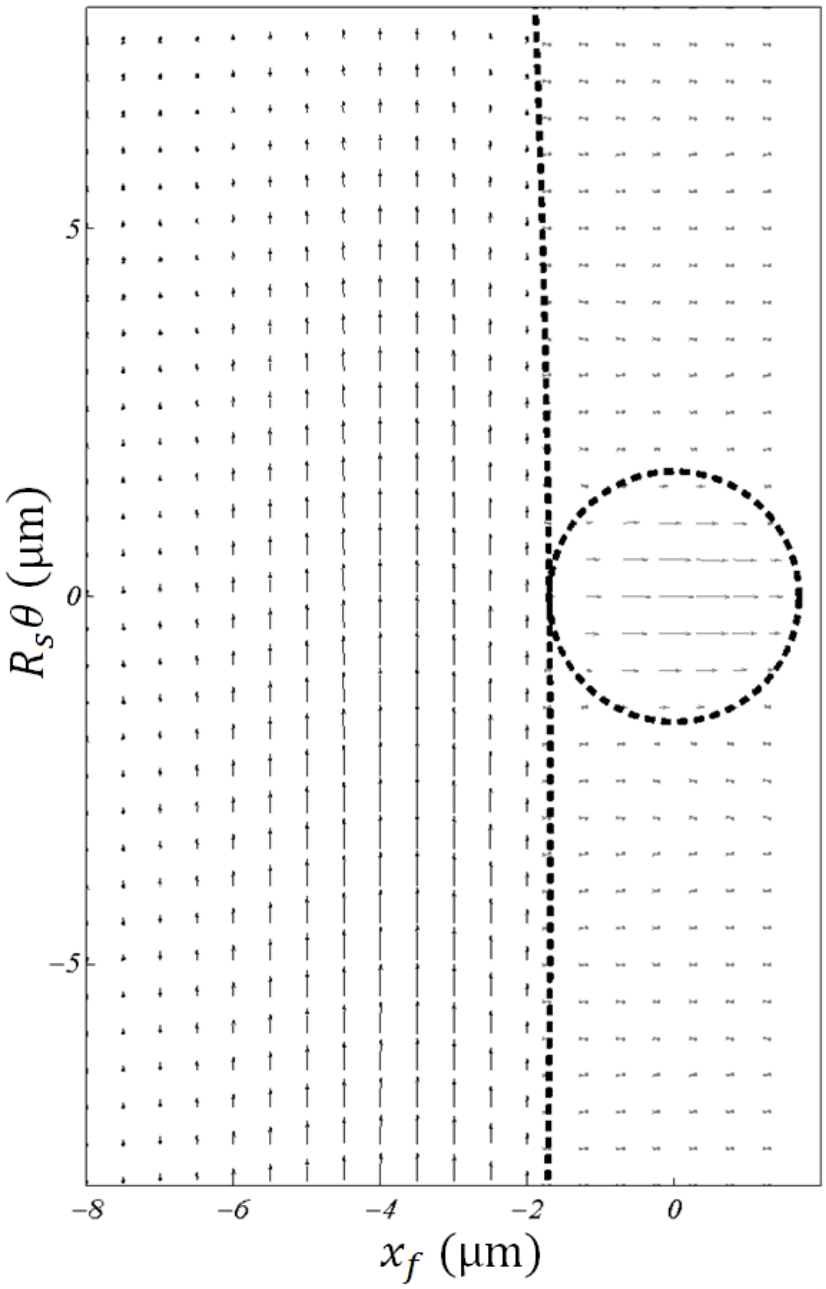

Figure 16. Vector plots of the native fiber field (grey) and transformed sphere fields (black) with a small offset between the equatorial plane and the fiber. Here all elements including boundary locations (dashed lines) have been found from the derived unitary transforms. Notice that the origin is located at the fiber center.

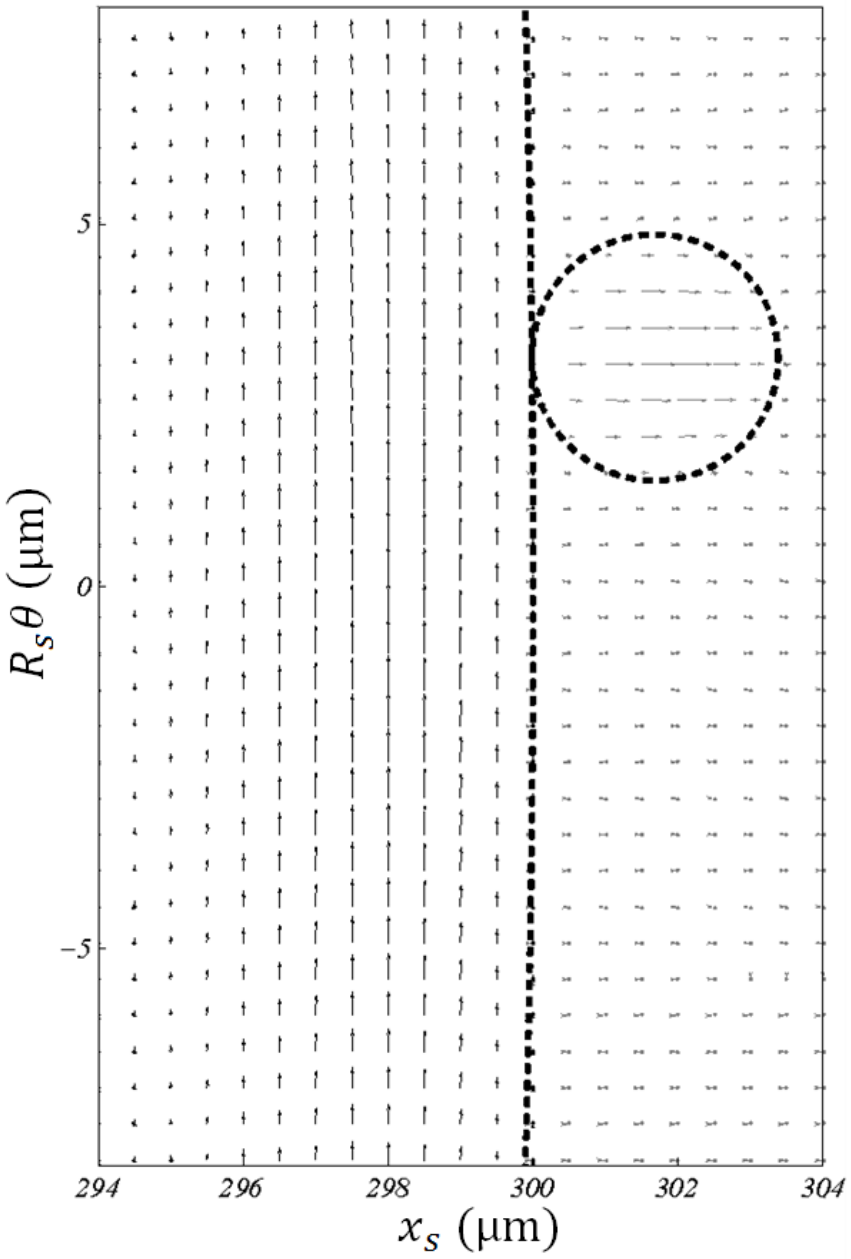

Figure 17. Vector field plots of the native sphere field (black) and the transformed fiber field (grey), where the polarization of the fiber field has been rotated to TE for demonstration of validity. Notice that the equatorial offset appears more pronounced in the sphere system, but is identical to Fig 16. Notice as well that the origin is now located at the sphere center.

The induced complexity of these transforms and the field equations themselves do not readily lend themselves to analytic analysis. The overlap integrals are therefore evaluated numerically with great care taken to prevent limitations due to numerical precision. To illustrate the difficulty faced in performing these computations here is the final integrand for fiber to microsphere coupling:

$$r^2 \left(-e^{i\, r \cos(\theta) \sin(\phi)\, \beta_f} \sin(\theta) \sin(\phi) \right.$$

$$\left(A\, J_i\left(\sqrt{\left(r\cos(\theta)\cos(\phi) - \cos(\theta\text{off})\,(R_o + S_o)\right)^2 + \left(r\sin(\theta) - \sin(\theta\text{off})\,(R_o + S_o)\right)^2}\right) \right.$$

$$\sqrt{k^2 n_s^2 - \beta_f^2}\,\Big)$$

$$\cos\Big(i\left(\tan^{-1}(r\cos(\theta)\cos(\phi) - \cos(\theta\text{off})\,(R_o + S_o),\, r\sin(\theta) - \sin(\theta\text{off})\,(R_o + S_o)\right) + P_b\Big)\Big)$$

$$\delta f_{in}\left(\sqrt{\left(r\cos(\theta)\cos(\phi) - \cos(\theta\text{off})\,(R_o + S_o)\right)^2 + \left(r\sin(\theta) - \sin(\theta\text{off})\,(R_o + S_o)\right)^2}\right) +$$

$$\frac{1}{K_i\left(a\sqrt{\beta_f^2 - k^2 n_o^2}\right)} A\, J_i\left(a\sqrt{k^2 n_s^2 - \beta_f^2}\right) K_i\left(\sqrt{\left(r\cos(\theta)\cos(\phi) - \cos(\theta\text{off})\,(R_o + S_o)\right)^2 + \right.$$

$$\left.\left(r\sin(\theta) - \sin(\theta\text{off})\,(R_o + S_o)\right)^2}\right)\sqrt{\beta_f^2 - k^2 n_o^2}\,\Big)$$

$$\cos\Big(i\left(\tan^{-1}(r\cos(\theta)\cos(\phi) - \cos(\theta\text{off})\,(R_o + S_o),\, r\sin(\theta) - \sin(\theta\text{off})\,(R_o + S_o)\right) + P_b\Big)\Big)$$

$$\left.\left.\delta f_{out}\left(\sqrt{\left(r\cos(\theta)\cos(\phi) - \cos(\theta\text{off})\,(R_o + S_o)\right)^2 + \left(r\sin(\theta) - \sin(\theta\text{off})\,(R_o + S_o)\right)^2}\right)\right) +$$

$$e^{i\, r \cos(\theta) \sin(\phi)\, \beta_f} \Big(\cos(\theta)\sin\Big(\tan^{-1}(r\cos(\theta)\cos(\phi) - \cos(\theta\text{off})\,(R_o + S_o),$$

$$r\sin(\theta) - \sin(\theta\text{off})\,(R_o + S_o)\Big) -$$

$$\cos(\phi)\cos\Big(\tan^{-1}(r\cos(\theta)\cos(\phi) - \cos(\theta\text{off})\,(R_o + S_o),\, r\sin(\theta) - \sin(\theta\text{off})\,(R_o + S_o)\Big)\Big)\sin(\theta)\Big)$$

$$\left(\frac{1}{\beta_f^2 - k^2 n_o^2}\, i\, \cos\Big(i\left(\tan^{-1}(r\cos(\theta)\cos(\phi) - \cos(\theta\text{off})\,(R_o + S_o),\, r\sin(\theta) - \sin(\theta\text{off})\,(R_o + S_o)\right) + \right.$$

$$P_b\Big)\Big)\,\beta_f \left(\frac{1}{K_i\left(a\sqrt{\beta_f^2 - k^2 n_o^2}\right)} A\, J_i\left(a\sqrt{k^2 n_s^2 - \beta_f^2}\right)\sqrt{\beta_f^2 - k^2 n_o^2} \right.$$

$$\Big(\Big(i\, K_i\Big(\sqrt{\left(r\cos(\theta)\cos(\phi) - \cos(\theta\text{off})\,(R_o + S_o)\right)^2 + \left(r\sin(\theta) - \sin(\theta\text{off})\,(R_o + S_o)\right)^2}\Big)$$

$$\sqrt{\beta_f^2 - k^2 n_o^2}\,\Big)\Big) \Big/ \Big(\sqrt{\left(r\cos(\theta)\cos(\phi) - \cos(\theta\text{off})\,(R_o + S_o)\right)^2 +$$

$$\left(r\sin(\theta) - \sin(\theta\text{off})\,(R_o + S_o)\right)^2}\Big)\sqrt{\beta_f^2 - k^2 n_o^2}\,\Big) - K_{i+1}\Big($$

$$\sqrt{\left(r\cos(\theta)\cos(\phi) - \cos(\theta\text{off})\,(R_o + S_o)\right)^2 + \left(r\sin(\theta) - \sin(\theta\text{off})\,(R_o + S_o)\right)^2}\Big)$$

$$\left(\left(\frac{i\,J_i\left(a\sqrt{k^2\,n_s^2-\beta_f^2}\right)}{a\sqrt{k^2\,n_s^2-\beta_f^2}}-J_{i+1}\left(a\sqrt{k^2\,n_s^2-\beta_f^2}\right)\right)\Big/\right.$$

$$\left(a\,J_i\left(a\sqrt{k^2\,n_s^2-\beta_f^2}\right)\sqrt{k^2\,n_s^2-\beta_f^2}\right)+\left(\frac{i\,K_i\left(a\sqrt{\beta_f^2-k^2\,n_o^2}\right)}{a\sqrt{\beta_f^2-k^2\,n_o^2}}-\right.$$

$$\left.\left.\left.K_{i+1}\left(a\sqrt{\beta_f^2-k^2\,n_o^2}\right)\right)\Big/\left(a\,K_i\left(a\sqrt{\beta_f^2-k^2\,n_o^2}\right)\sqrt{\beta_f^2-k^2\,n_o^2}\right)\right)\right)$$

$$\delta f_{out}\left(\sqrt{\left(r\cos(\theta)\cos(\phi)-\cos(\theta off)\,(R_o+S_o)\right)^2+\left(r\sin(\theta)-\sin(\theta off)\,(R_o+S_o)\right)^2}\right)-\frac{1}{k^2\,n_s^2-\beta_f^2}\,\dot{u}$$

$$\cos\left(i\left(\tan^{-1}\left(r\cos(\theta)\cos(\phi)-\cos(\theta off)\,(R_o+S_o),\,r\sin(\theta)-\sin(\theta off)\,(R_o+S_o)\right)+P_b\right)\right)$$

$$\beta_f\left(A\sqrt{k^2\,n_s^2-\beta_f^2}\;\left(\left(i\,J_i\left(\sqrt{\left(r\cos(\theta)\cos(\phi)-\cos(\theta off)\,(R_o+S_o)\right)^2+\right.\right.\right.\right.$$

$$\left.\left.\left.\left.\left(r\sin(\theta)-\sin(\theta off)\,(R_o+S_o)\right)^2}\right)\sqrt{k^2\,n_s^2-\beta_f^2}\right)\right)\Big/$$

$$\left(\sqrt{\left(r\cos(\theta)\cos(\phi)-\cos(\theta off)\,(R_o+S_o)\right)^2+\left(r\sin(\theta)-\sin(\theta off)\,(R_o+S_o)\right)^2}\right.$$

$$\left.\sqrt{k^2\,n_s^2-\beta_f^2}\right)-J_{i+1}\left(\sqrt{\left(r\cos(\theta)\cos(\phi)-\cos(\theta off)\,(R_o+S_o)\right)^2+\right.$$

$$\left.\left.\left(r\sin(\theta)-\sin(\theta off)\,(R_o+S_o)\right)^2}\right)\sqrt{k^2\,n_s^2-\beta_f^2}\right)\Big)-$$

$$\left(A\,i^2\,J_i\left(\sqrt{\left(r\cos(\theta)\cos(\phi)-\cos(\theta off)\,(R_o+S_o)\right)^2+\left(r\sin(\theta)-\sin(\theta off)\,(R_o+S_o)\right)^2}\right)\right.$$

$$\left.\sqrt{k^2\,n_s^2-\beta_f^2}\right)\left(\frac{1}{a^2\left(\beta_f^2-k^2\,n_o^2\right)}+\frac{1}{a^2\left(k^2\,n_s^2-\beta_f^2\right)}\right)\Big)\Big/$$

$$\left(\sqrt{\left(r\cos(\theta)\cos(\phi)-\cos(\theta off)\,(R_o+S_o)\right)^2+\left(r\sin(\theta)-\sin(\theta off)\,(R_o+S_o)\right)^2}\right.$$

$$\left(\left(\frac{i\,J_i\left(a\sqrt{k^2\,n_s^2-\beta_f^2}\right)}{a\sqrt{k^2\,n_s^2-\beta_f^2}}-J_{i+1}\left(a\sqrt{k^2\,n_s^2-\beta_f^2}\right)\right)\Big/\right.$$

$$\left(a\,J_i\left(a\sqrt{k^2\,n_s^2-\beta_f^2}\right)\sqrt{k^2\,n_s^2-\beta_f^2}\right)+\left(\frac{i\,K_i\left(a\sqrt{\beta_f^2-k^2\,n_o^2}\right)}{a\sqrt{\beta_f^2-k^2\,n_o^2}}-\right.$$

$$\left.\left.\left.K_{i+1}\left(a\sqrt{\beta_f^2-k^2\,n_o^2}\right)\right)\Big/\left(a\,K_i\left(a\sqrt{\beta_f^2-k^2\,n_o^2}\right)\sqrt{\beta_f^2-k^2\,n_o^2}\right)\right)\right)\right)$$

$$\delta f_{in}\left(\sqrt{\left(r\cos(\theta)\cos(\phi)-\cos(\theta off)\,(R_o+S_o)\right)^2+\left(r\sin(\theta)-\sin(\theta off)\,(R_o+S_o)\right)^2}\right)\Bigg)+$$

$$e^{i\,r\cos(\theta)\sin(\phi)\,\beta_f}\left(\cos(\theta)\cos\left(\tan^{-1}(r\cos(\theta)\cos(\phi)-\cos(\theta off)\,(R_o+S_o),\right.\right.$$
$$\left.r\sin(\theta)-\sin(\theta off)\,(R_o+S_o)\right)+$$
$$\left.\cos(\phi)\sin(\theta)\sin\left(\tan^{-1}(r\cos(\theta)\cos(\phi)-\cos(\theta off)\,(R_o+S_o),\,r\sin(\theta)-\sin(\theta off)\,(R_o+S_o)\right)\right)\right)$$

$$\left(\frac{1}{k^2\,n_s^2-\beta_f^2}\sin\left(i\left(\tan^{-1}(r\cos(\theta)\cos(\phi)-\cos(\theta off)\,(R_o+S_o),\,r\sin(\theta)-\sin(\theta off)\,(R_o+S_o)\right)+P_b\right)\right)$$

$$\beta_f\left(\left(\dot{u}\,A\,i\,J_i\left(\sqrt{\left(r\cos(\theta)\cos(\phi)-\cos(\theta off)\,(R_o+S_o)\right)^2+\left(r\sin(\theta)-\sin(\theta off)\,(R_o+S_o)\right)^2}\right.\right.\right.$$

$$\left.\left.\sqrt{k^2\,n_s^2-\beta_f^2}\right)\right)\Big/$$
$$\left(\sqrt{\left(r\cos(\theta)\cos(\phi)-\cos(\theta off)\,(R_o+S_o)\right)^2+\left(r\sin(\theta)-\sin(\theta off)\,(R_o+S_o)\right)^2}\right)-$$
$$\left(\dot{u}\,A\,i\sqrt{k^2\,n_s^2-\beta_f^2}\,\left(\left(i\,J_i\left(\sqrt{\left(r\cos(\theta)\cos(\phi)-\cos(\theta off)\,(R_o+S_o)\right)^2+\right.\right.\right.\right.$$
$$\left.\left.\left.\left.\left(r\sin(\theta)-\sin(\theta off)\,(R_o+S_o)\right)^2}\right)\sqrt{k^2\,n_s^2-\beta_f^2}\right)\right)\Big/$$
$$\left(\sqrt{\left(r\cos(\theta)\cos(\phi)-\cos(\theta off)\,(R_o+S_o)\right)^2+\right.$$
$$\left.\left(r\sin(\theta)-\sin(\theta off)\,(R_o+S_o)\right)^2}\sqrt{k^2\,n_s^2-\beta_f^2}\right)-$$
$$J_{i+1}\left(\sqrt{\left(r\cos(\theta)\cos(\phi)-\cos(\theta off)\,(R_o+S_o)\right)^2+\right.$$
$$\left.\left.\left(r\sin(\theta)-\sin(\theta off)\,(R_o+S_o)\right)^2}\sqrt{k^2\,n_s^2-\beta_f^2}\right)\right)\left(\frac{1}{a^2\left(\beta_f^2-k^2\,n_o^2\right)}+\right.$$

$$\frac{1}{a^2\left(k^2 n_s^2 - \beta_f^2\right)}\Bigg)\Bigg) \Bigg/ \Bigg(\Bigg(\frac{i J_i\left(a\sqrt{k^2 n_s^2 - \beta_f^2}\right)}{a\sqrt{k^2 n_s^2 - \beta_f^2}} - J_{i+1}\left(a\sqrt{k^2 n_s^2 - \beta_f^2}\right)\Bigg) \Bigg/$$

$$\left(a J_i\left(a\sqrt{k^2 n_s^2 - \beta_f^2}\right)\sqrt{k^2 n_s^2 - \beta_f^2}\right) + \Bigg(\frac{i K_i\left(a\sqrt{\beta_f^2 - k^2 n_o^2}\right)}{a\sqrt{\beta_f^2 - k^2 n_o^2}} -$$

$$K_{i+1}\left(a\sqrt{\beta_f^2 - k^2 n_o^2}\right)\Bigg) \Bigg/ \left(a K_i\left(a\sqrt{\beta_f^2 - k^2 n_o^2}\right)\sqrt{\beta_f^2 - k^2 n_o^2}\right)\Bigg)\Bigg)$$

$$\delta f_{in}\left(\sqrt{\left((r\cos(\theta)\cos(\phi) - \cos(\theta off)\,(R_o + S_o)\right)^2 + \left(r\sin(\theta) - \sin(\theta off)\,(R_o + S_o)\right)^2}\right) -$$

$$\frac{1}{\beta_f^2 - k^2 n_o^2}$$

$$\sin\left(i\left(\tan^{-1}\left(r\cos(\theta)\cos(\phi) - \cos(\theta off)\,(R_o + S_o),\, r\sin(\theta) - \sin(\theta off)\,(R_o + S_o)\right) + P_b\right)\right)$$

$$\beta_f \Bigg(\Bigg(\dot{u}\, A\, i\, J_i\left(a\sqrt{k^2 n_s^2 - \beta_f^2}\right) K_i\Bigg(\sqrt{\left((r\cos(\theta)\cos(\phi) - \cos(\theta off)\,(R_o + S_o)\right)^2 +$$

$$\left(r\sin(\theta) - \sin(\theta off)\,(R_o + S_o)\right)^2}\sqrt{\beta_f^2 - k^2 n_o^2}\Bigg)\Bigg) \Bigg/$$

$$\left(K_i\left(a\sqrt{\beta_f^2 - k^2 n_o^2}\right)\sqrt{\left((r\cos(\theta)\cos(\phi) - \cos(\theta off)\,(R_o + S_o)\right)^2 +\right.$$

$$\left.\left(r\sin(\theta) - \sin(\theta off)\,(R_o + S_o)\right)^2}\right) -$$

$$\Bigg(\dot{u}\, A\, i\, J_i\left(a\sqrt{k^2 n_s^2 - \beta_f^2}\right)\sqrt{\beta_f^2 - k^2 n_o^2}\left(\frac{1}{a^2\left(\beta_f^2 - k^2 n_o^2\right)} + \frac{1}{a^2\left(k^2 n_s^2 - \beta_f^2\right)}\right)$$

$$\Bigg(\Bigg(i K_i\Bigg(\sqrt{\left((r\cos(\theta)\cos(\phi) - \cos(\theta off)\,(R_o + S_o)\right)^2 +$$

$$\left(r\sin(\theta) - \sin(\theta off)\,(R_o + S_o)\right)^2}\sqrt{\beta_f^2 - k^2 n_o^2}\Bigg)\Bigg) \Bigg/$$

$$\Bigg(\sqrt{\left((r\cos(\theta)\cos(\phi) - \cos(\theta off)\,(R_o + S_o)\right)^2 +$$

$$\left(r\sin(\theta) - \sin(\theta off)\,(R_o + S_o)\right)^2}\sqrt{\beta_f^2 - k^2 n_o^2}\Bigg) -$$

$$K_{i+1}\Bigg(\sqrt{\left((r\cos(\theta)\cos(\phi) - \cos(\theta off)\,(R_o + S_o)\right)^2 +$$

$$\left(r\sin(\theta) - \sin(\theta off)\,(R_o + S_o)\right)^2}\sqrt{\beta_f^2 - k^2 n_o^2}\Bigg)\Bigg)\Bigg) \Bigg/$$

$$\left(K_i\left(a\sqrt{\beta_f^2 - k^2 n_o^2}\right)\left(\left(\frac{i J_i\left(a\sqrt{k^2 n_s^2 - \beta_f^2}\right)}{a\sqrt{k^2 n_s^2 - \beta_f^2}} - J_{i+1}\left(a\sqrt{k^2 n_s^2 - \beta_f^2}\right)\right)\Big/\right.$$

$$\left(a J_i\left(a\sqrt{k^2 n_s^2 - \beta_f^2}\right)\sqrt{k^2 n_s^2 - \beta_f^2}\right) + \left(\frac{i K_i\left(a\sqrt{\beta_f^2 - k^2 n_o^2}\right)}{a\sqrt{\beta_f^2 - k^2 n_o^2}} -\right.$$

$$\left.\left.K_{i+1}\left(a\sqrt{\beta_f^2 - k^2 n_o^2}\right)\right)\Big/\left(a K_i\left(a\sqrt{\beta_f^2 - k^2 n_o^2}\right)\sqrt{\beta_f^2 - k^2 n_o^2}\right)\right)\Big)\Big)$$

$$\delta f_{out}\left(\sqrt{\left((r\cos(\theta)\cos(\phi) - \cos(\theta off)\,(R_o + S_o)\right)^2 + \left(r\sin(\theta) - \sin(\theta off)\,(R_o + S_o)\right)^2}\right)\Big)\Big)^*$$

$$\cos(\theta)\,N_s\left(\sqrt{\frac{\pi}{2}}\; e^{i m \phi - \frac{m\theta^2}{2}}\; H_M\left(\sqrt{m}\;\theta\right) j_l(k r n_s)\sqrt{\frac{1}{k r n_s}}\;\delta s_{in}(r) +\right.$$

$$\left.\sqrt{\frac{\pi}{2}}\; e^{-\frac{m\theta^2}{2} + i m \phi - (r - R_o)\alpha_s}\; H_M\left(\sqrt{m}\;\theta\right) j_l(k n_s R_o)\sqrt{\frac{1}{k n_s R_o}}\;\delta s_{out}(r)\right)$$

The numerical overlap integral is iteratively computed over decreasing fiber diameter for a fixed microsphere diameter. This is done so that one can predict for a given wavelength and microsphere diameter what fiber diameter is best suited to both maximize forward coupling to the microsphere and minimize output coupling into higher mode families. Output coupling into

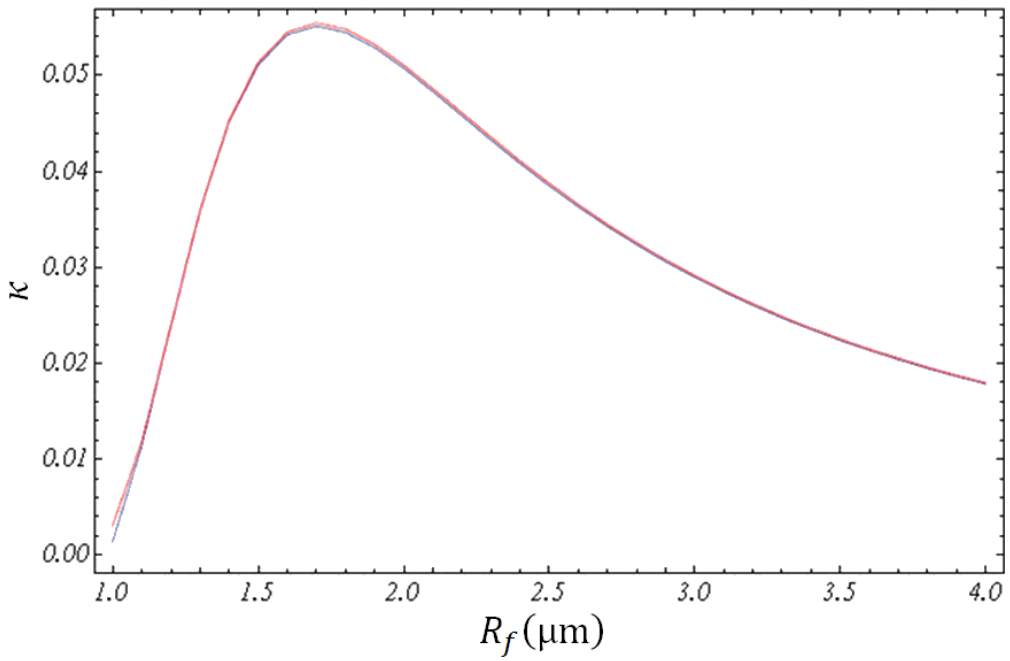

Figure 18. The coupling amplitude between the fundamental modes of the fiber and microsphere vs. fiber radius for input (red) and output (blue) coupling directions. Notice that they are not perfectly symmetric, however they are very close.

higher order fiber modes can be suppressed as the fiber will have some minimum diameter where only fundamental mode coupling occurs [14]. The results of the input and output coupling show high symmetry with peak values of $T = |\kappa|^2$ on the order of 10^{-4} as seen in Fig. 18 and Fig. 19. The calculated peak values are comparable to the measured peak values for the experimental system.

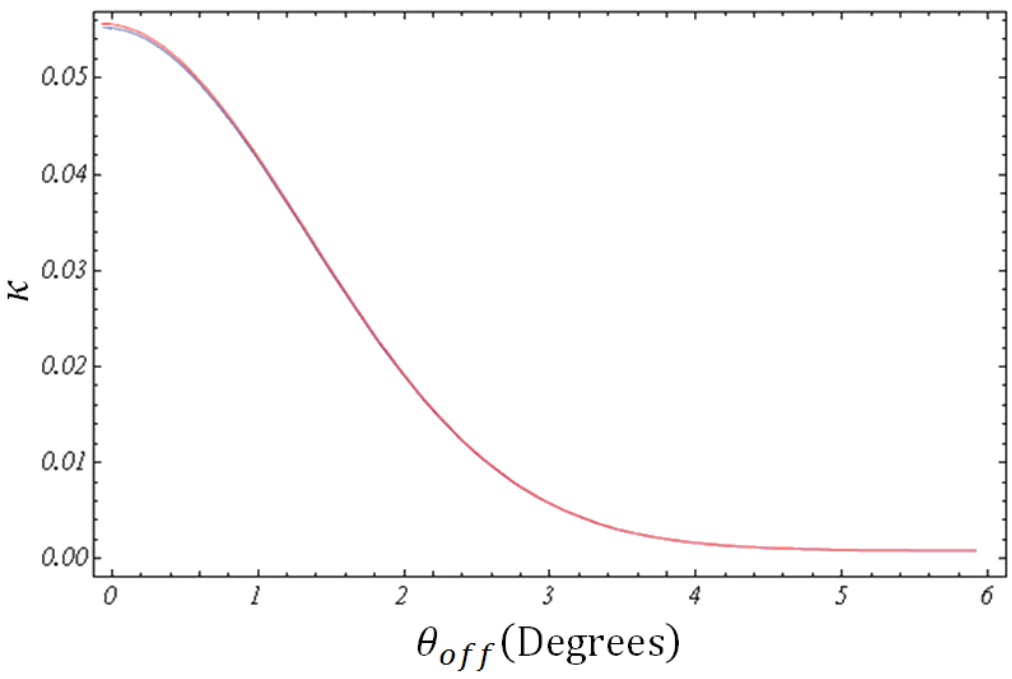

Figure 19. Amplitude transmission coefficient shown as a function of misalignment angle between the sphere's equatorial plane and the fiber's z axis.

It has been previously discussed that the input/output coupling coefficients can be unequal if the waveguides are not strictly phase matched. While this is rigorously true the relative difference should be small for guides which are weakly coupled. This can be thought of in terms of the interaction energy terms C_{ij}. For a weakly coupled system the perturbation of the modes due to the presence of a second guide is small and as such the interaction energy terms are also small. As shown below in Fig. 20 even as phase matching is decreased and $\beta_s - \beta_f$ gets large the difference between input/output transmission (Fig. 18) continues to decrease because C_{ij} decreases more rapidly than phase mismatch increases. One may note that this should be expected because, while it has not been explicitly alluded to, the integrals which represent C_{ij} also contain phase matching terms which lead to their nonlinear reduction as $\beta_s - \beta_f$ gets large. Notice as well in Fig. 21 that even when the modes are perfectly phase matched the relative

difference is still of order 0.7% which indicates that the difference is most likely due to numeric limitations in evaluating the coupling coefficients rather than a physical effect. Ultimately, we find the difference in the amplitude coefficients to be of the order of 0.7% for a typical aligned configuration, see Fig. 21 below, and of the order of a few percent for a system which is misaligned, Fig. 22 below. In either case these differences are small and may be safely neglected in our ring cavity treatment.

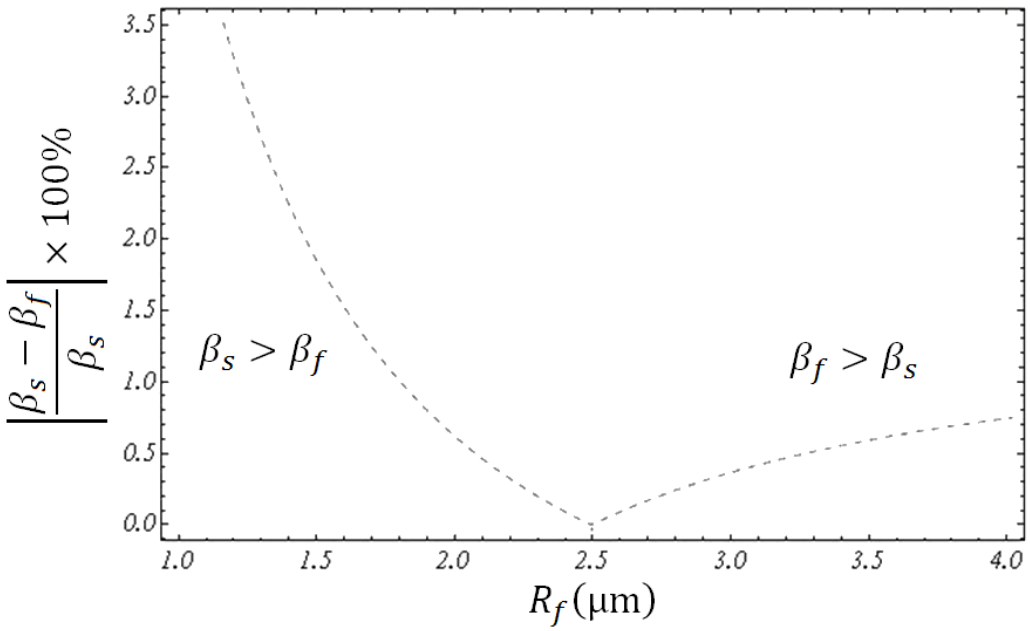

Figure 20. Absolute percent phase mismatch between fiber and microsphere as the fiber radius is reduced.

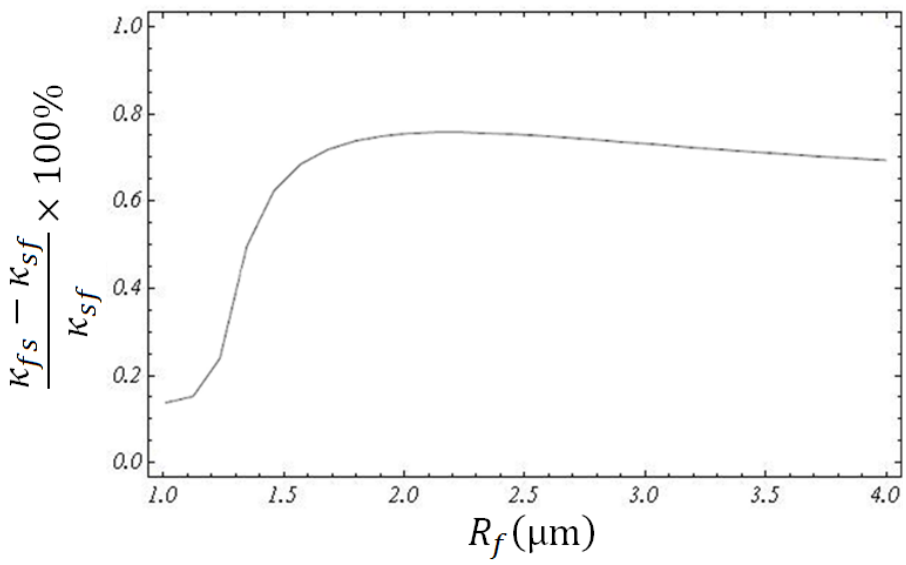

Figure 21. The percent difference between input and output coupling plotted as a function of fiber radius. Notice that while the peak value is around 0.7% the difference reduces dramatically as the guides become more weakly coupled.

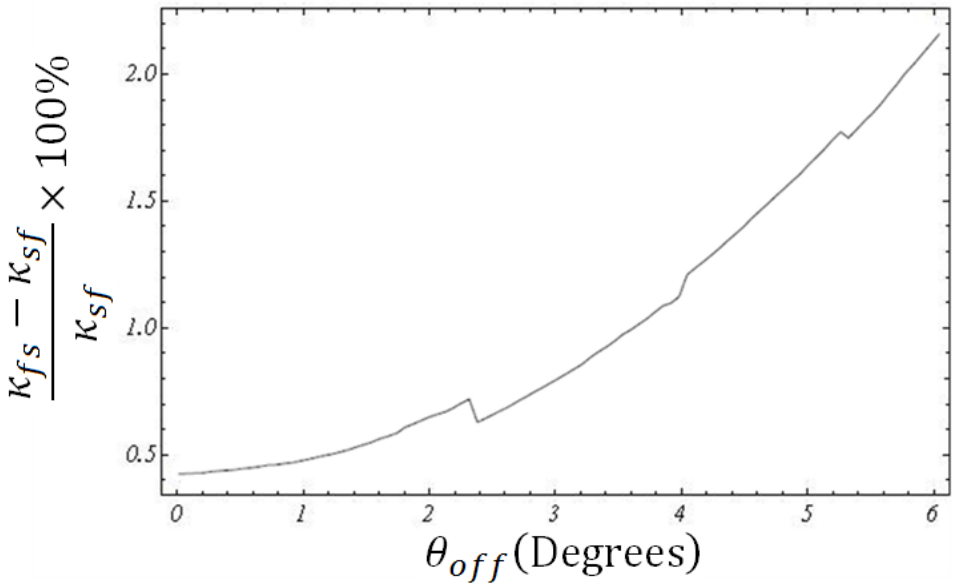

Figure 22. Percent difference between input and output coupling as a function of equatorial alignment angle. Note that the jumps are caused by limited numeric precision in the calculations.

We have now independently demonstrated that the ring cavity treatment of equal input/output transmission probabilities is a fair approximation to the real modal system. Furthermore, while it is technologically impossible at the moment to experimentally determine the mode of the microsphere that we are observing at a particular frequency, due to uncertainty in geometric measurements of the microsphere, we have found that the peak transmission probabilities as determined from the ring cavity model are of the same order as those predicted in the independent coupled-mode analysis. Up to this point we can conclude that the ring cavity resonance model is a reasonable representation of the system.

Determining the cavity loss:

The next aspect of the ring cavity model which must be verified is the treatment of cavity loss. The loss in this case is composed of two components and these must be treated separately. The first mechanism of cavity loss is absorption while the second is scattering.

Thermal Bistability:

In an optical absorption process the absorbed optical energy is converted into thermal energy. This can be understood strictly from a conservation of energy perspective as without re-radiation of the optical power the material remains in an excited state, increasing the mean temperature. This provides us with a mechanism for differentiating the loss mechanisms of the microsphere because scattering is loss without heating. We must then devise a means of measuring the heating associated with absorption and understand how to characterize that in terms of a cavity loss coefficient. This is not an insurmountable task as the observed optical properties and thermal properties are intrinsically linked by both the thermal dispersion in the index of refraction of the guide and the change in guide geometry due to thermal expansion.

We know that the cavity will be resonant when there are an integer number of wavelengths l in one round trip. Thus a particular cavity resonance can be expressed as

$$\lambda_o = \frac{2\pi R_s n_s}{l} \tag{112}$$

where the effective index of refraction has been assumed to be approximately the nominal index of refraction. Now let us see how this resonant wavelength is affected by temperature dependence in the index and radius. In terms of frequency we find

$$\nu_o \equiv \frac{c}{\lambda_o} = \frac{c\,l}{2\pi R_s n_s}, \tag{113}$$

$$\frac{d\nu_o}{dT} = -\frac{c\,l}{2\pi R_s n_s}\left(\frac{1}{R_s}\frac{dR_s}{dT} + \frac{1}{n_s}\frac{dn_s}{dT}\right) = -\nu_o\left(\frac{1}{R_s}\frac{dR_s}{dT} + \frac{1}{n_s}\frac{dn_s}{dT}\right).$$

The known values for the thermal expansion coefficient [27] and index dispersion [28] are $1/R_s(dR_s/dT) = 5.5 \times 10^{-7}K^{-1}$ and $dn_s/dT = 11.3 \times 10^{-6}K^{-1}$ respectively at $1550\ \mathrm{nm}$. This leads to a temperature dependence in the resonant frequency of a particular mode of about $d\nu_o/dT = -1.6\ \mathrm{GHz/K}$ which has been experimentally verified [29]. If we now include the temperature dependence of the resonance frequency in the previous Lorentzian resonance structure we find that the throughput power can be expressed as,

$$P_t(t) = P_f\left(1 - m\frac{\left(\frac{\Delta\nu}{2}\right)^2}{\left(b\,T(t) + \nu(t)\right)^2 + \left(\frac{\Delta\nu}{2}\right)^2}\right), \tag{114}$$

where $b = 1.6\ \mathrm{GHz/K}$ and both the temperature and laser scan frequency relative to ν_o have been expressed explicitly as a function of time. We can then derive an expression for the microsphere's temperature change from equilibrium, T [29] by considering the difference between heating due to optical absorption and cooling due to external processes:

$$\frac{dT}{dt} = \Upsilon \frac{P_f m}{Mc} \frac{\left(\frac{\Delta\nu}{2}\right)^2}{(b\,T(t) + \nu(t))^2 + \left(\frac{\Delta\nu}{2}\right)^2} - \frac{T}{\tau_{thermal}}, \tag{115}$$

where Υ is the ratio of absorption to total loss, $\tau_{thermal}$ is the thermal lifetime and Mc is the mass of the microsphere ($\rho = 2200\,\mathrm{kg \cdot m^{-3}}$) times the specific heat capacity ($c = 741\,\mathrm{J \cdot kg^{-1} \cdot K^{-1}}$) of fused silica, giving the total heat capacity of the microsphere. Now we must characterize the total cooling rate $\Gamma \equiv 1/\tau_{thermal}$. For this we can envision the creation of an experimental sample, as seen in Fig. 23 and Fig. 24, which is very limited in terms of thermal conduction into the suspension mechanism, leaving predominantly the conduction loss into the surrounding gas, as bodies of this size have negligible convection losses and small blackbody radiation losses for temperatures within a few K of equilibrium.

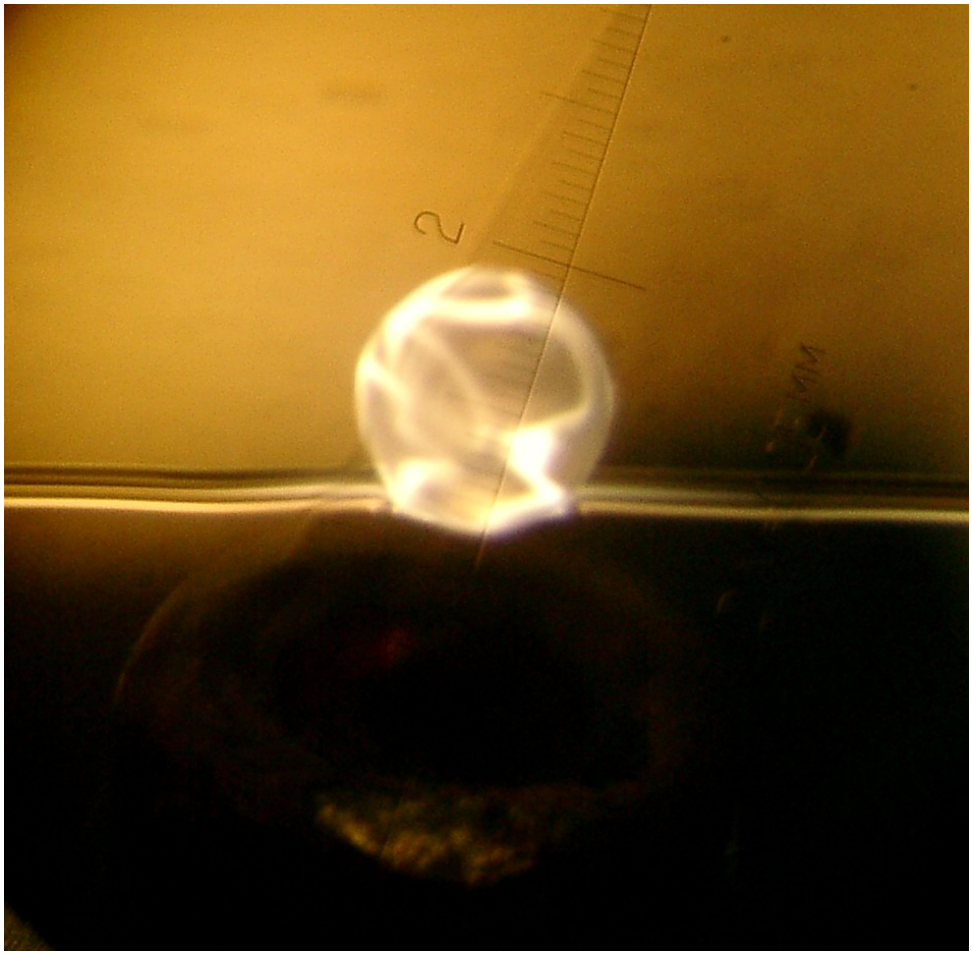

Figure 23. Creation process of thermal-conduction-limited microsphere. The object in the lower field of view is the tip of a jeweler's torch fed by a hydrogen-oxygen mix. The patterns within the sphere are internal reflections of the blackbody radiation ($\sim 2000^{o}$C) of the microsphere.

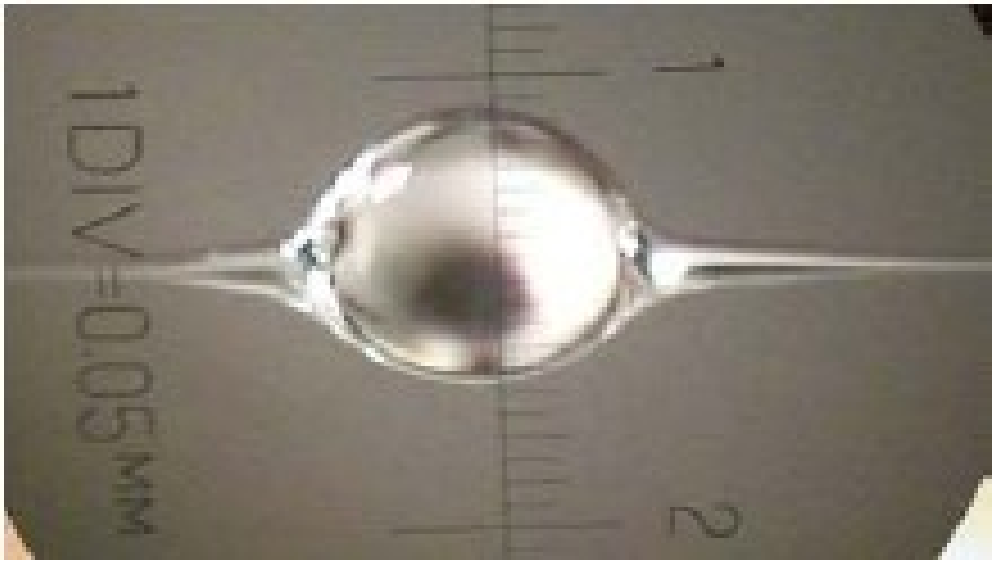

Figure 24. Thermal-conduction-limited microsphere suspended on a tapered fiber. A sphere of diameter ~600 μm is suspended on a tapered fiber of diameter ~3 μm.

With the realization of an experimental sample with limited thermal conductivity into the suspension mechanism as seen above in Fig. 24, the thermal lifetime can be expressed as

$$\tau_{thermal} = \frac{Mc}{4\pi R_s k_{air} + 16\pi {R_s}^2 \sigma \, \epsilon \, {T_{rm}}^3}, \tag{116}$$

where k_{air} is the thermal conductivity of the ambient atmosphere, σ is the Stefan-Boltzmann constant, $\epsilon = 0.87$ is the emissivity of fused silica and T_{rm} is an approximation for the equilibrium temperature of the cavity . The thermal lifetime can now be directly measured. To measure the thermal lifetime the microsphere is placed in a vacuum chamber and probed with a very weak probe diode laser ($< 0.5\ \mu\mathrm{W}$) at 1550 nm. A second powerful ($3\ \mathrm{W}$) 532 nm $\mathrm{Nd{:}YVO_4}$ beam is focused through a laser window, located on the side of the chamber, onto the center of the microsphere, as seen in Fig. 25 and Fig. 26 below. This allows one to heat the microsphere a few

degrees above room temperature and directly measure the thermal relaxation rate which is the inverse of the thermal lifetime.

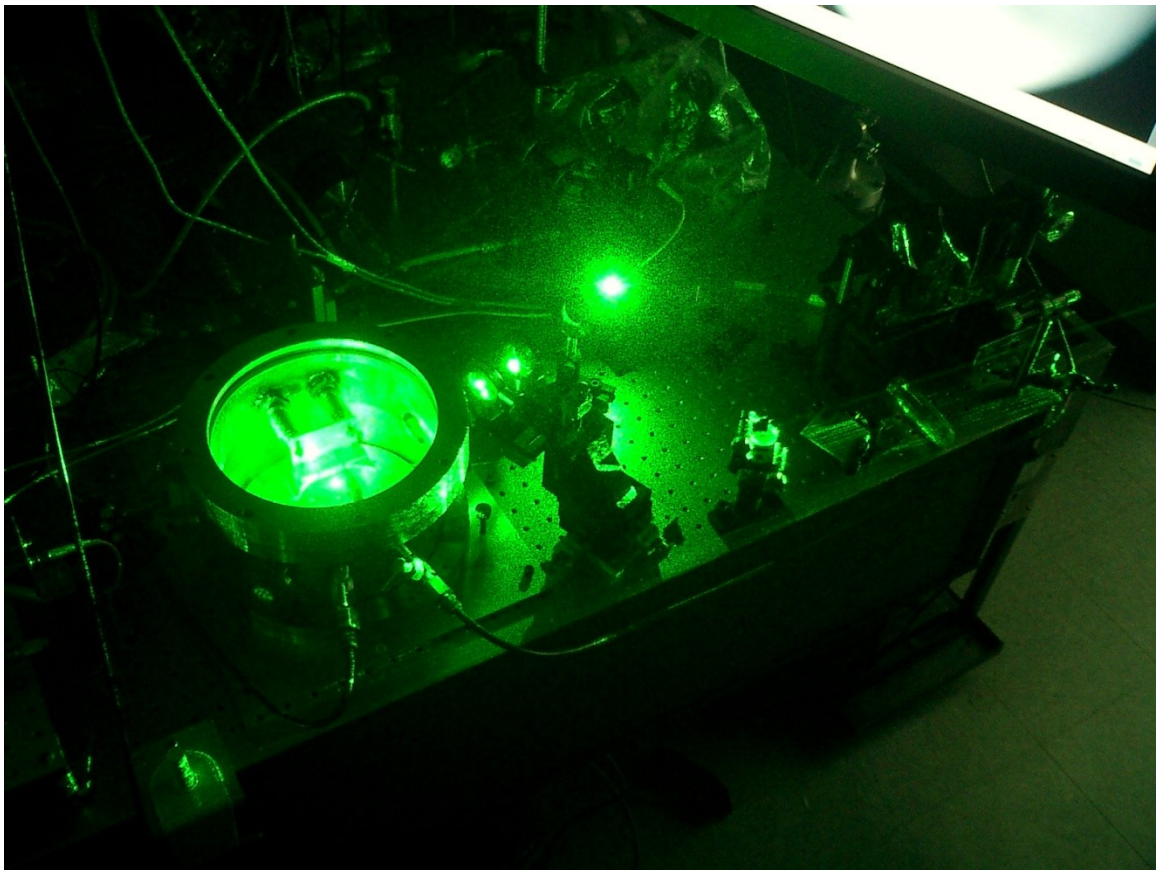

Figure 25. Thermal lifetime experiment. A 532-nm laser, off camera, is focused into the center of the chamber where a microsphere is located.

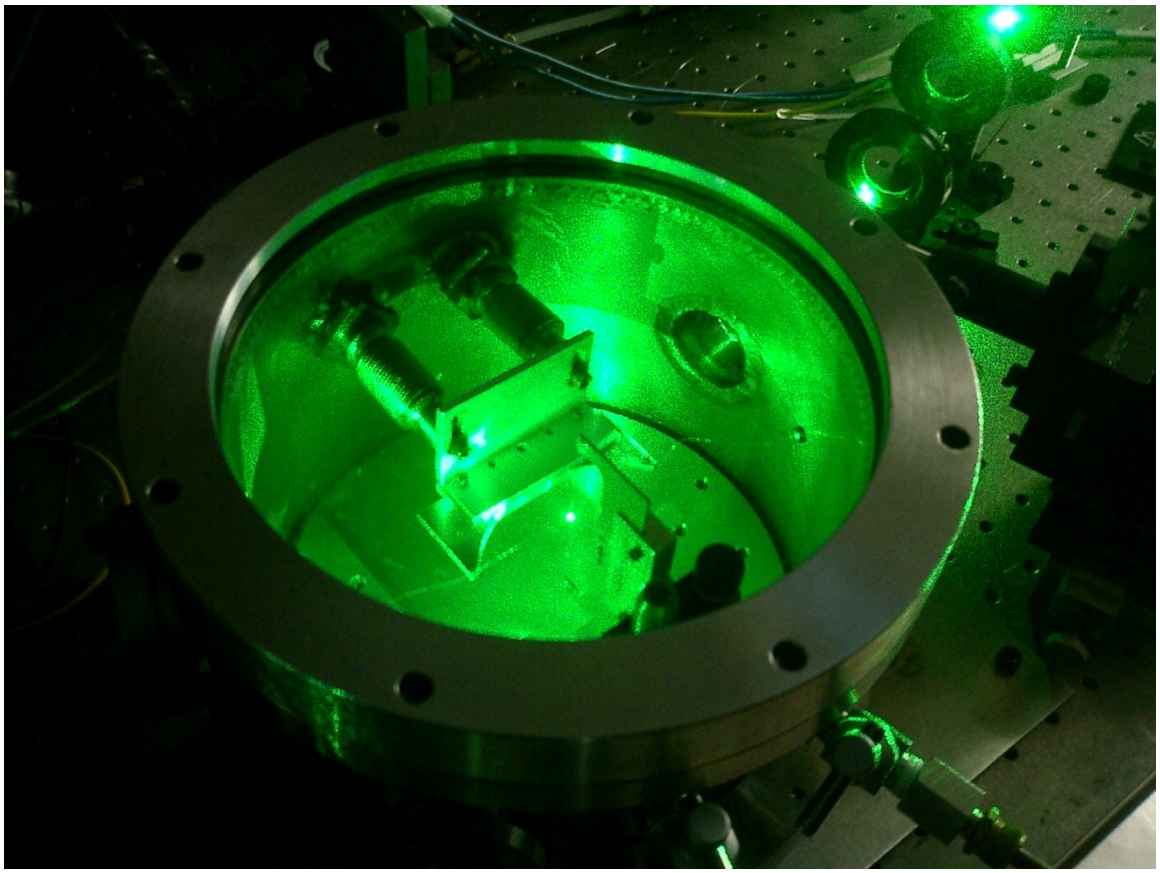

Figure 26. Close-up of a thermal lifetime experiment. A 532 nm laser is focused into the center of the chamber where a microsphere is located. The microsphere is the bright object in the center of the field of view.

The thermal lifetime is measured from pressures ranging from 0.1 Torr to 744 Torr. The dynamic behavior of the thermal lifetime serves both as a means of verifying that the conduction loss into the suspension mechanism has been minimized and also as an independent means of verifying the theory as the thermal accommodation coefficient is found from the trace and compared to known values. As seen in Fig. 27 the agreement is very good, with measured values of 0.79 ± 0.01 over the course of 4 experiments in ambient air, while typical values for air on glass are around 0.80 [30].

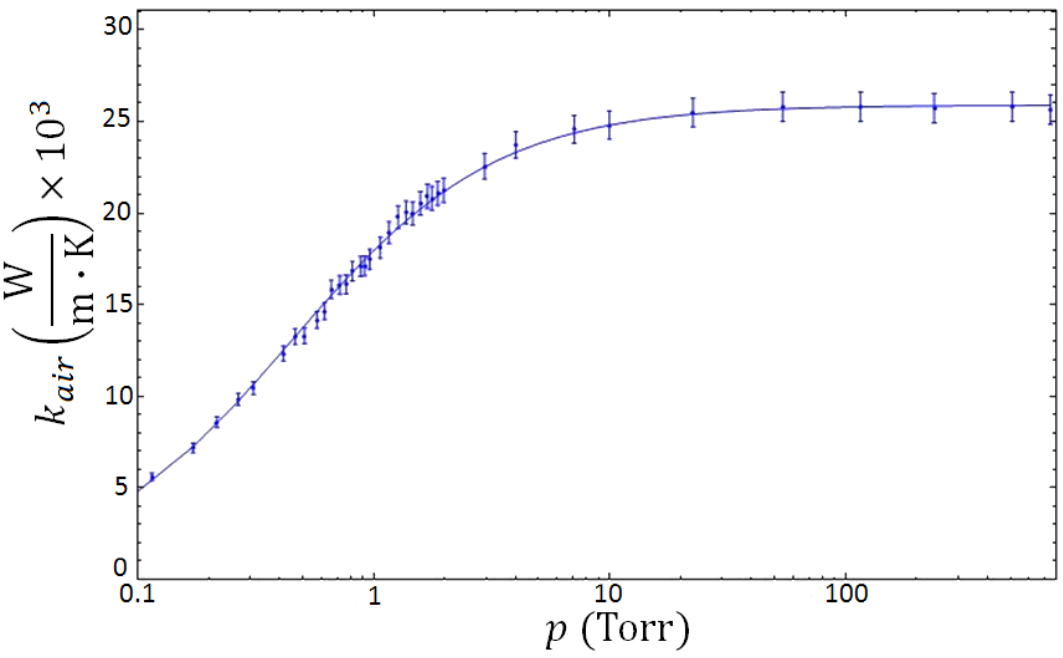

Figure 27. Measured thermal conductivity of air as a function of pressure for a prolate spheriod of minor radius 325 μm. The solid line is a fit from a thermal conductivity model with one free parameter, the accommodation coefficient of the surrounding gas on the fused-silica surface.

With the thermal relaxation rate determined, the strong probe laser is turned off and the probe laser is increased in power to induce heating due to absorption. Notice that the temperature tuning parameter is negative, so that as the laser is linearly scanned up in frequency, the thermal frequency shift of the mode will be counter to the laser scan direction causing apparent narrowing of the trace, while when the laser scans down in frequency, the thermal shift of the mode will be in the direction of laser scan producing apparent broadening. All of the parameters of a particular mode are first measured at low power/ fast scan rate such that no thermal effects are present. The probe laser power is then increased by roughly 3 orders of magnitude (to about $100\ \mu\mathrm{W}$) and the scan rate is reduced by 3 orders of magnitude (to about $10\ \mathrm{mHz}$) such that the mode will be in thermal equilibrium throughout the scan. The only free parameter remaining in the bistability response theory is the parameter Υ which is used to

quantify the ratio of absorption loss to total intrinsic loss from the dynamic fit as seen in Fig. 28 which shows the result of a typical experiment and fit to the observed response.

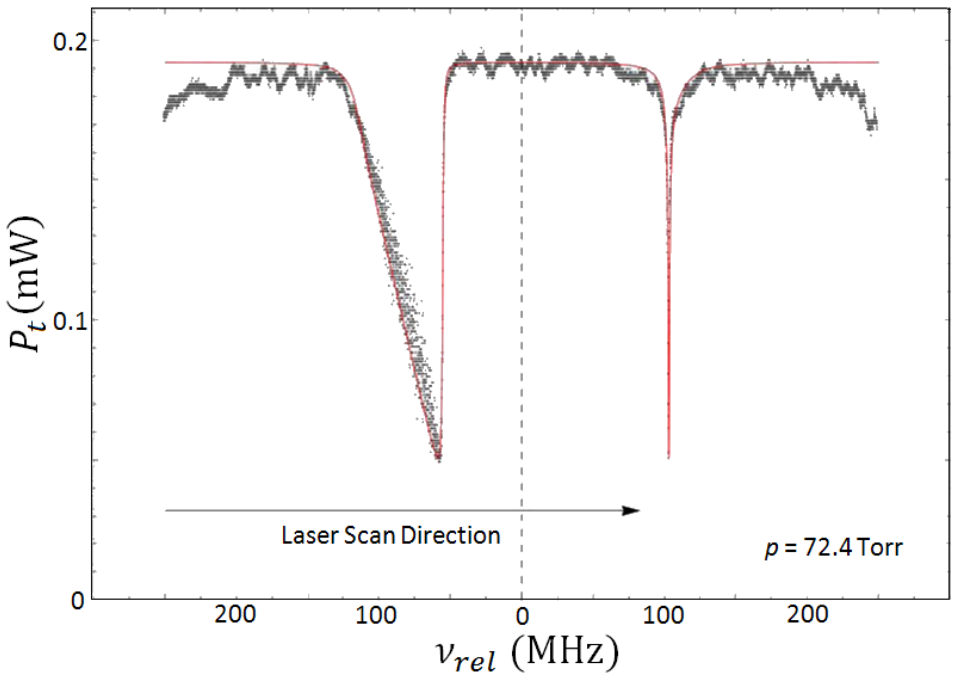

Figure 28. Observed thermal bistability response of the microsphere (black) and fit from the model to the response (red). From the fit we can find the fraction of total loss that is caused by absorption.

Fitting gives the fraction of intrinsic losses due to absorption, but the actual absorption is still ambiguous as we have two potential intrinsic loss solutions which could produce the same observed unperturbed modal characteristics (Q, m) depending on the system's coupling loss; see Eq. (15). In order to determine which of the two solutions for x (the ratio of coupling to intrinsic loss) represents our physical system we must also determine the coupling regime of the cavity; this is treated in detail in the next section. Furthermore, we have treated the total intrinsic loss as simply the sum of absorption and scattering losses which excludes any potential radiation losses from the cavity. For cavities of our dimensionality (~ 1 mm) the radius of curvature is sufficiently large, and confinement sufficiently strong, that radiation losses are a

very small fraction of the total intrinsic losses and can be safely ignored [31] in our treatment. With the radiation losses ignored and the coupling regime of the cavity determined we can then infer the cavity's absorption coefficient and scattering coefficient from the total intrinsic loss. What we have found is that for an average microsphere the amount of measured absorption corresponds well to that which would be expected from approximately a single molecular layer of water residing on the surface (bulk material absorption is negligible at $\lambda = 1.5\ \mu\mathrm{m}$). Fused silica is well known to form a surface hydroxide (water) layer, through chemisorption [31], which has previously been found to have a thickness of roughly one molecular layer [31-32], agreeing well with our measurement of absorption losses. Furthermore, from the model above we can estimate that in these particular bi-tapered thermal resonator samples, Fig. 24, that absorption losses account for roughly 5%-10% of the total intrinsic loss. These thermal bi-tapered samples, on average, have been found to have very low loaded $Q's$ when compared to typical samples (roughly 10-100x lower) which given the amount of manipulation required to create them strongly supports a dominating rise in scattering loss due to surface contaminants as also indicated by the above model. We have further observed that samples with vastly different loaded $Q's$ are measured to have roughly invariant coupling and absorption losses, sample to sample, which again serves to verify dominating scattering losses generated during the creation process. With this, we can reasonably conclude that our treatment of loss within the ring cavity model is valid and move forward.

Determining the Cavity Quality Factor and Coupling Regime:

Now we are left with the verification of the last two critical aspects of the ring cavity model. We must determine if our treatment of cavity quality factor in terms of spectral linewidth is reasonable and further we must also verify that we indeed have three separate coupling regimes as we would expect for a harmonic oscillator-like system. Fortunately, both

can be found directly from the cavity's transient response to an abrupt (sub-cavity lifetime) incident power change. In all of the preceding treatment we have analyzed a steady-state response to infer behavior; let us now look into the transient response.

Transient cavity response:

Clearly from the analysis performed for the ring cavity we would expect the intracavity power to decay as a pure exponential and as such we could trivially treat its transient response to a rapid decrease in pump power. While this is straightforward, much more information can be garnered from the full response of the throughput field to an arbitrary power off/on event. Let us begin by assuming the cavity round trip losses are small and we are sufficiently close to resonance such that the sum over cavity round trips in Eq. (2), substituted into Eq. (3), can be replaced by an integral over all time in the fractional time required to reach steady state $t'' \equiv n_{rt}\tau_{rt}$:

$$E_t(t) = rE_f(t) - \frac{T}{\tau_{rt}}\int_0^\infty E_f(t-t'')e^{-K(1+i\theta)t''}\,dt'', \tag{117}$$

where n_{rt} is the number of round trips, and the field decay rate K and cavity detuning in units of half linewidths θ have been inserted explicitly using the relations found from Eq. (34), Eq. (47), and Eq. (30). To aid in the analysis of the time dependence of the integrand let us further change variables as $t' = t - t''$. With this we find

$$E_t(t) = rE_f(t) - \frac{T}{\tau_{rt}}e^{-K(1+i\theta)t}\int_{-\infty}^{t} E_f(t')e^{K(1+i\theta)t'}\,dt', \tag{118}$$

where the limits of integration have been redefined for consistency with the substitution. We can now take the time derivative of each side to find the differential equation that describes the transient throughput response as:

$$\frac{dE_t(t)}{dt} = r\frac{dE_f(t)}{dt} + K(1+i\theta)\left(\frac{T}{\tau_{rt}}E^{-K(1+i\theta)t}\int_{-\infty}^{t} E_f(t')E^{K(1+i\theta)t'}\,dt'\right) \qquad (119)$$

$$-\frac{T}{\tau_{rt}}e^{-K(1+i\theta)t}E_f(t)e^{K(1+i\theta)t}.$$

With simplification and substitution we arrive at the final form of the useful differential equation for throughput transient response,

$$\frac{dE_t(t)}{dt} = r\frac{dE_f(t)}{dt} - K(1+i\theta)\left(E_t(t) - rE_f(t)\right) - \frac{T}{\tau_{rt}}E_f(t). \qquad (120)$$

When solved numerically we find not only the field decay rate but also there are three distinct response regions based on the coupling regime; see Figs. 29-31 below. It is important when solving the above differential equation that a realistic fiber field switching and modulation is used as this can severely affect the observed response of the system as the switching lifetime becomes comparable to the cavity lifetime. The switching response is then taken as single exponential with the lifetime determined experimentally. We determine the WGM's loaded quality factor and dip depth from the steady state response prior to modulating the probe laser. When the probe laser is modulated we observe a distinct turn on and turn off response that varies with coupling regime. In fact what we are observing is a measure of the interference between the fiber and microsphere fields. This is only observable because the cavity lifetimes are much longer than probe switching lifetimes so for all intents and purposes the incident fiber field is steady state while the cavity fields are transient. As the fiber field is switched either on or off the field in the cavity responds more slowly than the switched probe, allowing observation of the cavity output/probe interference. Thus we can infer that the observation of a zero crossing in the throughput field represents a phase reversal in the total throughput field. The knowledge of phase then is the knowledge of coupling regime because for an undercoupled

mode, seen in Fig. 29, the steady-state cavity output is weaker than the probe field and the throughput field will have the same phase as the probe. In an overcoupled case, seen in Fig. 31, the steady-state cavity output is stronger than the probe field and as such the throughput field will have a π phase with respect to the probe and thus a zero crossing as the cavity equilibrates. Finally, for a critical coupling regime, seen in Fig. 30, we can only observe a load and unload cycle as at equilibrium there is no observed throughput power. The large power pulse in the overcoupled ringdown does not represent any form of energy conservation violation but rather is a result of nothing more than the energy storage of the cavity, as the cavity field escaping is no longer partially canceled by destructive interference with the fiber field.

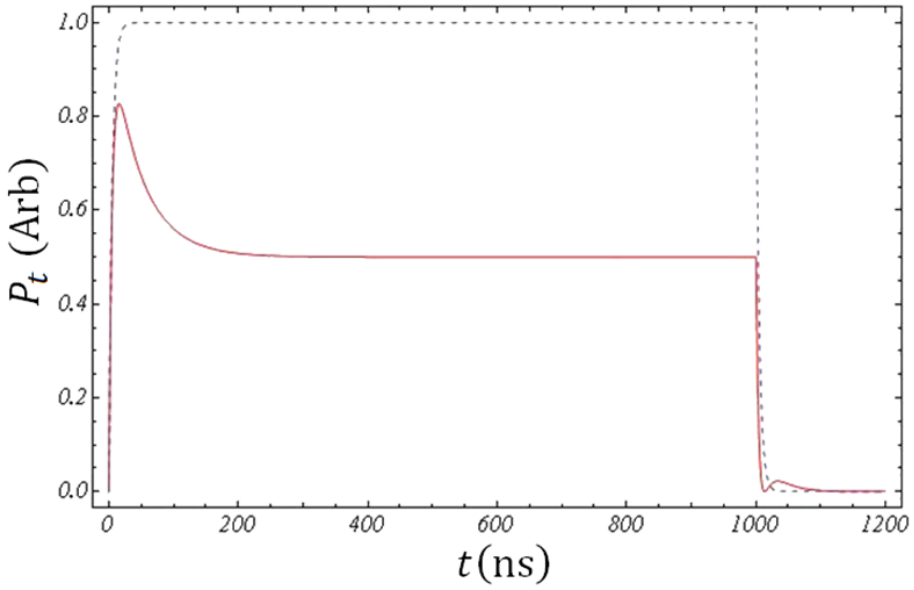

Figure 29. Undercoupled cavity transient response on resonance for the model (red) for a given input pulse (blue). The system parameters are $\lambda = 1.5\ \mu\text{m}$, $Q_l = 3.1 \times 10^7$ *and* $m = 0.5$. *The pulse is turned on and off exponentially with a characteristic time of* $5\ ns$.

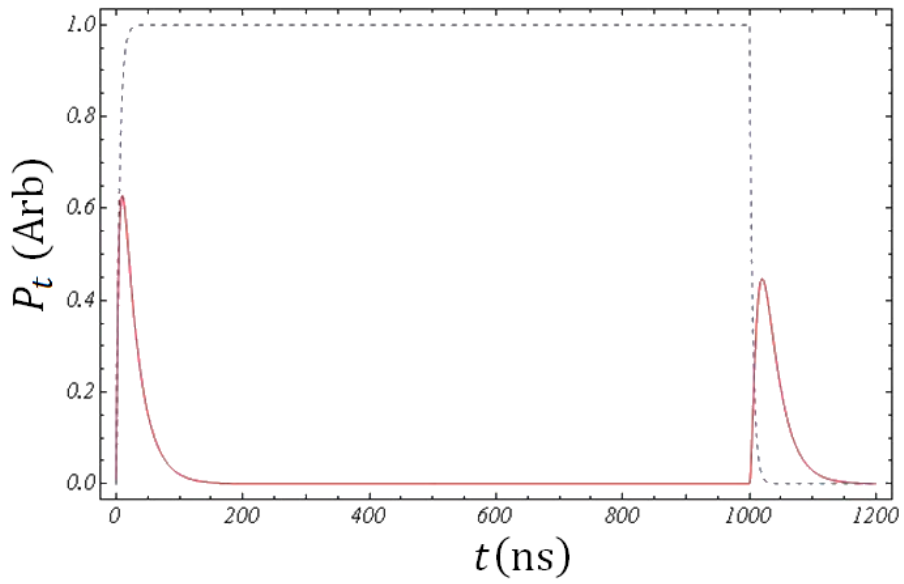

Figure 30. Critically coupled transient response on resonance for the model (red) for a given input pulse (blue). The system parameters are $\lambda = 1.5\ \mu\text{m}$, $Q_l = 3.1 \times 10^7$ *and* $m = 0.5$. *The pulse is turned on and off exponentially with a characteristic time of* $5\ ns$.

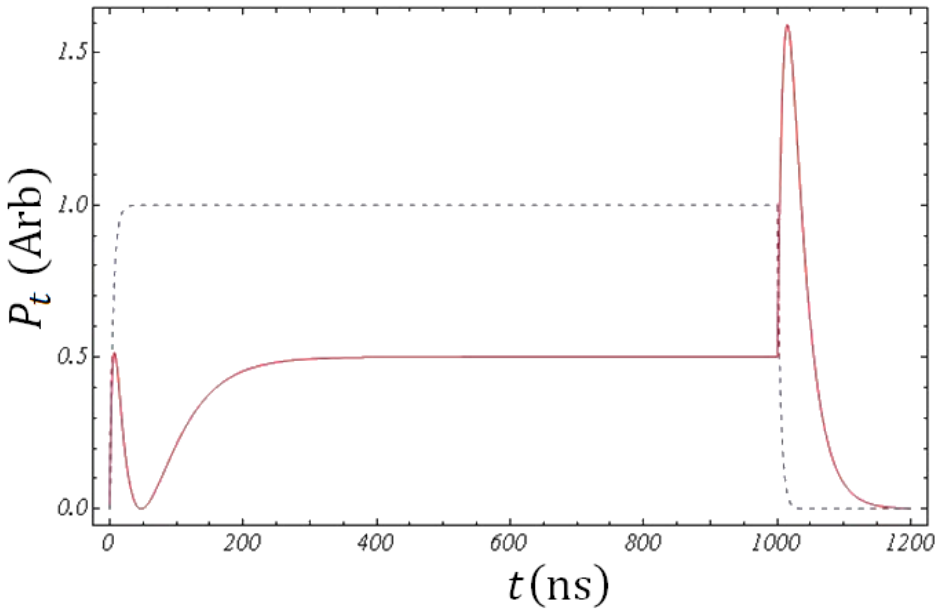

Figure 31. Overcoupled transient response on resonance for the model (red) for a given input pulse (blue). The system parameters are $\lambda = 1.5\ \mu\text{m}$, $Q_l = 3.1 \times 10^7$ *and* $m = 0.5$. *The pulse is turned on and off exponentially with a characteristic time of* $5\ ns$.

We have now demonstrated both that the prediction of harmonic-oscillator-like damping response regimes (coupling regimes) and the treatment of cavity output phase in the ring cavity model are quite valid. Furthermore, the predicted coupling regimes above have been experimentally verified by a rigorous comparison between the dip depth response to an increase in cavity loss and the transient response. The two methodologies are in perfect agreement. Formally this technique allows us to determine both the coupling regime and the cavity Q in a single experiment.

While one would like to directly find the cavity Q from the fits of the above traces, if one is to verify with high certainty that no internal mode dephasing is occurring a traditional cavity ringdown experiment must still be performed. However, we must consider how the probe-cavity interference will affect the measurements as the probe power is switched off. Shown below in Fig. 32 is a theoretical comparison between the overall throughput transient response from Eq. (120) and the typical single exponential cavity ringdown one would expect beginning at the probe switch off time (~1000 ns). Notice that we can see the pure cavity ringdown after the interaction with the fiber field has substantially decreased (~1050 ns).

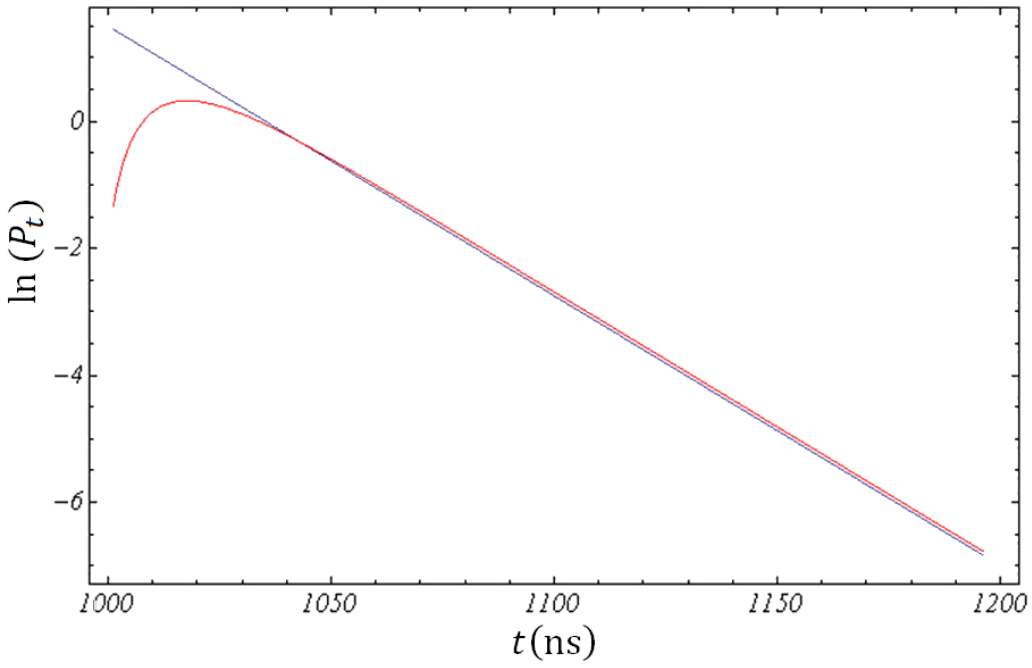

Figure 32. Comparison between modeled transient response on resonance (red) and single exponential decay (blue). The system parameters are $\lambda = 1.5\ \mu\text{m}$, $Q_l = 3.1 \times 10^7$ *and* $m = 0.5$. *The pulse is turned on and off exponentially with a characteristic time of* $5\ ns$.

Clearly then the switching lifetime will be critical in determining cavity Q with high accuracy. The switching time is adjusted to 1 ns and the cavity lifetime is measured directly from the cavity ringdown as seen in Fig. 33 below. There is no measurable disagreement between the decay rate predicted by the linewidth determination of the decay rate and its direct measurement. However, because the region of high certainty of a pure cavity response, no interference effects, is only found after considerable time after switching the power has substantially decreased and the signal to noise ratio is very low. Thus the uncertainty in measured values is quite high and this is unacceptable for high level verification.

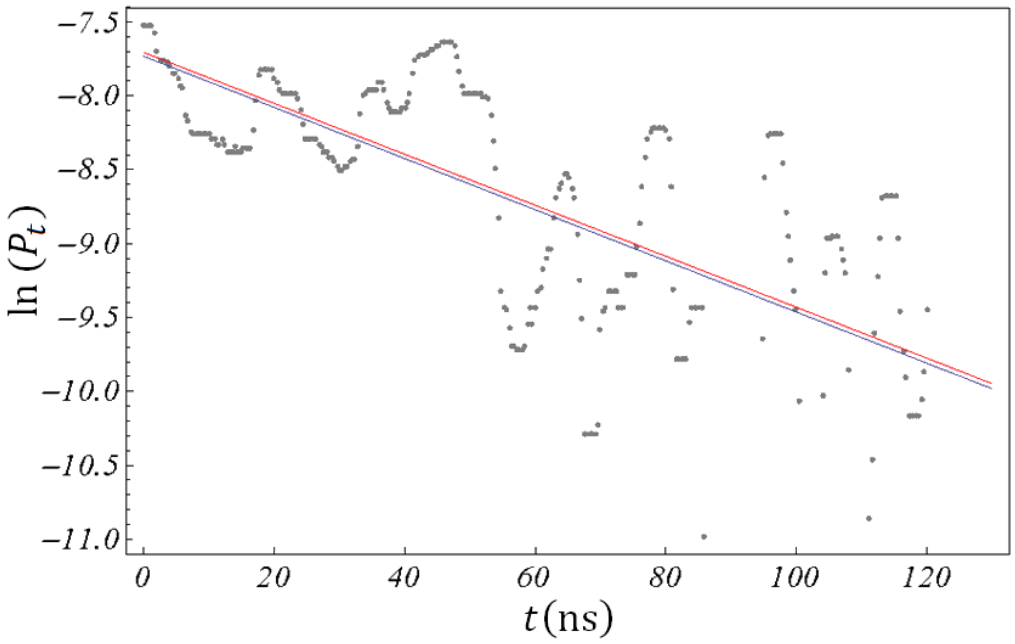

Figure 33. Measurement of the cavity decay rate. Here the grey curve is the measured data; the red trace is a single exponential fit and the blue trace is derived from the linewidth measurement. Notice the experimental trace is noisy, but appears linear on a log scale which is indicative of single exponential decay. The measured system parameters are $\lambda = 1.538\ \mu\text{m}$, $Q_l = 4.2 \times 10^7$ *and* $m = 0.5$. *The pulse is turned off exponentially with a characteristic time of* $1\ \text{ns}$.

Unfortunately, due to low power limitations of fast-response optical detectors the direct measurement of cavity ringdown cannot be significantly improved in accuracy. However, we can devise another methodology which maintains high power, but still allows the determination of the cavity lifetime. In this methodology we again rely on a transient cavity response, but in this case we look not at the fill/decay cycle but rather we look at an apparent phase shift in a sinusoidally modulated input power which has been modulated on sub-cavity-lifetime time scales. These experiments are traditionally performed by measuring the phase shift of the output power in the drop signal (transmitted signal). However, as has been discussed previously, this signal in our system has a very poor signal to noise ratio which greatly increases the uncertainty in determining the cavity Q. What is done instead is to measure the phase shift

of the through signal which has a very good signal to noise ratio. Unfortunately this type of apparent phase shift is dependent not just on the retention time of the field within the cavity but also the phase change of the field itself when it enters and exits the cavity making the response coupling-regime dependent. This makes analytic analysis very difficult without making a great many assumptions as was done in [33] where both the scattered and transmitted signal must be monitored simultaneously to achieve low precision results. However, we can employ the same numerical techniques which were employed in the cavity's fill/decay response. The methodology is identical with the only exception being the replacement of the square wave input with a sinusoidal input. Shown below are modeled throughput phase (experimental data is shown in the next section) shifts from a sinusoidally modulated power input at a frequency of 1 MHz for both an overcoupled, Fig. 34, and undercoupled, Fig. 35, mode with a cavity Q of 1×10^8 and a dip depth of $m = 70\%$. In this case the undercoupled and overcoupled cavity lifetimes are identical, but the observed phase shifts are significantly different. Empirically we find that the maximization of the observed throughput phase shift occurs for either coupling regime when the ratio of the modulation period to cavity lifetime is approximately 25. This maximization is important in that the larger phase shift allows for increased accuracy in determination of Q. Finally, because we look at the phase shift over many cycles, this increases accuracy in a statistical manner and provides the most accurate measure of cavity Q we have thus far demonstrated.

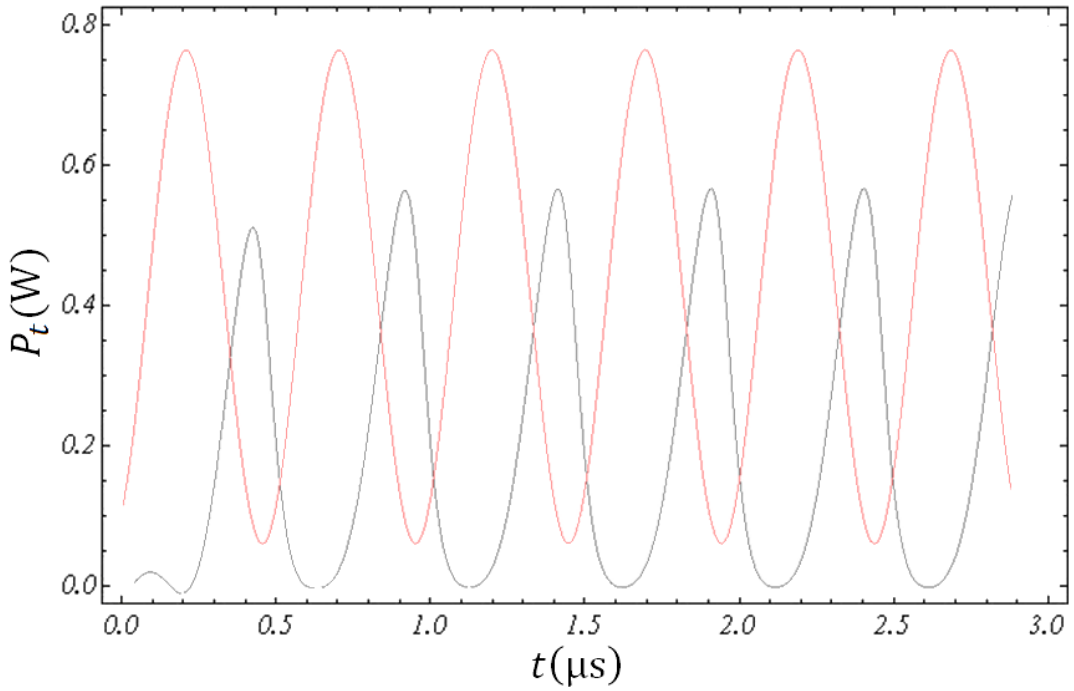

Figure 34. Throughput (blue) phase-shifted from the drive signal (red) for an overcoupled mode with a dip depth of 70% and a loaded cavity Q of 1×10^8.

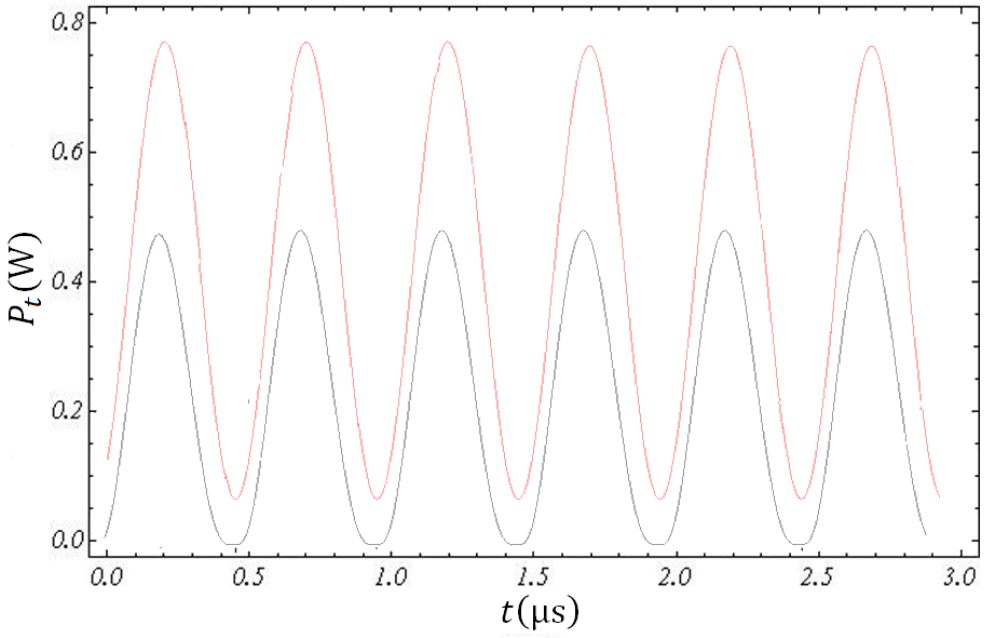

Figure 35. Throughput (blue) phase-shifted from the drive signal (red) for an undercoupled mode with a dip depth of 70% and a loaded cavity Q of 1×10^8.

Let us now verify that line broadening due to internal cavity dephasing is not occurring and that the spectral width measurements are adequate to determine the loaded cavity Q. We have developed the tools to do this by rigorous comparison of the loaded cavity Q found from spectral width, cavity ringdown, transient response for a square wave input, and phase-sensitive cavity ringdown response. We first measure the loaded cavity Q from the spectral width; see Fig. 36 below. We find that $Q_l = 5.87 \times 10^7 \pm 10\%$ where the high uncertainty is due to an asymmetry in the mode. We then proceed to modulate the power with a square wave, Fig. 37 below, and from the fit we find the mode is undercoupled with a $Q_l = 5.95 \times 10^7 \pm 5\%$. Next we look only at the direct cavity ringdown, Fig. 38 below, and find $Q_l = 5.90 \times 10^7 \pm 5\%$. Finally we modulate the power sinusoidally at a frequency of 1 MHz and measure the cavity phase shift, Fig. 39 below, which from the fit gives $Q_l = 5.97 \times 10^7 \pm 4\%$.

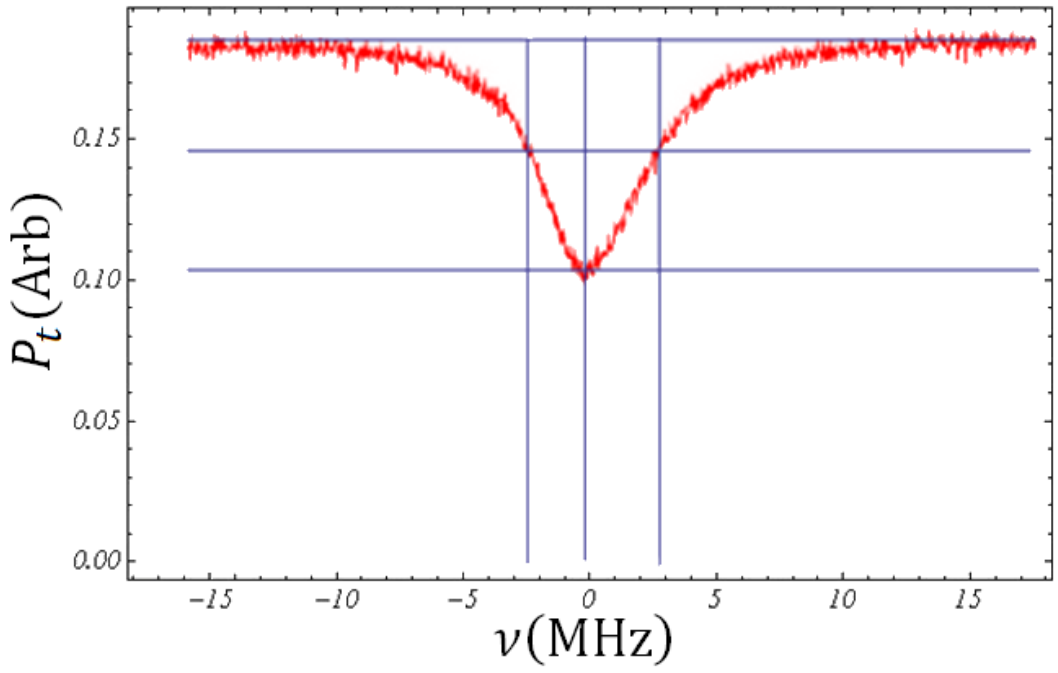

Figure 36. Measurement of the loaded cavity Q from spectral width. We find that $Q_l = 5.87 \times 10^7 \pm 10\%$.

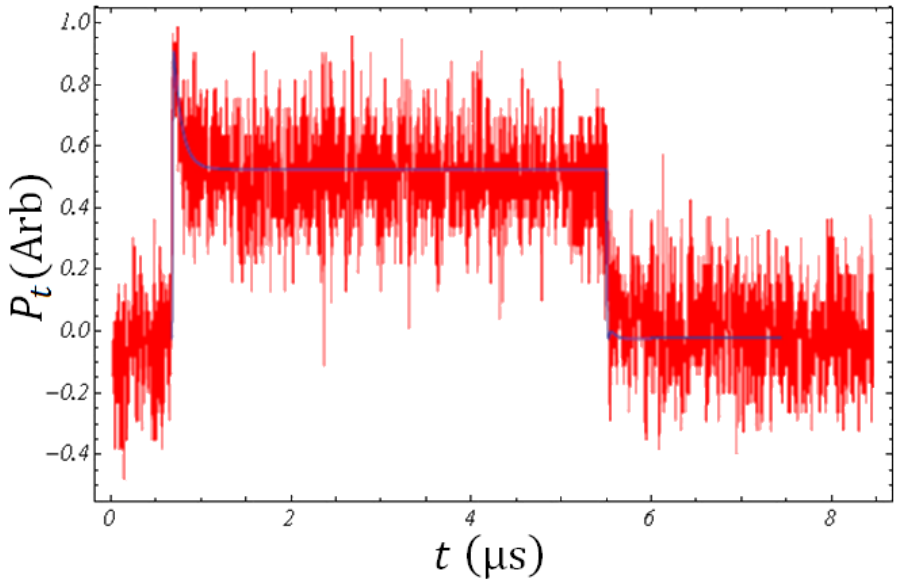

Figure 37. Measurement of the loaded cavity Q from the transient fill/decay response. We find that $Q_l = 5.95 \times 10^7 \pm 5\%$.

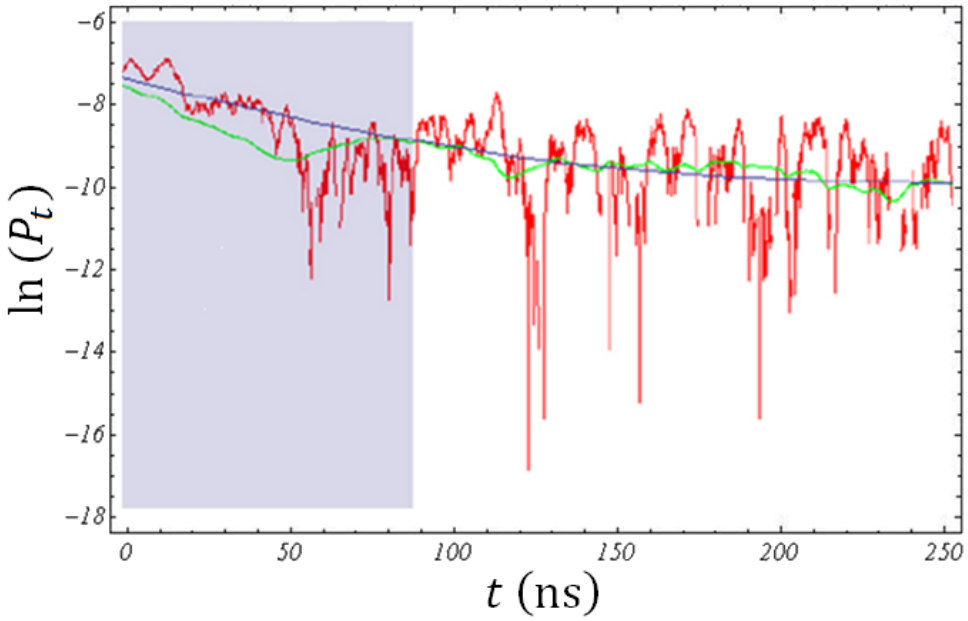

Figure 38. Measurement of the loaded cavity Q from the transient fill/decay response. The shaded region represents the turn-off time of the modulator which still includes cavity interference effects. We find that $Q_l = 5.90 \times 10^7 \pm 5\%$.

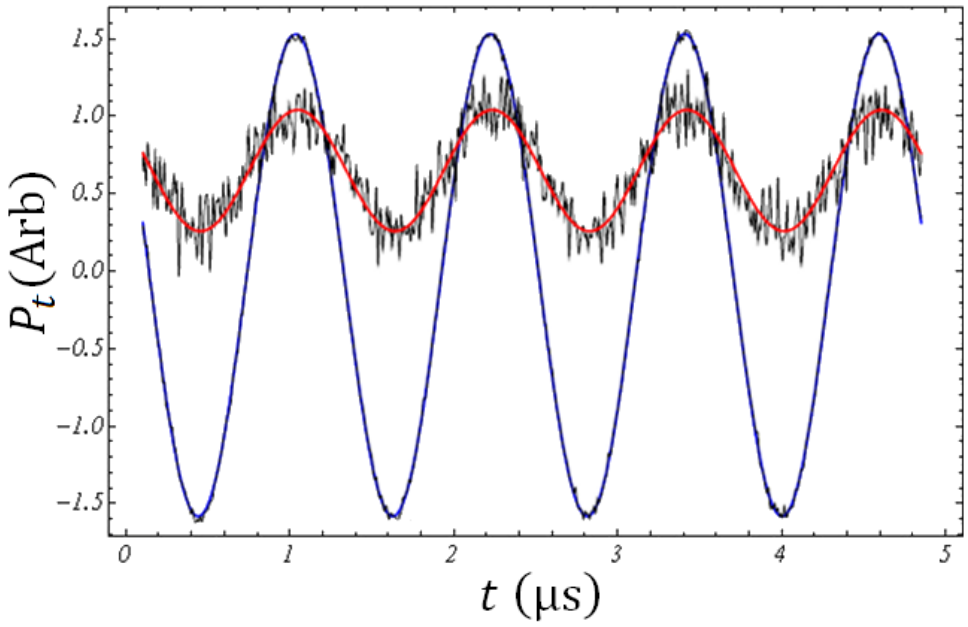

Figure 39. Measurement of the loaded cavity Q from the phase-sensitive cavity response. We find that $Q_l = 5.97 \times 10^7 \pm 4\%$.

The results of all of these various methods are in good agreement within their respective uncertainties and we can thus conclude that if cavity dephasing is present it is beneath the certainty to which we can reliably measure and is of no immediate threat to skew our results.

Putting the pieces together- a verified model:

We have verified the assumptions of cavity phase, harmonic-oscillator-like coupling regimes, weak and symmetric cavity coupling and small loss assumptions used in the derivations of the ring cavity model. Furthermore, we have demonstrated that the parameters inferred from the application of the ring cavity to a real experimental system are in good agreement with those same parameters as found from independent theoretical and experimental treatments.

With each assumption validated, and every numeric parameter verified to within a reasonable certainty, we can confidently move forward to extend this basic framework to include a myriad of different system configurations

Chapter 3 Coupled-Resonator Effects

It was shown in the previous analysis of coupling regime and Lorentzian resonance structure that the resonances of the microsphere can be thought of as harmonic oscillators. With a wealth of resonances in other systems, most notably atomic, which have historically been treated as harmonic oscillators one can ask if effects similar to those seen in atomic systems can be observed in a microsphere system. It is this harmonic analogy to atomic systems that leads some authors to describe whispering-gallery resonances of these dielectric structures as "optical atoms" [34]. If this analogy is indeed valid we would expect a number of atomic effects to be directly observable in an optical-atom system. In particular, because of the potential usefulness in optical circuits, we would like to create dramatic changes in system transmission at a particular frequency. We can then envision optical analogs of electromagnetically induced transparency and absorption as seen in atomic vapors. To do this we need to couple various resonances of our "optical atom". This is difficult, but not impossible (see Chpt. 5), to do with a single microsphere; we can, however, bring in another microsphere coupled to the first such that we induce coupled-resonance behavior.

Modification to the base model:

Let us begin by modifying the basic ring cavity model to allow input/output coupling to a second cavity through one of the mirrors which was previously treated as fully reflective; see Fig. 40 below.

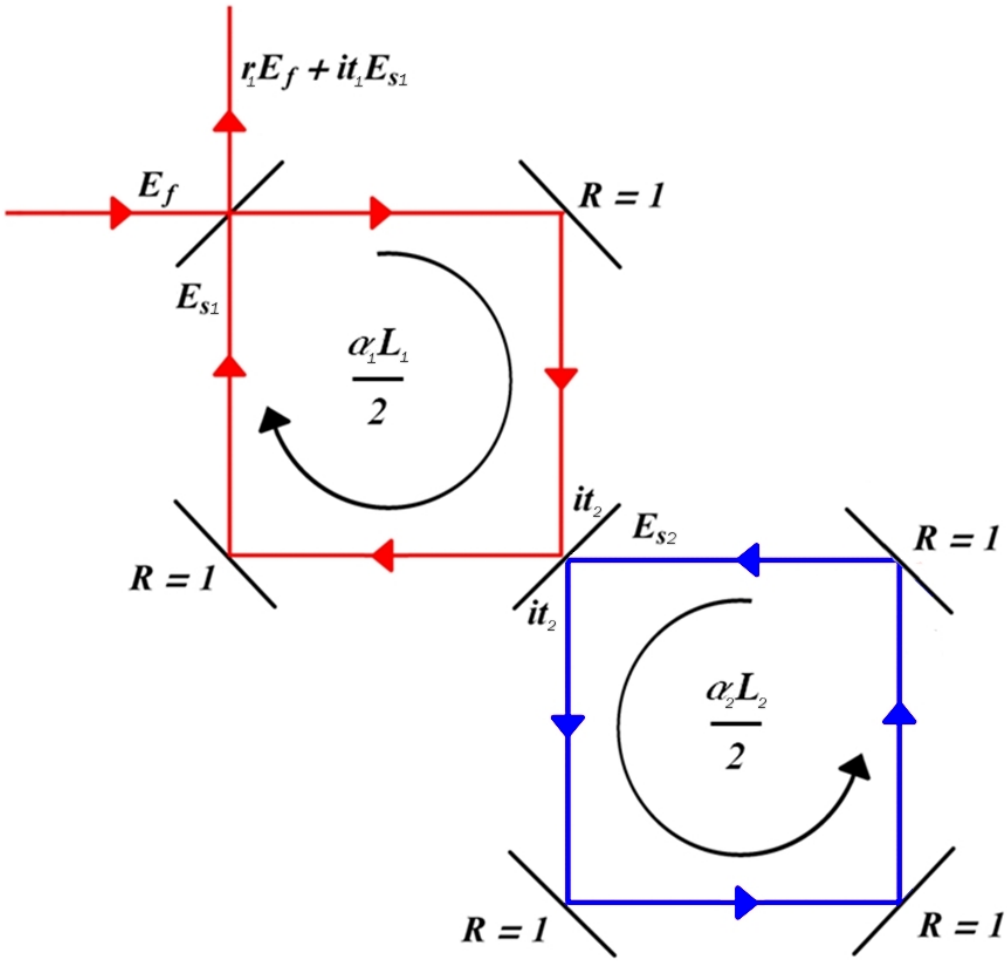

Figure 40. Modification of the basic ring cavity model to include coupling to another waveguide.

While the addition of a second cavity would offhand appear to add considerable mathematical complexity to the ring cavity model it does not. We already have the field for the first cavity, so with the modification that the far mirror is no longer perfectly reflective, we find

$$E_t = r_1 E_f + i t_1 E_{s1} = r_1 E_f - \frac{r_{eff} {t_1}^2 e^{-\frac{\alpha_1 L_1}{2}} e^{i\delta_1}}{1 - r_1 r_{eff} e^{-\frac{\alpha_1 L_1}{2}} e^{i\delta_1}} E_f \qquad (121)$$

where r_{eff} is the modified reflection coefficient that accounts for the second cavity. Notice now that the structure of the field input/output characteristics of the second resonator will be

independent of the specific nature of the field in the first resonator. Thus the solution we found for fiber-sphere coupling is also the solution we will find for sphere-sphere coupling with the proper change in parameters. The effective reflection coefficient that the first cavity field will see then is

$$r_{eff} \equiv \frac{E_{out}}{E_{in}} = r_2 - \frac{{t_2}^2 e^{-\frac{\alpha_2 L_2}{2}} e^{i(\delta_1+\delta)}}{1 - r_2\, e^{-\frac{\alpha_2 L_2}{2}} e^{i(\delta_1+\delta)}} \tag{122}$$

where the cavity detuning has been written in terms of a relative detuning from the first cavity resonance, $\delta_2 \equiv (\delta_1 + \delta)$. Notice that the implicit simplicity of this mechanism easily lends itself well to higher-order coupled-cavity systems as one must only iteratively replace the far reflection coefficient with an effective coefficient structurally identical to Eq. (122). While this procedure is generalized we will confine our conclusions to only two coupled cavities as we are interested in analogous two-resonance atomic processes. We can once again take the square modulus of the through field to find the through power from the following:

$$\begin{aligned} A \equiv \Bigg(& e^{\alpha_1 L_1} T_1 \left(2e^{\frac{\alpha_2 L_2}{2}} cos(\Delta)\sqrt{1-T_2} + T_2 - 1 - e^{\alpha_2 L_2} \right) \\ & + 2e^{\frac{\Delta\alpha L_+}{2}} \Bigg(2 \left(cosh\left(\frac{\alpha_1 L_1}{2}\right) \left(cosh\left(\frac{\alpha_2 L_2}{2}\right) - cos(\Delta)\sqrt{1-T_2} \right) \right. \\ & \left. + cos(\delta_1)\sqrt{1-T_1}\left(cos(\Delta) - cosh\left(\frac{\alpha_2 L_2}{2}\right)\sqrt{1-T_2} \right) \right) \\ & - \left(cosh\left(\frac{\Delta\alpha L_-}{2}\right) + cos(\delta)\sqrt{1-T_1} \right) T_2 \Bigg), \end{aligned} \tag{123}$$

$$\begin{aligned} B \equiv \Bigg(& T_1 \left(2e^{\frac{\alpha_2 L_2}{2}} cos(\Delta)\sqrt{1-T_2} + e^{\alpha_2 L_2}(T_2 - 1) - 1 \right) \\ & + 2e^{\frac{\Delta\alpha L_+}{2}} \Bigg(2 \left(cosh\left(\frac{\alpha_1 L_1}{2}\right) \left(cosh\left(\frac{\alpha_2 L_2}{2}\right) - cos(\Delta)\sqrt{1-T_2} \right) \right. \\ & \left. + cos(\delta_1)\sqrt{1-T_1}\left(cos(\Delta) - cosh\left(\frac{\alpha_2 L_2}{2}\right)\sqrt{1-T_2} \right) \right) \\ & - \left(cosh\left(\frac{\Delta\alpha L_-}{2}\right) + cos(\delta)\sqrt{1-T_1} \right) T_2 \Bigg) \Bigg), \end{aligned}$$

where the coupled coefficients have been defined as

$$\begin{aligned} \Delta\alpha L_{-} &\equiv \alpha_1 L_1 - \alpha_2 L_2, \\ \Delta\alpha L_{+} &\equiv \alpha_1 L_1 + \alpha_2 L_2, \\ \Delta &\equiv \delta + \delta_1. \end{aligned} \tag{124}$$

The through power is then,

$$P_t = P_f \frac{A}{B}. \tag{125}$$

We can see in the through power plots below, Fig. 41, that over the physically justifiable parameter domain the mode of the first sphere can be induced to produce transparency or absorption at the resonance frequency, depending on the particular interaction with the second cavity. These effects are termed coupled-resonator-induced transparency and absorption and are abbreviated CRIT and CRIA respectively [34].

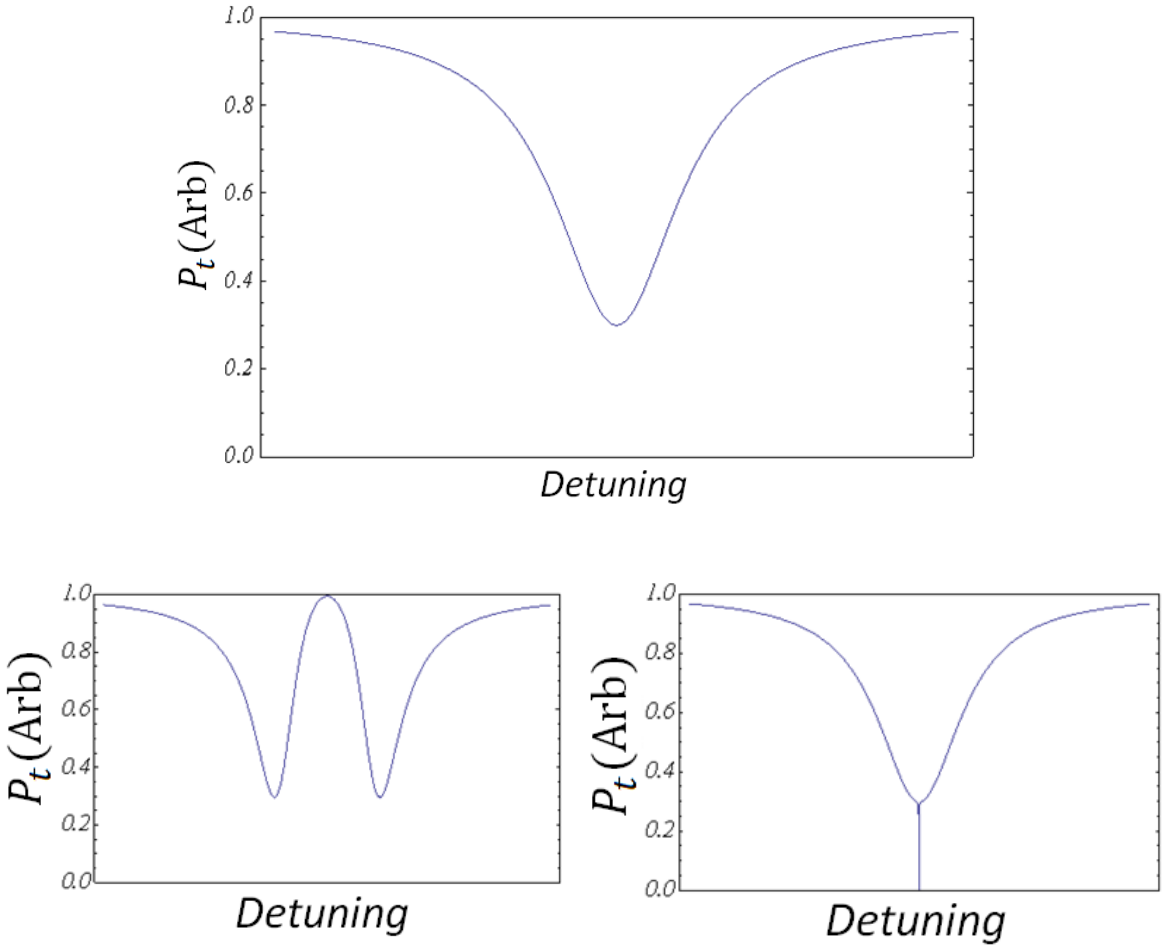

Figure 41. Coupled resonator frequency response. Top is the unperturbed mode of the first cavity, bottom left is an induced transparency (CRIT), bottom right is an induced absorption (CRIA).

Coupled-Mode Theory of Twin-Cavity Coupling:

At this juncture we must quantify what the physically justifiable parameters are for this coupled system. Clearly the fiber-sphere coupling coefficient can be taken to be of the same order as found previously. It is further reasonable to take both cavities' intrinsic losses to also be of the same order as was previously determined. The only parameter that we have no a priori knowledge of is then the coupling coefficient between the two cavities. Let us then employ the coupled-mode technique to this system as well.

Using identical methodology to fiber-sphere coupling, which we gain nothing by detailing again, the overlap integral and fields of the second cavity in the first cavity's coordinate system are found to be,

$$\kappa_{ss} = -\frac{\omega\epsilon_0}{4}({n_s}^2 - {n_o}^2)\iiint_{V_{s1}} (\boldsymbol{E}_{s1} \cdot \boldsymbol{E}_{ss}{}^*) r\cos(\theta)\, dr d\theta dz, \tag{126}$$

$$\boldsymbol{E}_{ss}(r,\theta,\phi) \equiv \boldsymbol{U}_{ss}(r,\theta,\phi) \cdot \boldsymbol{E_{s2}}\big(r_{ss}(r,\theta,z), \theta_{ss}(r,\theta,z), \phi_{ss}(r,\theta,z)\big),$$

$$\boldsymbol{H}_{ss}(r,\theta,\phi) \equiv \boldsymbol{U}_{ss}(r,\theta,\phi) \cdot \boldsymbol{H_{s2}}\Big(r_{sf}(r,\theta,z), \theta_{sf}(r,\theta,z), \phi_{sf}(r,\theta,z)\Big).$$

We can note that because of cavity coordinate symmetry the indices of the cavities are arbitrary and have been dropped from both the coupling coefficient and coordinate transforms.

Begin by considering two microspheres, equatorial planes coinciding, in contact with each other. When the overlap integrals are evaluated numerically for varying radial orders, denoted by q, of both microspheres, as seen in Fig. 42 below, we find peak coupling strengths which are slightly higher than those observed in fiber-microsphere coupling.

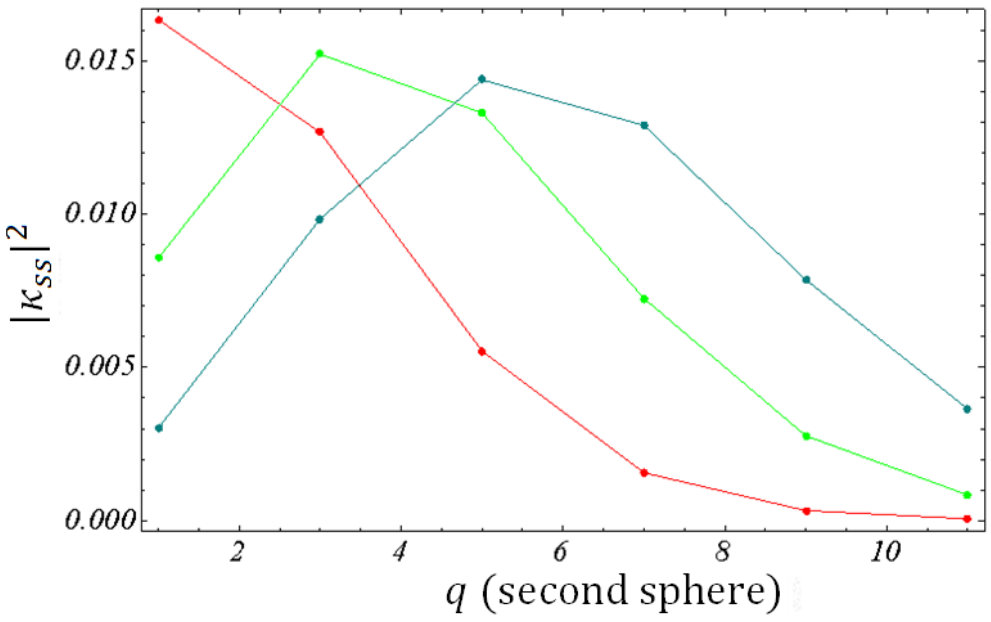

Figure 42. Coupling strength between various TE radial orders of symmetric $200\ \mu m$ *spheres at* $\lambda = 1550\ nm$*. Each trace represents a different radial order of the 1st sphere, where* q *= {1, 3, 5} for traces {red, green, blue} respectively.*

However, when the radial mode order is fixed at the fundamental and the polar order is increased in both microspheres, as seen in Fig. 43 below, we find a very rapid decrease in coupling strength between the cavities. This is simply due to a very rapid decrease in the spatial overlap of the fields due to the curved geometry of the interface between the resonators.

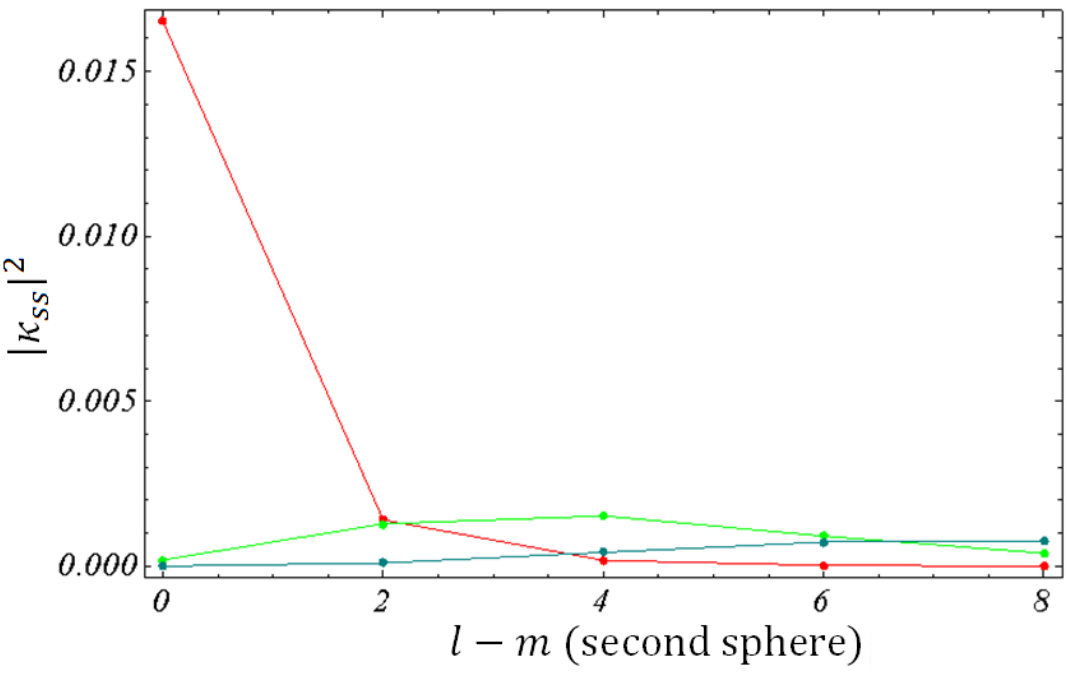

Figure 43. Coupling strength between various even TE polar orders of symmetric $200\ \mu m$ *spheres at* λ= $1550\ nm$. *Each trace represents a different polar order of the 1st cavity, where* l-m = *{0, 4, 8} for traces {red, green, blue} respectively.*

We can also evaluate the effect of placing a gap between the cavities, as shown in Fig. 44 below. As we would reasonably expect, the coupling strength falls off exponentially for all mode configurations due to the exponential decrease in the evanescent fields. The normalized falloff rate with distance will be shown to be an important tool for verification of these predictions and it is loosely only a function of the evanescent decay rate which is largely invariant to mode configuration, as seen in Fig. 45 below.

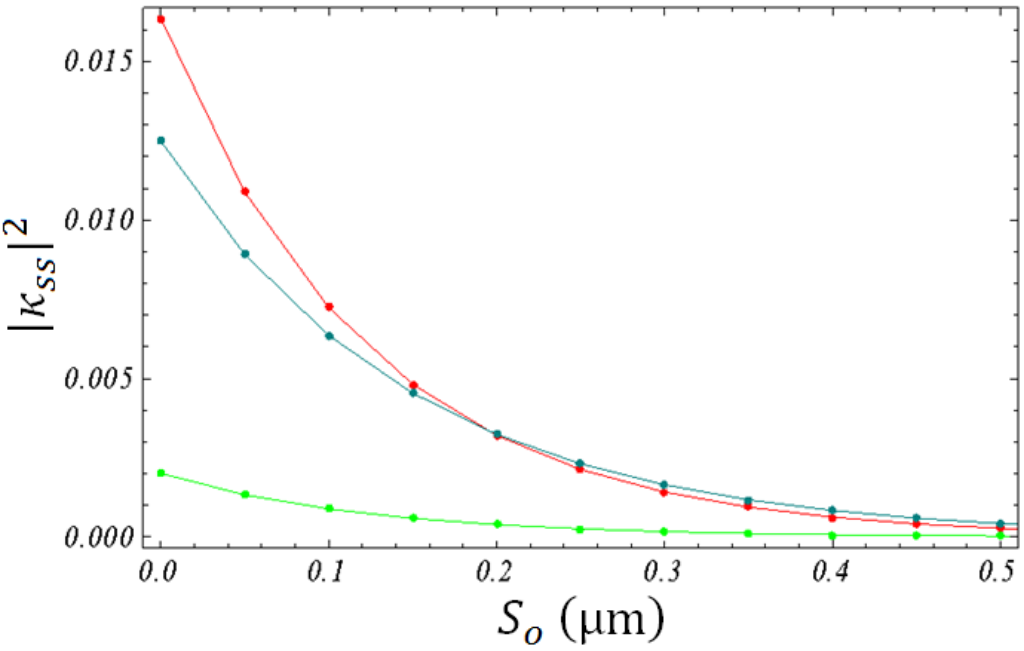

Figure 44. Coupling strength for various TE modal overlaps for symmetric $200\ \mu m$ *spheres vs. separation distance between cavities at* $\lambda = 1550\ nm$*. Here each trace represents identical mode coupling of the spheres, where {q, l-m} = {1, 0}, {10, 0}, {1, 2} traces {red, green, blue} respectively for both cavities.*

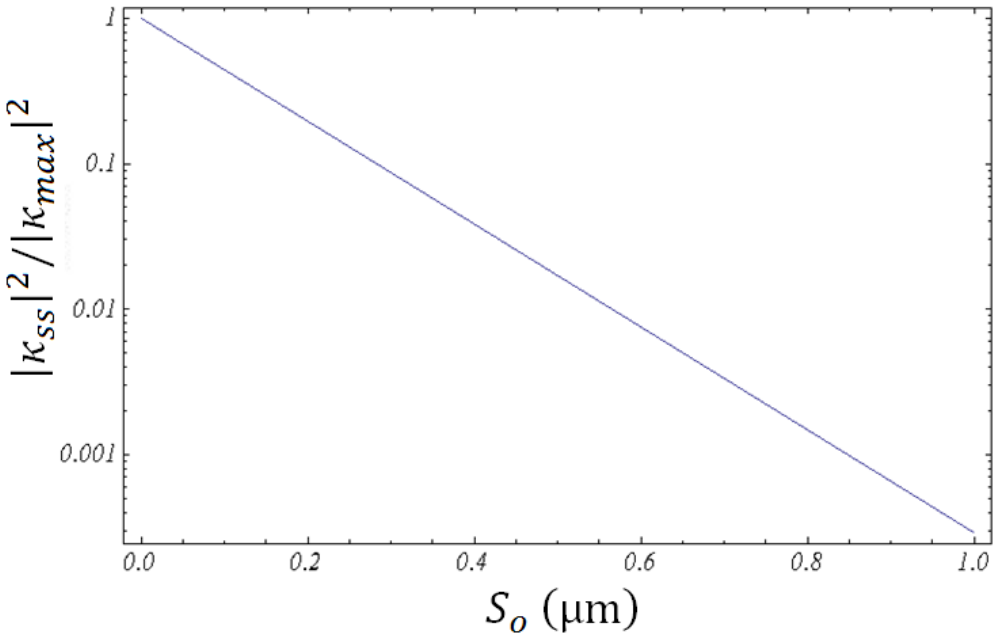

Figure 45. Peak coupling falloff as a function of separation distance for fundamental TE modes of $200\ \mu m$ *spheres at* $\lambda = 1550\ nm$ *in a log scale. Within* $1\ \mu m$ *the coupling has decreased by almost four orders of magnitude.*

From this we can conclude that peak coupling will occur between fundamental cavity TE modes (TM coupling is an order of magnitude weaker) with a peak magnitude of $|\kappa_{SS}|^2 = 1.5 \times 10^{-3}$, which is slightly higher than that for fiber-sphere coupling. However, given that coupling drops very rapidly as polar order is increased, due to a decrease in spatial overlap of the fields, this peak value represents a strong upper limiting case with physical infrequency.

Experimental Verification of the Model:

These results also indicate that the coupling between the cavities can be readily controlled by the creation of a variable gap between the cavities as seen in Fig. 44 and Fig. 45 above. This methodology was previously employed by our group in [34] to induce the CRIT behavior seen in Fig. 46 below.

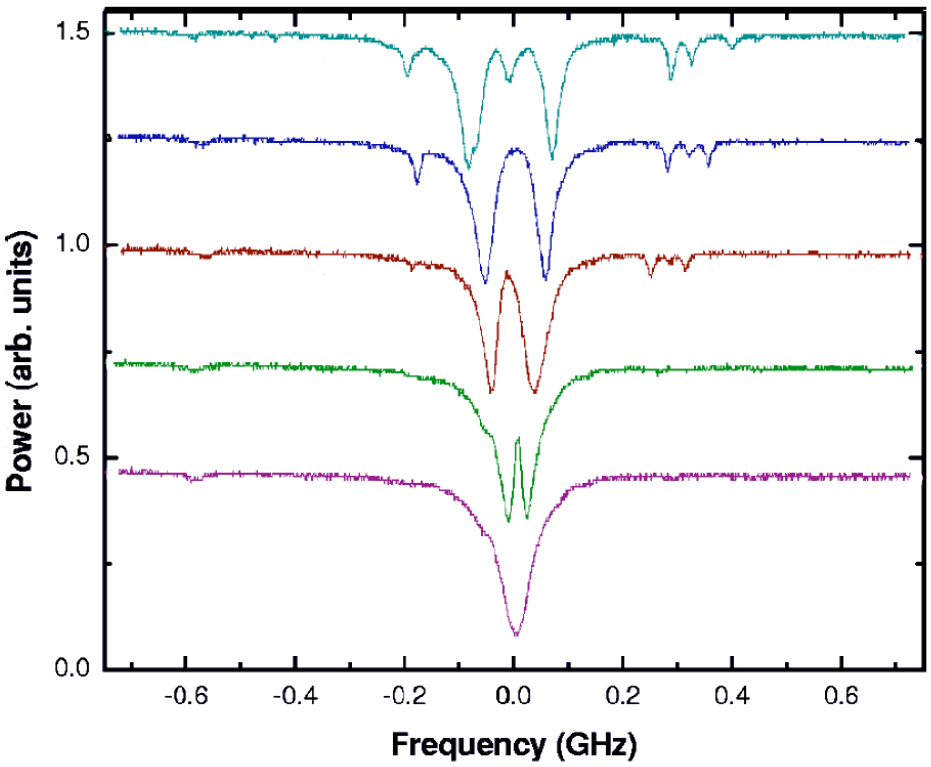

Figure 46. Coupled cavity response (CRIT) as separation distance is decreased. Each trace has been offset upwards. In the ascending direction the coupling strength is increased and the separation distance decreased until the cavities are in contact (top).

We can attempt to verify the conclusions of coupled mode theory by direct comparison to the experimental data above. Let us then assume that this data was recorded because the response was strong which implies near fundamental mode coupling behavior as seen in Fig. 42. Let us then linearly decrease the coupling distance in five steps from first sign of interaction to contact; using all other known physical parameters we find the behavior shown in Fig. 47 below.

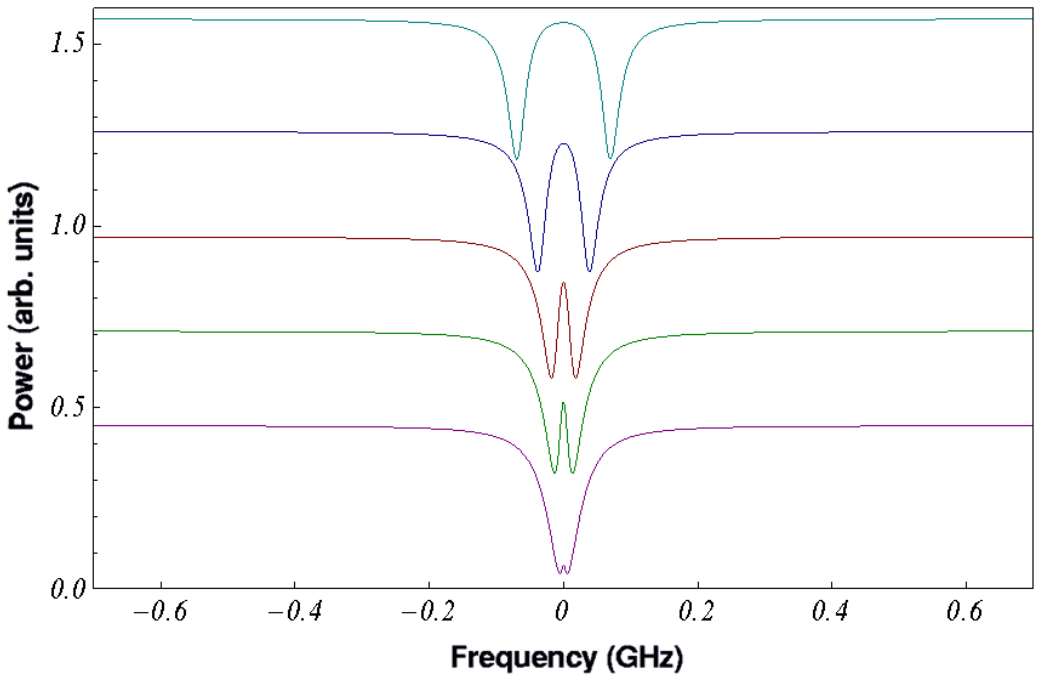

Figure 47. Predictions of induced transparency based on coupled mode theory. The interaction has been assumed to be between fundamental modes at λ= $1550\ nm$. *The values for coupling strength were found from coupled mode theory assuming each trace has reduced the gap distance* $175\ nm$.

The results of the coupled mode theory are then in very good agreement with the experimental data presented previously. However, the previous experiments relied exclusively on coincidental resonances between the cavity modes, which is inefficient. We would like to control the particular modes that are interacting as well as the coupling strength between them. To this end we have previously discovered that the index of refraction, and thus resonance frequency, is thermally sensitive. We could then envision modestly elevating the temperature of the second cavity to control the particular modes that are interacting. This is done by mounting the high-thermal-conductivity stem of the second cavity to a high-efficiency thermo-electric heating/cooling device (Nextherm model UMC60). Thus an external applied voltage directly controls the index of the second sphere and the modal interaction of the coupled

system. Early experiments show a frequency tuning range of roughly 10 GHz which is more than adequate for our needs. Although the physical surface area contact between the two cavities is small and the direct conduction limited, the thermal conduction into the air is strong enough to also cause frequency shifting of the first cavity. This can be mitigated somewhat by circulating a dry low pressure nitrogen stream between the two cavities as the temperature of the second cavity is increased. From the ring-cavity model previously presented we predict control of both location and spectral magnitude of the transparency feature when the frequency of the second cavity is externally controllable as seen in Fig. 48 below. With these predictions in hand an experimental system is constructed and tested, with results shown in Fig. 49 below, for first-order agreement with the model.

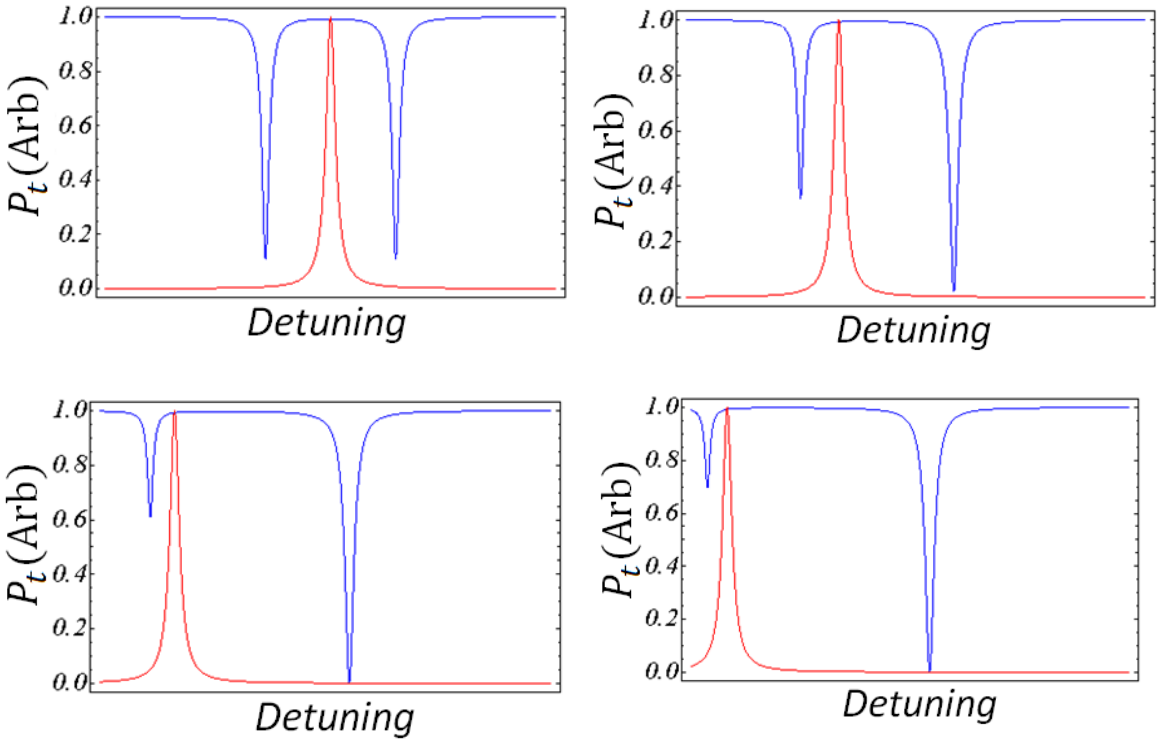

Figure 48. Effects of detuning on CRIT response. The system throughput trace is represented in blue while the second cavity resonance (not to scale) is represented in red. Thermal tuning can be used to control the width of the transparency window and its location.

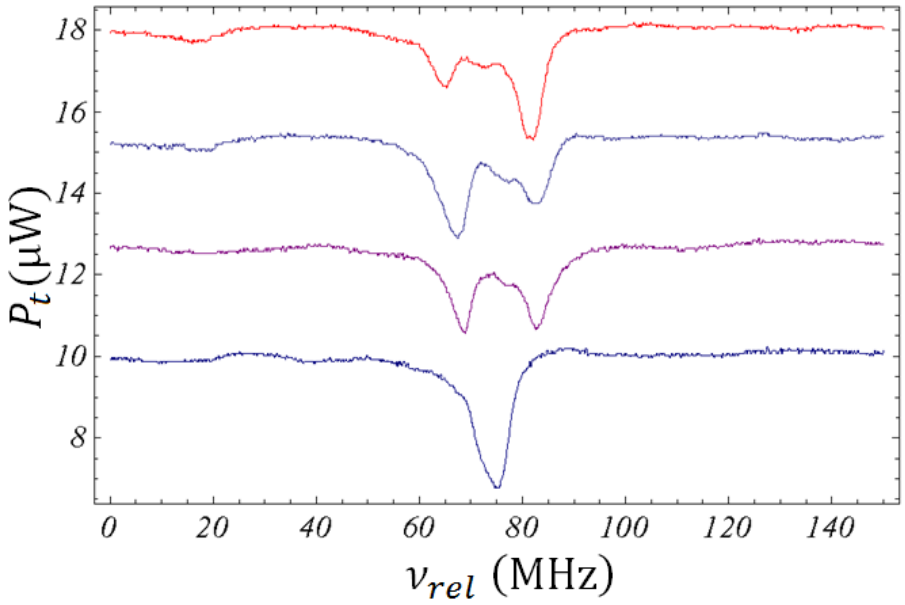

Figure 49. Experimental demonstration of thermal control of CRIT window. Each ascending trace has been offset by 2.5 μW.

The ring-cavity model likewise predicts control of the CRIA feature via external control of the second cavity's resonance, as seen in Fig. 50 below. However, as the experimental apparatus is only in a proof of concept stage these types of responses have yet to be experimentally verified. Based on the CRIT response we are confident that the control of the CRIA response can likewise be externally controlled with advancements in experimental methodology.

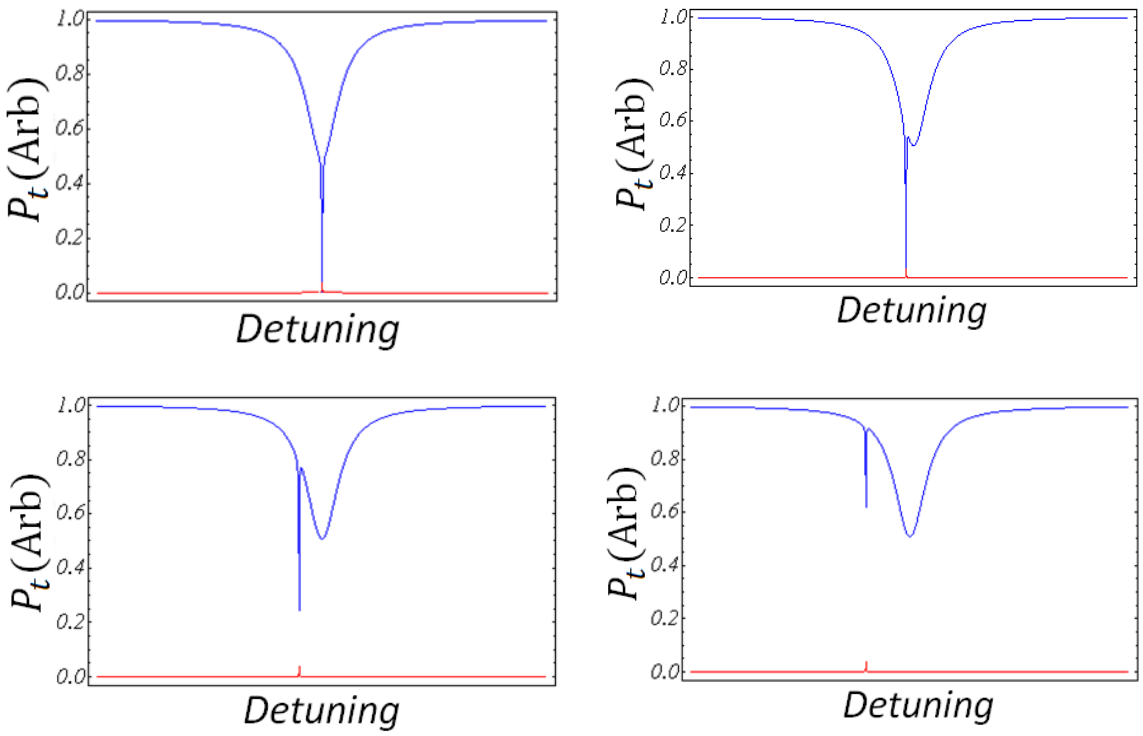

Figure 50. Detuning effects on CRIA response. The system throughput trace is represented in blue while the second cavity resonance (not to scale) is represented in red. Thermal detuning gives frequency control of the absorptive window.

Thermal frequency tuning offers the promise of not only mode selection for interaction, but also some control on the central frequency, or frequency width, of either the induced transparency or absorption window.

Discussion:

It has been shown that coupled cavities produce effects which are analogous to those observed in atomic systems. The strength of the effects have been directly characterized by applying coupled-mode theory to predict reasonable ranges of interaction strength and these predictions were further used to accurately reproduce the outcome of experiment. It has further been demonstrated that thermal control of the index of refraction of the second cavity

can be an effective tool to control both mode selection for interaction and frequency location of the induced feature.

Chapter 4 Optical Plasmonic Coupling

While we have shown that the coupling between waveguides can be controlled by geometric considerations we would like to control the properties of the cavity modes themselves. In particular, control of the amount of power contained in the evanescent portion of the field would allow enhancement of almost all potential applications. To this end we could consider increasing the index of refraction of the surrounding medium, i.e. placing the system in solution, which would decrease the confinement and increase the evanescent fraction of power. This is effective, but rather limiting in application as increased absorption due to the solution is extremely detrimental to the cavity *Q*. Rather than focus on confinement let us look instead into processes which provide strong near-field effects. One of the most well known and widely explored of the near-field processes is that which occurs at a metal interface. Much like in the principle of tunneling in quantum mechanics, when an electromagnetic wave is evanescently incident on a material with large but finite conductance, more specifically a material with a complex dielectric constant, a small portion of the field exists just under the surface [35]. This is the metal's equivalent of an evanescent field at a dielectric interface. This field is termed a surface plasmonic wave and has a characteristic decay length (just as our evanescent field) into the surface termed the skin depth. In an infinite system these fields are coherent oscillating induced charges which travel along the surface. If the dimensional freedom is reduced, say to a finite length and depth, these coherent charge oscillations can become resonant much as would be expected in an optical cavity, and more importantly the boundaries affect the plasmonic

resonance frequencies. Furthermore, just as seen in the tapered fibers, when the dimensionality of the metal is further reduced to characteristic scales on the order of the skin depth the field at the surface can itself become highly evanescent. With this in mind we could envision placing these nano-structures on the surface of our optical cavities such that they are coherently pumped optically at the plasmonic resonance by the evanescent optical field of the cavity. This would then lead to coherent charge oscillations in the nanostructure at the optical frequency increasing the near field due to resonant plasmonic enhancement. One can now consider the consequence of conservation of total power, in that as the near field and thus evanescent fields are enhanced in power it is reasonable to consider this a process of shifting optical power from the interior to the evanescent portion of the optical field. Let us then begin with determining the nanostructures of the most pertinence to our optical system and then move into potential applications.

Plasmonic enhancement modeling and theory:

For a surface plasmonic resonance to be of use to our studies we require some level of control over the frequency of the resonance to provide frequency overlap with our existing laser sources. While with all possible tools at our disposal any structure could potentially be created, we must limit ourselves to structures which can be generated in-house using a wet chemical method. The structures generated in a typical wet synthesis method have structures that are spherical, cylindrical or inhomogeneous in geometry; see Fig. 51. Of these three basis geometries both the spherical and inhomogeneous structures have weak resonance-frequency dependence on characteristic dimensionality [36] and furthermore the frequency degeneracy, or near degeneracy in the inhomogeneous case, of the geometric cavity modes leads to resonance broadening; thus these structures do not meet our needs. The cylindrical nanostructures, on the other hand, have broken symmetry in the longitudinal dimension which

lifts the frequency degeneracy and leads to narrower linewidths whose frequency depends not on a characteristic dimension, but rather the ratio of length to diameter, termed the aspect ratio [36].

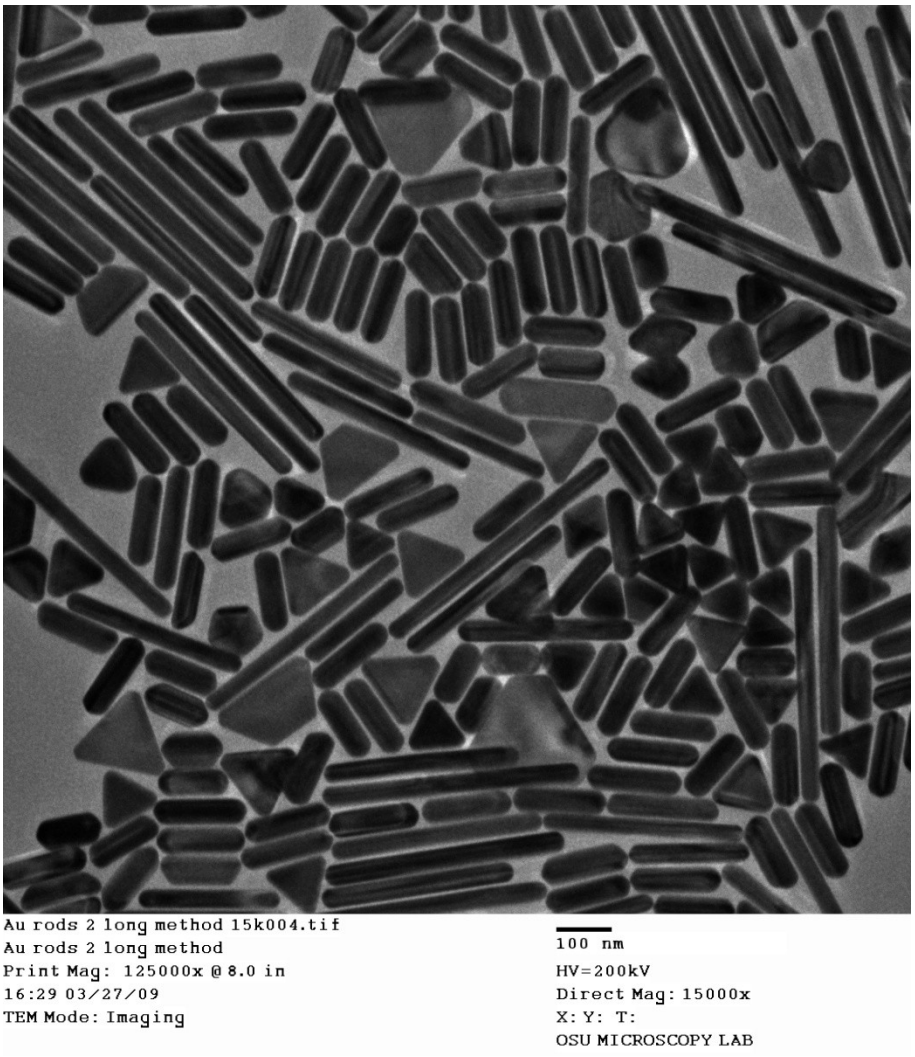

Figure 51. Typical structures produced when metal nanoparticles are created in a wet synthesis method, shown after initial separation of small platelets and spheres has been performed.

With a particular structure chosen we are tasked with choosing material composition and further understanding how to control the resonance frequency. Material choice is straightforward as plasmonic waves of all types are known to be strongest in materials with

closed d-shells [37-38], the so called noble metals, so our selection is limited to either gold or silver. Silver is eliminated outright because of problems with surface oxidation and thus gold is our material of choice.

To first order one can calculate the plasmonic resonance frequency of a gold nanorod from first principles using the simple dipole model for absorbance γ based on the Mie theory of scattering [36],

$$\gamma \propto \frac{{\epsilon_m}^{\frac{3}{2}}}{\lambda}\left(\frac{\left(\frac{1}{P_1}\right)^2 \epsilon_2}{\left(\epsilon_1 + \left(\frac{1-P_1}{P_1}\right)\epsilon_m\right)^2 + {\epsilon_2}^2} + \frac{2\left(\frac{1}{P_2}\right)^2 \epsilon_2}{\left(\epsilon_1 + \left(\frac{1-P_2}{P_2}\right)\epsilon_m\right)^2 + {\epsilon_2}^2}\right), \tag{127}$$

where the eccentricity e, polarizability P_j and surrounding medium dielectric constant ϵ_m are defined as

$$e \equiv \sqrt{1 - \frac{1}{A^2}}, \tag{128}$$

$$P_1 \equiv \frac{1-e^2}{e^2}\left(\frac{1}{2e}\ln\left(\frac{1+e}{1-e}\right) - 1\right),$$

$$P_2 \equiv \frac{1-P_1}{2},$$

$$\epsilon_m \equiv (1-f)n^2 + f\epsilon_s.$$

Here the physical constants are aspect ratio A, real and imaginary components of the dielectric constant of gold ϵ_1 = (-24.15, -115.36) and ϵ_2 = (1.52, 11.14) at (800 nm, 1550 nm) respectively, dielectric constant of fused silica ϵ_s = (2.11, 2.09) at (800 nm, 1550 nm) respectively and fractional field overlap f of the field with the fused silica surface in a background medium of

index n. This fractional overlap must be included as the resonance frequency will be shown to be strongly dependent on the local dielectric constant and the nanorods will be placed on a step-index dielectric interface, thus the associated frequency shift must be accounted for. For validation, let us compare experimental absorbance data obtained from the commercial supplier Nanopartz to absorbance predicted from our above model, Eq. (127), as seen in Fig. 52.

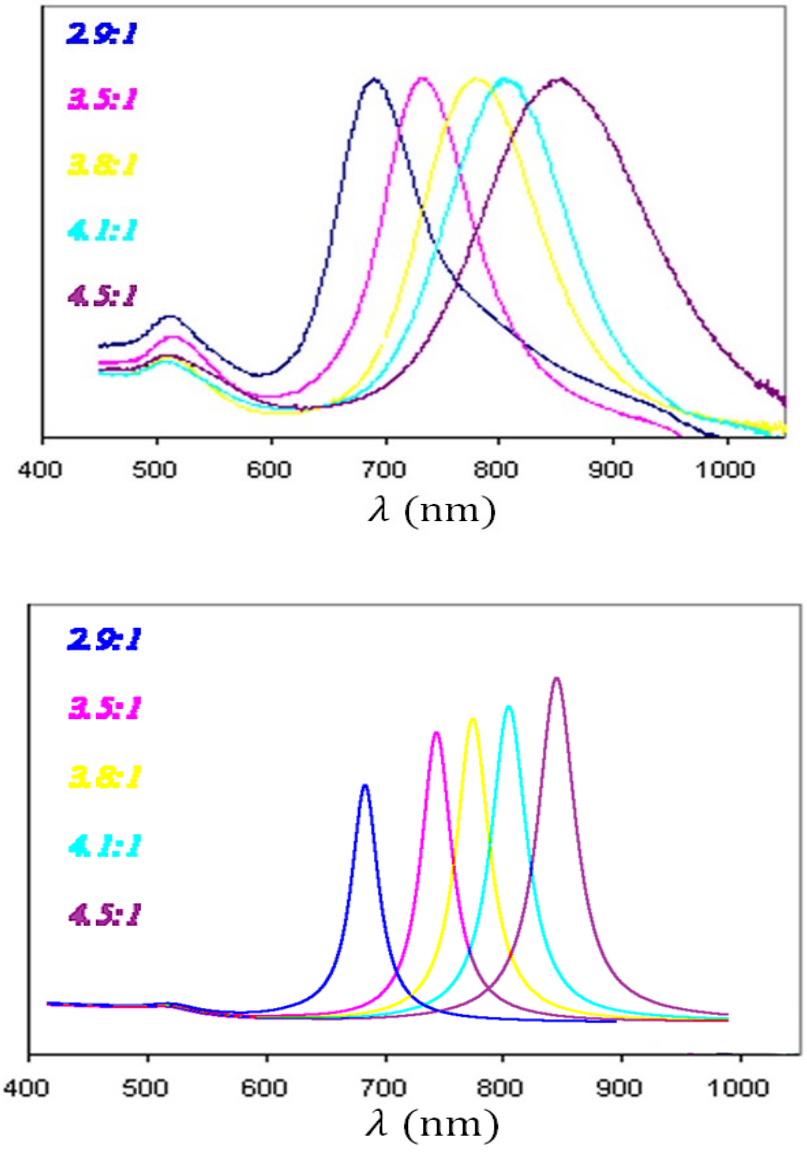

Figure 52. A direct comparison between normalized experimental absorbance data (top) and unnormalized predictions of the absorbance dipole model (bottom). The index of refraction in the model is taken to be 5% higher than that of bulk water to empirically account for the gold nanorod capping layer.

Clearly the dipole model has reasonable predictive capacity for plasmonic resonance frequency. However, one can observe that the model fails to predict both spectral width broadening as aspect ratio is increased and further the model does not account for the ratio of the short to long wavelength peaks. These comprise well known failures of this type of model [39]. Furthermore, as the aspect ratio gets large and the quadrupole excitation is no longer negligible the dipole model will predict peaks which are red shifted from those which are observed experimentally. However, in our range of interest the largest error will be less than 100 nm, which is only a fraction of the spectral width, for nanorods of aspect ratio 12:1 used in NIR experiments. For our immediate purposes, reasonable predictive capacity of plasmonic resonance frequency is all that is required, and as such we will move forward. Notice that the short-wavelength peak is not affected by aspect ratio. This peak is the transverse resonance which is largely invariant to aspect ratio for the same reason as the plasmon resonance of a spherical nanoparticle is only weakly dependent on diameter. This effect is directly related to the rotational invariance of mode structure in both spheres and cylindrical cross sections. We can further observe that the stronger long wavelength peak scales nicely with aspect ratio. This is termed the longitudinal resonance and it is both stronger and narrower due to a single degree of freedom in mode structure. Clearly we must then focus our efforts on excitation of the controllable longitudinal plasmonic resonance.

However, before we attempt to synthesize these particles, we must still account for the dielectric discontinuity of nanorod placement on a microsphere. The problem with defining the surrounding material dielectric constant in the dipole model is graphically represented to scale for the fiber-microsphere interaction region in Fig. 53 below, and for the remainder of the circumference in Fig. 54 below. In either case we can clearly observe that some form of average

surrounding dielectric constant must be used, or rather a fractional interaction effect as alluded to previously.

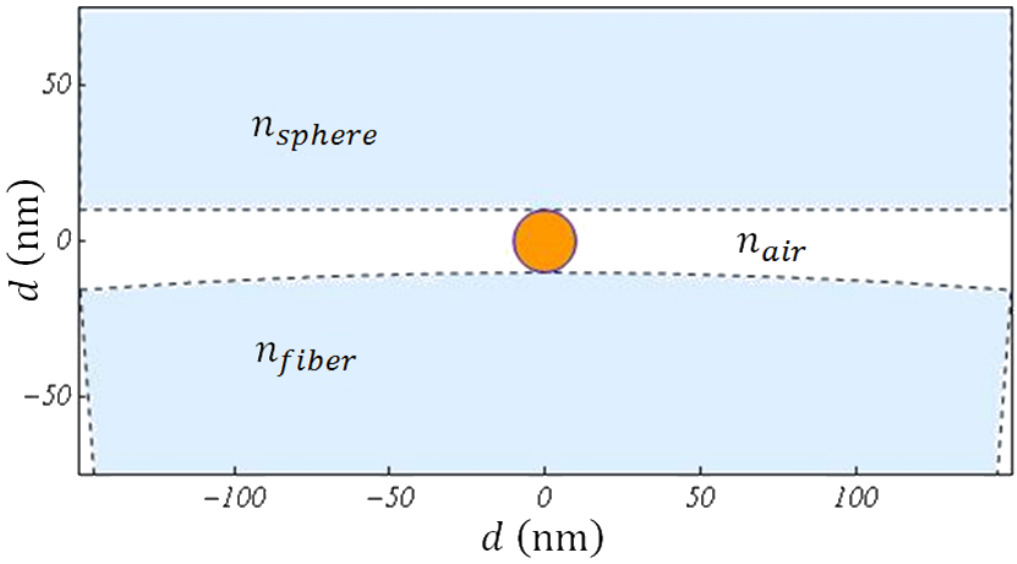

Figure 53. Cross section of a nanorod placed between a microsphere and fiber in the coupling region. The nanorod is between the two surfaces and all aspects are to scale for a typical configuration.

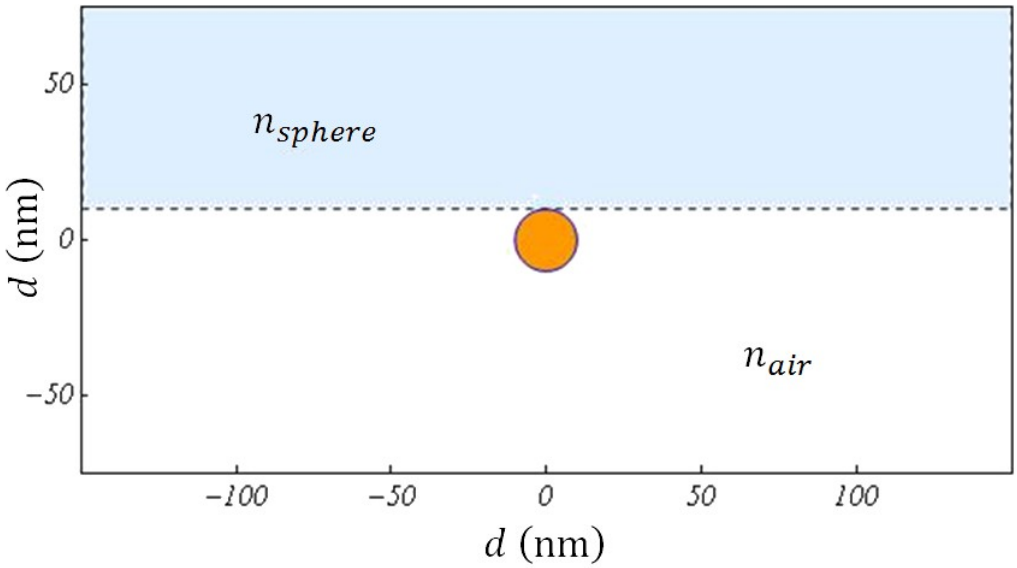

Figure 54. Cross section of a nanorod placed on the surface of a microsphere. All aspects are to scale for a typical configuration.

As a rigorous field model for these effects is extremely complicated, and a high accuracy measure of the expected frequency shifts is not required due the large spectral width of the resonances, geometric considerations are used to approximate the fractional field interaction used in Eq. (128). Some results, for the situation shown in Figs. 53 and 54, i.e., nanorods on a microsphere in air, are shown in Figs. 55-57.

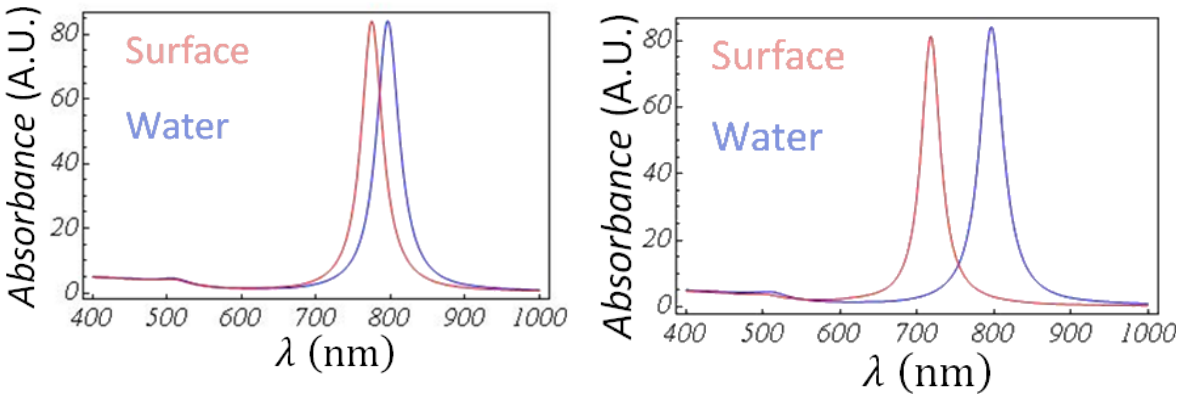

Figure 55. Comparison between plasmonic resonance for nanorods in the coupling region (red, left) and those along the remaining equatorial plane (red, right). The aspect ratio is taken as 4:1 and the surface interaction fraction f is taken as 70% and 35% respectively. Both are compared to what would be experimentally measured after synthesis in solution (blue).

From the comparisons in Fig. 55 for 4:1 gold nanorods we can observe that in the coupling region the resonance frequency is approximately what would be measured in water with about a 25 nm blue shift, but outside the fiber region the resonance is blue shifted by around 100 nm. These shifts are far larger for high aspect ratio rods as seen below in Fig. 56 for 11:1 nanorods. In the coupling region the resonance has blue shifted by 65 nm from water while outside this region the blue shift is 175 nm. While we have shown that the simple dipole model does not accurately predict broadening, which will serve to minimize the effects of the dielectric induced

blue shifts, it does become clear from the preceding analysis that we must decide if we are interested in enhancing the overall field or just the field in the coupling region.

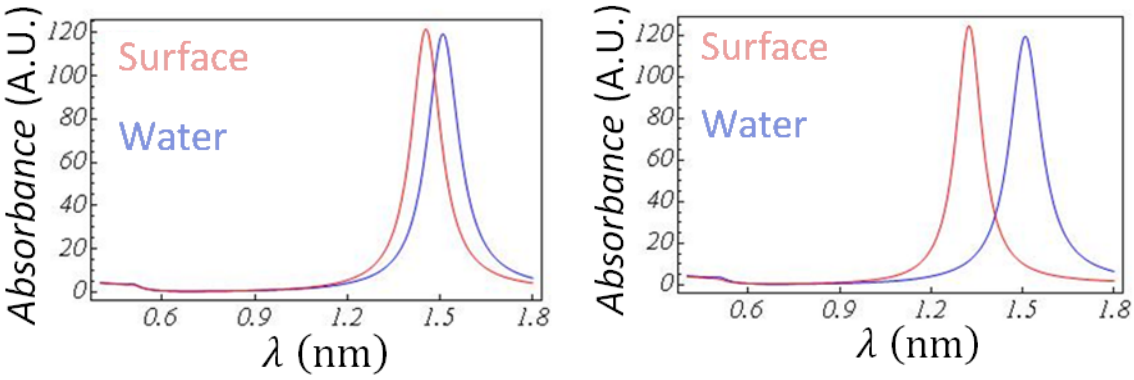

Figure 56. Comparison between plasmonic resonance for nanorods in the coupling region (red, left) and those along the remaining equatorial plane (red, right). The aspect ratio is taken as 11:1 and the surface interaction fraction f is taken as 70% and 35% respectively. Both are compared to what would be experimentally measured after synthesis in solution (blue).

In principle, we could take advantage of this effect to minimize the coupling effects of the nanorods by intentionally using rods that are too long in order to shift the coupling region plasmonic resonance away from the pump laser while maintaining resonance for the remaining regions as seen in Fig. 57 below. On the other hand, the opposite could be done to limit strong plasmonic enhancement of the evanescent field to the coupling region only.

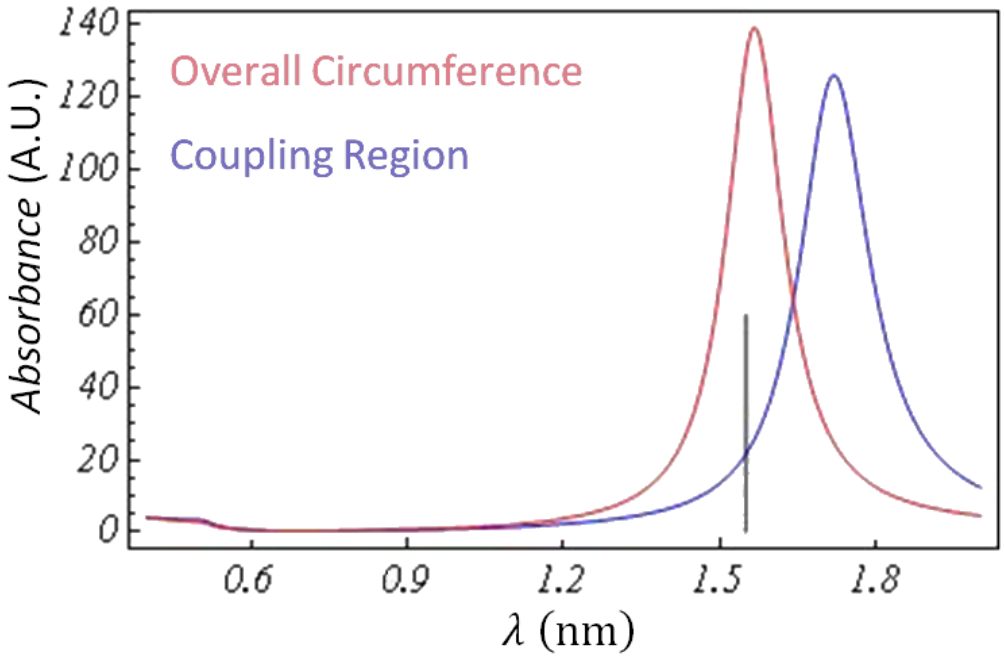

Figure 57. Prediction of control of overall enhancement and coupling region enhancement by the intentional choice of 13:1 aspect ratio nanorods. The pump wavelength is indicated by the black vertical line. Notice the overall evanescent field will be enhanced while the field in the coupling region should only be marginally perturbed.

With the necessary predictive capacity for the resonance behavior of the gold nanorods in place we can move forward to synthesis and adhesion.

Basic experimental chemistry:

The wet synthesis method employed to generate nanorods is termed a sequential seed-mediated growth process [40] and it produces single crystalline (notice the near vertical lines in Fig. 58 below) gold nanorods of pentagonal cross section with diameters of the order of 20 nm.

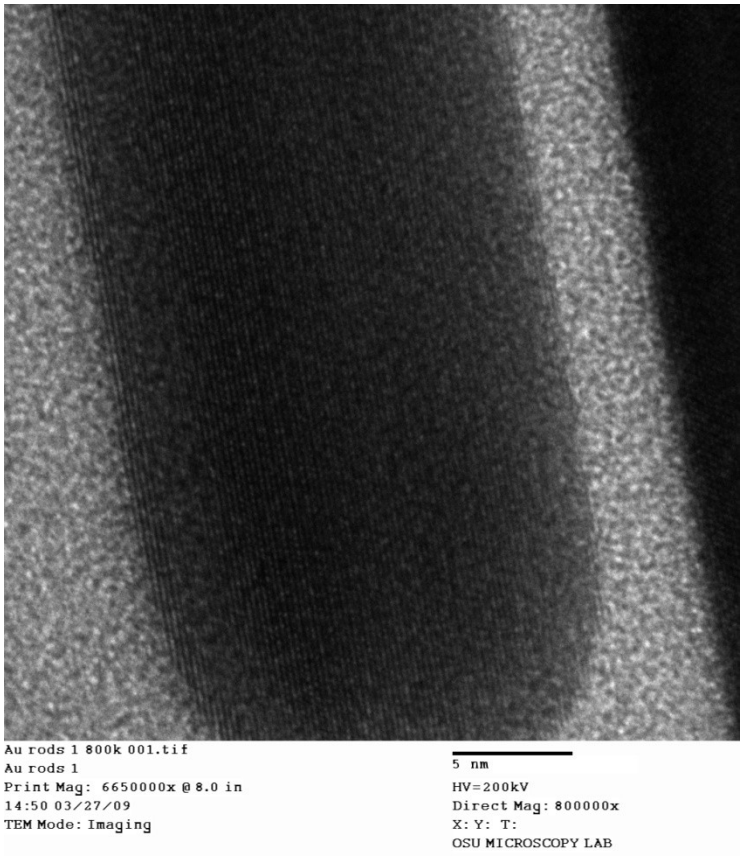

Figure 58. High resolution TEM image of the lattice structure and single crystalline nature of gold nanorods produced in-house. The lattice is visible as fringes running across the nanorod's diameter.

In this methodology ~4-nm-diameter single-crystalline gold seeds are first synthesized from gold salts in solution, in the presence of both a weak reducing agent and a citrate capping agent. The resulting seed crystals are chemically capped with citrate to prevent aggregation and the growth process is completed in 4-5 hours. Three solutions of activated gold ions are then created in an analogous manner to the growth solution for seeds. These solutions however, use a much weaker reducing agent so that self-activated growth cannot occur without perturbation (seeding) and the presence of a cationic surfactant-based capping material to encourage growth along a particular crystal lattice direction. The resulting solutions are then extremely chemically

active and much care must be taken to remove contaminants from containers as any particulate present will initiate growth. A small quantity of gold seeds is then added to the first activated growth solution. Growth occurs very rapidly and if left undisturbed until the reaction completes the resulting nanorods will have an aspect ratio of approximately 4:1 and a longitudinal resonance wavelength of about 800 nm. To create longer rods one must use the still-growing rods from the first solution as seeds in the next activated solution and then repeat this procedure to seed the final solution. The ultimate aspect ratio of the resulting rods in the final solution is a direct product of how large the growth rate was at each seeding step. If in the steps of using rods as seeds they are still extremely active (taken about 5 s after initial seeding) and growing when used, the resulting rods will have a final aspect ratio of about 18:1 with a longitudinal resonance wavelength of about 1.8 μm. If each solution has largely stopped reacting before each seeding step (4-5 hrs) the resulting nanorods will have an aspect ratio of about 13:1 and a longitudinal resonance wavelength of about 1.6 μm. Our lasers are roughly centered at 800 nm and 1.55 μm, so we focus on producing either 4:1 or 13:1 nanorods, respectively. In any of the aforementioned growth procedures the resulting solution has a low yield of nanorods (of the order of a few percent) with respect to other shapes. The structures which are not rod-like will only contribute to cavity loss if deposited on a microresonator and as such must be removed prior to use. Mass separation can be performed using either gravity sedimentation or low speed centrifugation to remove both nanospheres and small platelets, increasing the nanorod yield to a few tens of percent. However, neither process is effective at removing large platelets as they have roughly the same mass as the nanorods. Further increases in yield can be had if either the initial growth is chemically altered to produce fewer large platelets, or a reducing agent is further added to the final solution to attack the sharp edges of the platelets, thus reducing their mass. In the literature both methods of increasing

yield have been shown to reach about 99%. However, in-house we have only produced 50% and 75% yields with these methods respectively as seen in Fig. 59 (left) and (right) respectively.

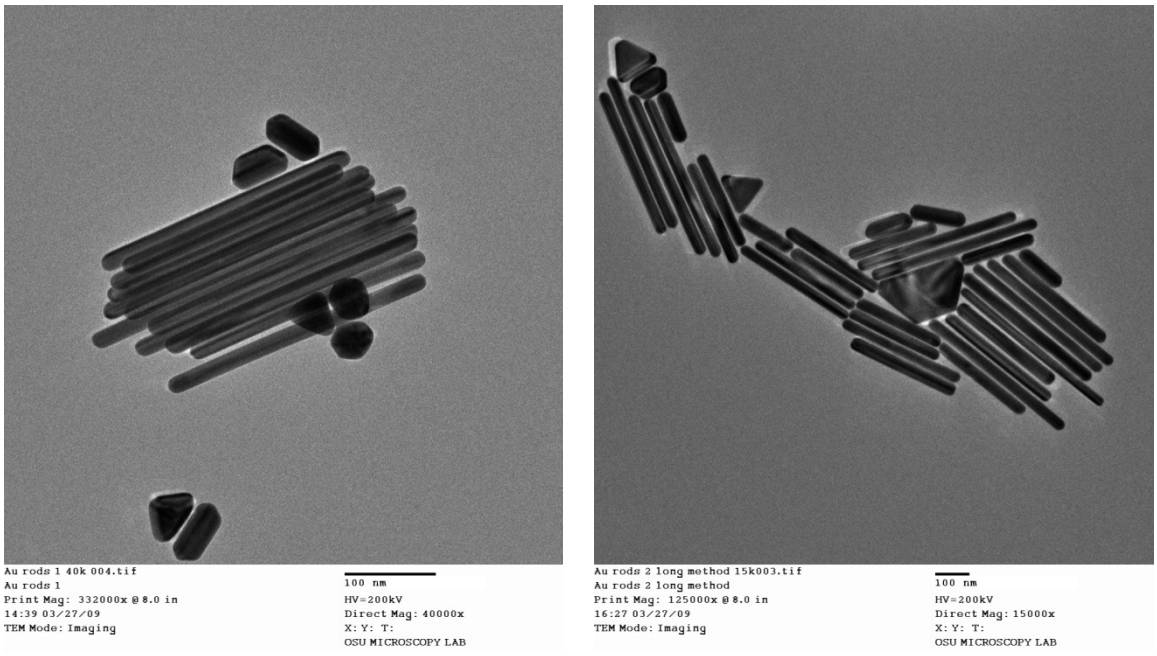

Figure 59. High-aspect-ratio nanorod yields for chemically modified growth process (left) and platelet reduction by reagent (right).

Although these yields are reasonable for use in our studies, we have found control over aspect ratio and dispersion in aspect ratio of long rods to be extremely difficult. In particular, the aspect ratios produced in the above studies were 14.5 ± 2 and 15.6 ± 3 respectively and these results show very poor repeatability.

In previous studies of plasmonic enhancement of microsphere cavities the nanorods were grown directly on the surface [41]. This was shown to be effective at the wavelength used (800 nm) but much as the solution grown nanorods have been shown to have low initial yields the surface grown nanorods had yields of only 30 percent. In these previous studies the relative increase in surface scattering of the non-contributing elements was small, so yield was not a

matter of concern. However, as one scales to longer wavelengths which require larger rods the non-contributing elements are a larger fraction of the pump wavelength and as such can produce a dominating increase in scattering. As we have little control over the distribution of surface grown features we would prefer to grow the nanorods in a separate solution which can be filtered and then adhere them directly to the cavity surface.

This can be accomplished Coulombically because the capping layer of the uncharged gold nanorods in solution is cationic, which has a large net positive charge. While the surface of the fused-silica cavity is negatively charged, due to surface hydroxides, the net charge has been demonstrated to be too weak to permanently adhere the capped nanorods. We are then tasked with functionalizing the cavity surface to create a strong negative charge. This can be done in one of two ways. The first method is an extension of previous work performed in-house to adhere nanocrystals to the cavity [41]. In this methodology the cavity is coated with a charged polymer (polyelectrolyte) which forms a thin (~1 nm) charged film on the surface. The polymer is typically a highly branched organic molecule with molecular weights of several hundred kilograms per mole. The adhesion to the surface of the cavity is dominated by the branched molecules effectively tangling producing a "web" on the surface. Thus the particular charge of the polymer is a matter of selection and is not a strict requirement for cavity adhesion. While we have had success with a number of ionic polymers allowing adhesion of nanorods to the functionalized cavity surface, the optical properties were severely impacted due to a combination of increased absorption and/or scattering of the cavity field by the thin polymer film.

The second adhesion method is a pure chemical treatment. We take advantage of the surface hydroxide layer and use a chemical procedure which first breaks the silicon-hydroxide bond and

then replaces the hydroxide with a functionalized molecule which forms the overall molecular structure of a silane (silicon structural equivalent of methane). Our choice of functionalizing molecule then gives us control over the final surface charge of the cavity. The most effective functionalizing molecule used to date is a methyl group [42] that has been shown to produce less than a factor of two decrease in the cavity quality factor, which is quite acceptable. These functionalized microspheres have been repeatedly demonstrated to produce very high surface adhesion rates for nanorods in solution, as seen below in Fig. 60.

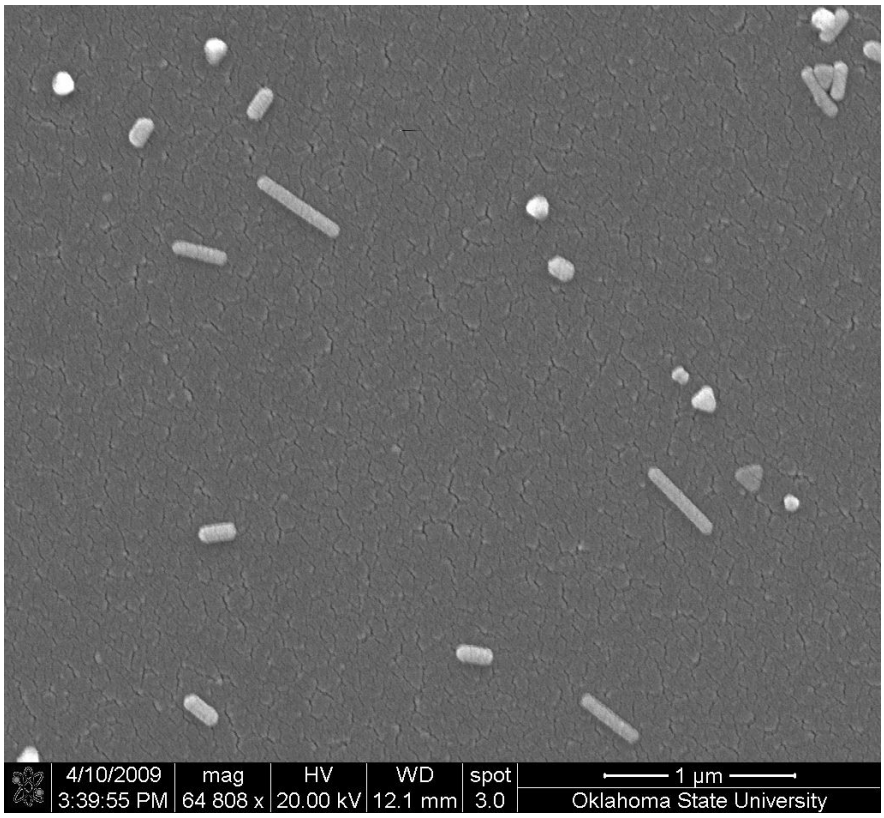

Figure 60. Direct surface adhesion of nanorods from a filtered growth solution, as seen in an SEM of the surface of a silanized microsphere.

With the cavity adequately functionalized the adhesion process is straightforward. A growth solution which has been previously mass-separated is briefly centrifuged at high RPM (~13,000)

to settle all the solids in solution to the bottom. The resulting supernatant, which contains the remaining charged chemicals from growth, is drawn off and replaced with deionized water. This is repeated numerous times until the capped nanorods are suspended only in deionized water. Care must be taken in this process as each round of purification increases the likelihood of disrupting the capping layer of the nanorods and inducing aggregation. The functionalized cavity is then dipped in the nanorod solution for varying lengths of times. Upon removal, the cavity is further rinsed in deionized water to remove any unbonded structures. As would be expected, we have directly observed that the final surface density of nanorods is directly related to the amount of time the cavity is held in solution, in the short time (seconds) limit. We have further found that there is a finite upper limit (10s of minutes) to the final surface density achievable, which is far short of surface saturation. This appears to be due to some residual charged molecules in the purified nanorod solution bonding to the functionalized sites, thus limiting nanorod adhesion.

Experiments using plasmonic enhancement:

With controlled growth and adhesion demonstrated we can envision a myriad of experiments involving these evanescently enhanced cavities. Given that we have increased the strength of the evanescent field of the cavity we can reasonably expect the modified resonator to couple more strongly to adjacent waveguides and also to show a marked increase in environmental sensitivity. We could then characterize the particular experiments into two categories: those which rely on enhanced waveguide coupling, and those which rely on increased environmental sensitivity. Enhanced coupling experiments will first be used to validate the nature of the plasmonic enhancement effect before it is then used for some practical application. Then with the effect validated the increased environmental sensitivity will be used to probe the local environment around the cavity.

Coupling and loss enhancement:

Just as in the previous study using surface grown nanorods [41] we can determine the increase in coupling and loss by directly measuring both the cavity transmission probability and intrinsic loss coefficient before and after the application of nanorods to the surface. This is done through our knowledge acquired in the ring cavity analysis. If one directly measures the cavity's loaded quality factor and dip depth we will find two physical solutions for the ratio of coupling loss to intrinsic loss x that can produce the measured parameters. If we further determine the cavity's coupling regime through either the cavity's transient response to a change in incident power or an invasive increase in cavity loss we will be able to eliminate one of the two solutions giving us explicit measurement of both the cavity's transmission coefficient and intrinsic loss. In particular the coefficients are found to be

$$T = \frac{\pi\, n_{eff} L}{\lambda Q_l}\left(1 - (-1)^n \sqrt{1-m}\,\right), \tag{129}$$

$$\alpha_i L = \frac{\pi\, n_{eff} L}{\lambda Q_l}\left(1 + (-1)^n \sqrt{1-m}\,\right),$$

where n represents the coupling regime, $n = \{0,1\}$ for undercoupled and overcoupled respectively. With this we can readily define the coupling enhancement factor F_c and intrinsic loss enhancement factor F_i as

$$F_c \equiv \frac{T_a}{T_b} = \frac{\frac{1}{Q_a}\left(1 - (-1)^{n_a}\sqrt{1-m_a}\right)}{\frac{1}{Q_b}\left(1 - (-1)^{n_b}\sqrt{1-m_b}\right)}, \tag{130}$$

$$F_i \equiv \frac{\alpha_{ia}}{\alpha_{ib}} = \frac{\frac{1}{Q_a}\left(1 + (-1)^{n_a}\sqrt{1-m_a}\right)}{\frac{1}{Q_b}\left(1 + (-1)^{n_b}\sqrt{1-m_b}\right)},$$

where the subscripts b and a represent before and after the addition of the nanorods to the surface.

Method	*AR / λ_p*	*Yield*	*Dip Time*	*Fc / Fi $\lambda = 0.8\ \mu m$*	*Fc / Fi $\lambda = 1.5\ \mu m$*
Surface Grown	*4:1 / 0.8 μm*	*30%*	*NA*	*100 / 1*	*2 / 2*
Purchased	*4:1 / 0.8 μm*	*99%*	*15 s*	*300 / 1*	*10 / 10*
Chemically modified	*14.4:1 / 1.65 μm*	*50%*	*15 s*	*4 / 10*	*20 / 20*
Chemically modified	*14.4:1 / 1.65 μm*	*50%*	*10 min*	*NA*	*1500 / 1500*
Platelet reduction	*15.6:1 / 1.75 μm*	*75%*	*15 s*	*4 / 10*	*20 / 20*
Platelet reduction	*15.6:1 / 1.7 5 μm*	*75%*	*5min*	*NA*	*300 / 100*

Table 1 Peak approximate results of various gold nanorod growth and application methods. Here $\boldsymbol{\lambda_p}$ is the plasmonic resonance wavelength for nanorods of aspect ratio AR and enhancement results are shown for both $\lambda = 0.8\ \mu m$ and $\lambda = 1.5\ \mu m$

In the above summary table, Table 1, of the results of various application times and growth methods, we can note that the peak enhancement is seen for the wavelength which is closer to the plasmonic resonance frequency. Furthermore, we note that the amount of coupling enhancement increases with the final surface density as indicated by the higher enhancement seen for longer dipping times. However, as a consequence of the higher surface densities we can also observe that the intrinsic loss is also enhanced. Further we observe that the measured increase in intrinsic loss is less for higher yields of the particular growth solution, confirming the ansatz stated previously concerning non-contributing elements.

Localization of enhancement:

While the observed dependence on wavelength and nanorod yield in the increased intrinsic loss and coupling are good indicators that the observed effects are plasmonic in nature, the homogeneous surface distribution of nanorods will produce uniform spatial enhancement on the surface making it impossible to definitively distinguish the plasmonic nature of the effect. However, if we could localize the enhancement region we could spatially probe the cavity and directly observe the increase in both coefficients when nanorods are present in the coupling interface confirming the coefficient increases are due to the nanorods.

Clearly a dipping methodology will not be appropriate as this will always produce a homogeneous surface distribution. In a direct extension of the work of Dr. Flanders [43] a nanowire is grown from nanorods suspended in solution using a directed dielectrophoretic method. This methodology has been extended in house to produce nanowires which are very long (~1 mm) by mimicking the procedures associated with crystal growth. That is, the electrodes are constructed from finely sharpened, rotationally symmetric copper wires, forming needles. These are connected to linearly opposed stages so that the electrode gap distance can be slowly increased during the growth process, as seen in Fig. 61 below. Thus a fine short nanowire can be “drawn out” to a very long wire with peak aspect ratios on the order of 1000. We have observed during this process that the required peak-to-peak drive voltage and frequency, 2 V @ 10 Hz, are much lower than typically reported in the literature and we associate this with both the drawing methodology and the larger aspect ratio of rods in our particular solutions (4:1).

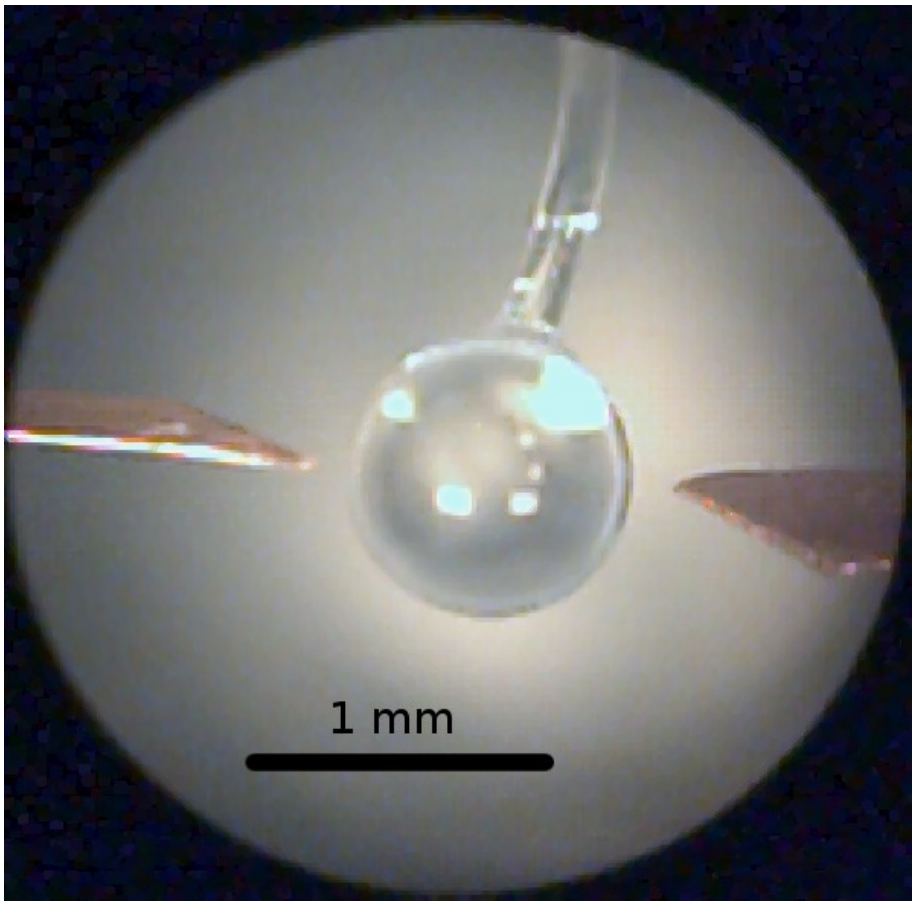

Figure 61. Microsphere shown between electrodes after a nanowire is grown in solution. Note that the nanowire is present between electrodes but not visible in the image due to its dimension.

After the nanowire is grown between the electrodes a microsphere, controlled by a high resolution stage, is carefully lowed under the electrode gap so that the equatorial plane is aligned to the nanowire, as seen in Fig. 61. The microsphere is then drawn directly upwards through the gap, which breaks the nanowire free of the electrodes and places it in the proper location on the microsphere. Great care must then be taken as the microsphere breaks the surface of the solution during removal, since the surface tension of the solution can break and/or displace the nanowire from the initial contact point. Once out of solution the nanowire will remain permanently attached to the contact point on the surface of the microsphere due to

induced dipole forces caused by a small remaining charge in the nanowire. This mechanism for adhesion is confirmed by the nanowire having limited affinity for the fused-silica surface in the polar solution, composed mostly of water, in which the nanowire is grown.

With the nanowire in place on the surface, the cavity is probed spatially and the coupling and intrinsic loss enhancements are simultaneously measured by comparing to a spatial profile of the cavity taken prior to placement of the nanowire. Although the nanowires are not single-crystalline in nature, the plasmonic resonance of any nanowire fragments still exists at the typical central frequency but is broadened by the additional impedance loss associated with internal boundaries [44-45]. Surface positioning is recorded by measuring the *z* axis position of the tapered pump fiber with respect to the upper pole of the microsphere with a micrometer and measuring the rotation angle that the pump fiber makes with the stem of the microsphere as seen from above in a high-definition CCD camera. This provides us 2D surface positioning data which can later be directly correlated with SEM (scanning electron micrograph) images of the surface of the sphere. The coupling enhancement is found to clearly be maximized when the pump fiber is located over the spatially localized nanowire feature, as seen in Fig. 62 below.

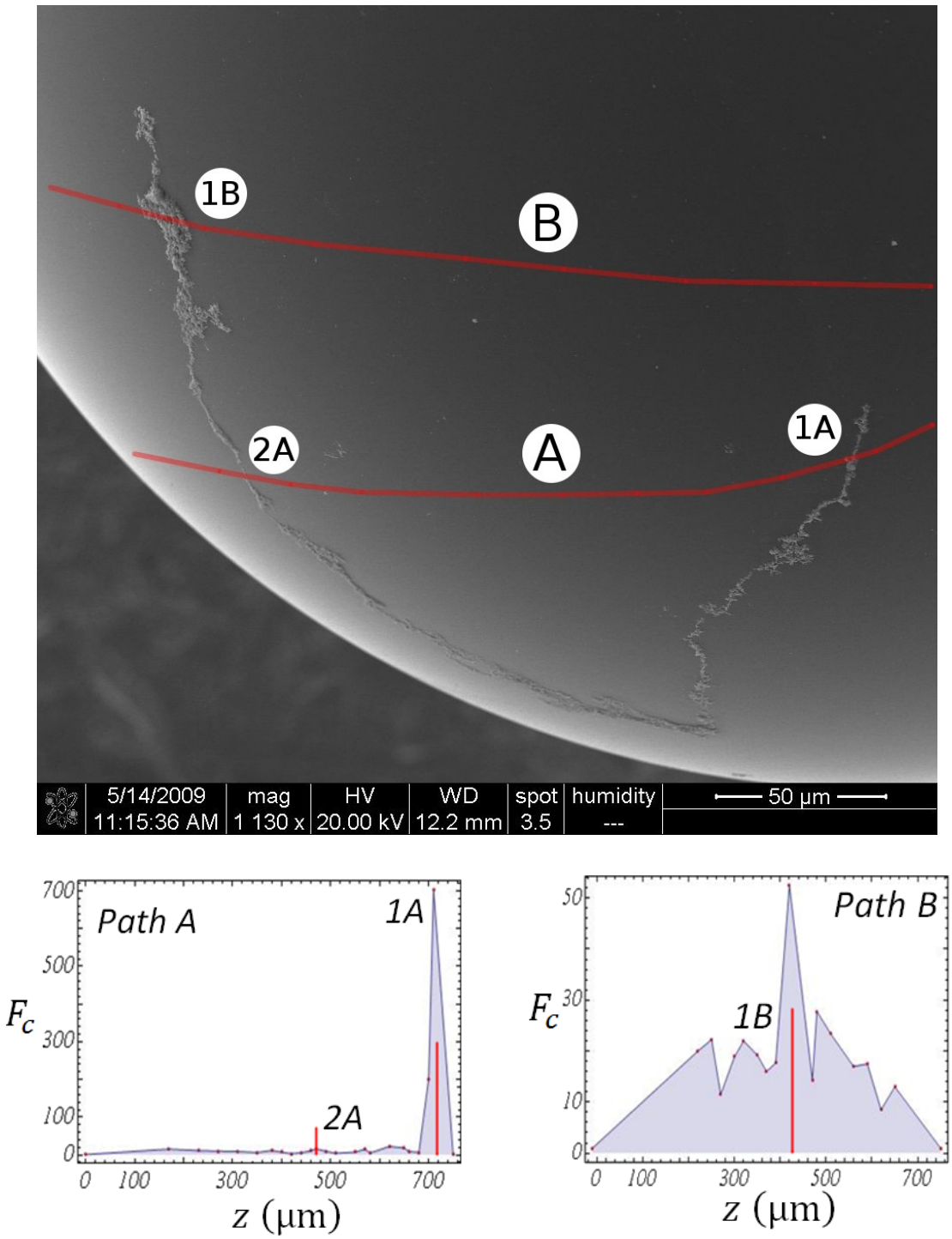

Figure 62. Coupling enhancement F_c as a function of surface position along two different paths labeled A and B.

We can make a number of observations concerning this data. We must note that we are not exciting a resonance in the overall nanowire due to its extreme aspect ratio. Rather the nanowire as placed on the surface is highly dendritic, or tree like, composed of branches which have aspect ratios of the order of 12:1 as seen in Fig. 63 below. These structures have a very large dispersion in the mean aspect ratio, where what could be considered the largest is on the order of about 12:1.

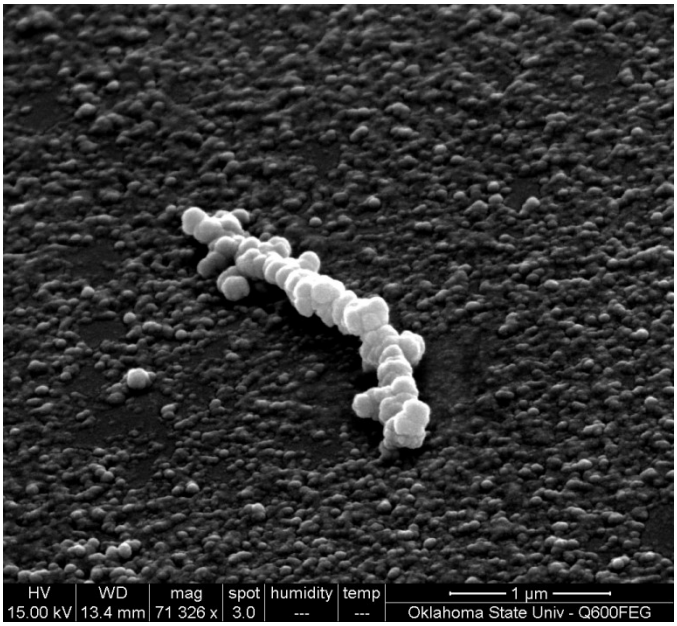

Figure 63. SEM image of an isolated dendrite fragment as seen on the surface of the microsphere.

In high density regions these dendrite structures lie atop one another, as seen in Fig. 64 below, and this serves to both broaden the plasmonic resonance and dramatically increase scattering loss. The increase in loss limits the usefulness of the technique in practical applications outside that of mere verification.

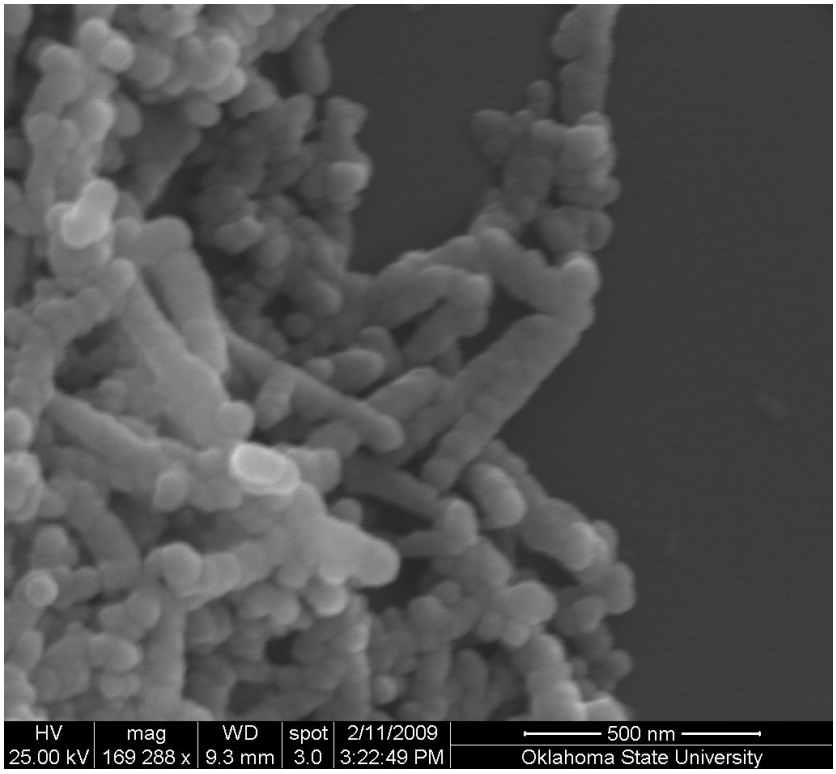

Figure 64. Stacked dendritic structures observed in high density regions. Each individual dendrite has an aspect ratio of approximately 12:1.

As one would expect because scattering occurs over the whole propagation path the scattering loss enhancement is largely invariant to position with the exception of propagation paths which include a significant portion of the nanowire. Furthermore, we can observe that the mean enhancement factor is greater than one in regions which contain no wire. This is due to residual nanorod fragments from the solution adhering homogenously to the surface as seen in the background in Fig. 63 above. We must also note that these dendritic structures as placed on the surface are not completely environmentally inert and will tend to break down over time, even when stored in dark conditions, as seen in Fig. 65 which was taken approximately two months after growth, adhesion, and storage.

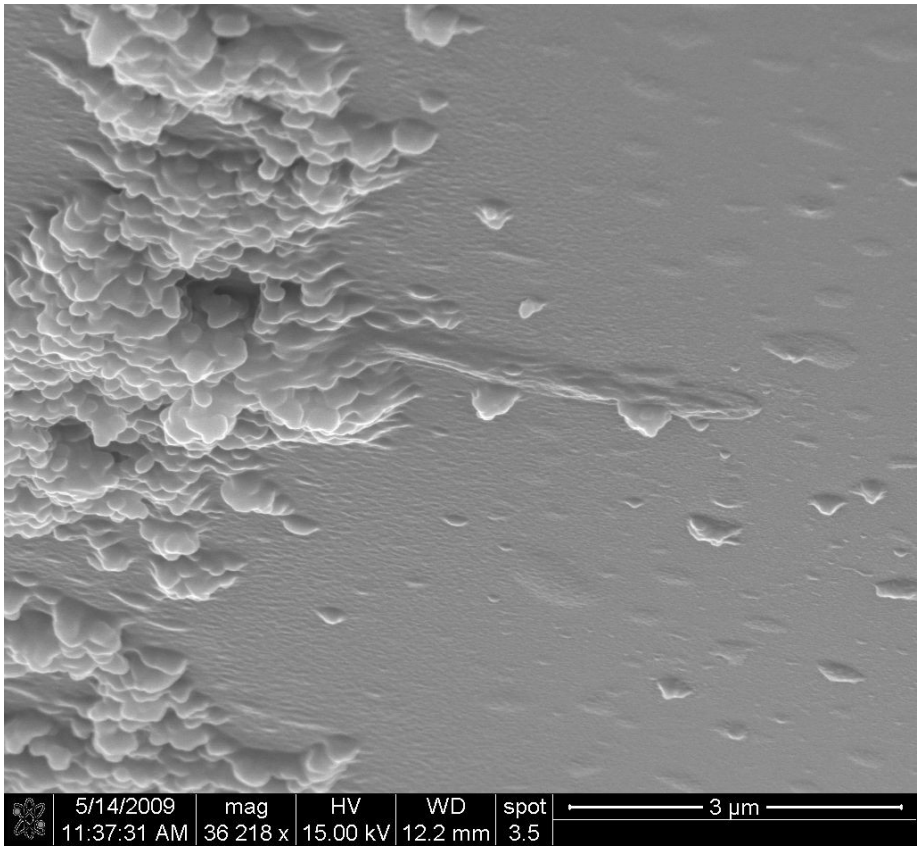

Figure 65. Adhered nanowire structures imaged approximately two months after growth, adhesion, and storage. Notice the structures appear melted in comparison to the previous image.

The correlated increase in coupling associated with the nanowire as found on the surface thus gives us reasonable, *in situ*, verification that these effects are directly associated with optical plasmonic resonances of these gold nanostructures.

Plasmonic switching:

Given that we are exciting plasmonic resonances which comprise a finite number of oscillating electrons, one can envision "stealing" the electrons from the oscillation induced by a weak probe beam through the introduction of a strong pump beam. This is termed saturation

and has been demonstrated on gold nanorods in the literature using high-intensity pulsed lasers [46-47].

Consider the consequence of placing gold nanorods in the gap between coupled cavities. Assume that these cavities are co-resonant and exhibiting an induced transparency feature with the nanorods present. If we then bring in an external beam from a high intensity pump laser, which has been detuned from the probe laser enough that it has no frequency overlap with the co-resonant WGMs, this pump laser will saturate the plasmonic resonance, thus switching off the coupling between cavities at the probe frequency. In this configuration we have created an optical delay by trapping the light at the probe frequency in the now isolated outer cavity. When the pump beam is extinguished the cavities once again couple strongly and the delayed light will be released to propagate through the system.

Now envision two evanescently coupled linear waveguides with a finite region of plasmonic coupling enhancement. Assume all of the power is initially in the first guide and that the separation is such that coupling only occurs in the nanorod region. Further assume that the strength of enhanced coupling is such that at the output port the power is equally distributed between the guides. Then if one were to send a counterpropagating strong pump pulse down the second guide we would switch off the power in that guide on a time scale of the order of the plasmonic lifetime. As the lifetime of a resonance is inversely related to the spectral width we could expect switching times of the order of the plasmonic lifetime, about 15 fs, which would provide power modulation rates limited only by pulse repetition frequencies [47].

One can endlessly perform these *gedanken* experiments but the question remains: can all-optical control of evanescent coupling be achieved?

We do not have access to a pulsed laser and as such we must attempt control with continuous sources. If one is to implement a practical device there are a number of applications where continuous sources would be strictly required anyway. We can choose one of two configurations for optical control of the plasmonic coupling enhancement. In the first method, a counterpropagating mode of a nanorod-coated microsphere is excited with a second tapered fiber. In the second, a free-space laser beam is tightly focused onto the coupling region between a fiber and nanorod-coated microsphere.

When a counterpropagating pump mode is used for saturation much care must be taken to avoid strong coupling between the counterpropagating mode and the probe fiber even though the propagating power is in the opposite direction to our detectors. This is because the backscattered radiation from the much more powerful pump mode can obscure the change in probe power measured in the forward detector array. Shown below in Fig. 66 and Fig. 67 are the results of the aforementioned experiment for undercoupled and overcoupled probe modes, respectively.

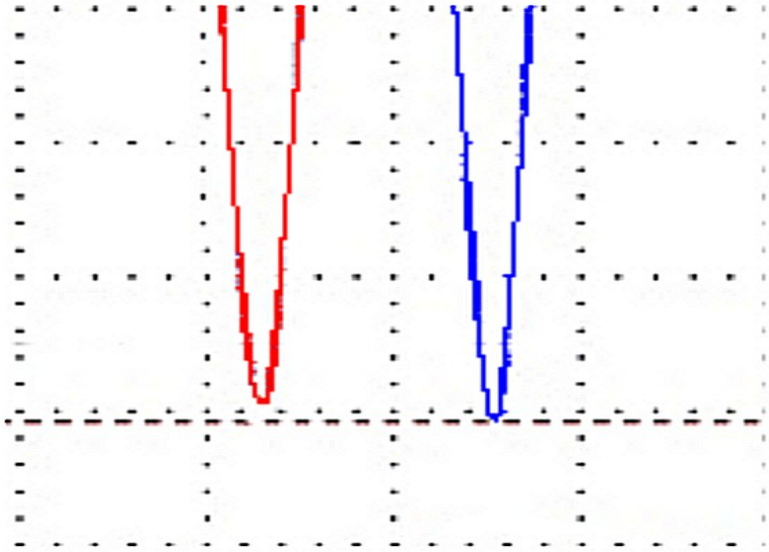

Figure 66. Optical control of coupling in an undercoupled probe mode. The oscilloscope traces have been overlapped for clarity. The blue trace is the natural mode while the red is the controlled mode. Notice the mode's dip depth reduces, i.e., the mode becomes more undercoupled, when the plasmonic enhancement is reduced optically. The approximate change in m is of order 1%.

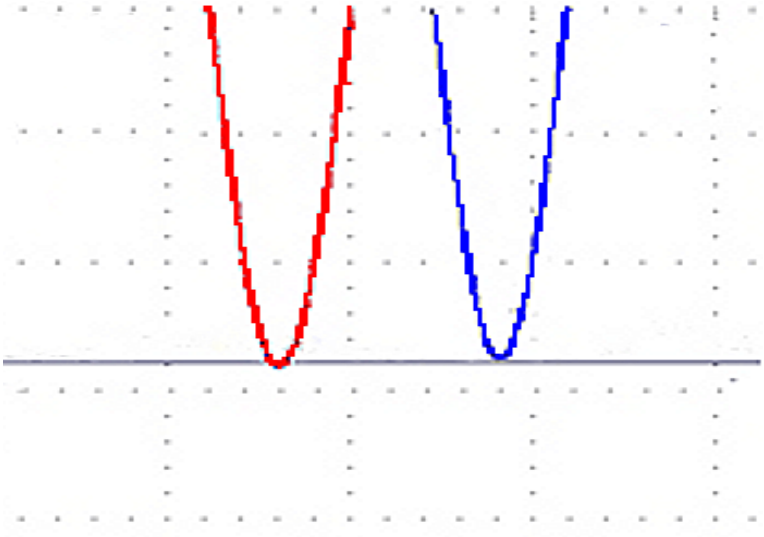

Figure 67. Optical control of coupling in an overcoupled probe mode. The oscilloscope traces have been overlapped for clarity. The blue trace is the natural mode while the red is the controlled mode. Notice the mode's dip depth increases, i.e., the mode becomes less overcoupled, when the plasmonic enhancement is reduced optically. The approximate change in m is of order 1%.

Using counterpropagating modes we were able to demonstrate an average change in observed dip depth of about 1%. The amount of control was severely impacted by heating due to absorption of the powerful pump mode which is approximately one-thousand times more powerful than the probe. We achieved circulating intensities of around 300 kW/cm^2 in the pump mode at a wavelength of 1650 nm for the probe intensity of 1 W/cm^2 at a wavelength of 1550 nm.

Free space beams were used in two configurations, each focused to a spot size on the order of the coupling region coupling (~5 μm). First a free-space 1650-nm beam is focused onto the coupling region at an intensity of 500 kW/cm^2. Changes of less than a percent, under our signal to noise ratio, were observed but were inconclusive. Next we attempted to use the transverse resonance to saturate the plasmonic resonance. A 532-nm DPSS laser at a power of roughly 3 W was focused to an intensity of 100 MW/cm^2 on the interaction region. Very large changes were observed in dip depth (~10%), but these could not be rigorously isolated from thermal effects and thus remain inconclusive.

While the experimentally measured changes in coupling where not as large as we had hoped, presumably due to our continuous-wave sources, we can with reasonable certainty conclude that optical control of evanescent coupling has been demonstrated. Far larger levels of control are anticipated with pulsed sources which would provide much higher intensities and largely mitigate the heating problems encountered above.

Chemical sensing enhancement:

With the evanescent field enhanced, we can reasonably expect our system, when used as a traveling wave evanescent sensor, to increase in sensitivity [8]. To determine the sensitivity increase both the tapered fiber and microsphere are immersed in deionized water. The

polyelectrolyte coated cavity without rods present is exposed to an absorbing analyte in increasing concentrations while the mode's quality factor and dip depth are monitored. The cavity is then removed from the bath, rinsed, and nanorods are grown on the surface as in [48].

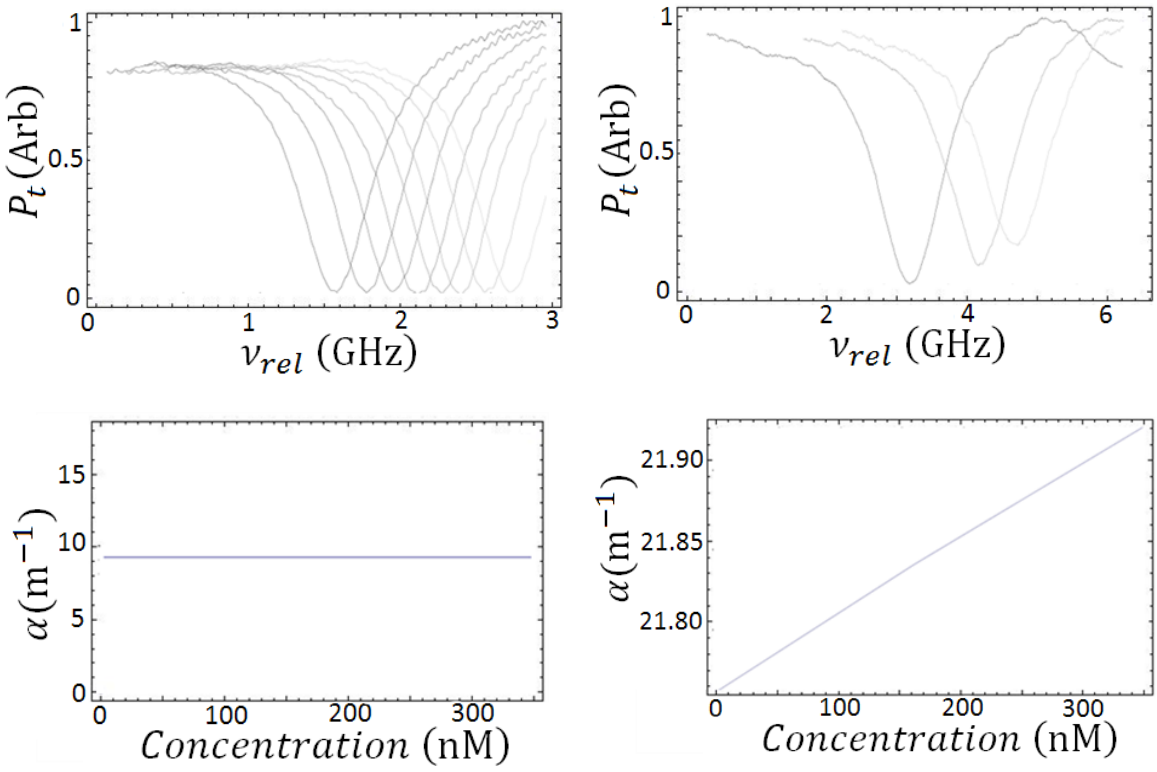

Figure 68. Sensitivity to analyte absorption before (left) and after (right) the addition of nanorods to a polyelectrolyte coated microsphere.

The experiment is then repeated on a mode with similar initial conditions in both quality factor and dip depth. The particular analyte that was chosen was SDA-2072, because of its strong absorption at 1.5 µm; however it is not water soluble. As SDA is soluble in methanol and methanol is soluble in water the SDA was dissolved to its solubility limit in methanol and this solution was used as our analyte. In Fig. 68 above the top images are the observed dips while

the lower images are the calculated sensitivities for both native (left) and enhanced (right) samples respectively. The concentration reported is the effective concentration of SDA in the deionized water bath.

Over the range of measured analyte concentrations the cavity without nanorods shows no sensitivity to analyte concentration while over the same range the nanorod-coated cavity shows a sensitivity of $5 \times 10^{-4}\ \mathrm{m}^{-1}/\mathrm{nM}$ in measured intrinsic loss. These experiments are performed over a number of modes both before and after coating to limit the impact of mode selection.

Although addition of nanorods dramatically increases the sensitivity over that of the polyelectrolyte coated resonator, this increased sensitivity is still markedly less than that of a bare resonator. This may, however, simply be because dye molecules are adsorbed on bare silica but not the polyelectrolyte coated silica. Further investigation is warranted.

Surface Enhanced Raman Scattering:

It is well known that when a field is incident on a solution Raman scattering causes new emission lines which are either blue shifted or red shifted from the pump wavelength. These are respectively termed anti-Stokes and Stokes lines and are due to inelastic interactions with the molecule. Raman scattering is distinct from typical Rayleigh scattering in that no frequency shift is associated with elastic Rayleigh scattering. However, it is also known that these Raman shifts scale in amplitude as the inverse of the wavelength. Previous experiments performed in-house have not observed Raman emission from the microsphere because intensities in the evanescent fields were not high enough to produce signals above the noise level of the equipment. With the level of near-field enhancement we have at the nanorod-solution interface we could potentially increase the emission strength to an observable level. Raman

signals produced in this manner are termed surface-enhanced Raman and can be quite large for confined nanostructures compared to typical Raman scattering [49].

In this series of experiments, all elements outside of the Raman active material were first confirmed to produce no measurable signal within our equipment's signal to noise ratio. This includes any fiber-coupled equipment in the experimental setup as well as both the fused silica itself and the methyl groups used to functionalize the microsphere's surface. With a given microsphere verified to produce no additional frequency components the surface is coated with nanorods and a particular Raman material is tested. We had initially hoped that Raman scattering from the surface would be captured in a microsphere mode leading to additional cavity enhancement and a strong observable signal on the pump fiber. Unfortunately, this proved to not be the case and signals measured in this manner could not be differentiated with certainty from the equipment noise floor. To overcome this limitation, an end-polished untapered fiber was used to capture the power scattered perpendicular to the propagation direction just outside the optical resonance plane of the microsphere. This scattered signal was then analyzed for additional frequency components.

The first material tested was the surfactant capping layer CTAB surrounding the nanorods. CTAB has been shown to be weakly Raman active with a broad low-energy Stokes peak shifted by between $160\ \mathrm{cm}^{-1}$ and $200\ \mathrm{cm}^{-1}$. The noise floor of the spectrum analyzer was tested when pumped directly by the pump fiber in the anticipated Raman region, shown in Fig. 69 below. With the region confirmed to be structureless the microsphere was brought into contact with the pump fiber and sampled, with the results shown in Fig. 70 below.

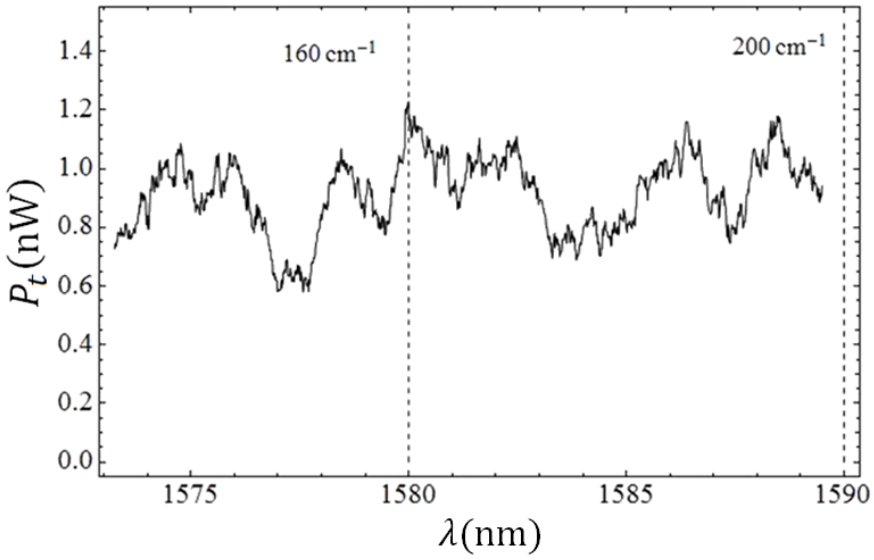

Figure 69. Signal noise floor for the anticipated Raman region for CTAB pumped at $\lambda = 1541.1\,nm$. *CTAB has a low-energy broad Raman shift in the region* $160\,cm^{-1}$ *to* $200\,cm^{-1}$ *as shown by the dashed lines above. Notice that there is no structure to the noise in this region.*

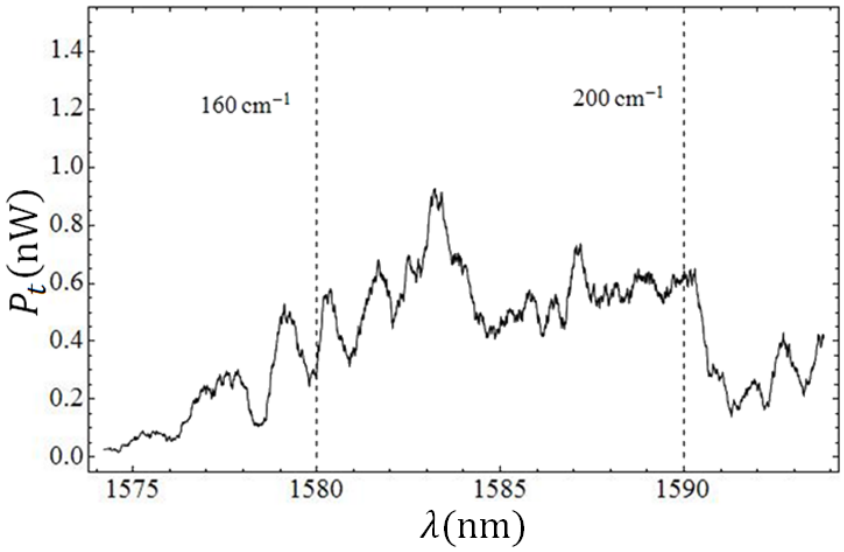

Figure 70. Side scattered Raman signal for CTAB pumped at pumped at $\lambda = 1541.1\,nm$. *CTAB has a low-energy broad Raman shift in the region* $160\,cm^{-1}$ *to* $200\,cm^{-1}$ *as shown by the dashed lines above. Notice that the scattered power now has structure in the Raman region.*

These results were encouraging so pure ethanol was the next material to be tested. The ethanol was applied as a droplet to the fiber-microsphere system such that the entire surface was sufficiently wetted. Once again a noise floor reference was established prior to sampling for Raman scattering; see Fig. 71 below. The microsphere was brought into contact with the fiber and the side scattered light was sampled as seen in Fig. 72 below. With the surface wetted with ethanol we can clearly observe a new frequency component which corresponds to the first strong Stokes line of ethanol located at $884\ \mathrm{cm}^{-1}$.

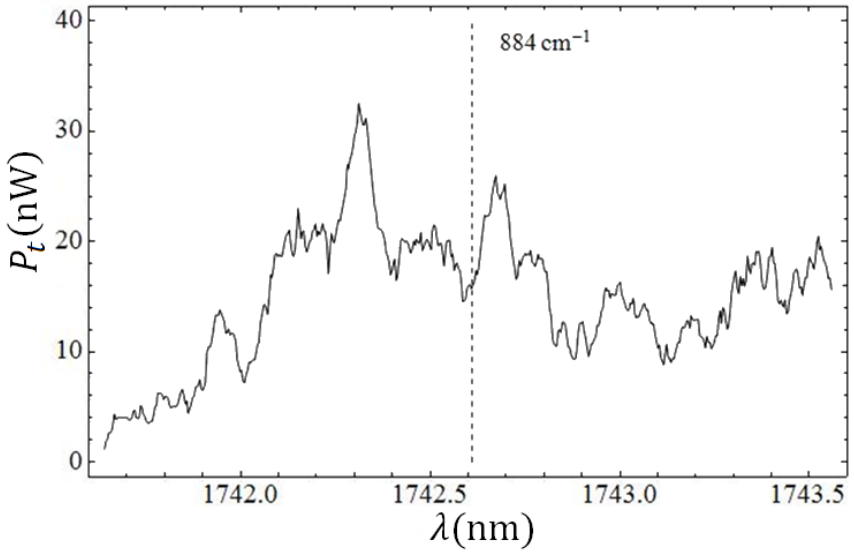

Figure 71. Noise floor for the spectrum analyzer in the region we expect to observe Raman scattering in ethanol when pumped at $\lambda = 1510.0\ nm$. *The first strong Raman line in ethanol is found at* $884\ cm^{-1}$.

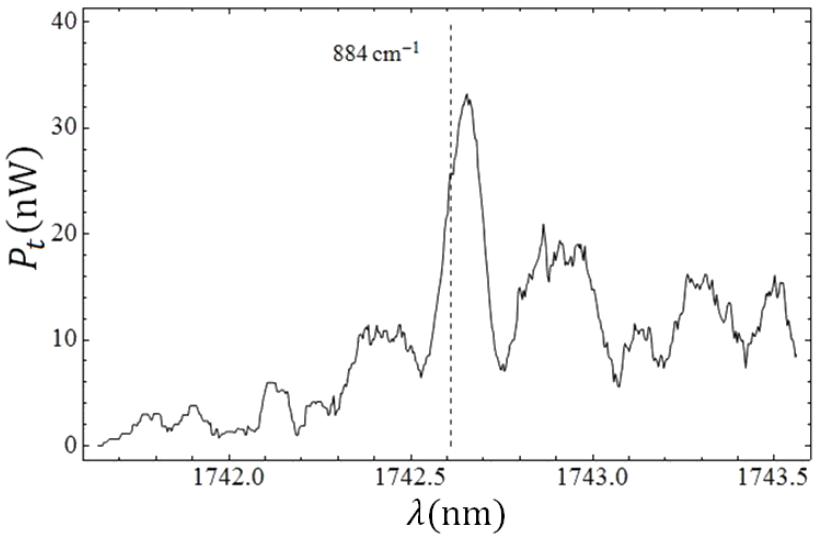

Figure 72. Side scattered power from the microsphere showing Raman scattering in ethanol when pumped at $\lambda = 1510.0\ nm$. *The first strong Raman line in ethanol is found at* $884\ cm^{-1}$.

In ethanol the agreement with the anticipated Raman shift and the measured shift were quite good; see Fig. 72. The small disagreement is likely due to uncertainty in the pump wavelength. Unfortunately, during these experiments we also discovered that the ethanol appeared to destroy the surface chemistry that Coulombically held the nanorods on the sphere surface. This was apparent in a rapid decrease in both the cavity's quality factor and the power transmitted through the tapered fiber as the surface ethanol dried. The cavity Q's dropped to the point where modes were no longer observable, and the transmitted power along the fiber fell by five orders of magnitude due to contamination floated in from the sphere. Additional experiments confirmed that this was not a unique phenomenon as additional samples exhibited the same behavior in ethanol. Moreover, when these experiments were repeated with strong organic solvents with large Raman scattering intensities, such as carbon tetrachloride, the effect was compounded and the experiment was destroyed in a time scale shorter than the necessary scan time to produce a side scattered power spectrum.

While the scattered Raman lines observed in this course of experiments are weak, we can with reasonable certainty confirm that we have observed these effects. Additional work will still be needed to understand the surface chemistry of adhering the nanorods as we must learn to protect the adhesion from aggressive solvents before stronger Raman scattering liquids can be used to fully establish the effect.

Discussion

We have demonstrated that both single crystalline nanorods and multi-crystalline nanowires can be produced and used to enhance the external, evanescent field of the cavity. Further methodology has been developed to adhere these structures to the surface in a semi-permanent manner usable for experiments. The effects associated with the gold nanostructures have been demonstrated to be plasmonic resonant in nature. We have applied these fundamental effects to show optical control of coupling between waveguides and enhanced sensitivity in evanescent sensing for both absorption and Raman emission. We expect further sensitivity in both of these fields as control over nanorod aspect ratio and size dispersion is improved in future work.

Chapter 5 Cross Polarization Coupling

In an early series of experiments it was observed that when one pumped the cavity on resonance with linear polarization aligned to one of the cavity's polarizations, peaks of orthogonally polarized light were observed in the throughput. These effects are termed cross polarization coupling (CPC) and must be explored rigorously if we are to infer information from the ring-cavity analysis mechanism. Unlike the experiments reported on previously, we have no *a priori* knowledge of where these effects are being generated. We must then explore every potential cause of the effect until a reasonable solution is found.

These polarization coupling effects do not appear to cause any type of fundamental broadening of the resonances because modes with and without CPC effects have been tested to have similar spectral widths. However, typical measurements on the dip depth of the system are taken without polarization analysis. What effect would CPC have on this? In the polarization parallel to the pump, the cavity output field is out of phase with the pump field, destructively interfering, which in turn produces a dip in the throughput when there is intrinsic (scattering) loss in addition to the coupling loss. In the perpendicular component there is no pump field and thus the CPC output, which is also out of phase, is observed as a peak. In the event that the photodiode used to measure the power at the output of the system has no polarization analysis we can expect direct power addition of the two orthogonal polarization components. Clearly if a power dip is added to a power peak the apparent dip depth can be greatly reduced. In the extreme this has been observed to produce "ghost modes," which are modes with equal dip

depths and CPC peaks. In these rare cases the sum of the two polarization components erases the observable dip in through power if polarization analysis is not performed.

Figure 73 is a direct observation of the CPC effect and its consequences. The cavity is fiber coupled and pumped with approximately linearly polarized light in the cavity's TE (transverse electric) polarization basis. Simultaneous measurements are then made on the system throughput using separate detectors preceded by TE and TM (transverse magnetic) polarization analyzers, as well as another detector with no polarization analysis. The TE and TM output are added, in real time, and compared to the unpolarized detector response. The concurrence of the unpolarized intensity detector response with the direct addition of the orthogonal polarizations suggests strongly that if the experimental parameters were to be determined without an understanding of the polarization response, the inferred parameters could be in grievous error.

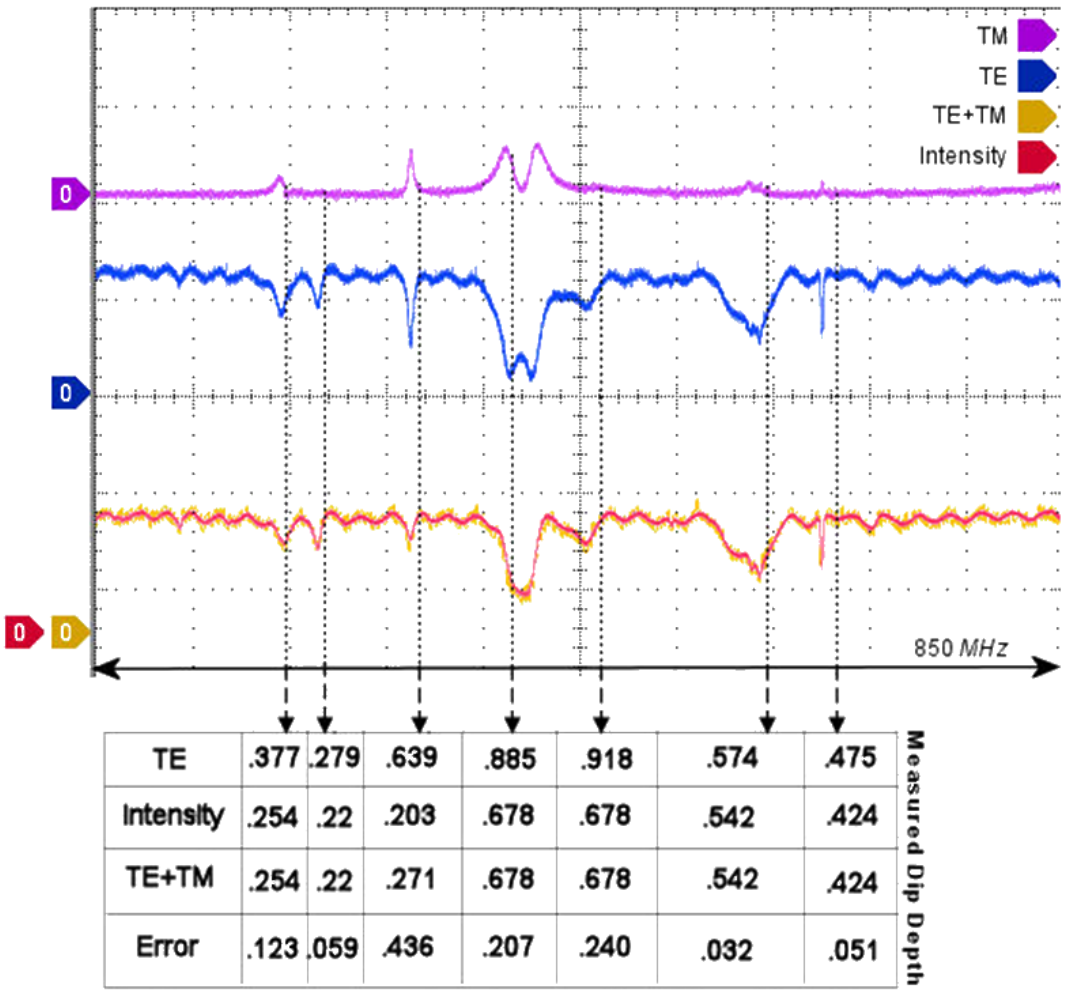

TE	.377	.279	.639	.885	.918	.574	.475
Intensity	.254	.22	.203	.678	.678	.542	.424
TE+TM	.254	.22	.271	.678	.678	.542	.424
Error	.123	.059	.436	.207	.240	.032	.051

Measured Dip Depth

Figure 73. The system is pumped with a pure TE cavity polarization. The resulting TE and TM fiber outputs are summed (yellow trace) and compared to an unpolarized intensity trace (red). The table lists several examples of the respective dip depths.

Modeling of cross polarization coupling:

We begin to attempt to understand these effects by extending previous successful theoretical work. Coupled mode theory, as it was previously derived in pure vector form, can be readily evaluated to predict any direct field interaction polarization effects.

Coupled mode theory:

There are two field effects which will directly cause cross polarization coupling, or CPC, effects. One is the difference in polarization basis, i.e. the curvature in the sphere polarization. This effect is almost entirely mitigated in our system due the very small field overlap region as seen in Fig. 74 below. The divergence angle between the surface and a linear approximation is on the order of 1^{o} at absolute maximum which is then a difference in the dot product of the fields from pure linear polarization of approximately 0.01%.

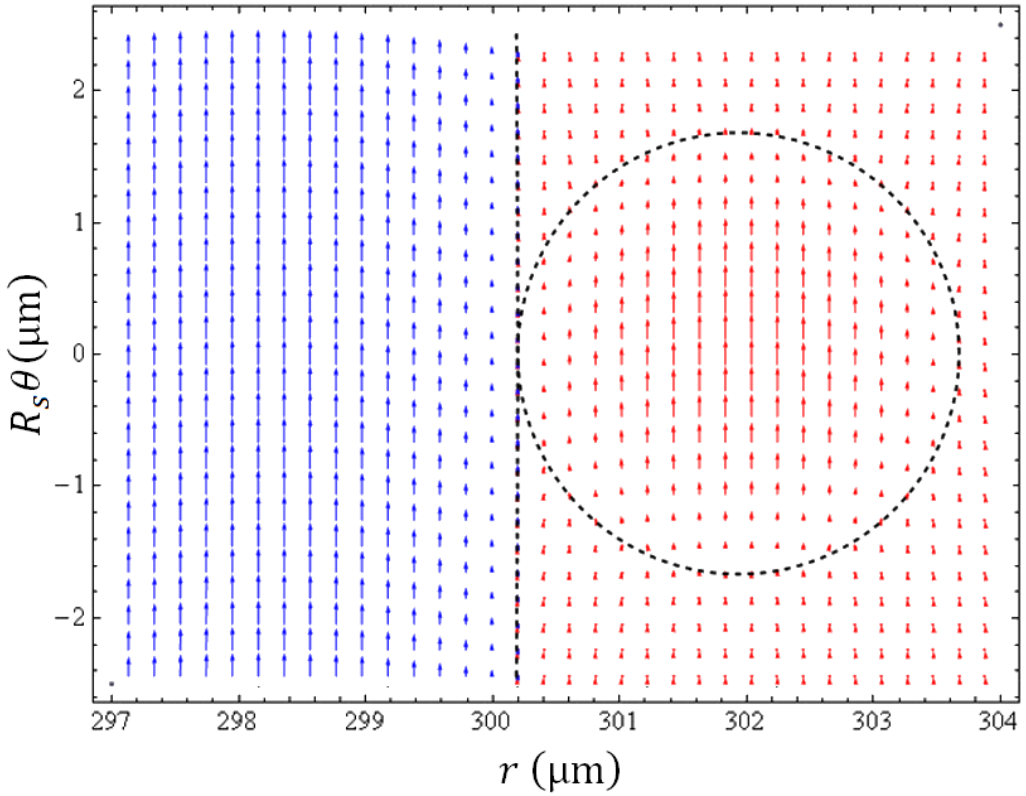

Figure 74. The interaction region in fiber sphere coupling. Notice that the fiber field shows a much large deviation from pure y-polarization than the cavity field over the region of interest.

The second effect is much stronger and that is the non-uniformity of the fiber field at the dielectric fiber-air interface which can be as much as 30^{o} divergent from linear polarization, as seen in Fig. 75 below. While the non-uniformity is antisymmetric about the *y* axis and thus the effect will cancel for perfect alignment, when the alignment is not ideal significant power can transfer between the fiber and the orthogonal sphere mode.

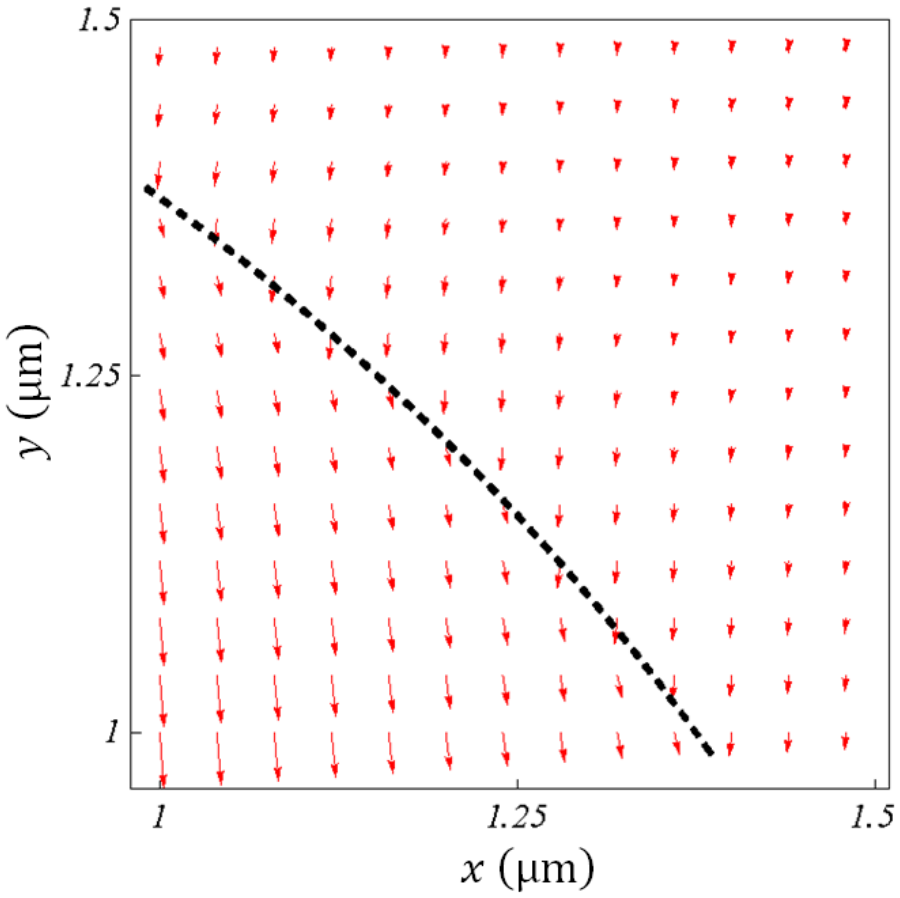

Figure 75. Vector field plot of the electric field of a fundamental fiber mode at an angle of 45° *above the x axis. These non-uniformities are antisymmetric when mirrored about either the x or y axis.*

The overlap integrals are calculated for a number of different modal configurations of the microsphere over varying angular misalignments and these results are plotted vs. fiber diameter to determine peak expected coupling coefficients. Peak CPC field coupling coefficients are

found to be on the order of one-thousand times smaller than the coefficient for direct coupling. These levels of input/output CPC are far too low to produce the amount of experimentally measured orthogonal power. We must also note that the input/output CPC coefficients found from the above methodology can be as much as a factor of two different. This is an artifact of using the unperturbed waveguide solutions as systemic solutions. Without the additional modifications to the field induced by the adjacent dielectric structure the fields are not truly solutions to Maxwell's equations for the system for either polarization. However, for the much larger main polarization component this dielectric effect is a small correction, while for the very small minor polarization component the correction can result in a significant relative increase in field strength. Proper solutions for the system can be expected to balance the input/output CPC which would be expected to be near the mean of the independent solutions. For this reason the larger of the two calculated coefficients is taken as an upper limit on the strength of input/output CPC as seen below (Fig. 76).

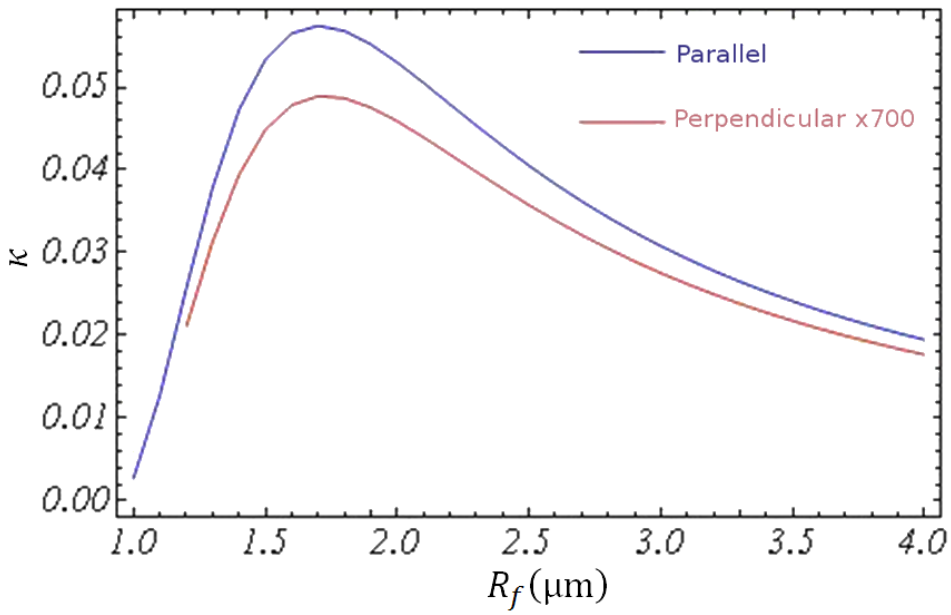

Figure 76. The coupling coefficient shown for both parallel and orthogonal polarizations in the same system.

Potential Causes of Polarization Coupling Behavior:

The first direct observation of CPC effects was during an unrelated thermal experiment. One of the requirements of this particular experiment was to determine the coupling regime of the system via phase sensitive-cavity ringdown experiments. A fiber-coupled Mach-Zehnder high speed modulator was employed to induce a transient cavity response. However, initial results were inconclusive, in contrast to earlier results obtained using a free space acousto-optic modulator. It was suspected (correctly, as it turned out) that an incident polarization mismatch to the modulator's polarization-preserving input fiber was allowing some of the orthogonal polarization to leak through unmodulated. To test this suspicion, a thin-film polarization analyzer (20:1 extinction ratio) was placed at the fiber output of the total system and the output was observed for both the pump (modulator) polarization and the orthogonal polarization. The placement of the analyzer at the output of the total system was done just for convenience, as it is time consuming to remove the modulator and test it independently. This turned out to be

quite serendipitous, as an intriguing effect was seen when the scanning diode laser was resonant with the in-place microsphere; after the modulator input polarization was corrected, power peaks were observed in the polarization orthogonal to the pump, as seen in Fig. 77. Orthogonally polarized light leaking through the modulator had produced dips, not peaks.

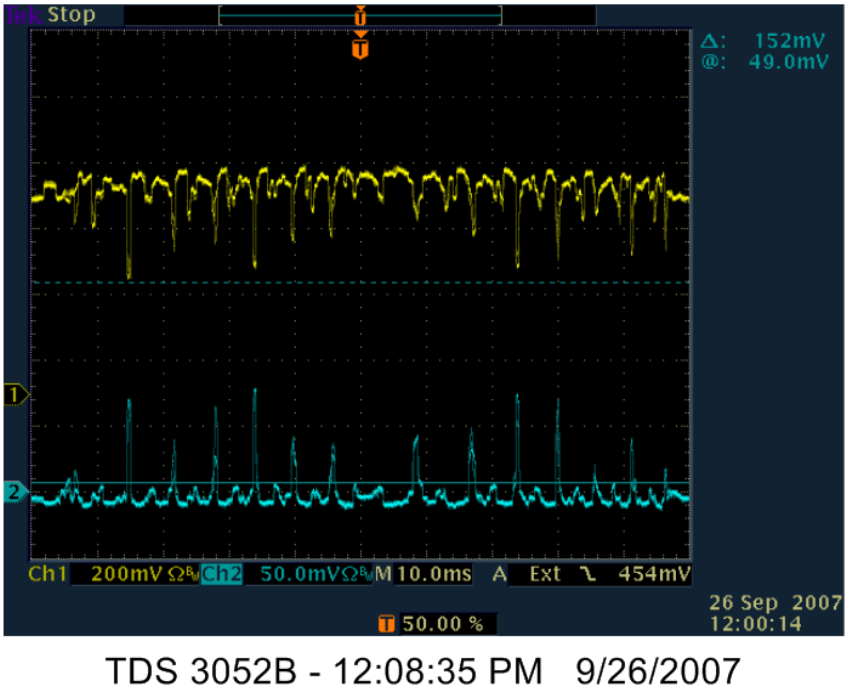

Figure 77. An oscilloscope trace showing modes of the pump polarization (yellow trace) and the unpumped orthogonal polarization (blue trace). Note that the blue trace is scaled up by a factor of four with respect to the yellow trace.

Polarization Analyzer:

After correction of the modulator the initial culprit for the orthogonal transmitted power was the thin-film analyzer. While a failure of this device could lead to transmitted orthogonal power, it could not lead to the creation of power peaks from a signal that contained only power dips. However, the analyzer is the first link in the discovery process and must therefore be addressed before more complex experiments are conducted. To rule out any

possible effect of the low isolation ratio of the thin film analyzer, a 400:1 polarizing beam splitter was used in its place. Only the transmitted signal was monitored at this juncture. No change was seen in the strength of the effect and more importantly the strength of the effect appeared to vary from one sphere resonance to the next.

Alignment of Polarization Basis:

An apparatus was constructed that allowed for both the incident and orthogonal polarizations of the throughput to be monitored simultaneously. A NIR fiber-coupled collimator was aligned to the axis of the polarizing beam splitter. Power detectors were then aligned to the transmitted and reflected signals and the whole system was calibrated for equal power distribution and connected to the oscilloscope. This then allows one to monitor the output power in both the pump and orthogonal polarizations simultaneously.

As discussed in the preceding section the fundamental polarization basis of the fiber field is Cartesian while that of the sphere is tangent to the spherical surface. A misalignment between the analyzer and sphere basis could produce peaks which looked to be CPC [50]. If we assume the sphere has perfect symmetry (this is not strictly true) then the placement of the fiber anywhere along the surface causes nothing more than a rotation of the respective inherent polarization basis from the lab basis. For example consider placement of the pump fiber on the sphere at $45°$ latitude. The sphere's TE polarization is tangent to the surface which is now at a $45°$ angle to the lab's basis. Thus what appears to be linearly polarized pump light at $0°$ in the lab basis could be at an arbitrary angle with respect to the basis of the sphere. What appears to be CPC could in fact be evidence of pumping modes of both polarizations. Ideally one could directly measure the position of the fiber on the sphere's surface and adjust its placement so the analyzer is in the sphere's basis. However, this is experimentally quite challenging as the

characteristic dimensions of the system are on the order of 700 μm and 2 μm for the resonator and pump fiber diameters, respectively. This difficulty is further enhanced by the fact that the material which comprises these structures is transparent. It is therefore difficult to visually determine the sphere's basis with high certainty. To counter this, the aforementioned analyzer array was rebuilt to allow for one degree of rotational freedom; see Fig. 78. With the sphere in contact one can use the lack of degeneracy over a finite frequency region between the two polarization spectra of the sphere to assure proper basis alignment with reasonable certainty. This is done by simply making successive adjustments to the input polarization and the orientation of the polarization detector array until it is clear that WGMs of only one polarization are being pumped.

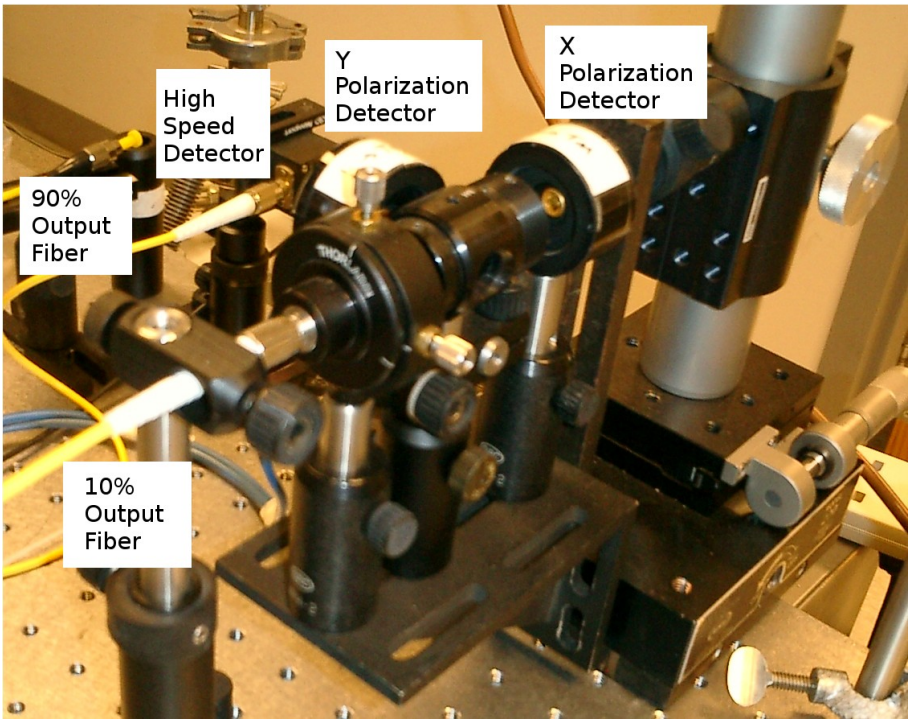

Figure 78. Polarization detector array. The axis of rotation for the array is along the input fiber axis. Also pictured is the transient high speed detector. The x polarization axis is parallel to the detector base while the y axis is perpendicular.

To further verify that the basis for the detector array is aligned properly to the sphere modes, a second fiber, or drop fiber, is brought into contact with the sphere diametrically opposed to the pump fiber. The output from this fiber will be pure transmission, with no interference between the cavity output and the remaining pump field; this output coupled into a second polarization-dependent detector array allows one to probe the sphere modes' polarizations unambiguously in the lab's Cartesian basis. We have only to calibrate the respective angles between the throughput and drop signal detector arrays in order to align the detector basis to the sphere basis.

Fiber-Sphere Geometry:

To verify that the alignment between the pump fiber and the microsphere is not leading to polarization effects a sphere was created on an un-tapered fiber, rather than at the end of the fiber. An example is shown in Fig. 79. This configuration allows for the sphere to be mounted on a rotational stage with its axis of rotation being in the sphere's equatorial plane. Thus experimentally we can check the confluence of angular misalignment and equatorial offset on the CPC strength. This configuration allows the sphere to be rotated a full 360 degrees while in contact with the pump fiber. CPC does not appear to depend strongly on any geometric alignment.

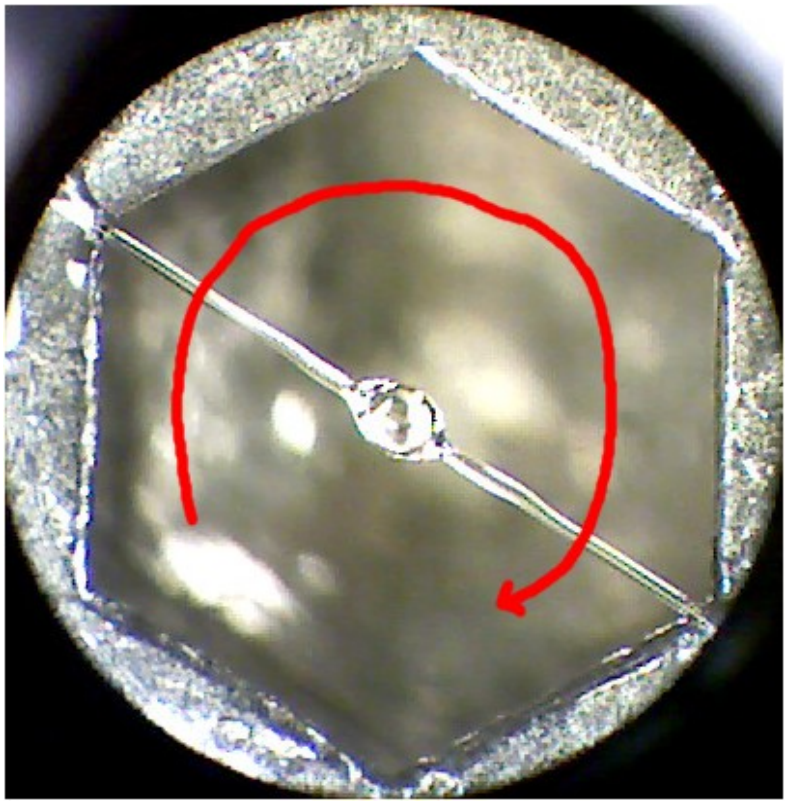

Figure 79. A prolate microsphere created on an optical fiber. The sphere is then mounted in the geometric center of a 3/16 inch bolt head.

Precessional Modes:

In a perfect sphere the electromagnetic resonances will follow a closed circular path creating a resonance plane parallel to the placement of the pump fiber. However, any slight ellipticity of the resonator causes the resonance to have a single preferential resonance plane, the equatorial plane. If we pump the elliptic cavity from a plane that is not equatorial, the resonance light path will not close. Rather, the optical orbital angular momentum vector will precess about the sphere's axis [51]. Thus light will simultaneously be coupled out into the pump fiber and into a drop fiber in the same plane of latitude, as indicated graphically in Fig. 80 where the pump and drop fibers are both at 45° latitude above the equatorial plane. The

polarization of the precessional modes experimentally maintains that of the pump polarization. That is, if the pump light is polarized tangent to the surface of the sphere at the contact point of the pump fiber the light which couples out along the drop fiber will also be polarized along the tangent of the sphere, but now at the location of the contact point of the drop fiber. This can be a little misleading as the measured polarization angle of the pump fiber and drop fiber powers will not necessarily be the same (in Fig. 80 the drop fiber field will be rotated 90° with respect to the pump fiber polarization).

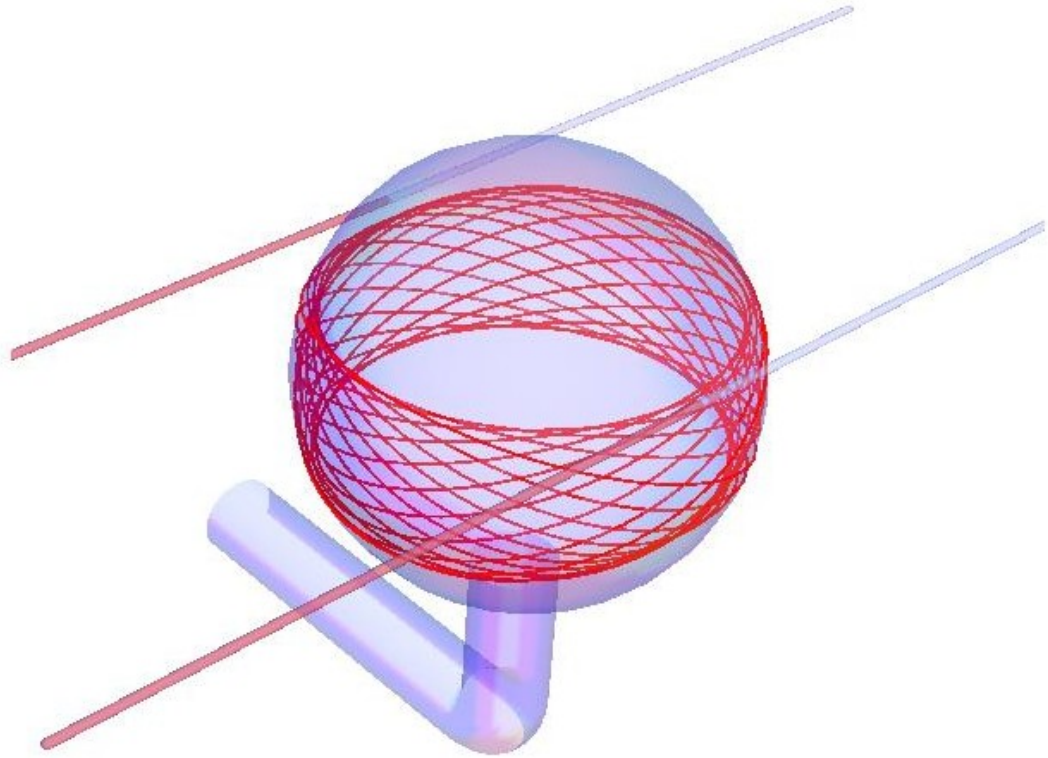

Figure 80. Optical path of a precessional mode of the cavity (cross-hatched structure). The spheroidal symmetry axis is vertical and the angular momentum vector of the mode precesses about this axis.

Fused Silica Birefringence in the Fiber:

Fused silica is well known to exhibit strain-induced birefringence [52]. Experimentally this means that any fiber or fiber component which is bent, or strained, will turn the linearly injected polarization into an arbitrary elliptical polarization. Because the state of polarization ellipticity is rather arbitrary, correcting the polarization back to linear can be difficult. In order to correct the polarization we take advantage of the strain-induced birefringence and employ a three stage compression polarization controller. This device compresses the fiber in three locations, acting effectively as three fractional waveplates, allowing the creation of any arbitrary polarization state. While practical, these devices can not completely linearize the incident field; this in turn could lead to apparent CPC effects. To both test the relative polarization alignment of the other system components and to test the effect of a small nonlinearity in the polarization output of the system the polarization controller was removed and replaced with a straight piece of optical fiber. The system now had no bends in any fiber component and should be polarization-maintaining. The polarization was then controlled by the addition of a zeroth-order half waveplate in the free space beam before injection into the fiber. The small degree of previous nonlinearity in the field had no apparent effect on the observed CPC and the remainder of the system was confirmed to be in good polarization alignment with the lab frame and exhibited good polarization-preserving behavior.

Fused Silica Birefringence in the Taper:

The tapered fibers which are used for evanescent coupling are created by brushing a hydrogen-oxygen torch under a cleaned section of optical fiber while symmetrically pulling on both ends of the fiber. This procedure produces symmetric up and down tapers (bi-tapers) which are adiabatic, i.e., induce no power transfer to higher order fiber modes in the taper transition. This process is quite effective and repeatable, but as we are quite literally pulling on

the fiber we must confirm the polarization characteristics of the taper itself. In order to properly determine the polarization behavior of a single taper the bi-tapered system must be decoupled. This is done by first confirming that a bi-tapered fiber-sphere system is producing CPC. The tapered fiber is then intentionally broken in the center. The broken end of the down taper is then placed in a collimator and aligned to a polarization detector array, as shown in Fig. 81. A free-space beam with known polarization characteristics is then coupled into the fiber and the effect on the polarization state due to the taper is measured. The taper was found to have no apparent effect on the polarization state of light propagating through it.

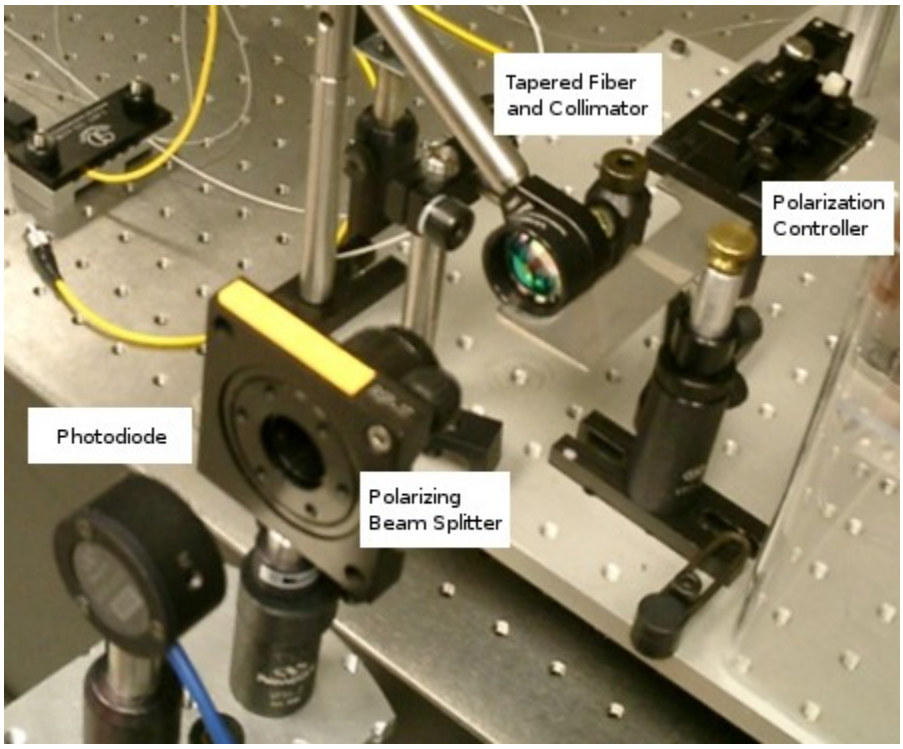

Figure 81. Testing of the tapered fiber for polarization effects.

Fused Silica Birefringence in the Sphere:

Fused silica exhibits strain-induced birefringence, as was mentioned previously. Perhaps the creation of the spheres, by melting the tip of a clean optical fiber in a hydrogen-oxygen torch, is causing some residual stress at the surface which induces a small degree of birefringence. Considering that a single photon on average will propagate within a high *Q* resonance ($\sim 10^8$) for tens of meters it would take only a small degree of birefringence to ultimately lead to a large degree of polarization rotation in the natural basis of the sphere modes. As a first step we could directly use a sphere as a ball lens: pass a polarized source through it and see if ellipticity is produced as seen in Fig. 82 below.

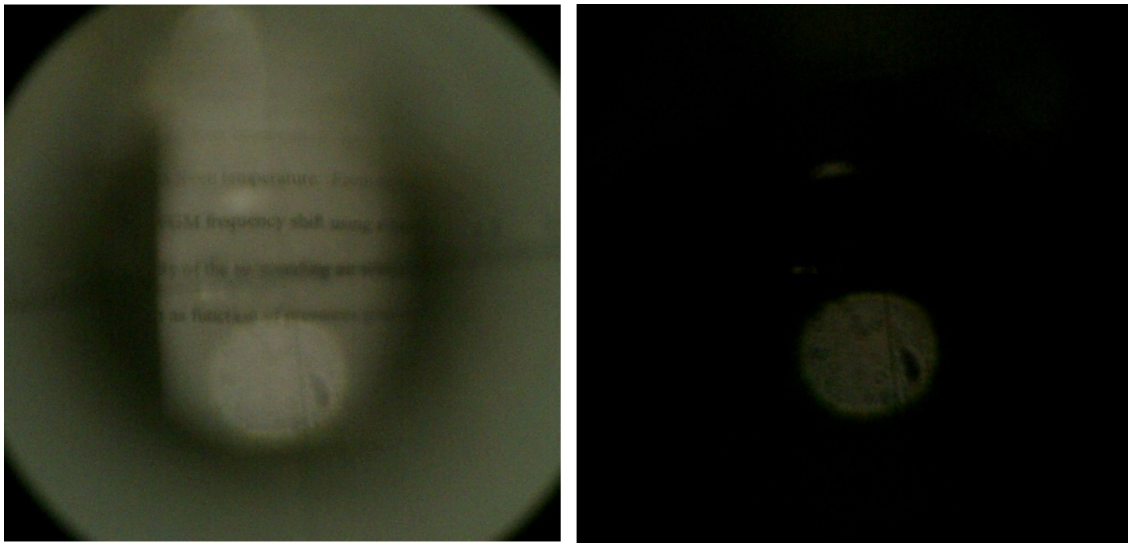

Figure 82. A source image (text) is focused through a microsphere placed between polarizers. The left image is parallel polarizers and the right is crossed polarizers. Notice there is no apparent transmission through the crossed polarizers. This result implies that the incident linear polarization is not affected strongly by single-pass propagation through the sphere.

Secondary testing relies on the mechanism which could leave residual strain on the sphere, namely surface annealing during thermalization. In this series of experiments multiple spheres

of the same basic geometry are annealed for progressively longer times. Each sphere is then tested for its level of CPC compared to typically prepared samples and the other annealed samples. After accounting for known experimental variables no statistical variance is found from typical samples.

Fused Silica Optical Nonlinearity:

One of the many striking features of the CPC effect is that its development appears to depend most strongly on two factors; the first is the cavity quality factor while the second is the modal dip depth. As either of these two measures is increased the CPC strength appears to also increase. From one perspective this is to be expected as both dip depth for a given intrinsic loss and quality factor are direct measures of circulating intracavity power and any measure of output power should scale likewise with these parameters. This observation does bring into question the possibility of a nonlinear optical process enhancing the effect. Optical self-focusing and self-modulation through the Kerr nonlinearity in fused silica is known to cause induced birefringence [53]. The intensity thresholds for these effects are on the order of $\mathrm{GW/cm^2}$ for weakly birefringent fibers [3, 54] such as common commercial fused-silica fibers. These intensity levels for continuous-wave devices such as the microcavity are quite high but at the lowest limit may be obtainable to within a few orders of magnitude with a very high-*Q* WGM. Given the level of resonant enhancement for these high-*Q* WGMs strong nonlinear responses are not strictly required to cause observable effects. To experimentally determine if a nonlinear process is driving the strength of CPC, the on-resonance power in the linear polarization and the on-resonance power in the orthogonal polarization are taken over an order of magnitude change in the incident power (160 μW to 7 μW or circulating Intensities of approximately 5

MW/cm^2 to 0.2 MW/cm^2). Each power is then plotted vs. incident power, as shown in Fig. 83. No nonlinear relationship is found.

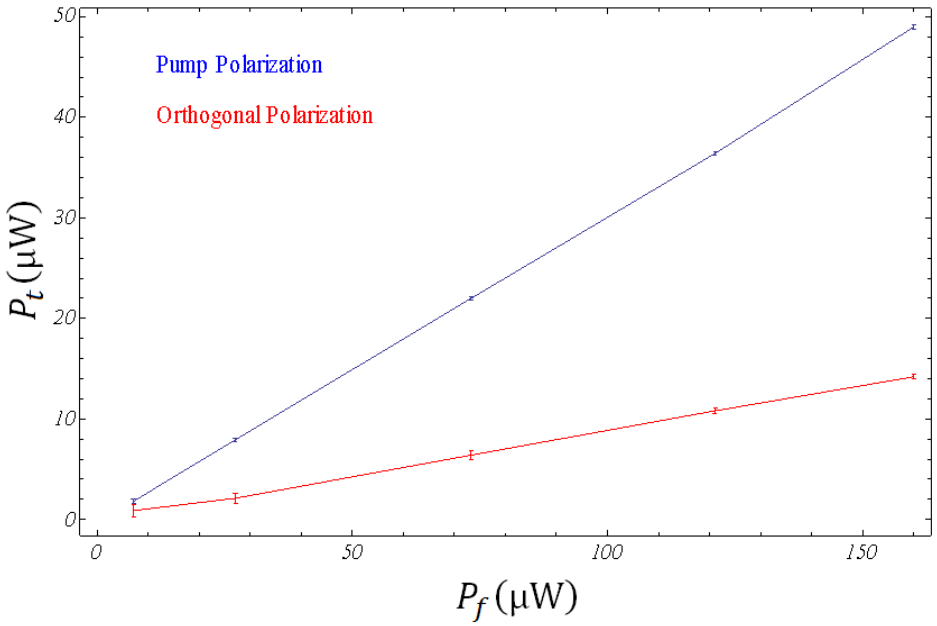

Figure 83. Pump polarization modal power on resonance and CPC peak power on resonance over an order of magnitude change in incident power. Notice that the CPC power is linear to within the limits of uncertainty of the experiment.

Scattering:

In this conversion process scattering events can lead to intermodal coupling between orthogonally polarized co-resonant modes. In effect, as the light is scattered its relative polarization can be rotated, and if there so happens to be another mode at that same frequency but with an orthogonal polarization, significant power transfer can occur in the cavity between polarizations. It could be possible then to observe power peaks in the through signal in the orthogonal polarization. The output peaks in the orthogonal polarization due to this effect will always be found at frequencies of the sphere's orthogonal modes. Unfortunately, these resonances may not be measurable when directly pumped by the fiber as we rely on the relative

coupling strength between fiber and sphere modes when attempting to measure a resonance and not all modes will couple with a strength in the range required for the dip to be measurable within a particular frequency region. Therefore, the absence of an observed directly pumped resonance does not rule out the possibility of intermodal polarization coupling. With the aforementioned detector array one can readily test experimentally the correlation between orthogonal sphere modes and orthogonal output peaks. The observed orthogonal peaks corresponded almost exclusively with the pump polarized modes of the sphere rather than those orthogonal modes which where observable. Unfortunately, because we can only observe a small fraction of the modes that are potentially available in the orthogonal polarization these correlations are inconclusive at this juncture.

Scattering events which could lead to intermodal coupling should also have a component which is directly backscattered [55]. Given that the eigenfrequencies of the modes are not dependent on propagation direction, significant power could then build in the counterpropagating direction. To test for counterpropagating power, a bi-directional 50/50 fiber-coupled splitter was reverse installed before the fiber-sphere interaction region. In this manner half of any counterpropagating power can be picked off and sent to a detector without interfering with the injection power. This signal is then monitored simultaneously along with the forward direction polarization-dependent detection while the system is frequency scanned (one must correlate the CPC to reverse transmission peaks if present). When the experiment was underway no correlated counterpropagating power was observed due to CPC, but another effect was seen.

The fiber, because the end faces are approximately parallel, acts as a secondary cavity with linear Fabry-Pérot type resonances. While these resonances are broad and weak in comparison with those of the sphere they do lead to pumping of counterpropagating frequency-degenerate

modes while scanning (as indicated by sharp dips in the Fabry-Pérot resonances). This effect must be eliminated to rule this out as a potential culprit for CPC. One can intentionally deface the output fiber face destroying the *Q* of the linear cavity modes, but this leads to high and unpredictable output beam divergence, a problem for the calibrated detector array which relies on proper collimation. The most direct way to address this issue is then to install a fiber coupled optical isolator after the fiber-sphere interaction region to suppress reflections from the fiber's end face. However, at every location within the system where a butt connection (black vertical lines in the experimental setup diagram Fig. 2) is employed to connect fiber components, a separate coupled linear cavity is created and the isolator will not suppress these modes. To address this, gel with the same index of refraction as fused silica and virtually no absorption in the NIR is placed between each fiber splice in the system, thus converting a system of many coupled resonators into one large resonator whose modes the optical isolator can suppress. With this in place the experiment was conducted again and now no measurable power was obtained in the counterpropagating direction. However, since backscattering might be significantly weaker than polarization-changing scattering, this result is also inconclusive.

Modified Ring Cavity Model:

Based on the experiments above we have preliminarily concluded that the observed polarization effects are associated with a combination of an internal intermodal coupling mechanism (a fundamental source of these effects) and a misalignment of the relative polarization basis of the cavity and detector (a trivial source).

Let us ignore for the moment any internal coupling between orthogonal cavity modes, and envision pumping a critically coupled transverse electric (TE) cavity mode equatorially with a linear polarization, vertical in the lab basis. Without any form of polarization analysis on the

through signal we would observe a dip as the laser scanned through the resonance. Now we place a polarizer before our detector such that the polarizer is aligned vertically in the laboratory reference frame, i.e., aligned to the polarization basis of the cavity mode. In this configuration we again observe the same dip on resonance as we had previously. Let us then rotate both the incident linear polarization and the polarization analyzer by 45 degrees. As the field then encounters the resonance only the component of the incident polarization which is in the cavity mode's polarization basis (vertical) will experience a dip. Thus on resonance in our polarization analyzer we would again observe a dip, but the measured dip depth would be modified from our initial measurement. However, if we now rotate our analyzer to be orthogonal to the 45 degree incident linear polarization, we observe no through power off resonance, but we will observe power peaks on resonance. What has occurred is a functional rotation in the output polarization state due to power drop of one component of the incident polarization. We term this direct polarization conversion (DPC) and it is an artifact of the misalignment between the cavity and detector polarization bases.

Let us now assume that there are cavity resonances of both polarizations present with overlapping spectral widths with each equally pumped by an incident 45 degree polarization. Due to the polarization orthonormality of the two cavity modes we would expect to observe two distinct resonances depending on whether our analyzer was set vertically or horizontally as these represent the cavity's TE and TM polarizations respectively in our example. Without an internal coupling mechanism between the cavity modes that is exactly what one would expect. However, that is not what has been observed experimentally. Experimentally we observe interference between the orthogonally polarized cavity modes when the detector basis is properly aligned and the incident pump is linearly polarized at 45 degrees. Moreover, the structure of the observed interference changes when the relative phase between components

of the incident linear polarization is changed, e.g. for a 45-degree linearly polarized incident field the field vector can be pointed in either the first or third quadrants. This internal polarization coupling (IPC) is almost certainly associated with an internal scattering mechanism [56].

Both DPC and IPC can be readily understood from a simple internally coupled ring cavity model. In this model the pump field E_f, with polarization components E_{fk}, is incident on a partially transmitting front mirror with real reflection and imaginary transmission coefficients of r_k and it_k respectively for each polarization with the remaining cavity mirrors taken to be lossless. Each polarization is taken to have round trip power losses of $\alpha_k L$ and detuning from the cavity's natural frequencies of δ_k. Within this cavity a pointwise scattering plane is inserted just beyond the primary pump mirror, shown offset in Fig. 84 below. This plane is represented by the transmission (scattering) and reflection (no scattering) coefficients t_s and r_s, where the scattered light is assumed to rotate polarization by 90°. We must note that in a physical system the scattering will not occur just at the interface mirror where the orthogonal modes are pumped by the same source. Rather scattering will occur throughout the cavity. Because of this, our model, when fit to experimental data, will give an effective coefficient which represents the cumulative effects of both orthogonal scattering and phase mismatch. This effective coefficient is thereby a lower limit on the true orthogonal scattering amplitude within the cavity.

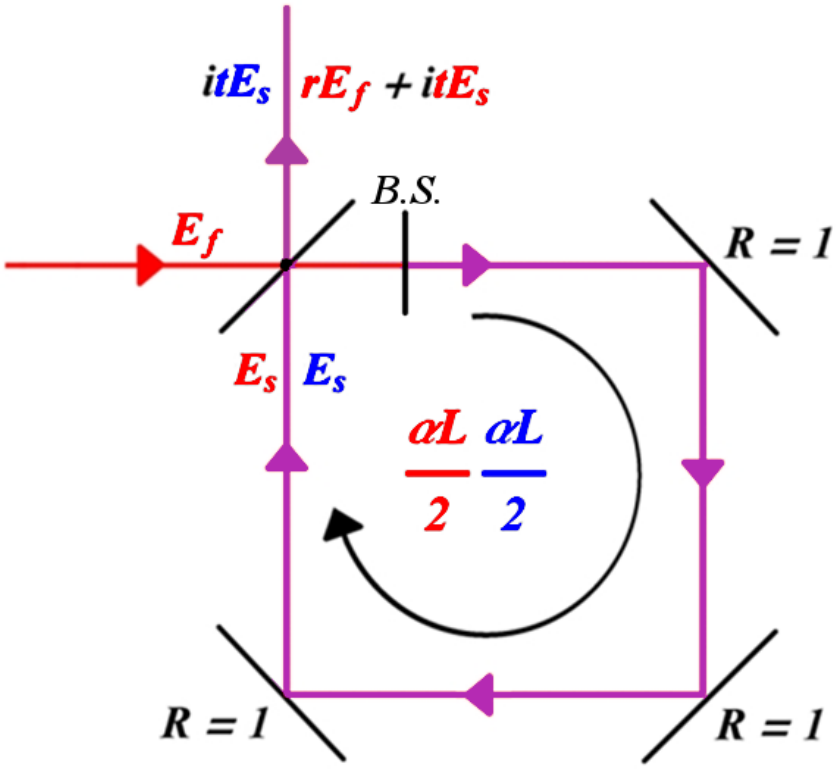

Figure 84. Modified ring cavity. Colored terms represent different polarizations.

The fields are constructed just as we have done previously over round trips as

$$E_{s1} = (it_1 r_s E_{f1} + r_2 t_s E_{s2}) e^{-\frac{\alpha_1 L}{2}} e^{i\delta_1} \sum_{n=0}^{\infty} \left(r_1 r_s e^{-\frac{\alpha_1 L}{2}} e^{i\delta_1} \right)^n, \tag{131}$$

$$E_{s2} = (it_2 r_s E_{f2} + r_1 t_s E_{s1}) e^{-\frac{\alpha_2 L}{2}} e^{i\delta_2} \sum_{n=0}^{\infty} \left(r_2 r_s e^{-\frac{\alpha_2 L}{2}} e^{i\delta_2} \right)^n,$$

where the indices (1,2) indicate the two polarizations of the cavity, and the pump field is allowed to have components in both of these polarization directions. Notice that the cavity fields are internally coupled by the scattering and must be separated before use:

$$E_{s1} = \frac{ir_s\left(E_{f2}t_s t_2 r_2 + E_{f1}t_1\left(e^{\frac{\alpha_2 \mathrm{L}}{2} - i\delta_2} - r_2 r_s\right)\right)}{\left(e^{\frac{\alpha_1 \mathrm{L}}{2} - i\delta_1} - r_1 r_s\right)\left(e^{\frac{\alpha_2 \mathrm{L}}{2} - i\delta_2} - r_2 r_s\right) - r_1 r_2 t_s^2}, \tag{132}$$

$$E_{s2} = \frac{ir_s\left(E_{f1}t_s t_1 r_1 + E_{f2}t_2\left(e^{\frac{\alpha_1 \mathrm{L}}{2} - i\delta_1} - r_1 r_s\right)\right)}{\left(e^{\frac{\alpha_1 \mathrm{L}}{2} - i\delta_1} - r_1 r_s\right)\left(e^{\frac{\alpha_2 \mathrm{L}}{2} - i\delta_2} - r_2 r_s\right) - r_1 r_2 t_s^2}.$$

We must then enforce power conservation in the cavity in an analogous manner to the basic single cavity. We turn off the losses, put the entire system on resonance and pump the cavity with only one linear polarization. For this the output fields become

$$E_{t1} = r_1 E_{f1} + it_1 E_{s1} = E_{f1}\left(r_1 - \frac{t_1^2 r_s(1 - r_2 r_s)}{(1 - r_1 r_s)(1 - r_2 r_s) - r_1 r_2 t_s^2}\right), \tag{133}$$

$$E_{t2} = it_2 E_{s2} = E_{f1}\left(-\frac{t_s r_s t_1 t_2 r_1}{(1 - r_1 r_s)(1 - r_2 r_s) - r_1 r_2 t_s^2}\right).$$

With these fields a power conservation equation can be constructed from the incident power and the sum of the respective square moduli (powers) as,

$$A \equiv T^2 r_s t_s r_s^* t_s^* + \left((T-2)r_s + r_s^2\sqrt{1-T} - \sqrt{1-T}(t_s^2 - 1)\right) \times \tag{134}$$

$$\left(r_s^*(T-2) + T(r_s^*)^2\sqrt{1-T} + \sqrt{1-T}(1-(T-1)(r_s^2)^* - (t_s^2)^*)\right),$$

$$B \equiv \left(2r_s\sqrt{1-T} + (T-1)r_s^2 + t_s^2 - 1\right) \times$$

$$\left(2r_s^*\sqrt{1-T} + (T-1)(r_s^2)^* + (t_s^2)^* - 1\right),$$

$$\frac{A}{B} = 1.$$

For simplicity, the fiber-sphere coupling coefficients have been set equal ($T_1 = T_2 \equiv T$). Using the express power conservation, $r_s^* r_s + t_s^* t_s = 1$ we find that this is true when either

$$(r_s = -r_s^*,\ t_s = t_s^*), \tag{135}$$

or

$$(t_s = -t_s^*,\ r_s = r_s^*),$$

which then defines the phase difference between the scattering reflection and transmission coefficients to be π as one might expect because of the assumed symmetric coupling between the two polarizations across the scattering plane. On physical grounds, we select the solution in which the phase change is on the scattered field.

In the following (Figs. 85-93), the Q values given are the loaded Q's (Including coupling loss) and the detuning of the incident light from resonance with mode i ($i = 1, 2$) is given by ν_i. Then, as in Eq. (29), $\delta_i = 2\pi n_{eff} L \nu_i / c$ (the two modes, though orthogonal, are assumed to have the same n_{eff}). In Figs. 85-88, $\lambda = 1.55$ μm was assumed.

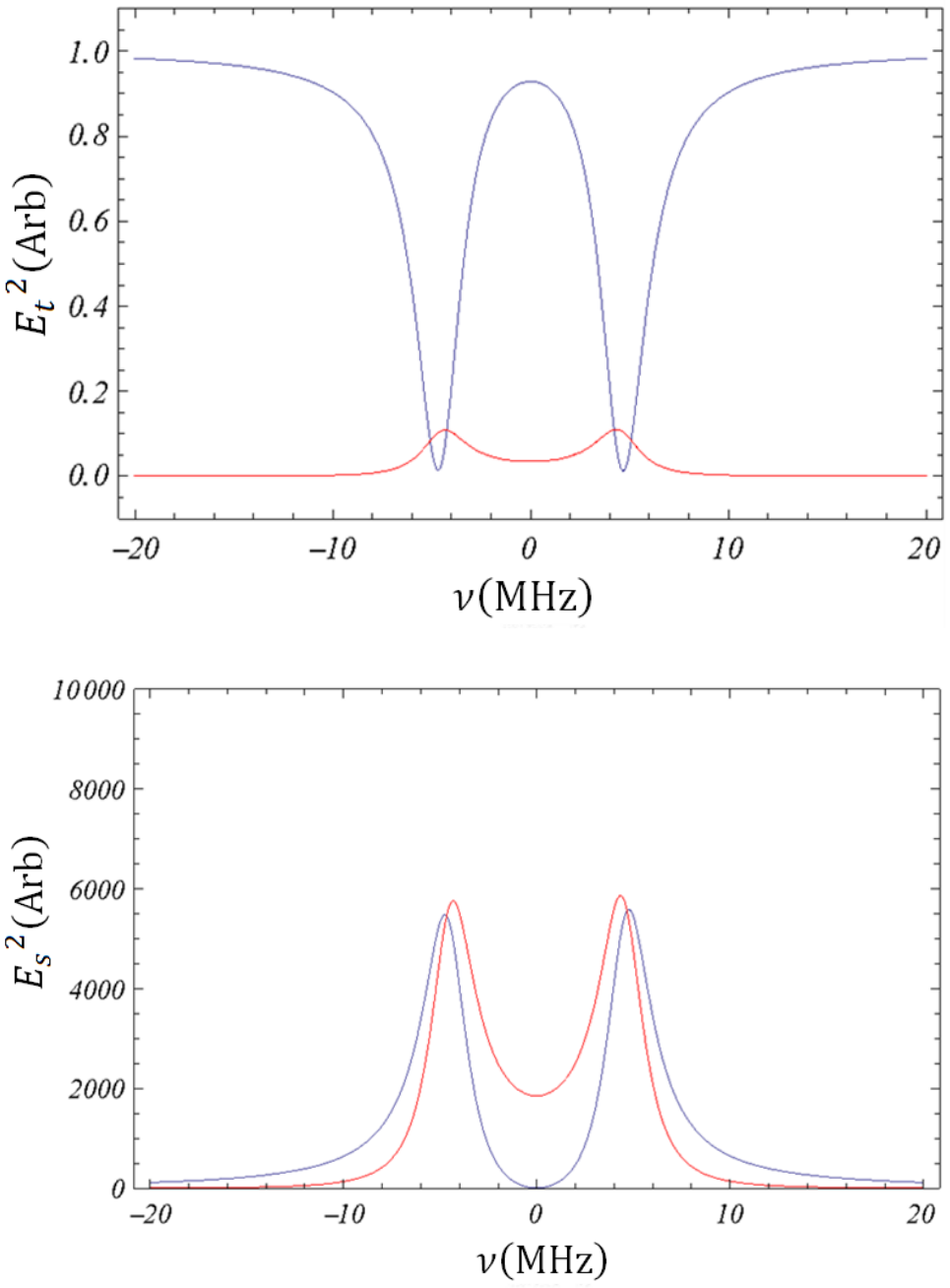

Figure 85. Mode splitting expected from internal scattering for a critically coupled $Q_1 \approx 3 \times 10^8$ *pump mode (blue) and critically coupled* $Q_2 \approx 4 \times 10^7$ *orthogonal mode (red) with* $\nu_1 = \nu_2 \equiv \nu$.

Setting $r_s = i\,\chi$ we find that the fields exhibit symmetric splitting even for small scattering power coefficients $|\chi|^2 \approx 10^{-8}$ as seen in Fig. 85 above for a cavity pumped with only one polarization. The reader may note that what we have done is a generalization of the coupled-resonator model. This generalization covers any power transfer effects between resonances, whether in another cavity or within the same cavity. Furthermore, it also models backscattering within the cavity, and the mode splitting due to it [55], by simply changing the interpretation of the scattering coefficients. When considering backscattering our predicted onset of induced mode splitting is in good agreement with the amplitudes discussed in the literature [55]. Thus the generalized model also predicts both CRIT and CRIA behavior but the particular intermodal polarization coupling model above has one interesting feature that could not occur in the previous model. Because the interaction is occurring between modes of the same cavity, each with a distinct linear polarization, we can see interference between the modes for certain choices of the incident polarization state.

That is, when the incident polarization has some particular phase relationship between the orthogonal components, e.g., elliptically polarized, we would expect a change in the interference observed in the system throughput as seen in Fig. 86 below.

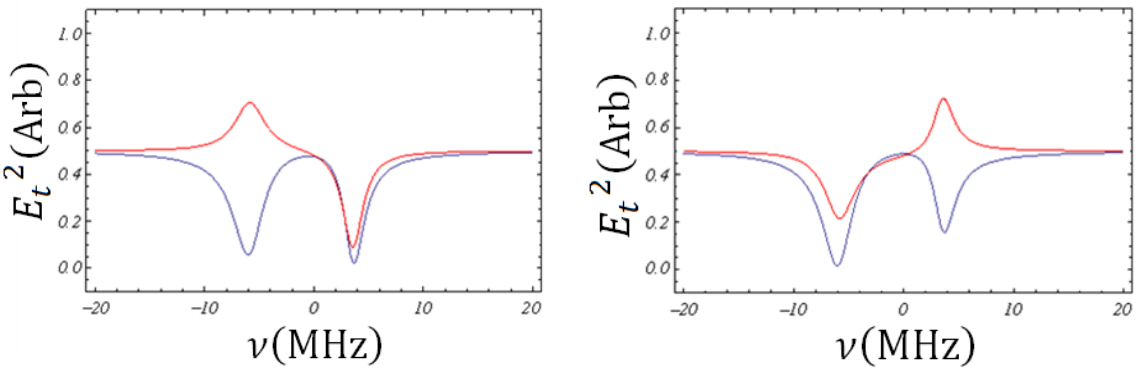

Linearly polarized at 45^o (+ in Quadrant 1) *Linearly polarized at 45^o (+ in Quadrant 3)*

Figure 86. Mode splitting interference expected from internal scattering for a critically coupled $Q_1 \approx 3 \times 10^8$ pump mode (blue) and critically coupled $Q_2 \approx 4 \times 10^7$ orthogonal mode (red) with $\nu_2 \equiv \nu$ and $\nu_1 \equiv \nu + 4.5$ MHz. The cavity is pumped with a 45° linear polarization pointing into the first quadrant (left) and third quadrant (right).

These features are unique to a cavity with internal mode couplings in the sense that no external effects can lead to this type of phase dependence on linearly polarized pump fields. In principle, then, measurement of this cavity response can allow one to construct the Stokes vector for any arbitrary polarization state incident on the system without the need for additional external waveplates.

It is also of note here that mode splitting will only occur for relatively strong scattering given modes which are both undercoupled. Interestingly, for one linear polarization (TE or TM) if the pump mode of input power P_{f1} is undercoupled and the orthogonal mode is so strongly overcoupled that it would not be experimentally observable the scattering power coefficient which is required to produce experimentally observable effects is reduced by more than two orders of magnitude for the same modes to $|\chi|^2 \approx 10^{-10}$ as seen in Fig. 87 below. The amount of power transferred into the orthogonal mode and then out to the pump fiber, P_{t2}, is the product of the circulating power of the pump mode P_{s1}, the scattering power coefficient

$|\chi|^2 = \mathfrak{s}$, the orthogonal mode transmission coefficient T_2 and four times the inverse of the total round-trip loss γ_2 of the orthogonal mode: $P_{t2} \cong 4\mathfrak{s}P_{s2}T_2/\gamma_2$. Comparing to the case of an undercoupled orthogonal mode, and assuming the orthogonal loaded cavity Q's are roughly the same, $\gamma_{oc} \approx \gamma_{uc}$, and that both cases have the same circulating pump power, if one is to observe identical transmitted orthogonal power for both coupling regimes of the orthogonal modes we must then have

$$\frac{\mathfrak{s}_{oc}}{\mathfrak{s}_{uc}} = \frac{T_{uc}}{T_{oc}}, \tag{136}$$

which, given $T_{oc} \gg T_{uc}$, leads to the dramatically lower scattering coefficients for overcoupled modes, $\mathfrak{s}_{oc} \ll \mathfrak{s}_{uc}$, alluded to above.

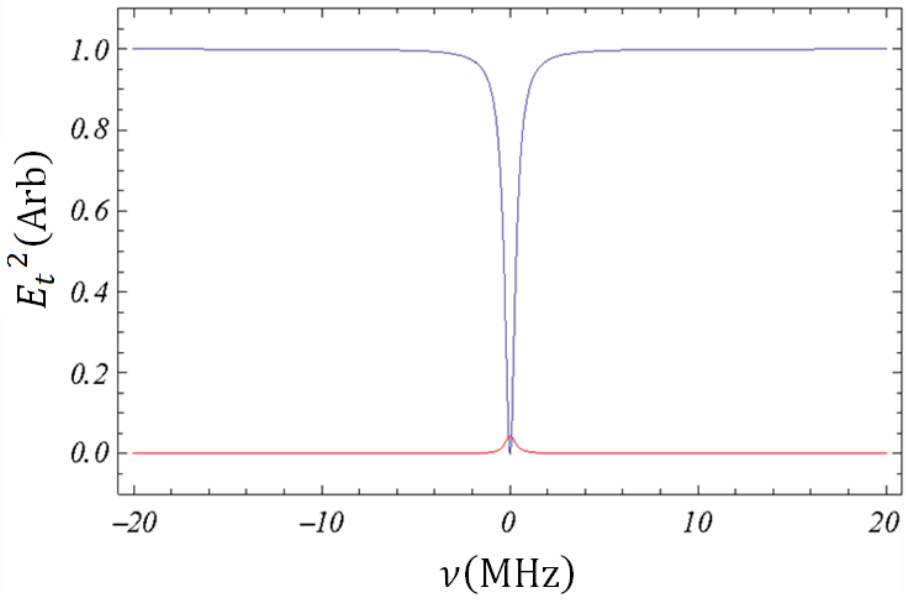

Figure 87. Production of CPC orthogonal polarization peaks from internal scattering for a critically coupled $Q_1 \approx 3 \times 10^8$ pump mode (blue) and critically coupled $Q_2 \approx 4 \times 10^7$ orthogonal mode (red) with $\nu_1 = \nu_2 \equiv \nu$.. Here the scattering coefficient is $|\chi|^2 \approx 10^{-10}$.

Furthermore, when the orthogonal mode is strongly overcoupled, its additional outcoupling losses tend to increase its spectral width, thus increasing the probability of coincidental co-resonances between it and the pump mode as seen in Fig. 88 below.

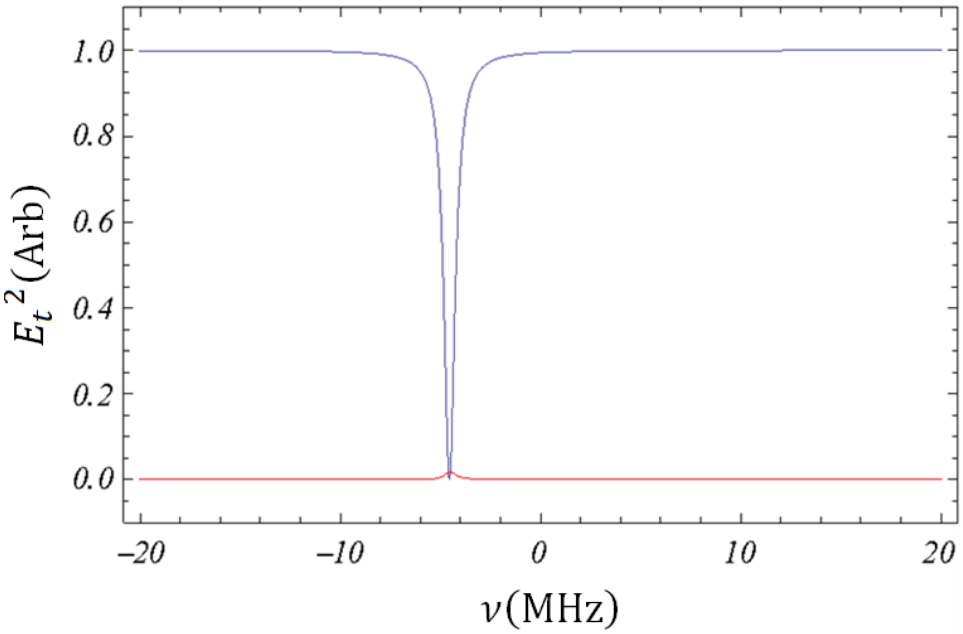

Figure 88. Increased probability of CPC orthogonal polarization peaks from internal scattering for the critically coupled $Q_1 \approx 3 \times 10^8$ detuned pump mode (blue) and the strongly overcoupled ($m = 0.04$) $Q_2 \approx 4 \times 10^7$ orthogonal mode (red) with $\nu_2 \equiv \nu$ and $\nu_1 \equiv \nu + 4.5$ MHz. Here the scattering coefficient is $|\chi|^2 \approx 10^{-10}$.

Because we have previously observed that both the alignment of the polarization analyzer to the cavity basis (DPC) and the incident pump polarization state (IPC) will affect the experimental observations of the system we must construct a model of not just the cavity interactions, but rather the entire experimental apparatus. We begin by setting the phase difference between pump polarization components. This is done in a simple manner (because we are only interested in components and not the full Stokes vector) as

$$E_{f1} = cos(\eta)\sqrt{P_i}, \tag{137}$$

$$E_{f2} = sin(\eta)\sqrt{P_i}e^{i\phi},$$

were P_i is the incident power, η the mean angle the polarization makes with respect to the cavity basis and ϕ the phase angle between the polarization components. We then construct the total throughput field from the cavity and fiber fields as

$$\boldsymbol{E_t} = \langle (r_1 E_{f1} + it_1 E_{s1}), (r_2 E_{f2} + it_2 E_{s2}) \rangle^T. \tag{138}$$

Thus the fields and power observed in the polarization analyzer basis will be,

$$\boldsymbol{E_A} = \begin{pmatrix} \cos(\Omega) & -\sin(\Omega) \\ \sin(\Omega) & \cos(\Omega) \end{pmatrix} \cdot \boldsymbol{E_t}, \tag{139}$$

$$P_{A1} = |\boldsymbol{E_A} \cdot \langle 1,0 \rangle|^2,$$

$$P_{A2} = |\boldsymbol{E_A} \cdot \langle 0,1 \rangle|^2,$$

where Ω is the angle the polarization analyzer makes to the cavity basis, $\boldsymbol{E_A}$ is total vector field incident on analyzer with power components P_{A1} and P_{A2} observed on detectors 1 and 2 respectively. Finally, the power observed on the intensity detector will be

$$P_I = \boldsymbol{E_t}^* \cdot \boldsymbol{E_t} = \boldsymbol{E_A}^* \cdot \boldsymbol{E_A} = P_{A1} + P_{A2} \tag{140}$$

The full model as derived above is a dynamic model of the system in the sense that without changing the modes of the cavity under observation, the lab conditions can be dynamically varied and the model must remain predictive. Thus the dynamic response in itself can be used as a verification tool.

Experimental verification of the model:

We are not directly able to measure the scattering amplitude between cavity modes. However, using dynamic modeling we can repeatedly probe the scattering response of a given set of coupled orthogonal cavity modes, without perturbing them, by repeatedly varying the external system parameters (incident polarization angle and phase, detector angle) and use the homogeneity of the repeated fit to the model to infer the actual scattering amplitude. To do this we first gain as much information as possible for both cavity modes of interest by pumping the cavity with either a TE or TM polarized pump. This allows us to measure cavity coupling and intrinsic loss in a least-perturbation regime, as well as the relative detuning between cavity modes. While we cannot, without further analysis, know the phase of the incident polarization, we can use the equipment in place to determine information about the incident polarization. For instance, if we observe that off resonance the measured power in each detector of our analyzer is rotationally invariant in Ω we know that the pump is circularly polarized. Linear polarization and angle can be determined by rotation of the analyzer and the requirement of power observation of only P_{A1} or P_{A2}. Furthermore, while the phase is not known, we can use the combination of the above technique and the non-symmetric cavity response on resonance (similar to Fig. 86) to find that we have changed the handedness of the pump polarization. This is done iteratively for many pump polarizations, and through requiring that the model fit all, we are able to reduce the uncertainty in the inferred scattering coefficient in a statistical manner. The external parameters are varied in Figs. 89-93 over many incident polarization states and detector angles and in each we require predictive dynamic modeling accuracy. The experimental data (black) is simultaneously fit to the predicted behavior for both cavity polarizations, TE (blue) and TM (red), while the intensity traces are only analyzed for structural agreement with the model (pink). The experiment was conducted at a wavelength of 1.55 μm for undercoupled

(TE, TM) modes with quality factors (Q_1, Q_2) and dip depths (m_1, m_2) of (6.9, 7.3)$\times 10^7$ and (0.68, 0.58) respectively.

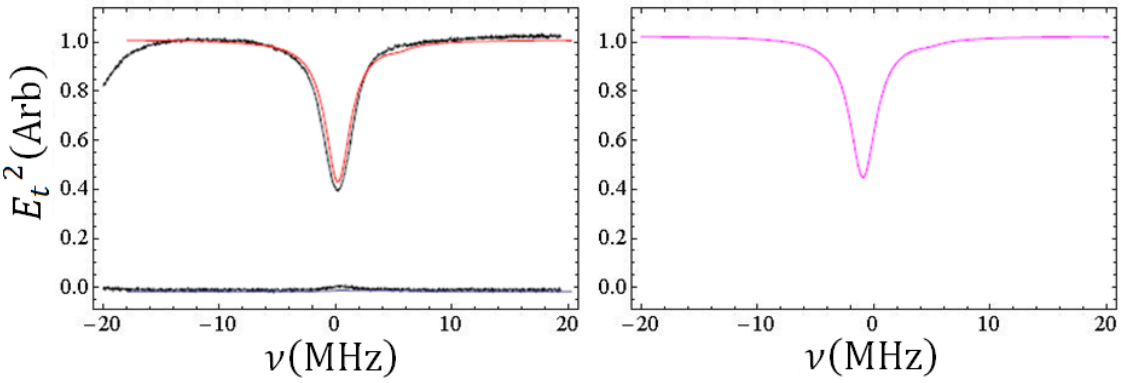

Figure 89. Experimental and theoretical response of the cavity for an approximately pure TM input polarization with $\nu_2 \equiv \nu$ *and* $\nu_1 \equiv \nu - 1$ MHz.

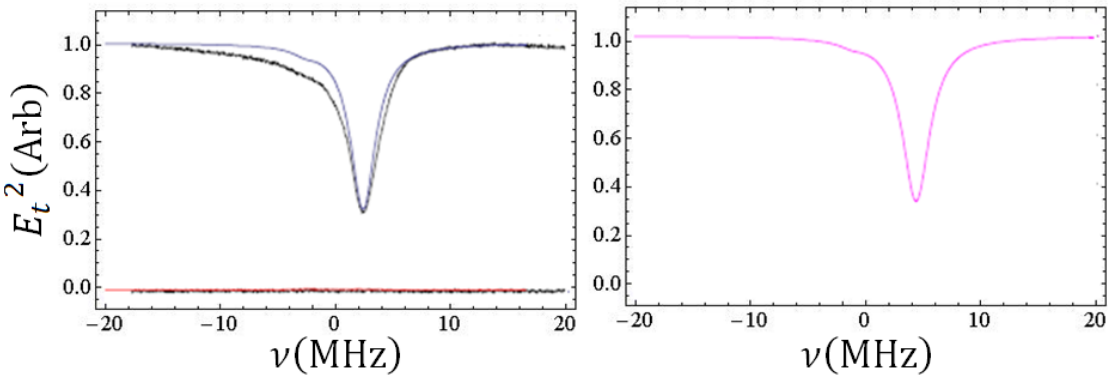

Figure 90. Experimental and theoretical response of the cavity for an approximately pure TE input polarization with $\nu_2 \equiv \nu$ *and* $\nu_1 \equiv \nu - 2$ MHz..

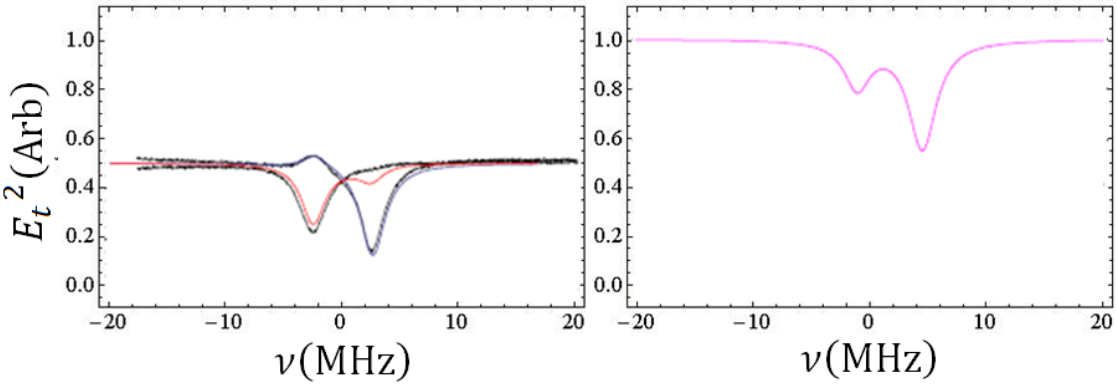

Figure 91. *Experimental and theoretical response of the cavity for an approximately known incident linear polarization at an angle of* $\boldsymbol{\Omega} = 45^{\circ}$ *with* $\nu_2 \equiv \nu$ *and* $\nu_1 \equiv \nu - 2$ MHz. *From the model we find that the field vector points into the first quadrant (*$\phi \approx 0$*).*

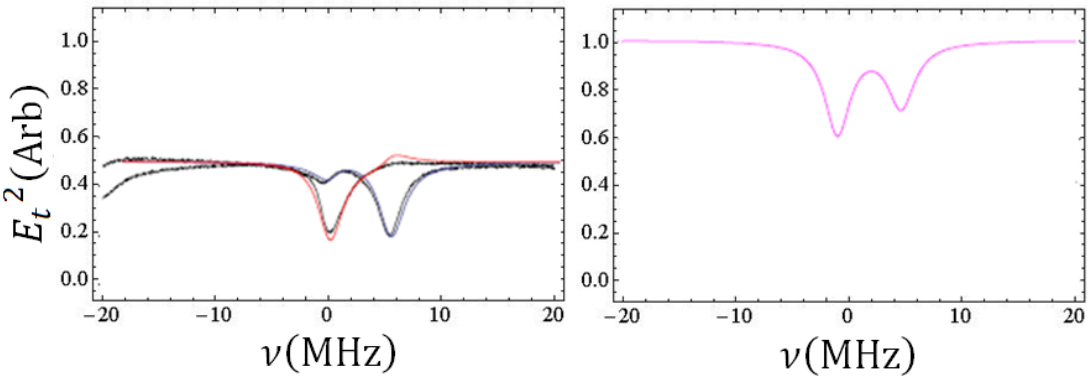

Figure 92. Experimental and theoretical response of the cavity for a known incident elliptic polarization at an angle of $\Omega = 45^{\circ}$ *with* $\nu_2 \equiv \nu$ *and* $\nu_1 \equiv \nu - 2$ MHz. *From the model we find that the field vector points into the third quadrant (*$\phi \approx 1.2\,\pi$*).*

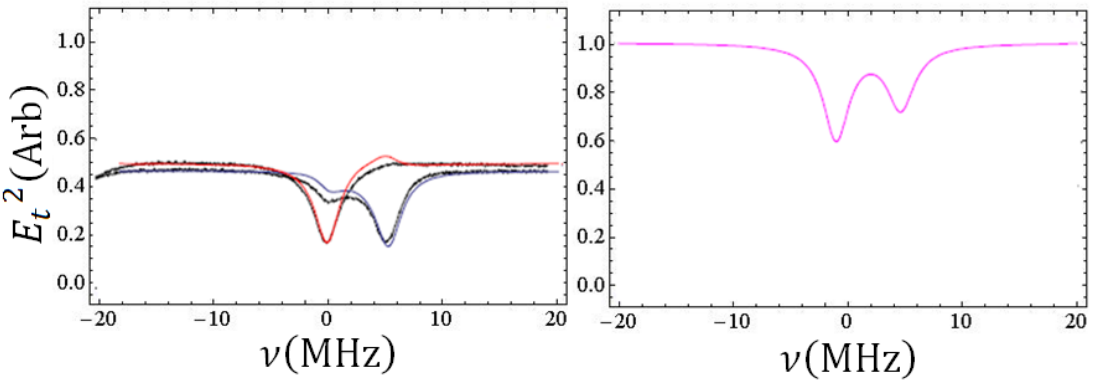

Figure 93. Experimental and theoretical response of the cavity for a known incident elliptic polarization at an angle of $\Omega = 45°$ *with* $\nu_2 \equiv \nu$ *and* $\nu_1 \equiv \nu - 2$ MHz. *From the model we find that the field vector points into the third quadrant (*$\phi \approx 0.85\,\pi$*).*

From the above fits we can infer that the cross polarization scattering power coefficient is roughly $|\chi|^2 \approx 2.5 \times 10^{-9}$ which is reasonable, given that the expected upper limit value for all scattering loss is roughly 5×10^{-8} [31] .

As another method of verification we can also look at the probability of observing a CPC peak given a particular known coupling regime for the orthogonal modes. We take a particular cavity and place it in contact with a thick region of the tapered coupling fiber such that the strongest coupled pump mode has a dip of 50% and is undercoupled. We then know that all modes, visible or otherwise, are undercoupled, and we collect the number of CPC peaks and the overall number of observable resonances to find the average probability of observing orthogonal power above our uncertainty (roughly 2% of the pump power) given an observable pump resonance. We then increase the coupling such that both undercoupled and overcoupled modes are available, by placing the cavity at a thin region of the fiber, such that the deepest modes are critically coupled. The same data is taken to find the probability of observation. Just as predicted from the ring cavity model, the probability of observing a CPC peak given an observable pump resonance is far larger when overcoupled modes are present, as compared to

the case of an undercoupled spectrum. Further, the amount of power transmitted into the fiber in the orthogonal polarization is approximately 30x larger for an overcoupled spectrum as compared to an undercoupled spectrum, as seen in Table 2 below.

Approximate Coupling Regime of TE Pump Spectrum	*Number of Observable Pump Modes per GHz*	*Percent of Modes Producing CPC Power Greater than 2% of Pump Power*	*Peak CPC Power Compared to Pump Power*	*Mean CPC Power Compared to Pump Power*
Undercoupled $(\bar{m} = 0.2)$	28	0%	0.56%	0.14%
Critically Coupled $(\bar{m} = 0.75)$	60	10%	4.8%	1.9%
Overcoupled $(\bar{m} = 0.35)$	158	30%	13.6%	4.0%

Table 2. Comparative analysis of the probability of observing a significant CPC event given a particular coupling regime in the TE pump polarization.

Discussion:

We have demonstrated that the observed CPC peaks are the result of two independent processes: direct polarization conversion (DPC) and internal polarization coupling (IPC). The DPC has been shown to stem from a polarization basis misalignment between the cavity and detector. Further, the IPC has been shown to be the result of an internal intermodal coupling mechanism by demonstrating cross polarization interference when the cavity is pumped with a linearly polarized source at an angle of 45°. Without internal processes no interference would be expected as the states are formally orthogonal. We have further produced a generalized ring cavity model which treats not only CPC but also backscattering and multiresonator couplings, where in each case mode-splitting, CRIT and CRIA can be expected. This generalized model was used to construct a dynamic model of the experimental apparatus accounting for geometric and

phase effects. This dynamic model has been used to directly measure the phase angle between orthogonal polarization components of the pump field. This could prove to be a beneficial method of measuring an arbitrary polarization state of laser light in optical fibers, *in situ*, in a one step process. While we have not unambiguously demonstrated that these internal couplings are driven by internal scattering centers the predicted amplitudes are in reasonable agreement with both theoretical predictions [31, 56] and previous measures of backscattering within these types of cavities [31, 55].

Chapter 6 Summary of Conclusions

Coupled mode theory, as applied to fiber-microsphere coupling, has been reformulated such that the fields and associated coordinate transforms are fully vectoral. Previous treatments have used scalar approximations, due to limited available computational power, which lead to debate of energy conservation centered on nonsymmetrical input/output coupling predictions. Furthermore, this previous treatment also contained non-unitary coordinate transforms when misalignments in the waveguides were included leading to skewed results. My reformulated vector treatment has ended the debate on energy conservation as the input/output coupling is found to be symmetric to within numeric precision. My treatment has further allowed for misalignments in the system to be fully characterized. This model was then applied to cross polarization couplings, which occurs due to non-uniformity in the fiber polarization; the results set an upper bound on the expected coupling strength. Unfortunately, the calculated cross polarization input/output couplings are not symmetric due to the neglect of the adjacent dielectric interface on the waveguide modes. Proper modification of the fields at the interface is expected to symmetrize the coupling. This type of coupling has been found to be weak in comparison to direct coupling, and for most applications, can be safely neglected. Finally, these predictions of coupling strength serve to verify the weak coupling assumptions used in the ring cavity models.

Coupled mode theory was also used for the first time to treat coupling between microresonators. The results of these calculations are critical in understanding coupled

resonator effects. I have found that the peak coupling strengths, for either TE or TM polarizations, are slightly larger than those of fiber-microsphere coupling and they occur between fundamental microsphere modes. Radial mode coupling is found to be larger, in general, than polar order mode coupling due to the curved geometry of the interface which leads to a rapid decrease in coupling as polar mode order is increased. For radial mode orders coupling strength is dominated by phase mismatch between dissimilar mode orders. Much like fiber-microsphere coupling TE polarized modes are found to couple roughly ten times more strongly than TM polarized modes. Finally, these results were used in a modified coupled ring cavity model and compared with experiment. The results are in good agreement.

I have constructed a new type of microresonator, a spheriod suspended on a tapered fiber. This resonator has very limited thermal conduction pathways into the suspension mechanism, while maintaining high mechanical strength, allowing characterization of thermal conduction into the local atmosphere. Characterization of the efficiency of this transfer has allowed us to predict the thermal accommodation coefficient with an unprecedented accuracy which is needed to further measure the fraction of intrinsic loss due to absorption in bistability experiments. This absorption loss has been attributed to a molecular layer of water on the surface of an uncoated sphere in good agreement with previous work. Measurements of absorption loss serve to verify the assumptions of weak absorption used in the derivation of the ring cavity models.

I have developed a novel technique for determining the cavity quality factor and coupling regime. I have applied phase sensitive cavity ringdown to the through signal of the fiber-microsphere system. This technique includes interference effects between the output field of the cavity and the remaining field of the pump fiber which causes the observed phase shift to depend on the input modulation frequency. Theoretical modeling of this response has allowed

me to empirically maximize the observed phase shift from the reference signal allowing increased precision in these measurements. High precision measurements taken in this manner have been compared to more traditional methods (spectral width, transient fill decay cycle and cavity ringdown) and not only are they in good agreement, they demonstrate that the assumption of limited mode dephasing in the ring cavity model is valid.

We have demonstrated a number of novel methods for plasmonically enhancing the evanescent field of the cavity. In previous studies gold nanorods were chemically grown on the surface of the microsphere which has limited controllability. In the new methodology, gold nanorods are grown in solution and then processed to control the desirable characteristics. The microsphere's surface is then chemically modified in a manner that both preserves the cavity quality factor, which is novel, and charges it for Columbic adhesion of the gold nanorods. We have demonstrated enhancement at 800 nm which is comparable to previous studies. Furthermore, we have demonstrated large enhancement at the much longer telecommunication wavelengths around 1550 nm. Unfortunately, we have found that intrinsic scattering loses from the non-resonant gold structures on the surface are much larger at these wavelengths and additional work is needed to increase nanorod yield and homogeneity in solution prior to application to the cavity. Furthermore, I have developed techniques based on both crystal growth and dielectrophoresis that allow for the growth of extreme aspect ratio composite nanowires. The aspect ratio of these composite wires is as high as 1000. I have used these composite nanowires to verify the localization of plasmonic evanescent enhancement. These nanowires have been shown to not only dramatically increase coupling but also intrinsic loss. For these nanowires to be of greater benefit, work must still be conducted to decrease non-contributing elements which increase cavity loss.

I have used plasmonically enhanced resonators in a number of novel potentially beneficial applications. I have demonstrated an increase in sensitivity to analyte absorption over an unenhanced sample. I have further demonstrated that an enhanced resonator is capable of producing measurable Raman scattering signals which could dramatically increase the usefulness of traveling wave evanescent sensors for species characterization. Finally, using saturation of the plasmonic resonance with a strong pump beam I have demonstrated all optical control of coupling which could be valuable in ultrafast optical switching and optical delays. In each of these potential applications I have only demonstrated proof of concept work and much work remains to be done on each application in the future.

I have been the first to observe and characterize intermodal polarization coupling within the microresonator system, a never before treated fundamental effect. To understand this effect I have generalized the simple ring cavity model to allow for arbitrary coresonant mode coupling. This generalized model can be used to treat coupled resonators, mode splitting due to backscatter within the cavity, as well as intermodal polarization coupling within the cavity. The ring cavity model was used to construct a larger model of the experimental lab by the inclusion of both an arbitrary input polarization state and polarization basis misalignment between the cavity and detector to split the experimentally observed polarization effects into a trivial effect (DPC) and the never before seen fundamental effect (IPC). Using the model dynamically, in the sense that the modes are left unperturbed and external parameters are varied, I have shown good agreement with experimental results that allow for inferred measure of both the polarization scattering amplitude within the cavity and phase of an arbitrary incident polarization state. Work remains to be done on controlling the scattering amplitude to either mitigate IPC in telecommunication devices (switches, multiplexers) or increase IPC to create fiber coupled polarization analyzers.

Chapter 7 Bibliography

1. D. W. Vernooy, A. Furusawa, N. P. Georgiades, V. S. Ilchenko, and H. J. Kimble, "Cavity QED with high-Q whispering gallery modes," Phys Rev A **57**, R2293-R2296 (1998).
2. D. Braunstein, A. M. Khazanov, G. A. Koganov, and R. Shuker, "Lowering of threshold conditions for nonlinear effects in a microsphere," Phys Rev A **53**, 3565-3572 (1996).
3. A. T. Rosenberger, "Nonlinear Optical Effects in the Whispering-Gallery Modes of Microspheres," in *Operational Characteristics and Crystal Growth of Nonlinear Optical Materials*, (SPIE, 1999), 179-186.
4. S. I. Shopova, G. Farca, A. T. Rosenberger, W. M. S. Wickramanayake, and N. A. Kotov, "Microsphere whispering-gallery-mode laser using HgTe quantum dots," Appl Phys Lett **85**, 6101-6103 (2004).
5. M. Cai, O. Painter, K. J. Vahala, and P. C. Sercel, "Fiber-coupled microsphere laser," Opt Lett **25**, 1430-1432 (2000).
6. V. V. Vassiliev, V. L. Velichansky, V. S. Ilchenko, M. L. Gorodetsky, L. Hollberg, and A. V. Yarovitsky, "Narrow-line-width diode laser with a high-Q microsphere resonator," Opt Commun **158**, 305-312 (1998).
7. T. J. Kippenberg and K. J. Vahala, "Cavity opto-mechanics," Opt Express **15**, 17172-17205 (2007).
8. A. T. Rosenberger, "Analysis of whispering-gallery microcavity-enhanced chemical absorption sensors," Opt Express **15**, 12959-12964 (2007).
9. G. Farca, S. I. Shopova, and A. T. Rosenberger, "Cavity-enhanced laser absorption spectroscopy using microresonator whispering-gallery modes," Opt Express **15**, 17443-17448 (2007).
10. F. C. Blom, D. R. vanDijk, H. J. W. M. Hoekstra, A. Driessen, and T. J. A. Popma, "Experimental study of integrated-optics microcavity resonators: Toward an all-optical switching device," Appl Phys Lett **71**, 747-749 (1997).
11. S. Liu and Y. Chen, "Optical fiber ring cavity being able to store incident beam and it's applications," Journal of Modern Optics **44**, 109-117 (1997).
12. A. E. Bate, "Note on the whispering gallery of St Paul's Cathedral, London," P Phys Soc **50**, 293-297 (1938).
13. B. E. Little, J. P. Laine, and H. A. Haus, "Analytic theory of coupling from tapered fibers and half-blocks into microsphere resonators," J Lightwave Technol **17**, 704-715 (1999).
14. M. J. Humphrey, "Calculation of Coupling Between Tapered Fiber Modes and Whispering-Gallery Modes of a Spherical Microlaser," (Oklahoma State University, Stillwater, OK, 2004).
15. A. T. Rosenberger, (personal communication, 2003-2009).
16. M. J. Humphrey, E. Dale, A. T. Rosenberger, and D. K. Bandy, "Calculation of optimal fiber radius and whispering-gallery mode spectra for a fiber-coupled microsphere," Opt Commun **271**, 124-131 (2007).

17. E. Hecht and A. Zajac, *Optics,* 2nd ed. (Addison-Wesley Pub. Co., Reading, Mass., 1987), 676 p.
18. S. T. Thornton and J. B. Marion, *Classical dynamics of particles and systems,* 5th ed. (Brooks/Cole, Belmont, CA, 2004), 656 p.
19. J. D. Jackson, *Classical electrodynamics,* 3rd ed. (Wiley, New York, 1999), 808 p.
20. W. P. Huang, "Coupled-Mode Theory for Optical Wave-Guides - an Overview," J Opt Soc Am A **11**, 963-983 (1994).
21. A. W. Snyder and J. D. Love, *Optical waveguide theory*, Science paperbacks 190 (Chapman and Hall, London ; New York, 1983), 734 p.
22. W. W. Hansen, "A new type of expansion in radiation problems," Phys Rev **47**, 139-143 (1935).
23. J. A. Stratton, *Electromagnetic theory,* 1st ed., International series in physics (McGraw-Hill book company, inc., New York, London, 1941), 615 p.
24. H. A. Haus and W. Huang, "Coupled-Mode Theory," Proceedings of the IEEE **79**, 13 (1991).
25. J. R. Pierce, "Coupling of Modes of Propagation," J Appl Phys **25**, 179-183 (1954).
26. R. W. Boyd, *Nonlinear optics,* 2nd ed. (Academic Press, San Diego, CA, 2003), 578 p.
27. "CRC handbook of chemistry and physics," (Chapman and Hall/CRCnetBASE, Boca Raton, FL, 1999).
28. T. Toyoda and M. Yabe, "The Temperature-Dependence of the Refractive-Indexes of Fused-Silica and Crystal Quartz," J Phys D Appl Phys **16**, L97-L100 (1983).
29. J. P. Rezac, "Properties and Applications of Whispering-Gallery Mode Resonances in Fused Silica Microspheres," (Oklahoma State University, Stillwater, 2002).
30. S. C. Saxena and R. K. Joshi, *Thermal accommodation and adsoption coefficients of gases*, CINDAS data series on material properties (McGraw-Hill, New York, 1981).
31. M. L. Gorodetsky, A. A. Savchenkov, and V. S. Ilchenko, "Ultimate Q of optical microsphere resonators," Opt. Lett. **21**, 453-455 (1996).
32. D. W. Vernooy, V. S. Ilchenko, H. Mabuchi, E. W. Streed, and H. J. Kimble, "High-Q measurements of fused-silica microspheres in the near infrared," Opt Lett **23**, 247-249 (1998).
33. J. Barnes, B. Carver, J. M. Fraser, G. Gagliardi, H. P. Loock, Z. Tian, M. W. B. Wilson, S. Yam, and O. Yastrubshak, "Loss determination in microsphere resonators by phase-shift cavity ring-down measurements," Opt Express **16**, 13158-13167 (2008).
34. A. Naweed, G. Farca, S. I. Shopova, and A. T. Rosenberger, "Induced transparency and absorption in coupled whispering-gallery microresonators," Phys Rev A **71**, - (2005).
35. H. Raether, *Surface plasmons on smooth and rough surfaces and on gratings*, Springer tracts in modern physics 111 (Springer-Verlag, Berlin ; New York, 1988), pp. x, 136 p.
36. S. Link, M. B. Mohamed, and M. A. El-Sayed, "Simulation of the Optical Absorption Spectra of Gold Nanorods as a Function of Their Aspect Ratio and the Effect of the Medium Dielectric Constant," J PhysChem B **103**, 3073-3077 (1999).
37. J. P. Wilcoxon, J. E. Martin, and P. Provencio, "Optical properties of gold and silver nanoclusters investigated by liquid chromatography," J Chem Phys **115**, 998-1008 (2001).
38. M. Pereiro and D. Baldomir, "Structure of small silver clusters and static response to an external electric field," Phys Rev A **75**, 033202 (2007).
39. P. K. Jain, S. Eustis, and M. A. El-Sayed, "Plasmon Coupling in Nanorod Assemblies: Optical Absorption, Discrete Dipole Approximation Simulation, and Exciton-Coupling Model," The Journal of Physical Chemistry B **110**, 18243-18253 (2006).

40. N. R. Jana, L. Gearheart, and C. J. Murphy, "Wet Chemical Synthesis of High Aspect Ratio Cylindrical Gold Nanorods," The Journal of Physical Chemistry B **105**, 4065-4067 (2001).
41. S. I. Shopova, C. W. Blackledge, and A. T. Rosenberger, "Enhanced evanescent coupling to whispering-gallery modes due to gold nanorods grown on the microresonator surface," Appl Phys B-Lasers O **93**, 183-187 (2008).
42. S. C. Hsieh, S. Meltzer, C. R. C. Wang, A. A. G. Requicha, M. E. Thompson, and B. E. Koel, "Imaging and manipulation of gold nanorods with an atomic force microscope," J Phys Chem B **106**, 231-234 (2002).
43. B. Ozturk, B. N. Flanders, D. R. Grischkowsky, and T. D. Mishima, "Single-step growth and low resistance interconnecting of gold nanowires," Nanotechnology **18**, 175707 (2007).
44. C. Sonnichsen, T. Franzl, T. Wilk, G. v. Plessen, and J. Feldmann, "Plasmon resonances in large noble-metal clusters," New Journal of Physics **4**, 93.91-93.98 (2002).
45. F. Neubrech, T. Kolb, R. Lovrincic, G. Fahsold, A. Pucci, J. Aizpurua, T. W. Cornelius, M. E. Toimil-Molares, R. Neumann, and S. Karim, "Resonances of individual metal nanowires in the infrared," Appl Phys Lett **89**, 253104 (2006).
46. G. Hong-Mei, Z. Zhang-Kai, X. Si, S. Hao, S. Xiong-Rui, L. Min, and W. Qu-Quan, "Intensity-Dependent Optical Nonlinear Absorption and Refraction of Gold Nanorods," Chinese Physics Letters **24**, 3443-3446 (2007).
47. M. Pelton, M. Liu, S. Park, N. F. Scherer, and P. Guyot-Sionnest, "Ultrafast resonant optical scattering from single gold nanorods: Large nonlinearities and plasmon saturation," Phys RevB (Condensed Matter and Materials Physics) **73**, 155419-155416 (2006).
48. S. I. Shopova, C. W. Blackledge, A. T. Rosenberger, and N. F. Materer, "Gold nanorods grown from HgTe nanoparticles directly on various surfaces," Appl Phys Lett **89**, 023120 (2006).
49. Z. Q. Tian, B. Ren, and D. Y. Wu, "Surface-enhanced Raman scattering: From noble to transition metals and from rough surfaces to ordered nanostructures," J Phys Chem B **106**, 9463-9483 (2002).
50. P. Bianucci, C. R. Fietz, J. W. Robertson, G. Shvets, and C. K. Shih, "Whispering gallery mode microresonators as polarization converters," Opt Lett **32**, 2224-2226 (2007).
51. M. L. Gorodetsky and V. S. Ilchenko, "High-Q Optical Whispering-Gallery Microresonators - Precession Approach for Spherical Mode Analysis and Emission Patterns with Prism Couplers," Opt Commun **113**, 133-143 (1994).
52. A. M. Smith, "Birefringence Induced by Bends and Twists in Single-Mode Optical Fiber," Appl Optics **19**, 2606-2611 (1980).
53. H. G. Winful, "Polarization Instabilities in Birefringent Nonlinear Media - Application to Fiberoptic Devices," Opt Lett **11**, 33-35 (1986).
54. P. L. Baldeck, F. Raccah, and R. R. Alfano, "Observation of Self-Focusing in Optical Fibers with Picosecond Pulses," Opt Lett **12**, 588-589 (1987).
55. B. E. Little, J. P. Laine, and S. T. Chu, "Surface-roughness-induced contradirectional coupling in ring and disk resonators," Opt Lett **22**, 4-6 (1997).
56. L. Deych, (personal communication, 2009).

VITA

ELIJAH BRANDON DALE

Candidate for the Degree of

Doctor of Philosophy

Thesis: COUPLING EFFECTS IN DIELECTRIC CAVITIES

Major Field: Physics

Biographical:

Personal Data: Born in Arizona on April 1, 1977

Education: Received Bachelor of Science degree in Physics from Oklahoma State University, Stillwater, OK in Dec. 2005; Completed the requirements for the Doctor of Philosophy degree in Physics at Oklahoma State University in May 2010.

Experience: Owner, E and M Mechanical Services from 1995-1996. General Manger, Silver Dollar Café from 1996-1998. Geotechnical lab technician and field inspector, Terracon Consultants from 1998-2002. Employed by Oklahoma State University, Dept. of Physics, as an undergraduate research assistant from 2003-2006. Employed by Oklahoma State University, Dept. of Physics, as a graduate teaching assistant and graduate research assistant from 2006 to present.

Professional Memberships: American Physical Society, Optical Society of America

Name: Elijah Brandon Dale Date of Degree: May 2010

Institution: Oklahoma State University Location: Stillwater, Oklahoma

Title of Study: COUPLING EFFECTS IN DIELECTRIC MICROCAVITIES

Pages in Study: 194 Candidate for the Degree of Doctor of Philosophy

Major Field: Physics

Scope and Method of Study: The simple four-mirror ring cavity model of microsphere resonances is extended to include internal polarization coupling and dual-cavity coupling. This model is extended into the time domain allowing measurement of the cavity quality factor and coupling regime using phase sensitive cavity ringdown. Coupled-mode theory is numerically employed to characterize the strength of dual-cavity coupling and direct polarization coupling between fiber and microsphere modes. Furthermore, the microsphere's evanescent field has been enhanced by applying gold nanorods grown in solution directly on the cavity surface. These enhanced resonators are used to demonstrate sensing enhancement and all optical coupling control.

Findings and Conclusions: Time domain phase sensitive cavity ringdown on the through signal is used to show that modal dephasing is below measuremental uncertainty. The calculation of dual sphere coupling predicts that the peak coupling strength is slightly greater than fiber-microsphere coupling and will occur between fundamental cavity modes. It is found that mode phase matching dominates radial mode order coupling while spatial overlap dominates polar mode order coupling. Nanowires, grown from solution, have been grown with aspect ratios in excess of 1000. These wires have been placed directly on the microsphere and used to demonstrate the localization of evanescent field enhancement. Gold nanorods grown in solution have been directly adhered to the cavity surface allowing control of plasmonic character while still in solution. These enhanced cavities have been shown to exhibit similar levels of coupling enhancement at wavelengths of 800 nm to surface grown nanorods (~300) and much larger enhancement at wavelengths of 1550 nm (~1500). These enhanced cavities have been shown to increase sensitivity of traveling wave evanescent sensors. They have also been shown to produce surface enhanced Raman scattering, which has the potential to demonstrate species identification. Optical control of plasmonic enhancement has been demonstrated and used to control the observable dip-depth of the cavity resonance. Finally, internal polarization coupling between orthogonal cavity modes has been observed and understood from a modified ring cavity scattering model; the results are in good agreement with experiment.

ADVISOR'S APPROVAL: Dr. Albert T. Rosenberger